DESIGN OF NOVEL NANOSIZED CERIA-BASED MULTICOMPONENT COMPOSITE OXIDES FOR CATALYTIC APPLICATIONS

Thesis

Submitted to Osmania University

For the Degree of

Doctor of Philosophy

in Chemistry

by

P. Bharali, M.Sc.

Indian Institute of Chemical Technology

Hyderabad – 500 607, India

April – 2009

This thesis is dedicated to my beloved parents – the source of inspiration

Indian Institute of Chemical Technology
(Council of Scientific & Industrial Research)
Uppal Road, Hyderabad - 500 607, India
Tel (O): +91-40-27191714; (R) 27175406
Fax: (O) +91-40-27160921
E-mail: bmreddy@iict.res.in, mreddyb@yahoo.com

Dr. B.M. Reddy
Deputy Director
Inorganic and Physical Chemistry Division

CERTIFICATE

This is to certify that the thesis entitled **"Design of Novel Nanosized Ceria-based Multicomponent Composite Oxides for Catalytic Applications"** submitted by **Mr. P. Bharali** is absolutely based upon his own work under my supervision and that neither this thesis nor any part of it has been submitted for any degree/diploma or any other academic award anywhere before.

Dated: 6th April 2009

(B.M. Reddy)

DECLARATION

I hereby declare that the work presented in this thesis entitled **"Design of Novel Nanosized Ceria-based Multicomponent Composite Oxides for Catalytic Applications"** is entirely original and was carried out by me independently in the Indian Institute of Chemical Technology (IICT) under the supervision of Dr B M Reddy, Deputy Director, IICT. I further declare that it has not formed the basis for the award of any degree, diploma, fellowship or associateship or similar title of any University or Institution.

Date: 6th April 2009 Pankaj Bharali

Inorganic and Physical Chemistry Division
Indian Institute of Chemical Technology
Hyderabad – 500 607, India

ACKNOWLEDGMENT

During the period I have been working for this thesis, a lot of people helped me and supported me in a variety of ways. I am indebted to all of them. Here, I would like to distinguish and express my special thanks.

First of all I would like to express my gratitude to my supervisor Dr B M Reddy, Deputy Director, IICT, Hyderabad, for his support, guidance, advice and valuable discussions during the course of the whole research work presented in this thesis. He has always a lot of good ideas, many of which nobody else has ever thought of. What is still better is that he always has the time to discuss these. I am always indebted to him.

This work would not have been possible without the support of many people namely, Prof Dr W Grünert and Prof Dr M Muhler from Ruhr University, Bochum, Germany; Dr Y Yamada and Dr T Kobayashi from AIST-Osaka, Japan; Prof S E Park from Inha University, Republic of Korea; Dr S Loridant from IRCE-Lyon, France; Prof Dr P G Smirniotis and Dr A Khan from University of Cincinnati, Ohio, USA, and Dr P Lakshmanan from Universite Pierre et Marie Curie, France.

I would like to tender my deepest gratitudes to Dr J S Yadav, Director, IICT and Dr M Lakshmi Kantam, Head, Inorganic and Physical Chemistry Division for the necessary facilities and infrastructure. I also express my gratitude to Dr M Mohan Rao and Dr A Venugopal, Scientists, I & PC Division, IICT for their help and support.

I take this opportunity to convey my hearty admiration to all my teachers from my school days to post graduation level. I also express my thankfulness to the teaching staff of Department of Chemistry, Osmania University, Hyderabad, Department of Chemistry, Gauhati University, Guwahati and Scientific staff of Material Science Division, NEIST, Jorhat. Special appreciations are due to Prof J N Ganguli, Professor, Department of Chemistry, Gauhati University, Guwahati and Dr R L Goswamee, Scientist, Material Science Division, NEIST, Jorhat.

I express my thanks to the technical and supporting staff of IICT for their timely help and support.

Special thanks to all the group members, Pranjal, Thrimurthulu, Patil, Narayana Rao, Krishna Reddy, Thirupathi, and Lakshmi, without whose unconditional help and support, this

study would not have been successful. I also extend my thanks to newly joined group members Hanuma Reddy, Kaviraj, Dhaneswar, Srinivas, Naga Prasad and Basir for their support.

I would like to acknowledge the friends who have always been with me; specially, Ashok, Babita, Lakshindra, Kesur, Sandeep, Gokul da, Anil da, Dipak da, Manash da, Bipul, Kula, Gyan Jyoti, Sanchay, Lakshi, Saitannya, Bhaskar, all my friends from NEIST-Jorhat, all my IICT-hostel mates, and fellow research scholars of I & PC Division, IICT.

Words are few to express my appreciation to my parents, my uncle, my brother, sister, and other family members, Baruah da, Ananta da, Bubul da, and my wife Luish Lema, whose dedication, love, encouragement, and persistent confidence in me has taken the load off my shoulder. At last, I would like to thank everybody who was important to the successful realization of the thesis, as well as expressing my apology that I could not mention personally one by one.

I would like to acknowledge the financial support from the Council of Scientific and Industrial Research (CSIR), New Delhi in the form of junior and senior research fellowships, Department of Science of Technology (DST), New Delhi for travel grant and DAAD, Germany for financial assistance during my stay at Ruhr University of Bochum, Germany.

Date: 6th April 2009 Pankaj Bharali

CONTENTS

CHAPTER 2: EXPERIMENTAL SECTION

CHAPTER 7: CATALYTIC ACTIVITY STUDIES

Abstract

Cerium dioxide (CeO_2) containing materials have attracted much interest in recent years owing to their broad range of applications in various fields, ranging from catalysis to ceramics, fuel cell technologies, gas sensors, solid state electrolytes, ceramic biomaterials, etc., in addition to the classical application of CeO_2 as an additive in the so-called three-way catalysts (TWC) for automotive exhaust treatment. Particularly, the presence of CeO_2 in various catalyst systems has been found to be effective in the promotion of catalytic reactions for CO_2 activation, CO oxidation, CO/NO removal, and catalytic combustion of CH_4. Very recently, it has also been employed in the deNOx catalysis too. The most important property that makes ceria as an excellent catalytic material is its oxygen storage and release capacity (OSC) via the redox shift between Ce^{4+} and Ce^{3+} under oxidizing and reducing conditions, respectively. Despite the widespread use and application, pure ceria has poor thermal stability and known to sinter at high temperatures, which leads to deactivation of the catalyst. Therefore, much effort has been devoted in recent years to design suitable CeO_2-based composite oxide systems, which can enhance the thermal (textural) stability of ceria without diminishing its special features, such as its unique redox properties and its high oxygen mobility. Moreover, the redox and catalytic properties of ceria and its composite oxides are dependent upon some other factors, which include particle size, phase modification, structural lattice defects, and chemical nonstoichiometry. In addition, fine tuning of the particle size of a catalyst in nanometer scale results in increasing the specific surface area and changing its morphology, thus providing a larger number of more reactive edge sites as well as better catalytic performance. Ceria easily forms solid solutions with other transitional-metals and rare-earth elements. Especially, solid solutions of ceria with Group IV transitional-metals deserve particular attention for their applicability in various technologically important catalytic processes. CeO_2–ZrO_2 solid solutions have been employed in various reactions which include three-way catalysis, CO oxidation, methanol decomposition to syngas, steam reforming of ethanol, catalytic combustion of hydrocarbons, catalytic wet oxidation of methane, alcohol dehydration, and so on. Hafnia (HfO_2) and zirconia (ZrO_2) are called twin oxides because of their similar chemical and physical properties. They are iso-structural in the bulk and this close correlation in properties is due to the identical valence states and nearly identical ionic radii for Hf and Zr. Hafnia-based materials can be used in solid electrolytes for fuel cells,

oxygen gas sensors, refractories, coating for oxidation resistance, control rods for nuclear reactor, and so on. Therefore, it was interesting to investigate the structural and catalytic properties of novel nanosized ceria-hafnia composite oxides.

However, the unsupported oxides are susceptible to a fall in the surface area due to sintering and it leads to a decrease in the stability of the structure during high temperature applications thereby loosing its oxygen buffering capacity. In order to exploit them without loosing their unique redox features, it is very essential to synthesize nanocomposites where the active phase is stabilized over a stable inert support. Highly dispersed active oxides deposited on the surface of an inert support have been intensively studied for many years, mainly due to their applications as catalytic systems. The essential requirements of a better support are nonreactivity with the dispersed phase and high specific surface area. The catalytic performances of supported metal oxide catalysts are determined by many parameters, the most important being the metal oxide loading, pretreatment conditions, molecular structure, electronic structure, and support oxide type and composition. Currently, ceria-based systems are usually supported on transition aluminas and titania, with the aim of achieving better dispersion of the active phase and improvement of the oxygen exchange rate. Silica is another most widely available supports with excellent chemical resistance, thermal stability and high specific surface area, which can enhance dispersion and thereby catalytic activity of the dispersed active oxides. In this present investigation, ceria-hafnia and a series of catalytically important supported nanosized ceria-hafnia [CeO_2–HfO_2/M_xO_y; (M_xO_y = SiO_2, TiO_2, and Al_2O_3)] composite oxides possessing high specific surface area, better thermal stability, superior sintering resistance, and desired redox properties have been synthesized. The thermal and structural stability of the supported ceria-based solid solutions are strongly influenced by the synthetic methodology. In this study, soft chemical routes namely coprecipitation and deposition coprecipitation techniques were adopted for preparation of unsupported and supported mixed oxides respectively. The prepared samples were further subjected to thermal treatments from 773 to 1073 K in order to understand the nano-structural evolution and physicochemical characteristics of these complex oxide systems. Various physicochemical characterization techniques namely, thermal analysis (TG-DTA), X-ray diffraction (XRD),

transmission electron microscopy (TEM), Laser Raman spectroscopy (LRS), UV-visible diffuse reflectance spectroscopy (UV-vis DRS), X-ray photoelectron spectroscopy (XPS), Ion scattering spectroscopy (ISS), temperature programmed reduction (TPR), and BET surface area (SA) were employed to investigate these oxide systems. All the synthesized catalysts were evaluated for the potential oxygen storage capacity (OSC), CO oxidation and soot oxidation reaction. A few of the catalytic systems were also evaluated for the selective dehydration of 4-methylpentan-2-ol. The thesis has been organized into seven individual chapters.

Chapter 1 comprised of a thorough literature survey on nanostructured metal oxides with especial emphasis on cerium oxide and its composite oxides including structural, redox properties, and potential applications in catalysis with relevant references. A short introduction to the application of nanostructured metal oxides to different catalytic processes is also included. Importance of supported ceria-based materials has been discussed at length in this chapter. The main objectives and the scope of the present investigation are also clearly outlined.

The experimental procedures and the techniques employed in this investigation are descried in **Chapter 2**. The details pertaining to the preparative methodologies employed to obtain the unsupported and supported ceria-hafnia composite oxides are presented with appropriate references in this chapter. The experimental details related to BET SA, TG-DTA, XRD, LRS, UV-vis DRS, XPS, ISS, and TPR are given with necessary theoretical background. The experimental aspects of the potential OSC measurements, CO oxidation, soot oxidation reaction, and selective dehydration of 4-methylpentan-2-ol are also described in detail in this chapter. For comparison purpose unsupported ceria-zirconia was also prepared and characterized by different techniques and used for catalytic evaluation.

Chapter 3 deals with the preparation and intensive characterization of nanosized CeO_2–HfO_2 composite oxide by various spectroscopic and non-spectroscopic techniques. The CeO_2–HfO_2 (8:2 mole ratio based on oxides) catalyst was prepared by an aqueous coprecipitation method. The sample was subjected to heat treatments from 773 to 1073 K to have information on its thermal stability. For the purpose of comparison, by adopting

similar preparation method nanosized CeO_2–ZrO_2 composite oxide was also synthesized and calcined at different temperatures from 773 to 1073 K and characterized by different techniques. The XRD results suggest that the CeO_2–HfO_2 sample primarily consists of nanocrystalline cubic Ce–Hf oxides with composition $Ce_{0.8}Hf_{0.2}O_2$ over all the calcination temperatures. The samples are thermally quite stable and no phase segregation was observed up to the calcination temperature of 1073 K. On the other hand CeO_2–ZrO_2 crystallizes as cubic $Ce_{0.75}Zr_{0.25}O_2$ and $Ce_{0.6}Zr_{0.4}O_2$ depending on the calcination temperatures. The Raman measurements revealed the existence of cubic ceria-hafnia and ceria-zirconia phase and establish the generation of defects in the lattice leading to the formation of oxygen vacancies. The XPS line shapes and the corresponding binding energies indicated that the Ce is present in both 3+ and 4+ oxidation states and Hf and Zr are in 4+ oxidation states, respectively. ISS measurements indicated surface enrichment of cerium on the external surface of the composite oxide in the case of CeO_2–HfO_2, while such surface enrichment of cerium is not observed for the CeO_2–ZrO_2 sample. It could be confirmed from the plot of intensity ratio of Hf/Ce and Zr/Ce versus number of scans, which showed an increase with the number of scans in the former case, while a nominal decrease of intensity ratio was observed in the latter case. The SEM measurements conferred information on the external surface morphology of the catalysts. The TEM-HREM results confirmed that both the series of Ce-Hf and Ce-Zr-oxide nanocrystals have average particle dimension of ~4–5 nm when calcined at 773 K, and there was a nominal increase in the particle size upon increase of thermal temperature of the catalyst systems to 1073 K. The experimental images revealed that both the Ce-Hf and Ce-Zr-oxides are mainly in the cubic geometry. The UV-vis DRS measurements confer information about $Ce^{4+} \leftarrow O^{2-}$ and $Ce^{3+} \leftarrow O^{2-}$ charge transfer transitions. The TPR measurements were performed using both CO and H_2 as reducing gas for both the catalysts to evaluate the redox nature of the systems. The CO-TPR showed a remarkable lowering of the reduction temperature of the Ce-Hf-oxide compared to pure ceria and Ce-Zr-oxides. On the other hand H_2-TPR showed higher degree of reduction in the case of Ce-Hf than Ce-Zr-oxides. The thermogravimetric analysis under N_2 atmosphere gave information on the thermal behavior of the catalyst systems. BET surface area results showed that the catalysts possess

reasonably high specific surface area even up to highest calcination temperature 1073 K. The results pertaining to the structural characteristic of the nanosized composite oxides of CeO_2–HfO_2 and CeO_2–ZrO_2 systems are complied in this chapter and described in detail.

Chapter 4 deals with the preparation and physicochemical characterization of CeO_2–HfO_2/SiO_2 catalysts by various spectroscopic and non-spectroscopic techniques. The CeO_2–HfO_2/SiO_2 (8:2:10 mole ratio based on oxides) was obtained by a modified aqueous deposition coprecipitation method. These samples were subjected to various thermal treatments in the temperature range from 773 to 1073 K. The addition of silica remarkably enhances the surface area of the final catalyst. The use of silica in its preformed colloidal form gave additional advantage to synthesize highly dispersed nanosized composite oxide of Ce–Hf over silica surface. The XRD results suggest that the CeO_2–HfO_2/SiO_2 sample primarily consists of nanocrystalline cubic Ce–Hf oxides with composition $Ce_{0.8}Hf_{0.2}O_2$ over the amorphous SiO_2 surface at all the calcination temperatures investigated. However, the peak widths of the nanosized materials are so large that it is not easy to draw an exact statement whether small amounts of segregated phases are present or not. The Raman measurements also revealed the existence of cubic ceria-hafnia phase and indicated the formation of oxygen vacancies as a result of generation of lattice defects. The XPS patterns indicated that the Ce is present in both 3+ and 4+ oxidation states and Hf in 4+ oxidation state, respectively. However, stabilization of Ce^{3+} was observed at higher calcination temperatures. The ISS measurements indicated surface enrichment of cerium on the external surface of the composite oxide in the case of 773 K calcined sample, while such surface enrichment of cerium is not observed for the 1073 K calcined sample. It could be confirmed from the plot of intensity ratio of Hf/Ce versus number of scans, which showed an increase with the number of scans in the former case, while a nominal decrease of intensity ratio was observed in the latter case. The SEM measurements conferred information on the external surface morphology of the catalysts. The TEM-HREM results pertaining to CeO_2–HfO_2/SiO_2 indicated well-dispersed Ce–Hf oxide nanocrystals (~3 nm) over the surface of amorphous SiO_2 matrix when treated at 773 K, and there was no apparent increase in the crystallite size upon increasing the thermal treatment temperature to 1073 K. The experimental images revealed that the Ce–Hf- oxides are mainly in the

cubic geometry and exhibit high thermal stability. The UV-vis DRS measurements disclose information about $Ce^{4+} \leftarrow O^{2-}$ and $Ce^{3+} \leftarrow O^{2-}$ charge transfer transitions. The TPR (both CO and H_2) analyses indicated the interesting redox property of the catalyst system. All the results in details pertaining to this catalyst system are compiled in this chapter.

The preparation and structural evolution of CeO_2–HfO_2/TiO_2 system by various state-of-the art sophisticated techniques are presented in detail in **Chapter 5**. The CeO_2–HfO_2/TiO_2 composite oxide (8:2:10 mole ratio based on oxides) was obtained by a deposition coprecipitation method using ultrahigh dilute aqueous solutions of the corresponding metal salts. The addition of titania resulted into enhancement of surface area of the final catalyst. In this case, the XRD results suggest that the composite oxide calcined at 773 K primarily consists of poorly crystalline composite oxides of Ce-Hf and TiO_2-anatase phase and a better crystallization of these oxides occur with increasing calcination temperature. At high temperatures especially at 1073 K, however, titania might not remain as an inert carrier and form unfavorable compounds with ceria or hafnia. But the exact identification of such unfavorable compounds could not be confirmed by XRD measurements. Raman spectroscopy studies revealed the formation of cubic Ce-Hf-oxide and TiO_2-anatase phases along with the information about the oxygen vacancy formation in the crystal lattice. From Raman (visible-Raman studies) results formation of unfavorable rutile phase was observed. The XPS measurements indicated that the Ce is present in both 3+ and 4+ oxidation states and Hf in 4+ oxidation state, respectively. At higher temperatures Ce^{3+} was stabilized. The SEM measurements conferred information on the external surface morphology of the catalysts. The TEM-HREM results ascertained the formation of nanometer sized composite oxides of Ce-Hf with nominal increase in the grain size at higher calcination temperature. UV-vis DRS measurements conferred information on the lowering of crystal symmetry and consequent strain development at the cerium sites along with the information on the ligand to metal charge transfer transitions. The TPR analyses show the high reducibility of the catalyst system. The thermogravimetric analysis under N_2 atmosphere gave information on the thermal stability

of the catalyst system. More details on the nanostructural evolution of this interesting catalytic system are presented in this chapter.

Chapter 6 deals with structural and redox characteristics of CeO_2–HfO_2/Al_2O_3 samples under the effect thermal treatments. The CeO_2–HfO_2/Al_2O_3 composite oxide (8:2:10 mole ratio based on oxides) was obtained by a deposition coprecipitation method. The addition of alumina resulted into remarkable stabilization of $Ce_xHf_{1-x}O_2$ nanocrystals against thermal sintering at higher temperatures. Alumina remains as an inert carrier and does not form any unfavorable inert compounds with ceria or hafnia with the temperature range used in the present investigation. The XRD analysis of the sample calcined at 773 K revealed the presence of a cubic phase with the composition $Ce_{0.8}Hf_{0.2}O_2$. There is no evidence for phase segregation up to the calcination temperature of 1073 K. The presence of oxygen vacancies leading to the formation of defective fluorite structure is revealed by Raman spectroscopic analysis. The XPS measurements revealed the presence of Ce in both 4+ and 3+ oxidation states and Hf in 4+ oxidation states, respectively. The predominance of Ce^{3+} state at higher calcination temperature was observed. The SEM measurements conferred information on the external surface morphology of the catalysts. The TEM-HREM results ascertained the formation of nanometer sized composite oxides of Ce–Hf. The grain size does not increase above 10 nm upon increasing the calcination temperature from 773 to 1073 K. The UV-vis DRS measurements disclose information on the oxygen to metal (Ce^{4+}/Ce^{3+}) charge transfer transitions and the lowering of symmetry and consequent strain development at the cerium sites. The redox behavior of the catalyst was determined by TPR measurements. TG-DTA analysis was performed to evaluate the thermal stability of the catalyst system, which showed that the catalyst is thermally quite stable in the temperature of 1073 K. More details pertaining to this interesting catalytic system are presented in this chapter.

Chapter 7 deals with the catalytic activity studies of the synthesized catalyst systems for OSC, CO oxidation, soot oxidation, and selective dehydration of 4-methylpentan-2-ol, respectively. The catalysts were very active for all the reactions. The unsupported ceria-hafnia composite oxide is better in terms of OSC, CO oxidation, and soot oxidation ability compared to well reported ceria-zirconia composite oxide. The redox behavior is quite

interesting for the ceria-hafnia system. Among the supported ceria-hafnia catalyst systems alumina supported composite oxide showed higher activity for OSC, CO oxidation and soot oxidation reaction, respectively. All the three catalytic properties are interrelated, as observed from our experimental results and physicochemical characteristics of the composite oxide systems. The fourth reaction studied was selective dehydration of 4-methylpentan-2-ol, which is used as a test reaction to evaluate the acid-base character of oxide catalysts. Among all the catalysts silica supported ceria-hafnia system showed highest activity toward the dehydration of the 4-methylpentan-2-ol selectively.

On the whole, using soft chemical routes nanosized ceria-hafnia and different supported ceria-hafnia composite oxides could be successfully synthesized. Physicochemical characterization of all the catalyst systems showed that the catalysts are thermally quite stable, and possess very high surface area. The catalytic activity studies inferred that the catalysts are quite active for the reactions studied in the present investigation.

Chapter 1

This chapter comprised of a thorough literature survey on nanostrucutred metal oxides with especial emphasis on cerium oxide and its composite oxides including structural, redox properties, and potential applications in catalysis with relevant references.

GENERAL INTRODUCTION AND LITERATURE OVERVIEW

1.1 General Introduction to Metal Oxides

Metal oxides play a very important role in many areas of chemistry, physics, and materials science. The metal elements can form a large diversity of oxide compounds [1–6]. These elements can adopt many structural geometries with an electronic structure that can exhibit metallic, semiconductor, or insulator character.

1.1.1 Metal oxides and their Properties

Metal oxides represent one of the most important and widely employed classes of solid catalysts, either as active phases or supports. Metal oxides are used both for their acid-base and redox properties and constitute the largest family of catalysts in heterogeneous catalysis [1–8]. The three key features of metal oxides, which are essential for their application in catalysis, are (a) coordination environment of the surface atoms; (b) redox properties of the oxide; (c) oxidation state of the surface. Surface coordination environment can be controlled by the choice of crystal plane exposed and by the preparation procedures employed, however, specification of redox properties is largely a matter of choice of the oxide. The majority of oxide catalysts correspond to more or less complex transition metal oxides containing cations of variable oxidation-state. These cations introduce redox properties and, in addition, acid-base properties. The acid-base properties of the oxides are usually interrelated to their redox behavior. Many attempts were made in the literature to find correlations between acid-base and redox characteristics and the catalytic properties. It is obvious that both characteristics are not independent since cations are Lewis acids while lattice oxygen anions are basic and hydroxyl groups could be either acidic (Brønsted site) or basic. The acidic character of the cations depends on their positive charge and size while the basic character of the lattice oxygen anions depends on the ionic character of the metal-oxygen bonds [1,7,8].

Metal oxides are usually formed from their corresponding hydroxides, through calcination. Electro-statically neutral oxide surfaces expose both cations as well as oxygen atom anion sites, where as in the bulk the formal charge on oxygen can often be considered to be equal to –2, this is not the case on metal or metal oxide surfaces. The decreased Madelung energy on the surface makes charge transfer between cation and

anion on the surface less favorable. This can give rise to reactive O^- sites, or in the case of the adsorption of O_2, O_2^- anions which are known to be active in non-selective combustion pathways for reacting hydrocarbons. Dehydrated surfaces possess both Lewis acid cationic sites as well as Lewis base anionic sites. Water normally physisorbs at low temperature and readily dissociates on non-polar surfaces. This occurs on reducible as well as on non-reducible oxides. Protons attach to bridging oxygen sites and behave as Brønsted acids, where as the OH^- fragments adsorb to the cation sites and behave as Brønsted bases.

Oxides commonly studied as catalytic materials belong to the structural classes of corundum, rocksalt, wurtzite, spinel, perovskite, rutile, and layer structure. These structures are commonly reported for oxides prepared by normal methods under mild conditions [1,7]. Many transition metal ions possess multiple stable oxidation states. The easy oxidation and reduction (redox property), and the existence of cations of different oxidation states in the intermediate oxides have been thought to be important factors for these oxides to possess desirable properties in selective oxidation and related reactions. In general terms, metal oxides are made up of metallic cations and oxygen anions. The ionicity of the lattice, which is often less than that predicted by formal oxidation states, results in the presence of charged adsorbate species and the common heterolytic dissociative adsorption of molecules (i.e., a molecule AB is adsorbed as A^+ and B^-). Surface exposed cations and anions form acidic and basic sites as well as acid-base pair sites [1]. The fact that the cations often have a number of commonly obtainable oxidation states has resulted in the ability of the oxides to undergo oxidation and reduction and the possibility of the presence of rather high densities of cationic and anionic vacancies.

1.1.2 Nanostructured Metal Oxides and their Applications

Metal oxides are used in the fabrication of microelectronic circuits, sensors, piezoelectric devices, fuel cells, coatings for the passivation of surfaces against corrosion, and as catalysts. For example, almost all catalysts used in industrial applications involve an oxide as active phase, promoter, or “support.” In the chemical and petrochemical industries, products worth billions of dollars are generated every year through processes that use oxide and metal/oxide catalysts [9]. For the control of environmental pollution, catalysts or sorbents that contain oxides are employed to remove the CO, NOx and SOx species formed during the combustion of fossil-derived fuels [10]. Furthermore, the most

active areas of the semiconductor industry involve the use of oxides [11]. Thus, most of the chips used in computers contain an oxide component. In the emerging field of nanotechnology, a goal is to make nanostructures or nanoarrays with special properties with respect to those of bulk or single-particle species [12–14]. Oxide nanoparticles can exhibit unique physical and chemical properties due to their limited size and a high density of corner or edge surface sites. Particle size is expected to influence three important groups of properties in any material. The first one comprises the structural characteristics, namely, the lattice symmetry and cell parameters [15]. Bulk oxides are usually robust and stable systems with well-defined crystallographic structures. However, the growing importance of surface-free energy and stress with decreasing particle size must be considered: Changes in thermodynamic stability associated with size can induce modification of cell parameters and/or structural transformations [16,17], and in extreme cases, the nanoparticle can disappear because of interactions with its surrounding environment and a high surface-free energy [18]. To display mechanical or structural stability, a nanoparticle must have a low surface-free energy. As a consequence of this requirement, phases that have a low stability in bulk materials can become very stable in nanostructures. This structural phenomenon has been detected in TiO_2, VOx, Al_2O_3, or MoOx oxides [6,18]. Size-induced structural distortions associated with changes in cell parameters have been observed in nanoparticles of Al_2O_3, NiO, Fe_2O_3, ZrO_2, MoO_3, CeO_2, and Y_2O_3 [6]. As the particle size decreases, the increasing number of surface and interface atoms generates stress/strain and concomitant structural perturbations [19]. Beyond this “instrinsic” strain, there may be also “extrinsic” strain associated with a particular synthesis method that may be partially relieved by annealing or calcination [6]. On the other hand, interactions with the substrate on which the nanoparticles are supported can complicate the situation and induce structural perturbations or phases not observed for the bulk state of the oxide [20]. The second important effect of size is related to the electronic properties of the oxide. In any material, the nanostructure produces the so-called quantum size or confinement effects, which essentially arise from the presence of discrete, atom-like electronic states. From a solid-state point of view, these states can be considered as being a superposition of bulk-like states with a concomitant increase in oscillator strength [21]. Additional general electronic effects of quantum confinement experimentally probed on oxides are related to the energy shift of excitation levels and optical bandgap [22]. An important factor to consider when dealing with the electronic properties of a bulk oxide surface are the long-range effects of the Madelung field, which

are not present or limited in a nanostructured oxide [6,23]. Theoretical studies for oxides show a redistribution of charge when going from large periodic structures to small clusters or aggregates, which must be roughly considered to be relatively small for ionic solids while significantly larger for covalent ones [24,25]. The degree of ionicity or covalency in a metal-oxygen bond can, however, strongly depend on size in systems with partial ionic or covalent character; an increase in the ionic component to the metal–oxygen bond in parallel to the size decreasing has been proposed [6]. Structural and electronic properties obviously drive the physical and chemical properties of the solid, and the third group of properties is influenced by size in a simple classification. In their bulk state, many oxides have wide band gaps and a low reactivity [26]. A decrease in the average size of an oxide particle does in fact change the magnitude of the band gap [27], with strong influence on the conductivity and chemical reactivity [28]. Surface properties are a somewhat particular group included in this subject because of their importance in chemistry. Solid–gas or solid–liquid chemical reactions can be mostly confined to the surface and/or subsurface regions of the solid. As mentioned, the two-dimensional (2D) nature of surfaces has (1) notable structural consequences, typically a rearrangement or reconstruction of bulk geometries, and (2) electronic consequences, such as the presence of mid-gap states [6]. In the case of nanostructured oxides, surface properties are strongly modified with respect to 2D-infinite surfaces, producing solids with unprecedented sorption or acid/base characteristics [29]. Furthermore, the presence of under-coordinated atoms (like corners or edges) or O vacancies in an oxide nanoparticle should produce specific geometrical arrangements as well as occupied electronic states located above the valence band of the corresponding bulk material, enhancing in this way the chemical activity of the system [6,29–31].

1.2 Cerium Dioxide (CeO_2, Ceria): Structure and Properties

The most stable oxide of cerium is cerium dioxide, CeO_2, also called ceria or ceric oxide. When cerium salts are calcined in air or oxygen-containing environments, this tetravalent Ce(IV) oxide is formed (the sesquioxide Ce_2O_3 with trivalent Ce can be prepared in strongly reducing conditions but is unstable in air, water, and the like, readily converting to the dioxide). The color of CeO_2, when pure, is very pale yellow probably due to Ce(IV)-O(-II) charge transfer transitions. The color of the oxide is sensitive not only to stoichiometry but also to the presence of other lanthanides. Grossly, non-stoichiometric

ceria samples are reported to be blue related to the Ce(IV)-Ce(III) transitions. In addition, as the oxide is usually produced by the calcination of a precursor salt, the observed color depends on the extent of that calcination.

1.2.1 Abundance and Electronic Configuration of Cerium

Cerium is the most abundant member of the series of elements known as lanthanides (Ln) or rare earths elements in the Periodic Table in which the inner 4f electron shell is being filled. It is rated as the 25th most abundant element in the earth crust (among all the periodic elements). Among rare earths, it occurs at 60 ppm crustal abundance followed by lanthana at 30 ppm crustal abundance [32–34]. Nearly 50% of the available rare earth raw material consists of cerium in its oxide form. Interestingly it is the only rare earth element that can be easily separated from a mixture of other rare earth elements by simple chemical methods. The naturally occurring element cerium is made up of the isotopes ^{136}Ce 0.193%; ^{138}Ce 0.25%; ^{140}Ce 88.58%, and ^{142}Ce 11.07%. A radioactive alpha emitter ^{142}Ce has a half-life of 5 X 10^{15} years.

Cerium (atomic number 58, atomic weight 140.12) can be chemically present in two stable valence states, Ce^{4+} (ceric) and Ce^{3+} (cerous), and this property triggers several technological uses. The ceric ion is a powerful oxidizing agent but when associated with the strongly coordinating ligand oxygen, it is completely stabilized. Therefore, cerium oxide ($Ce^{4+}O_2$, also called ceria) is the form of cerium most widely used. First isolated as an impure oxide in 1803, the element was named after the earliest recognized asteroid ‘Ceres’ that in turn was named for the patron saint of Sicily, the roman goddess of food plants. It is noteworthy that the recognition of cerium as a unique element, and its relationship to other elements helped in the gradual development of the Periodic Table concept. About one hundred years ago or so, the separation and identification of all the individual 4f elements including cerium caused considerable confusion but led eventually to the understanding of atomic structure.

The ground state of all the neutral Ln atoms is probably either $[Xe]4f^n5d^16s^2$ or $[Xe]4f^{n+1}6s^2$, where the increase in n from 0 to 14 corresponds to the change from La (Z=57) to Lu (Z=71). Cerium is the second and most reactive member of the Ln series. It is very electro-positive and has predominantly ionic chemistry due to the low ionization potential for the removal of the three most weakly bound electrons. The energetics are such that for all lanthanides, the most stable state is a trivalent one (Ln^{3+}) with $[Xe]4f^n$

configuration; i.e. for Ce^{3+}, it is $[Xe]4f^1$. The 4f electrons have well-shielded inner orbitals which are not influenced by the external environment and hence the chemical behaviour of all Ln^{3+} ions, including Ce^{3+}, is very similar. At the start of the Ln series, the 5d orbitals are not much higher in energy than the 4f shell. However, in case of cerium a potential 4f–5d charge transition accounts for the absorption by Ce(III) compounds in the UV region just outside the visible region. The relative increased stability of empty $4f^0$, half-full $4f^7$, and completely full $4f^{14}$ shells for certain elements can cause oxidation states other than three also to be reasonably stable, in particular Ce^{4+} with a $[Xe]4f^0$ configuration.

Rare-earth minerals occur in a variety of geologic environments. Concentrations exist in igneous, sedimentary, and metamorphic rocks. The rare-earths are constituents in over 160 minerals [35], but only a few are recovered for commercial production. The more important minerals containing cerium are allanite (also known as orthite), bastnasite, cerite, and monazite [32,34,36,37]. Allanite, which is a silicate, containing rare earths, aluminium, calcium, and iron is widely found in the United States, Germany, Greenland, Madagascar, Russia, and Scandinavia. Bastnasite, which is essentially a rare earth fluorocarbonate, is the second most important commercial source for cerium and other light rare earths. The major deposit of bastnasite is found in Southern California. Cerite, which is a calcium-iron-rare earth silicate, is principally found in Sweden. Although its rare earth content is quite high, it is not abundant enough to be a primary source of the light rare earths. Monazite, which is the principal source of cerium, is a phosphate containing thorium and the light rare earths. The most important deposits are located in the United States (Florida and Idaho), Australia, Brazil, India, and South Africa.

1.2.2 Structural Properties and Nonstoichiometric Behavior of CeO_2

Ceria (CeO_2) is an interesting oxide with important applications in the areas of catalysis, electrochemistry, photochemistry, and materials science [32,38]. It is well known for its unique properties namely the ability to shift between reduced and oxidized states ($Ce^{3+} \leftrightarrow Ce^{4+}$) and to accommodate variable levels of bulk and surface oxygen vacancies. These characteristics make it suitable for use as support as well as catalyst in processes wherein reaction conditions fluctuate between oxidizing and reducing environments [37,39].

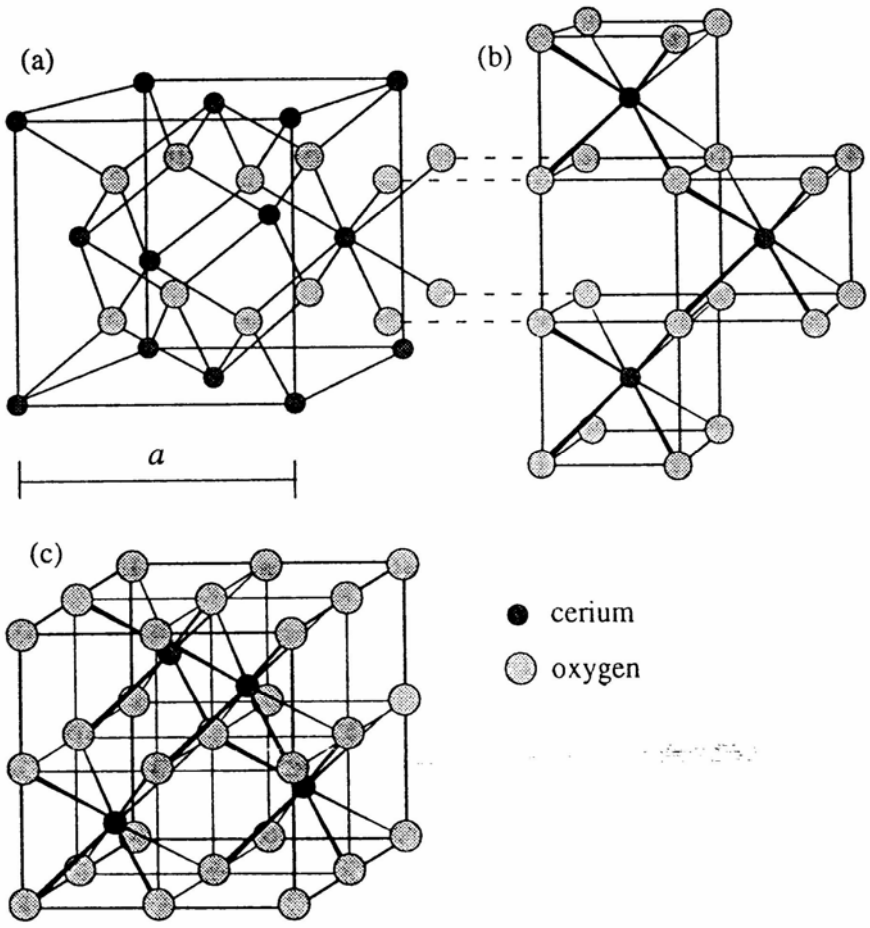

Figure 1.1: The crystal structure of CeO_2: (a) unit cell as a ccp array of cerium atoms. The ccp layers are parallel to the [111] planes of the f.c.c. unit cell. (b) and (c) are the same structure redrawn as a primitive cubic array of oxygens.

Ceria has the fluorite (CaF_2) structure, space group Fm3m (a = 0.541134 nm, JCPDS 34-394) with 8-coordinate cations and 4-coordinate anions [34,39]. In other words, each cerium cation is coordinated to eight equivalent nearest oxygen anions at the corner of a cube, each anion being tetrahedrally coordinated by four cations. It can be visualized as a cubic close-packed array of metal atoms with oxygens filling all the tetrahedral holes; the structure-determining OCe_4 coordination tetrahedral thereby shares all edges in three dimensions. The structure is illustrated in Fig 1.1. Extending this structure by drawing cubes of oxygen ions at each corner reveals the eightfold cubic co-ordination of each cerium, which alternately occupies the centre of the cube. It is therefore also possible to move the origin and redraw the elementary cell as a primitive cubic array of oxygen ions, Fig 1.1 (b, c), in which the eight coordination sites are alternately empty and occupied by

a cation. This clearly shows that there are large vacant octahedral holes in the structure, a feature, which will be significant when movement of ions through the defect structure is considered. Ceria has only one crystallographic form throughout the range of temperatures. It has a strong tendency to remain in the fluorite-structured lattice even after loosing considerable amount of oxygen, thus stabilizing a structure with an elevated number of oxygen vacancies [32].

Experiments of photoelectron spectroscopy and optical reflectivity measurements show a strong hybridization of the metal and oxygen orbitals [40–42], and the valence band, although dominated by O 2p character still contains a significant amount of metal character [43,44]. Thus, the charge on the metal cations in ceria is probably much smaller than the frequently assigned formal value of '4+' [43,44], and cerium oxide is best described as an ionocovalent compound or covalent insulator [42,44]. When treated in a reducing atmosphere at elevated temperatures, CeO_2 forms a continuum of oxygen-deficient, nonstoichiometric CeO_{2-x} oxides (with $0 < x \leq 0.5$) [45,46]. The ability of ceria to be easily reduced to nonstoichiometric oxides is related to the properties of fluorite structured mixed valence oxides to deviate from stoichiometry [32]. Even after CeO_2 loses considerable quantities of oxygen from its lattice and forms several oxygen vacancies, it retains the fluorite crystal structure and these suboxides are readily reoxidized to CeO_2 on exposure to an oxidizing environment. Reduced ceria results from the removal of O^{2-} ions from the CeO_2 lattice, which generates an anion vacant site according to the following scheme: (equation 1.1)

$$4\ Ce^{4+} + O^{2-} \rightarrow 4\ Ce^{4+} + 2\ e^-/\square + 0.5\ O_2 \rightarrow 2\ Ce^{4+} + 2\ Ce^{3+} + \square + 0.5\ O_2 \qquad (1.1)$$

Where $\square$ represents an empty position (anion-vacant site) originating from the removal of O^{2-} from the lattice, here represented as an oxygen tetrahedral site (Ce_4O). Electrostatic balance is maintained by the reduction of two cerium cations from 4+ to 3+. Upon reduction of Ce^{4+} ions to Ce^{3+}, the ceria lattice expands due to the disparity in the ionic radii of Ce^{4+} and Ce^{3+} ions (0.97 and 1.14 Å respectively) [47].

1.2.3 Defects in CeO_2

Defects in ceria lattice are the consequences of oxygen vacancy formation. Two types of oxygen vacancies can be created in ceria namely, intrinsic and extrinsic. Intrinsic

defects may be present because of thermal disorder or can be created by reaction between the solid and the surrounding atmosphere (i.e. redox processes) whereas extrinsic defects are formed by impurities or by the introduction of aliovalent dopants [32]. Thermally induced intrinsic defects can be broadly categorized into two, one cationic type (ΔE = 11.11 eV) and the other anionic type (ΔE = 3.2 eV). From variation in ΔE, it is evident that the predominant defect category is the anion type, which leads to the formation of pairs of oxygen vacancies [48]. Generally, these defects are present in low concentration and do not produce any deviation from stoichiometric composition. In ceria, however, a high concentration of defects can be formed by exposure to high temperatures, reducing gaseous atmospheres, or ultra high vacuum conditions. Upon reduction, ceria has excess metal compared to its anion content, that is to say its cation/anion ratio is greater than 0.5. There are, in principle, two ways in which CeO_2 can accommodate variation in composition. In the first case, oxygen vacancies are assumed to compensate the holes formed on reduction. When oxygen is removed, the crystal ends up with an overall positive charge. Then it is necessary to introduce two electrons for each oxygen ion removed in order to keep the crystal neutral. These electrons are associated with two cerium atoms that will change charge from 4+ to 3+. The effective charge of the anion vacancies is positive, thus neutralizing the negatively charged holes. The process illustrated in Fig 1.2(a) is generally represented as:

$$CeO_2 \leftrightarrow CeO_{2-x} + x/2\ O_2\ (g)$$

or

$$CeO_2 \leftrightarrow 2x\ Ce^{3+} + (1-2x)\ Ce^{4+} + (2-x)\ O + 0.5x\ O_2(g) \qquad (1.2)$$

The reaction implies that as x moles of atomic oxygen are removed from the lattice, the corresponding quantity of O^{2-} sites are occupied by oxygen vacancies, leaving 2-x moles of O^{2-} anions in their original positions. On the cation side, 2x moles of Ce^{3+} are formed, leaving 1−2x moles of Ce^{4+}.

The cationic defects may be formed by transfer of cerium cations located on the surface to an interstitial position and by the removal of two anions to the gas phase for each cerium interstitial formed. The process can be simply represented as in equation (1.3):

$$(1+x)\ CeO_2 \leftrightarrow Ce_{1+x}O_2 + x\ O_2\ (g) \quad (x<0.33) \qquad (1.3)$$

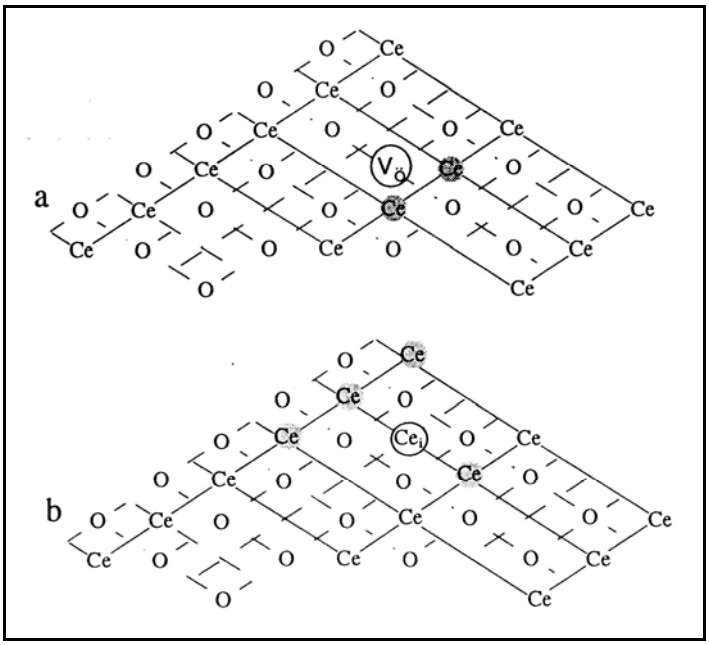

Figure 1.2: Schematic representation of (a) an oxygen vacancy ($V_{ö}$) and (b) a quadruply ionised cerium interstitial (Ce_i) in an idealised reduced CeO_2 surface. Ce^{3+} cations are shaded.

This situation is illustrated in Fig. 1.2(b), where one cerium(IV) cation is present in an interstitial position with four neighboring Ce^{3+} ions. From the above observations it is concluded that the predominant type of defects in oxygen-deficient ceria are anion vacancies and the lattice expands as a function of increasing defects. The cerium sublattice is not strongly perturbed by the defects, which instead cause the formation of a defective oxygen sublattice. The defective lattice is known to yield high oxygen vacancies and high ionic mobility in turn leading to enhanced redox ability and thus enhanced activity.

1.2.4 Transport Properties and Electrical Behavior of CeO_2

Electrical properties and other transport properties of oxides, such as oxygen diffusion, are mainly determined by the presence, concentration, and mobility of lattice defects. Oxygen transport materials have long been used as oxidation and ammoxidation catalysts, for which purpose the material must be susceptible to rapid reduction and reoxidation by the incorporation of gaseous oxygen in the lattice [48,49]. Transport properties of ceria play a key role in processes where the availability of oxidant from the

gas phase is not constant. Provided the diffusion of anions is sufficiently fast, a continuous supply of oxygen from the bulk to the surface guarantees a constant concentration of active surface oxidation sites, thus enabling a fast surface catalytic reaction in the absence of other kinetic limitations.

Ceria can be classified as a mixed conductor showing both electronic and ionic conduction. Its electrical properties are strongly dependant upon temperature, oxygen partial pressure and the presence of dopants. All these variables effect charge carrier concentration, which ultimately, together with charge carrier mobility, determines electrical conductivity. Generally electrons, holes and oxygen vacancies are the primary charge carriers in CeO_{2-x}. At high temperatures and low oxygen partial pressures, ceria behaves as n-type semiconductor and electrons liberated following reduction are the primary charge carriers [50,51]. Transition from n-type to p-type conduction is observed at lower temperatures and higher oxygen partial pressures near stoichiometric composition, where conductivity arises from holes introduced by impurities [52,53].

1.2.5 Oxygen Storage Capacity of CeO_2

The definition of the oxygen storage capacity (OSC) is the capability to store and release oxygen [39]. Equation (1.4) presents a very simplified picture of the redox behavior of CeO_2.

$$CeO_2 \leftrightarrow CeO_{2-x} + \tfrac{1}{2} O_2 \qquad (1.4)$$
$$Ce^{4+} \leftrightarrow Ce^{3+}$$

According to equation (1.4), the oxygen storage is formally considered as the amount of oxygen released (left to right) or stored (right to left) under the net reducing/net oxidizing excursions as represented pictorially in Figure 1.3. From the thermodynamic point of view, the standard potential for reduction of Ce^{4+} to Ce^{3+} is 1.74 V in solution, which indicates that Ce(IV) in solution is a strong oxidant [54]. In the solid state, the situation is different. CeO_2 crystallizes in the fluorite structure in which each cerium ion is co-ordinated by eight oxygen neighbours. This coordination stabilizes the Ce^{4+} state and makes the reduction of CeO_2 unfavorable. In fact, the fluorite structure of ceria is a direct result of the ionic nature of ceria, and of the charge and size of the ions. Model calculations have shown that it is formed when a sufficient number of CeO_2 units (about 50) are clustered together [55]. The

ability of CeO_2 to undergo a relatively easy reduction compared to other oxides, can in principle also be related to the general property of fluorite structure/mixed valence oxides to strongly deviate from stoichiometry [56]. It is worth recalling that of the two processes (reduction/oxidation), oxidation is fast [57], and occurs deep into the bulk even at room temperature (RT), whereas reduction typically occurs above 473 K [58].

According to Cho [39], two types of oxygen vacancies can be created in ceria namely, intrinsic and extrinsic. Intrinsic vacancies are created on reduction of ceria according to the following process (equation 1.5).

$$CeO_2 + \delta\ R \leftrightarrow CeO_{2-\delta} + \delta\ RO + \delta\ V_o \qquad (1.5)$$

Extrinsic vacancies are defects that are formed by a charge-compensating mechanism when a bivalent or trivalent cation M is introduced in to the CeO_2 lattice according to these two mechanisms (equations 1.6 and 1.7), where δ' and δ'' are the created extrinsic oxygen vacancies in the modified ceria:

$$(1-\alpha)\ CeO_2 + 0.5\alpha\ M_2O_3 \leftrightarrow Ce_{1-\alpha}M_\alpha O_{2-0.5\alpha} + \delta'\ V_o \qquad (1.6)$$

$$(1-\alpha)\ CeO_2 + \alpha\ MO \leftrightarrow Ce_{1-\alpha}M_\alpha O_{2-\alpha} + \delta''\ V_o \qquad (1.7)$$

The oxygen storage capacity of ceria can be benefited from either type of defect. Two types of measurements of OSC were distinguished by Yao and Yu Yao [59]. The so-called complete or ultimate oxygen storage capacity (total OSC), i.e. an oxygen storage measured under thermodynamic control, and the kinetic oxygen storage, (dynamic OSC), i.e. measured under kinetic control. The total OSC represents the widest 'limiting' amount of oxygen transferable from the catalyst at a given temperature and generally is limited in the case of CeO_2 by the formation of some non-stoichiometric CeO_{2-x} compounds. The capability of CeO_2-based materials to provide/abstract oxygen at the catalytic site is perhaps a better description of this OSC functionality, where spillover properties, creation and annihilation of oxygen vacancies and complex network of reaction/interactions play a vital role. Oxygen diffusion in ceria and related systems is of interest for several reduction and oxidation reactions. The rate of several catalytic oxidation reactions which occur anaerobically, i.e. without oxygen from the gas phase, but using oxygen from the solid, depends on oxygen diffusion parameter.

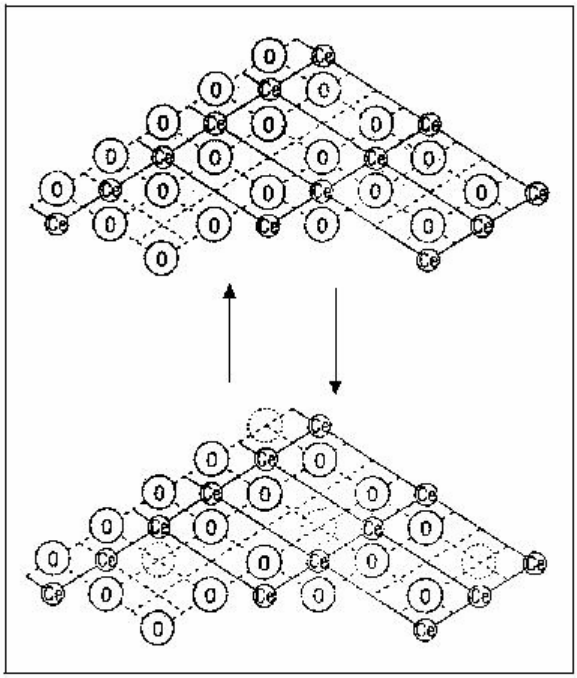

Figure 1.3: A schematic representation of Ce^{4+}/Ce^{3+} shifting with storage and release of oxygen.

In addition, reduction of ceria, which is believed to involve two distinct steps (surface and bulk reduction), may be dependent on the availability of bulk oxygen.

1.3 Catalytic Applications of Ceria-based Oxides

There are several emerging catalytic processes for which cerium oxide is being actively investigated. Some of them are outlined below.

1.3.1 Automotive Three-way Catalysis

A major technological application of steadily growing importance for cerium is as one of the catalytically active components used to remove pollutants from vehicle (auto-exhaust) emissions [32,59]. This market currently consumes a significant portion of the yearly production of cerium derivatives. The active form of cerium is the oxide that can be formed in situ by calcinations of a soluble salt such as nitrate or by deposition of slurried oxide. The most widely used exhaust control device consists of a ceramic monolith with a

thin-walled rectangular honeycomb structure that offers little resistance to the flow of gases (metallic monoliths are also possible). The accessible surface of this monolith system is increased by applying a separate coating, a wash coat, of a high surface area material such as gamma-alumina with the catalytically active species impregnated into this washcoat. The catalyst needs

- to oxidize unburnt hydrocarbons,
- to convert CO to CO_2, and
- to reduce NO_X

and hence is termed as a 'three-way' catalyst (TWC).

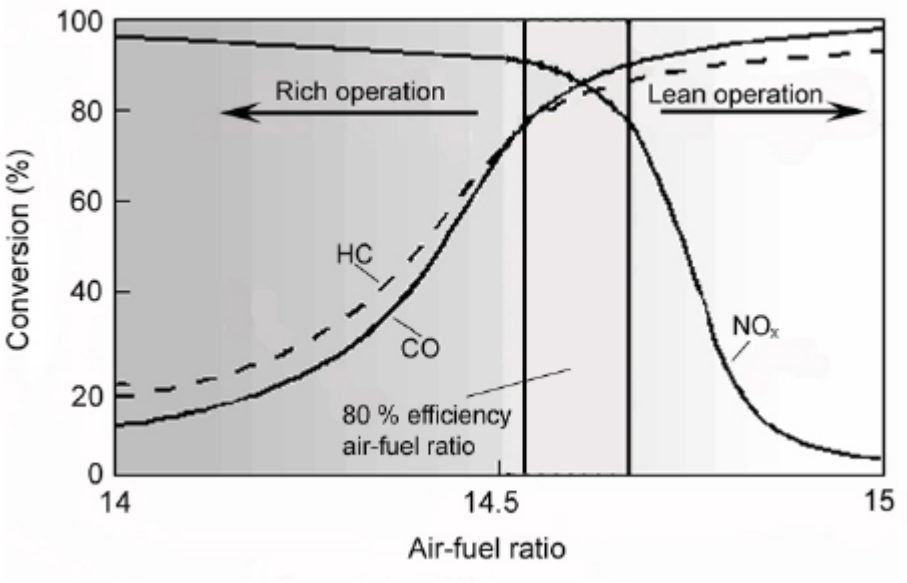

Figure 1.4: Conversion efficiency of NO_x, CO and HC as a function of the air-fuel ratio in a three-way catalytic converter.

The automotive three-way catalyst system operates under a certain range of air-to-fuel (A/F) ratios, controlled by an electric fuel-injection system linked to an oxygen sensor device. However, even the exhaust gases controlled by the system alternate between slightly rich to slightly lean conditions with an inevitable time lag in the system as it adjusts the ratio. Figure 1.4 shows the conversion efficiency of NO_x, CO and HC as a function of the air-fuel ratio in a three-way catalytic converter. The whole system forms a suitably encased catalytic converter that is placed between the engine and the muffler/silencer unit. In addition to platinum and other metals from the platinum group, the major active component in the current complex multi-functional systems is cerium oxide. Current

catalytic converters contain ~75 gms per converter of finely divided ceria dispersed within the washcoat. Most of the details of catalyst production are proprietary knowledge and patents only hint at the technology involved. Not only the chemical nature of the catalytic participants is crucial but also their spatial distribution with respect to one another is also important. Elucidation of the detailed behavior of cerium is difficult and complicated by the presence of other additives such as lanthanum oxide that perform related functions. Ceria plays several roles, namely

- as a stabilizer for the high surface area alumina,
- as a promoter of the water-gas shift reaction,
- as an oxygen storage component, and
- as an enhancer of the NO_X reduction capability.

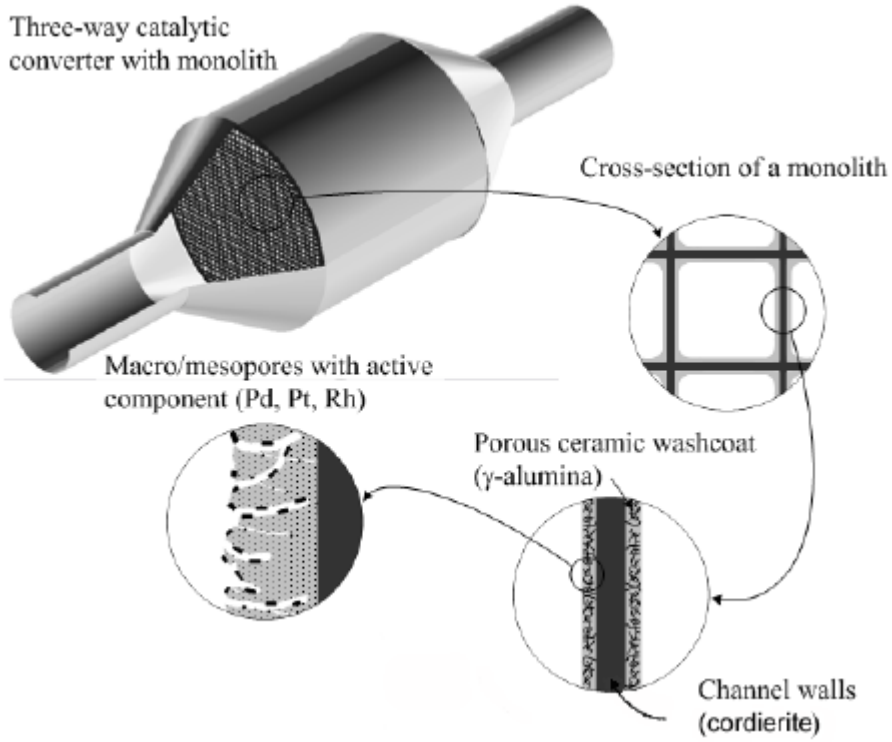

Figure 1.5: The structure of three-way catalytic converter.

The tendency of the high surface area gamma-alumina support to sinter and lose that crucial area during high temperature operation is retarded by the intimate addition of several per-cent of cerium oxide to that alumina. This function is also provided, probably more efficiently, by lanthanum. The mechanism is still under debate but may involve a surface Ln-aluminate species on the alumina. As already discussed, the term ‘oxygen

storage component' (OSC) is used to describe a material that stores oxygen under lean operating conditions, i.e. fuel-poor/air-rich, and releases it under fuel-rich/air-poor conditions to continue the oxidation of the unburnt hydrocarbons and the removal of carbon monoxide even when there is insufficient gaseous oxygen available. CeO_2 will readily provide elemental oxygen by going non-stoichiometric to CeO_{2-x} in those air-poor portions of the exhaust cycle and then re-oxidize to CeO_2, i.e. store oxygen, during the air-rich period. The role of cerium oxide however is more complex than just this oxygen storage capability. The three precious metals, namely Pt, Pd, and Rh, present as crystallites in auto exhaust catalysts, all interact with cerium oxide, boost the removal of surface oxygen from ceria and provide a synergistic enhancement of the oxidative properties of ceria. A typical diagram is presented in Figure 1.5 showing the structure of three-way catalytic converter. Furthermore ceria maintains the active metal (like rhodium) in a reducible form, a state that is best suited to catalyze the conversion of NO_X to nitrogen. Overall the influence of ceria in auto exhaust catalysts is to provide better low-temperature performance, especially in a reducing environment.

1.3.2 Combustion of Particulate Matter

The ability of cerium oxide to act as an oxidizing agent underlies the potential use of various cerium derivatives as additives to aid combustion. During the combustion process these derivatives probably decompose to extremely small oxide particles that catalyze the low temperature oxidation of carbon. Diesel exhaust often contains particulate matter (unburnt carbonaceous material) and, in order to reduce these particle emissions, the exhaust can be passed through a ceramic trap, a closed honeycomb. The exhaust gases flow through the walls of the porous ceramic and any particles present are filtered out. These traps can eventually plug up and they need regular regeneration by creating sufficiently high temperatures to burn off the deposits. In order to extend the lifetime of these traps and to reduce the temperature needed for regeneration a cerium carboxylate, in particular cerium naphthenate, is used as an additive to the fuel [60]. The cerium compound, dissolved in the fuel at a concentration equivalent to around 25–50 ppm by weight cerium oxide, is transformed into CeO_2 within the engine that in turn collects in the so-called trap oxidizer. This finely divided oxide, completely dispersed throughout the traps, produces conditions under which continuous regeneration effectively occurs; burn-off happens at a lower temperature because CeO_2 catalyzes the carbon

combustion. Like tetraethyl lead, volatile cerium compounds can act as antiknock additives in gasoline. In order to obtain the necessary volatilility and solubility, highly substituted beta-diketonates are required. Patent describes that compounds such as tetrakis (2,2,7 trimethyl-3,5-octanedionato) cerium is comparable to tetraethyl lead in performance [61].

1.3.3 Fuel Cell Processes

Much attention has been paid to produce hydrogen more efficiently for fuel cell applications. Hydrogen is usually produced by steam reforming, autothermal reforming or partial oxidation of natural gas, light oil fractions, and alcohols [62–64]. Recent literature on the production of hydrogen from renewable energy sources like natural gas and ethanol reveal that the catalytic materials consisting of Ce-Zr mixed oxides have emerged as key components in the catalytic formulations containing transition metal/metal oxides [65–68].

Hydrogen is now produced by steam reforming of hydrocarbons, and in the future natural gas predominantly composed of methane will be used more widely as the raw hydrocarbon. Partial oxidation of methane is another candidate for the hydrogen process. The development of processes that convert natural gas into liquid fuels such as gasoline and diesel is the subject of research for several groups around the world. The gas to liquid technology is the key route to convert natural gas into liquid fuels and then produce hydrocarbons using Fischer–Tropsch synthesis [69–71]. The most traditional route to convert natural gas into liquid fuels (gas to liquid – GTL) is to transform methane into synthesis gas, and then produce hydrocarbons using Fischer–Tropsch synthesis [69–71]. However, the generation of the synthesis gas accounts for between 50 and 75% of the total investment required [72]. Therefore, in order to make gas to liquid technology economically viable, it is necessary to reduce these costs. Presently, the commercial process to obtain synthesis gas is through steam reforming. This reaction is extremely endothermic and produces a carbon monoxide to hydrogen ratio that is not adequate to GTL process [73]. The partial oxidation of methane could be an alternative route to produce synthesis gas at a lower price [74,75]. This reaction is moderately exothermic, produces an adequate H_2/CO ratio for the Fischer–Tropsch synthesis and if it is associated to a technology that is able to separate oxygen from air, such as selective membranes, it will be a good option to lower the production cost of synthesis gas [76]. In

order to have a good performance for this reaction, the catalyst must have high activity, selectivity, and stability since one of the biggest problems in this process is the catalyst deactivation due to coke formation [77,78]. Mattos et al. investigated Pt/CeO_2, Pt/ZrO_2 and $Pt/CeZrO_2$ samples for the partial oxidation of methane [79]. They verified that the sample supported on the ceria–zirconia mixed oxide presented the best activity and stability for this reaction and the good selectivity for synthesis gas.

Water-Gas Shift (WGS) reaction is a key step in applications such as on-board H_2 production via reforming processes for fuel cell applications. In such applications, a successful low-temperature WGS catalyst will have to possess high activity as well as good structural stability under all reaction conditions. The WGS reaction is a side reaction of CO that enriches the H_2 content of the syngas enabling the fuel cell to use more H_2 than supplied by the fuel.

$$CO + H_2O \rightarrow CO_2 + H_2 \qquad (1.8)$$

The $CeZrO_x$ based oxide supports were found to be good candidates for gold nano particles. These formulations were shown to be very active for the WGS reaction and exhibited remarkable activity for low temperature water gas-shift (WGS) and generally more stable than catalysts supported on Fe_2O_3 [80].

Recently, Ni catalysts containing Ce-Zr mixed oxide exhibited excellent catalytic activity when compared to that of catalysts containing either ceria or zirconia. A catalyst $Ni/Ce_{0.25}Zr_{0.75}O_2$ exhibited highest H_2 production among all the catalytic formulations [81].

Considerable attention has been focused on carbon dioxide reforming of CH_4 (CDR) for the production of synthesis gas owing to both environmental and commercial reasons [53]. In this process, CH_4 and CO_2, which are well known green house gases are converted into valuable feed stock.

$$CO_2 + CH_4 \rightarrow 2\ CO + 2\ H_2 \qquad (1.9)$$

The product mixture of this reaction has a low H_2/CO ratio (1:1) that is desirable for direct use as a feedstock for the Fisher-Tropsch reaction to produce liquid fuels. Ceria-zirconia based catalysts have been shown to be suitable candidates for this reaction. $Ce_{0.8}Zr_{0.2}O_2$-NiO_x catalyst exhibited best catalytic performance in the CO_2 reforming of

methane, and the activity was maintained without loss during the reaction for 100 h [82]. $Pt/Ce_{0.5}Zr_{0.5}O_2$ catalyst exhibited good performance for CO_2 reforming of methane [83].

1.3.4 Catalytic Oxidation Processes

Selective CO removal from streams containing an excess of H_2 and significant amounts of CO_2 and H_2O is a current challenge in heterogeneous catalysis research especially in the preparation of H_2 suitable for polymer electrolyte membrane fuel cells (PEMFC) [84,85]. Typical effluents from hydrogen generated from hydrocarbons or alcohols by steam/autothermal reforming followed by the water–gas shift (WGS) reaction contain about 0.3–1.0% of CO in a large excess of H_2 (40–75%) and about 20–25% CO_2. CO levels, however, have to be reduced to below 100 ppm and, preferably, below 10 ppm for use in PEMFC. Methanation, after removal of CO_2 by pressure swing adsorption, the conventional strategy used for CO removal in NH_3 or H_2 chemical plants, is impractical in the fuel cell context, especially for "on-board" use in vehicles. Preferential oxidation of CO to CO_2 without simultaneously oxidizing H_2 to H_2O (PROX) is one of the solutions. However, the latter oxidation is more exothermic and, hence, favored at high temperatures. Selective catalysts active at low temperatures are needed.

Preferential (or selective) oxidation of CO has been recognized as one of the most straightforward and cost-effective methods to achieve acceptable CO concentrations (below ca. 100 ppm) [86,87]. After water-gas shift, to minimize the remaining CO content in the H_2 stream in order to avoid poisoning of the fuel-cell catalyst, preferential oxidation of CO is typically carried out. Increasing attention has been focused on the utilization of ceria-based materials as supports for the noble metals such as Pt, Pd, Au, and CuO for the preferential oxidation of CO [88–91].

$$CO + ½\ O_2 \rightarrow CO_2 \quad \text{and} \quad H_2 + ½\ O_2 \rightarrow H_2O \qquad (1.10)$$

Most of the work done in fuel cells is concerned with the use of hydrogen as fuel due to the mild characteristic of the oxidation product (water). Nevertheless, the main way to obtain hydrogen is by hydrocarbon steam reforming, which involves many reactors operating at different temperature conditions. The direct use of hydrocarbon in the fuel cell, without the necessity of reforming and purification reactors, will improve the global efficiency of the system. In this sense, among several different types of fuel cells currently

under development, solid oxide fuel cells (SOFCs) present the most promising characteristics in the direct use of fuels. The operation principle of these cells involves the reduction of molecular oxygen in the cathode, the diffusion of oxygen anions through the electrolyte, and the oxidation of the fuel by the oxygen anions in the anode [92]. This kind of cells has special advantages as environmentally friendly operation, higher fuel to electricity efficiency, and fuel flexibility [93]. Nevertheless, they currently operate at higher temperatures and this high operating temperature causes the degradation of electrodes, interfaces, cell performance, and limits the choice of materials and fabrication methods, thus increasing the costs of the cells [94]. Therefore, substantial efforts have been devoted in order to reduce the operating temperature. At present, ethanol and methane (or natural gas) are regarded as the most appropriate fuels to be used in SOFCs [95]. The first one, due to the natural availability of bio-ethanol and the second one, for its accessibility (natural gas) and physical properties. In a recent research, S. Larrondo et al. recognized the stable activity of Ce-Zr mixed oxides towards methane combustion below 1073 K without pre-treatment and no formation of carbonaceous deposits thereby revealed about suitability of these oxides for the anode materials in the solid oxide fuel cells [96].

Volatile organic compounds (VOCs) are considered as air pollutants as can cause harm to human health directly or indirectly. There are many different techniques for VOC removal such as adsorption, absorption, biofiltration, combustion, and catalytic oxidation. The choice of the techniques to use depends on the characteristics of the effluent to be treated such as VOCs nature, concentration, and waste gas flow rates. Catalytic oxidation can be applied effectively and at a lower cost in a wide range of VOCs concentrations and waste gas flow rates presenting an interesting solution for the VOC elimination [97]. Two types of catalysts can be used for the catalytic oxidation: metal oxides and supported noble metals. Recent investigations reveal that ceria based oxides exhibited good catalytic activity for the VOC oxidation. The complete oxidation of volatile organic compounds of different chemical natures, such as *1,2*-dichloroethane, trichloroethylene and *n*-hexane, over Ce–Zr mixed oxide catalysts has been studied in a conventional fixed bed flow reactor and it was shown that, $Ce_{0.5}Zr_{0.5}O_2$ showed the highest combustion activity for the abatement of chlorohydrocarbons, whereas pure ceria was found to be the most active in the oxidation of the non-chlorinated compound [98].

1.3.5 Fluid Cracking Catalysis

The demand for catalysts for converting crude oil to lower molecular-weight fractions, such as gasoline blending stock is ever increasing. In a fluid catalytic cracking (FCC) unit, although essentially only one type of catalyst, ion-exchanged zeolite, is used there are a variety of catalyst compositions available many of which contain lanthanides including cerium. FCC catalysts contain crystalline zeolites, the active component, and additives embedded in an inert matrix. The zeolite, an aluminosilicate faujasite Y-type with organic-molecule sized pores, requires cations within those pores for charge- neutrality, to give catalytic reactivity in the reactor and to provide thermal stability in the regenerator. Highly-charged ions, such as La^{3+} or Ce^{3+}, bound within those zeolite cages to negatively charged $[AlO_4]^-$ units, create a high electric field gradient strong enough to dissociate adsorbed water and provide a high surface acidity. Protonation of the organic molecules then produces the carbonium-ion intermediates that initiate the actual cracking reactions. Lanthanide cations can be exchanged into the zeolites by immersion in mixed lanthanide salt solutions. The Ln content can reach up 10% by weight of the zeolite. Cerium, because of the potential availability of the Ce^{4+} state that tends to hydrolyze at the ion-exchange pH's used, and because of the different catalyst production technologies practiced, is often partially removed from the precursor solutions. Nevertheless, the production of FCC catalysts accounts for significant amounts of the world's consumption of this element. The Ln's are used to give high cracking activity to FCC catalysts [99], especially to produce low-octane fuel from heavy crude-oil feedstocks. Consumption of lanthanides, and hence of cerium in FCC catalysts has altered during the decade of the 1980's because of increased demand for high-octane fuels, greater feedstock availability of lighter crudes, and changes in technology.

1.3.6 Removal of Sulfur Oxides

The control of sulfur oxide emissions, a source of acid rain, is becoming a very important concern. In the refinery catalytic-cracking process (FCC), as mentioned earlier, sulfur containing components in crude oils can give rise to sulfur oxide in the gases emitted from under the oxidizing conditions in the high-temperature (~1023 K) catalyst regenerator unit. An additive to the actual FCC-catalyst can capture this regenerator SO_X as sulphate and later release, in the cracking (hence reducing) region, a more easily

trapped form of sulfur, H_2S. Several catalyst additives containing cerium and/or lanthanides can act as the SO_X control agent. The properties required include the ready formation of a stable sulfate that can, however, be reduced at the operating temperatures of the riser reactor. Cerium oxide acts as a catalytic oxidizing agent in a spinel-based additive [100] to aid the conversion of SO_2 to SO_3 and promote the required sulfate formation. The mineral bastnasite is itself the most economical source of cerium and can be used directly at ~1% as the capture additive [101]. Here, in addition to the oxidizing role of cerium, all the lanthanides as oxides derived from the carbonate in the mineral are acting as the capture agents.

1.3.7 Other Catalytic Applications

Cerium also has uses in other commercial catalysts where the element's role is probably related to potential Ce(III)/Ce(IV) redox chemistry [102]. The dominant catalyst for the production of styrene from ethylbenzene is an alkali-promoted iron-oxide based material. The addition of a few percent of cerium oxide to this system improves activity for styrene formation presumably because of a beneficial interaction between the Fe(II)/Fe(III) and Ce(III)/Ce(IV) redox couples. The ammoxidation of propylene to produce acrylonitrile is carried out over catalytically active complex molybdates. Cerium, a component of several patented compositions [103], functions as an oxygen- and electron-transfer agent through its (III)/(IV) redox couple. The production of methanol by the reaction of CO and H_2, catalyzed by copper oxide, is a major industrial process. Some catalysts under development are derived from cerium-copper intermetallics, e.g. 50% Ce / 50% Cu [104]. An initial activation step converts the metal to a highly active and selective catalyst containing very finely divided copper on a ceria support.

Ceria and ceria based materials, mainly ceria-zirconia solid solutions act as catalytic materials for many processes for the production of important chemicals. This includes the conversion of coal or natural gas into i-C_4 hydrocarbons from CO hydrogenation, which is termed as isosynthesis [105], synthesis of dimethyl carbonate (DMC) [106], and dehydration of 4-methylpentan-*2*-ol into 4-methylpent-1-ene [107], a valuable monomer for plastics manufacture. In a recent study, it is reported that promotion of Ce-Zr hydroxide gel with sulfate ions resulted into super acidity [108] and have opened up a new class of solid superacids, which opens an array of potential applications in the acid catalyzed organic synthesis.

1.4 Non-catalytic Applications of Ceria-based Oxides

A number of other applications of ceria-based materials could be found in the open literature [109−117]. Cerium oxide is the most efficient polishing agent for most glass compositions [118]. This application consumes a significant portion of the cerium products produced annually. A major use for cerium compounds is the decolourization of glass. Glass can be decolorized by addition of Ce(IV) oxide to the glass melt. Economical additions of cerium, as cerium concentrate or pure cerium oxide, convert iron to the low-absorption Fe(II) form [119]. Most damage caused by light to exposed materials is due to UV radiation. Cerium(IV) in particular makes glass opaque to near UV-radiation but shows no absorption in the visible region and cerium(III) also shows UV absorbing behaviour but somewhat less marked than for cerium(IV) [119]. The photo-stability of pigments can be enhanced by addition of cerium oxide. It provides pigments with light fastness and prevents clear polymers from darkening in sunlight. Television glass faceplates are subjected to electron bombardment, which tends to cause browning of the glass due to the creation of color centers. This effect is suppressed by the addition of cerium oxide. When used in glass compositions (at a low weight percentage) along with comparable amounts of titanium oxide, cerium oxide produces a deep yellow coloration [120]. Cerium sulfides are used in glass and ceramics as colorants to replace toxic CdS [121]. Cerium oxide has a high refractive index, and is an opacifying agent in enamel compositions [122] used as protective coatings on metals. The addition of cerium oxide, for example, to zirconia produces a material with exceptional toughness and good strength [123]. Cerium oxide-doped zirconia is also used in thermal barrier spray coatings on metal surfaces [124]. Cerium oxide-based ceramics find applications in various domains like ceramic superconductors [125] and gas sensors [126]. Additionally, applications based on the optical properties of ceria-thin film optical devices [127], and UV-blocking agents (cosmetics) are also of significant interest [128].

1.5 Genesis of the Investigation

Ceria (CeO_2) is an interesting oxide industrially, applied widely in catalysis, material science, fuel cell processes and gas sensor technologies [6,32,38]. In recent years, ceria and ceria-based composite oxides have been extensively investigated for variety of reactions such as oxidation of CO [129,130], steam reforming of ethanol [65],

synthesis of dimethylcarbonate from methanol and CO_2 [106], direct conversion of methane to synthesis gas [131], iso-synthesis [105], dehydration of alcohols [107,132–134], oxidative dehydrogenation of ethylbenzene [135,136], removal of soot from diesel engine exhaust [137], removal of organics from waste-waters [138], and low-temperature water-gas shift reaction [32], apart from the conventional three-way catalytic applications to reduce the emissions of noxious pollutants such as CO, NO*x* and hydrocarbons from automobile exhausts [6,32,38,39,139,140]. The most important property that makes the ceria remarkable is its oxygen storage and release capacity (OSC) via the redox shift between Ce^{4+} and Ce^{3+} under oxidizing and reducing conditions, respectively [6,32,38]. It is well known that ceria can affect: (i) the thermal and structural stability of the catalyst carriers [141], (ii) the dispersion of supported metal [142], (iii) the oxidation and reduction of noble metals [143], (iv) the storage and release of oxygen in ceria containing catalysts [144] and (v) the decrease of carbon formation on the catalyst surface [145] etc. It is one of the most interesting oxides industrially because oxygen vacancy defects can be rapidly formed and eliminated, giving it a high OSC. The OSC is a result of the high reducibility of Ce^{4+}, which is a consequence of the high mobility of O^{2-} inside the ceria fluorite lattice [146]. However, pure ceria alone exhibits poor thermal stability and susceptible to sintering at high temperatures leading to catalyst deactivation [32]. Also, it is an established fact that ceria exhibits a cubic fluorite structure and sinters equally three dimensionally. Therefore, many studies have been carried out in this direction to increase the thermal stability and the OSC of ceria [32,139,147–149]. One of the best approaches to overcome this problem is substitution of another metal/metal oxide into the ceria lattice thereby facilitating the formation of composite oxides. Ceria easily forms solid solutions with other rare earth elements and with elements belonging to the transition-metal series. Literature reveals that mixed metal oxides play a very important role in many areas of chemistry, physics, material science and geochemistry [6,32,38,129,130,140]. Due to several reasons, the chemical behavior of mixed metal oxides may differ from single metal oxides. The combination of two metals in an oxide can lead to novel structural and electronic properties of the final oxide, consequently favoring its catalytic activity and selectivity. In some cases, cations in a mixed metal oxide can also cooperatively catalyze different steps of a chemical process. At a structural level, a dopant facilitates defect formation within the oxide host by generating stress into the lattice. In contrast, non-typical coordination modes of lattice host leading to deviation in dopant chemical nature may also be possible. As a result, metal-metal or metal-oxygen-metal

interactions in mixed metal oxides lead to perturbed electronic states compared to single metal oxides. Replacement of cerium ions by cations of different size and/or charge modifies ionic mobility inside the lattice resulting in the formation of a defective fluorite structured solid solution. Such modifications in the structure of ceria confer new properties to the catalysts, such as better resistance to sintering and high catalytic activity [39,150]. Most of the recent literature concerning alternative materials for TWC applications deals with ceria-zirconia based systems, the redox properties and chemical activity of pure ceria can be enhanced by introducing different types of metals (Ca, Cu, Tb, Mn, etc.) into the oxide lattice other than zirconium [151–153]. However, it is not clear what type of second metal is useful to improve both the stability at high temperature and the chemical activity by introducing O vacancies in the ceria. Therefore, it is interesting to investigate the effect of substitution of a new dopant to the ceria lattice.

As stated earlier, ceria based materials have the remarkable ability to regulate oxygen storage and release properties and therefore these materials are now inevitable in TWCs formulations. Under operating conditions, TWCs have to withstand very high temperature and oscillating chemical environment. Most of the recent literature related to the search of alternatives for use in TWC applications deals with ceria–zirconia based systems. However, it is now well established that the redox properties and thermal stability of ceria can be improved by incorporation of dopants other than Zr such as La, Hf, Pr, and Tb [129,130,148,154,155]. The ability to substitute one cation for another in a particular structure is dependent on several factors, such as the dimensions of the host/guest cation and the structural features of the pure oxide. During the formation of mixed oxide phases, the structural and energetic factors of the individual constituents are profoundly modified. In the case of pure ceria, the change of Ce(IV) into Ce(III) results in a volume increase, which would restrict further change due to the increased stress energy. Till date CeO_2–ZrO_2 solid solutions have been largely employed in various reactions which include three-way catalysis, CO oxidation, methanol decomposition to syngas, steam reforming of ethanol, catalytic combustion of hydrocarbons, catalytic wet oxidation of methane, alcohol dehydration, and so on. Hafnia (HfO_2) and zirconia (ZrO_2) are called twin oxides because of their similar chemical and physical properties. They are iso-structural in the bulk and this close correlation in properties is due to the identical valence states and nearly identical ionic radii for Hf and Zr. Hafnia-based materials can be used in solid electrolytes for fuel cells, oxygen gas sensors, refractories, coating for oxidation resistance, control rods for nuclear reactor, and so on [156–159]. Therefore, it was interesting to investigate

the structural and catalytic properties of novel nanosized ceria-hafnia composite oxides. However, the unsupported oxides are susceptible to a fall in the surface area due to sintering and it leads to a decrease in the stability of the structure during high temperature applications thereby loosing its oxygen buffering capacity [160]. In order to exploit them without loosing their unique redox features, it is very essential to synthesize nanocomposites where the active phase is stabilized over a stable inert support. In heterogeneous catalysis, catalytic activity scales with surface area. Hence, maximum dispersion of the particles is of extraordinary importance which makes the production of nanoscaled catalysts very tempting. The nanoparticle configurations are interesting from a practical viewpoint also as most of the applications are surface-sensitive, and a high surface-to-volume ratio in addition to improved redox properties, related to oxygen vacancy generation, can be reached by using nanosized materials. Highly dispersed active oxides deposited on the surface of an inert support have been intensively studied for many years, mainly due to their applications as catalytic systems [160]. The essential requirements of a better support are nonreactivity with the dispersed phase and high specific surface area [161]. The catalytic performances of supported metal oxide catalysts are determined by many parameters, the most important being the metal oxide loading, pretreatment conditions, molecular structure, electronic structure, and support oxide type and composition [162]. Currently, ceria-based systems are usually supported on transition aluminas and titania, with the aim of achieving better dispersion of the active phase and improvement of the oxygen exchange rate. Silica is another most widely available supports with excellent chemical resistance, thermal stability and high specific surface area, which can enhance dispersion and thereby catalytic activity of the dispersed active oxides [161].

Motivated by the unique and favorable characteristics of ceria-based materials for various catalytic applications, a systematic and comprehensive investigation was undertaken against the above background. In this study, ceria-hafnia and a series of catalytically important supported nanosized ceria-hafnia [CeO_2–HfO_2/M_xO_y; (M_xO_y = Al_2O_3, SiO_2, and TiO_2)] composite oxides possessing high specific surface area, better thermal stability, superior sintering resistance, and desired redox properties have been synthesized. The thermal and structural stability of the supported ceria-based solid solutions are strongly influenced by the synthetic methodology. In this study, soft chemical routes namely coprecipitation and deposition coprecipitation techniques were adopted for preparation of unsupported and supported mixed oxides respectively. Even though

coprecipitation, surfactant assisted synthesis, and hydro thermally derived samples exhibit high surface area, severe loss of surface area occurs during high temperature treatments. Stabilization of nanoparticles of ceria-hafnia solid solutions on another oxide support such as alumina, colloidal silica or titania could represent a suitable way to overcome the drawbacks associated with unsupported mixed oxides. The prepared samples were further subjected to thermal treatments from 773 to 1073 K in order to understand the nano-structural evolution and physicochemical characteristics of these complex oxide systems. Various physicochemical characterization techniques namely, thermal analysis (TG-DTA), X-ray diffraction (XRD), transmission electron microscopy (TEM), Laser Raman spectroscopy (LRS), UV-visible diffuse reflectance spectroscopy (UV-vis DRS), X-ray photoelectron spectroscopy (XPS), Ion scattering spectroscopy (ISS), temperature programmed reduction (TPR), and BET surface area (SA) were employed to investigate these oxide systems. All the synthesized catalysts were evaluated for the potential oxygen storage capacity (OSC), soot oxidation and CO oxidation reaction. A few of the catalytic systems were also evaluated for the selective dehydration of 4-methylpentan-2-ol. Thus, the thesis primarily deals with the synthesis, characterization and activity of various unsupported and supported ceria-hafnia composite oxides aiming at the enhancement of performance in terms of thermal stability and catalytic point of view.

1.6 Objectives of the Thesis

- The primary objective of the present work was to prepare nanosized unsupported ceria-hafnia and various supported ceria-hafnia mixed oxides possessing high specific surface area, better thermal stability, superior sintering resistance, high oxygen storage capacity and suitable redox properties.

- The intensive physicochemical characterization of the prepared catalyst formulations by employing various spectroscopic and non-spectroscopic techniques namely, thermogravimetry (TG-DTA), X-ray diffraction (XRD), temperature programmed reduction (TPR), scanning electron microscopy (SEM), transmission and high resolution electron microscopy (TEM-HREM), UV-vis diffuse reflectance spectroscopy (UV-vis DRS), Laser Raman spectroscopy (LRS), X-ray photoelectron spectroscopy (XPS), Ion scattering spectroscopy (ISS), and BET surface area.

- To evaluate the oxygen storage-release properties (OSC) of the synthesized catalysts.

- To test the catalytic activity of the synthesized catalysts for different important reactions namely, CO oxidation, soot oxidation, and dehydration of 4-methylpentan-2-ol, respectively.

1.7 References

[1] C. Noguera, Physics and Chemistry at Oxide Surfaces; Cambridge University Press: Cambridge, UK, 1996.

[2] H.H. Kung, Transition Metal Oxides: Surface Chemistry and Catalysis; Elsevier: Amsterdam, 1989.

[3] V.E. Henrich, P.A. Cox, The Surface Chemistry of Metal Oxides; Cambridge University Press: Cambridge, UK, 1994.

[4] A.F. Wells, Structural Inorganic Chemistry, 6th ed; Oxford University Press: New York, 1987.

[5] W.A. Harrison, Electronic Structure and the Properties of Solids; Dover: New York, 1989.

[6] M. Fernández-García, A. Martínez-Arias, J.C. Hanson, J.A. Rodríguez, Chem. Rev. 104 (2004) 4063.

[7] A. Brückner, Catal. Rev. Sci. Eng. 45 (2003) 97.

[8] B.M. Reddy, In Metal Oxides: Chemistry and Applications; J.L.G. Fierro, CRC Press, Taylor and Francis Group: Boca Raton, FL, 2006, ch. 8, 215.

[9] G. Ertl, H. Knozinger, J. Weitkamp (Editors), Handbook of Heterogeneous Catalysis; Wiley-VHC: Weinheim, 1997.

[10] M. Shelef, G.W. Graham, R.W. McCabe, In Catalysis by Ceria and Related Materials; A. Trovarelli (Editor); Imperial College Press: London, 2002; Chapter 10.

[11] A. Sherman, Chemical Vapor Deposition for Microelectronics: Principles, Technology and Applications; Noyes Publications: Park Ridge, NJ, 1987.

[12] H. Gleiter, Nanostruct. Mater. 6 (1995) 3.

[13] M. Valden, X. Lai, D.W. Goodman, Science 281 (1998) 1647.

[14] J.A. Rodriguez, G. Liu, T. Jirsak, C.Z. Hrbek, J. Dvorak, A. Maiti, J. Am. Chem. Soc. 124 (2002) 5247.

[15] P. Ayyub, V.R. Palkar, S. Chattopadhyay, M. Multani, Phys. Rev. B 51 (1995) 6135.

[16] N. Millot, D. Aymes, F. Bernard, J.C. Niepce, A. Traverse, F. Bouree, B.L. Cheng, P. Perriat, J. Phys. Chem. B 107 (2003) 5740.

[17] J.M. McHale, A. Auroux, A.J. Perrota, A. Navrotsky, Science 277 (1997) 788.

[18] V.M. Samsonov, N.Y. Sdobnyakov, A.N. Bazulev, Surf. Sci. 532–535 (2003) 526.

[19] R.C. Cammarata, K. Sieradki, Phys. Rev. Lett. 62 (1989) 2005.

[20] S. Surnev, G. Kresse, M.G. Ramsey, F.P. Netzer, Phys. Rev. Lett. 87 (2001) 86102.

[21] P. Moriarty, Rep. Prog. Phys. 64 (2001) 297.

[22] A.D. Yoffre, Adv. Phys. 42 (1993) 173.

[23] M. Fernández-García, J.C. Conesa, F. Illas, Surf. Sci. 349 (1996) 207.

[24] T. Albaret, F. Finocchi, C. Noguera, Faraday Discuss. 114 (2000) 285.

[25] M. Casarin, C. Maccato, A. Vittadini, Surf. Sci. 377–379 (1997) 587.

[26] J.A. Rodriguez, Theor. Chem. Acc. 107 (2002) 117.

[27] J.A. Rodriguez, S. Chaturvedi, M. Kuhn, J. Hrbek, J. Phys. Chem. B 102 (1998) 5511.

[28] R. Hoffmann, Solids and Surfaces: A Chemist's View of Bonding in Extended Structures; VCH: New York, 1988.

[29] E. Lucas, S. Decker, A. Khaleel, A. Seitz, S. Futlz, A. Ponce, W. Li, C. Carnes, K.J. Klabunde, Chem. Eur. J. 7 (2001) 2505.

[30] J.L. Anchell, A.C. Hess, J. Phys. Chem. 100 (1996) 18317.

[31] R. Richards, W. Li, S. Decker, C. Davidson, O. Koper, V. Zaikovski, A. Volodin, T. Rieker, J. Am. Chem. Soc. 122 (2000) 4921.

[32] A. Trovarelli, in: Catalysis by Ceria and Related Materials, Catalytic Science Series, World Scientific Publishing Company, UK, 2002, Vol. 2.

[33] S.R. Taylor, Geochim. Cosmochim. Acta. 28 (1964) 1973.

[34] B.T. Kilbourn, in: Cerium and Cerium Compounds, Ullmann's encyclopedia, Vol. 5, p. 728.

[35] K.A.Jr. Gschneidner, in: Fine Chemical for the Electronic Industry II: Chemical Applications for the1990's, D.J. Ando, M.G. Pellatt, Eds., Royal Society of Chemistry, 1991.

[36] J. Yan, in: Rare Earth Market- Challenge and Opportunity, China Rare Earth Information, 2000, Vol. 6.

[37] K.C. Taylor, in: Catalysis Science and Technology; Springer-Verlag: Berlin, 1984, Ch. 2.

[38] J. Kaspar, S. Bernal, A. Trovarelli, Eds., Recent Progress in Catalysis by Ceria and Related Compounds. Catal. Today 50 (1999) 173.

[39] A. Trovarelli, C. de Leitenburg, G. Dolcetti, Design Better Cerium-based Oxidation Catalysts, Chem. Tech. 27 (1997) 32.

[40] A. Fujimori, Phys. Rev. B 28 (1983) 2281.

[41] E. Wuillioud, B. Delley, W.D. Schneider, Y. Baer, Phys. Rev. Lett. 53 (1984) 202.

[42] F. Marabelli, P. Wachter, Phys. Rev. B 36 (1987) 1987.

[43] D.D. Koelling, A.M. Boring, J.H. Wood, Solid State Commun. 47 (1983) 227.

[44] G. Liu, J.A. Rodriguez, Z. Chang, J. Hrbek, C.H.F. Peden, J. Phys. Chem. B 108 (2004) 2931.

[45] J. Campserveux, P. Gernadian, J. Solid State Chem. 23 (1978) 73.

[46] R.J. Panlener, R.N. Blumenthal, G.E. Garnier. J. Phys. Chem. Solids 36 (1975) 1213.

[47] R.D. Shannon, C.T. Prewitt, Acta Cryst. B 25 (1969) 925.

[48] T.J. Mazanec, Solid State Ionics 70/71 (1994) 11.

[49] P. Gellings, Catal. Today 12 (1992) 1.

[50] H.L. Tuller, A.S. Nowick, J. Phys. Chem. Solids. 38 (1977) 859.

[51] I.K. Naik, T.Y. Tien, J. Phys. Chem. Solids. 39 (1978) 311.

[52] B.C.H. Steele and J.M. Floyd, Proc. British. Ceram. Trans. 72 (1971) 55.

[53] M.A. Panhans and R.N. Blumenthal, Solid State Ionics 60 (1993) 279.

[54] T. Moeller, The Lanthanides, in: Comprehensive Inorganic Chemistry, J.C. Bailar, H.J. Emeleus, R. Nyholm, A.F.T. Dickenson, Eds., Pergamon Press, Oxford, UK, 1982, Ch. 44.

[55] H. Cordatos, D. Ford, R.J. Gorte, J. Phys. Chem. 100 (1996) 18128.

[56] J.A. Killner, B.C.H. Steele, Mass Transport in Anion-Deficient Fluorite Oxides, in: Non-Stoichiometric Oxides, O.T. Sorrenson, Academic press, NY, 1981, Ch. 5, p. 233.

[57] A. Holmgren, B. Andersson, J. Catal. 178 (1998) 14.

[58] V. Perrichon, A. Laachir, G. Bergeret, R. Frety, L. Tournayan, O. Touret, J. Chem. Soc., Faraday Trans. 90 (1994) 773.

[59] H.C. Yao, Y.F. Yu Yao, J. Catal. 86 (1984) 254.

[60] A.M. Mourao, C.H. Falst, U.S. Patent 4,522,631 (11 June) 1985.

[61] R.E. Sievers, T.J. Wenzel, U.S. Patent, 4,251,233 (17 Feb) 1981.

[62] J.N. Armor, Appl. Catal. 176 (1999) 159.

[63] F. Joensen, J.R. Rostrup-Nielsen, J. Power Sources 105 (2002) 195.

[64] F. Auprêtre, C. Descorme, D. Duprez, Catal. Commun. 3 (2002) 263.

[65] D. Srinivas, C.V.V. Satyanarayana, H.S. Potdar, P. Ratnasamy, Appl. Catal. A: Gen. 246 (2003) 323.

[66] L.V. Mattos, E.R. De Oliveira, P.D. Resende, F.B. Noronha, F.B. Passos, Catal. Today 77 (2002) 245.

[67] S. Xu, X. Wang, Fuel 84 (2005) 563.

[68] F.B. Noronha, E.C. Fendley, R.R. Soares, W.E. Alvarez, D.E. Resasco, Chem. Engg. Journal 82 (2001) 21.

[69] J.R. Rostrup-Nielsen, Catal. Today 63 (2000) 159.

[70] T. Zhu, M.F. Stephanopoulos, Appl. Catal. A: Gen. 208 (2001) 403.

[71] V.R. Choudhary, A.M. Rajput, B. Prabhakar, A.S. Mamman, Fuel 77 (1998) 1803.

[72] I. Dykkjaer, T.S. Christensen, Stud. Surf. Sci. Catal. 136 (2001) 435.

[73] Y.H. Hu, E. Ruckenstein, J. Catal. 158 (1996) 260.

[74] J.R.R. Nielsen, Catal. Today 63 (2000) 159.

[75] J.H. Lunsford, Catal. Today 63 (2000) 165.

[76] D.B. Bukur, X. Lang, Y. Ding, Appl. Catal. A: Gen. 186 (1999) 255.

[77] S.C. Tsang, J.B. Claridge, M.L.H. Green, Catal. Today 23 (1995) 3.

[78] W.S. Dong, H.S. Roh, K.W. Jun, S.E. Park, Y.S. Oh, Appl. Catal. A: Gen. 226 (2002) 63.

[79] L.V. Mattos, E.R. De Oliveira, P.D. Resende, F.B. Noronha, F.B. Passos, Catal. Today 77 (2002) 245.

[80] D. Tibiletti, A. Amieiro-Fonseca, R. Burch, Y. Chen, J. M. Fisher, A. Goguet, C. Hardacre, P. Hu, D. Thompsett, J. Phys. Chem. B 109 (2005) 22553.

[81] S. Xu, X. Wang, Fuel 84 (2005) 563.

[82] H.S. Roh, H.S. Potdar, K.W. Jun, Catal. Today 93–95 (2004) 39.

[83] F.B. Noronha, E.C. Fendley, R.R. Soares, W.E. Alvarez, D.E. Resasco, Chem. Engg. J. 82 (2001) 21.

[84] D.L. Trimm, Z. Ilsen Önsan, Catal. Rev. Sci. Tech. 43 (2001) 31.

[85] T.V. Choudhary, D.W. Goodman, Catal. Today 77 (2002) 65.

[86] G. Avgouropoulos, T. Ioannides, C. Papadopoulou, J. Batista, S. Hocevar, H.K. Matralis, Catal. Today 75 (2002) 157.

[87] J.B. Wang, S. Lin, T. Huang, Appl. Catal. A: Gen. 232 (2002) 107.

[88] O. Pozdnyakova, D.Teschner, A. Wootsch, J. Kröhnert, B. Steinhauer, H. Sauer, L. Toth, C. Jentoft, A. Knop-Gericke, Z. Paál, R. Schlögl, J. Catal. 237 (2006) 1.

[89] O. Pozdnyakova, D.Teschner, A. Wootsch, J. Kröhnert, B. Steinhauer, H. Sauer, L. Toth, F.C. Jentoft, A. Knop-Gericke, Z. Paál, R. Schlögl, J. Catal. 237 (2006) 17.

[90] G. Panzera, V. Modafferi, S. Candamano, A. Donato, F. Frusteri, P. L. Antonucci, J. Power sources, 135 (2004) 177.

[91] P. Ratnasamy, D. Srinivas, C.V.V. Satyanarayana, P. Manikandan, R.S. Senthil Kumaran, M. Sachin, Vasudev N. Shetti, J. Catal. 221 (2004) 455.

[92] S. Park, R.J. Gorte, J.M. Vohs, Appl. Catal. A: Gen. 200 (2000) 55.

[93] S.P.S. Badwal, K. Foger, Ceram. Int. 22 (1996) 257.

[94] S.H. Clarke, A.L. Kicks, K. Pointon, T.A. Smith, A. Swann, Catal. Today 38 (1997) 11.

[95] S.L. Douvartzides, F.A. Coutelieris, A.K. Demin, P.E. Tsiakaras, AIChE J. 49 (2003) 248.

[96] S. Larrondo, M.A. Vidal, B. Irigoyen, A.F. Craievich, D.G. Lamas, I.O. Fabregas, G.E. Lascalea, N.E. Walsöe de Reca, N. Amadeo, Catal. Today 107–108 (2005) 53.

[97] E.C. Moretti, Chem. Eng. Prog. 98 (2002) 30.

[98] J.I. Gutierrez-Ortiz, B. de Rivas, R. Lopez-Fonseca, J.R. Gonzalez-Velasco, Catal. Today 107–108 (2005) 933.

[99] J. Scherzer, Rare Earths in Cracking Catalysts, in: Rare Earths, Extraction, Preparation and Applications, R.G. Bautista, M.M. Wong, Eds., Pub. TMS, 1988, p.317.

[100] A.A. Bhattachryya, G.M. Woltermann, J.S. Yao, J.A. Karch, W.E. Cormier, Ind. Eng. Chem. Res., 27 (1988) 1356.

[101] K. Baron, D.P. McArthur, U.S. Patent 4,341,661 (27 July) 1982.

[102] B.T. Kibourn, J. Less, Common Metals. 126 (1986) 101.

[103] J.F. Brazdil, R.K. Graselli, J. Catal. 79 (1983) 104.

[104] G. Owen, C.M. Howkes, D. Lioyd, J.R. Jennings, R.M. Lambert, R.M. Nix, Appl. Catal. 33 (1987) 405.

[105] Y. Li, D. He, Q. Zhu, X. Zhang, B. Xu, J. Catal. 221 (2004) 584.

[106] K. Tomishige, K. Kunimori, Appl. Catal. A: Gen. 237 (2002) 103.

[107] V. Solinas, E. Rombi, I. Ferino, M.G. Cutrufello, G. Colon, J.A. Navio, J. Mol. Catal. A: Chem. 204-205 (2003) 629.

[108] B.M. Reddy, P.M. Sreekanth, P. Lakshmanan, A. Khan, J. Mol. Catal. A: Chem. 244 (2005) 1.

[109] B.C.H. Steele, A. Heinzel, Nature 414 (2001) 345.

[110] M.H. Bocanegra- Bernal, S.D. de la Torre, J. Mater. Sci. 37 (2002) 4947.

[111] W.C. Maskell, Solid State Ionics 134 (2000) 43.

[112] J.H. Lee, J. Mater. Sci. 38 (2003) 4247.

[113] J.R. Jurado, Mater. Sci. 36 (2001) 1133.

[114] R.A. Shalliker, G.K. Douglas, J. Liq. Chromatogr. Relat. Technol. 21 (1998) 2413.

[115] C. Piconi, G. Maccauro, Biomaterials 20 (1999) 1.

[116] R.X. Li, S. Yabe, M. Yamashita, S. Momose, S. Yoshida, S. Yin, T. Sato, Mater. Chem. Phys. 75 (2002) 39.

[116] R.X. Li, S. Yabe, M. Yamashita, S. Momose, S. Yoshida, S. Yin, T. Sato, Solid State Ionics 151 (2002) 235.

[117] J. Khaladji, M. Peltier, Rare Earth Polishing Compositions, U.S. Pat. 4,942,69 (24 July) 1990.

[118] T.C. Schutt, Ceram. Bull. 51 (1972) 155.

[119] V.I. Arbuzov, N.B. Belyankina, Phys. Chem. Glasses. 16 (1990) 317.

[120] S. Xu, J. Non Cryst. Solids 112 (1989) 186.

[121] T. Chopin, D. Dupuis, Rare Earth Metal Sulfide Pigment Compositions, U.S. Pat. 5,401,309 (28 March) 1995.

[122] A.I. Nedeljkovic, R.L. Cook, The Vitreous Enameller, 26 (1975) 2.

[123] K. Tsukuma, Am. Ceram. Soc. Bull. 65 (1986) 1386.

[124] J.W. Holmes, B.H. Pilsner, Proc. Natl. Therm. Spray Conf. (1987) 259.

[125] J.M. Tranquada, S.M. Heald, A.R. Moodenbaugh, G. Liang, M. Croft, Nature 337 (1989) 720.

[126] N. Butta, L. Chinquegrani, E. Mugno, A. Tagliente, S. Pizzini, Sens. Actuators B 6 (1992) 253.

[127] Z.T. Al-Dhan, C.A. Hogarth, N. Riddleston, Phys. Status Solidi B 145 (1998)145.

[128] T. Masui, T. Yamamoto, H. Sakata, G. Mori, J. Adachi, J. Mater. Chem. 10 (2000) 353.

[129] B.M. Reddy, P. Bharali, P. Saikia, S.-E. Park, M.W.E. van den Berg, M. Muhler, W. Grünert, J. Phys. Chem. C 112 (2008) 11729.

[130] B.M. Reddy, P. Bharali, P. Saikia, A. Khan, S. Loridant, M. Muhler, W. Grünert, J. Phys. Chem. C 111 (2007) 1878.

[131] K. Otsuka, Y. Wang, M. Nakamura, Appl. Catal. A: Gen. 183 (1999) 317.

[132] M.G. Cutrufello, I. Ferino, V. Solinas, A. Primavera, A. Trovarelli, A. Auroux, C. Picciau, Phys. Chem. Chem. Phys. 1 (1999) 3369.

[133] M.G. Cutrufello, I. Ferino, R. Monaci, E. Rombi, V. Solinas, Top. Catal. 19 (2002) 225.

[134] B.M. Reddy, P. Lakshmanan, P. Bharali, P. Saikia, J. Mol. Catal. A: Chem. 258 (2006) 355.

[135] B.M. Reddy, P. Lakshmanan, S. Loridant, Y. Yamada, T. Kobayashi, C.L.-Cartes, T.C. Rojas, A. Fernandez, J. Phys. Chem. B 110 (2006) 9140.

[136] B.M. Reddy, K.N. Rao, G.K. Reddy, A. Khan, S.-E. Park, J. Phys. Chem. C 111 (2007) 18751.

[137] M. Machida, Y. Murata, K. Kishikawa, D. Zhang, K. Ikeue, Chem. Mater. 20 (2008) 4489.

[138] V. S. Mishra, V. V. Mahajani, J.B. Joshi, Ind. Eng. Chem. Res. 34 (1995) 2.

[139] M. Ozawa, K. Matuda, S. Suzuki, J. Alloys Compd. 303–304 (2000) 56.

[140] R.D. Monte, J. Kasper, J. Mater. Chem. 15 (2005) 633.

[141] A. Piras, A. Trovarelli, G. Dolcetti, Appl. Catal. B: Environ. 28 (2000) L77.

[142] M.C.J. Bradford, M.A. Vannice, Catal. Today 50 (1999) 47.

[143] M.J. Tiernan, O.E. Finlayson, Appl. Catal. B: Environ. 19 (1998) 23.

[144] A. Holmgren, B. Andersson, D. Duprez, Appl. Catal. B: Environ. 22 (1999) 215.

[145] S. Wang, G.Q. Lu, Appl. Catal. B: Environ. 19 (1998) 267.

[146] S. Damyanova, C.A. Perez, M. Schmal, J.M.C. Bueno, Appl. Catal. A: Gen. 234 (2002) 271.

[147] B.M. Reddy, A. Khan Catal. Surv. Asia 9 (2005) 155.

[148] B.M. Reddy, P. Saikia, P. Bharali, Y. Yamada, T. Kobayashi, M. Muhler, W. Grünert, J. Phys. Chem. C 112 (2008) 16393.

[149] B.M. Reddy, A. Khan, P. Lakshmanan, M. Aouine, S. Loridant, J.C. Volta, J. Phys. Chem. B 109 (2005) 3355.

[150] M. Sugiura, Catal. Surv. Asia, 7 (2003) 77.

[151] M. Fernandez-Garcia, A. Martinez-Ariaz, A. Iglesias Juez, C. Belver, A.B. Hungria, J.C. Conesa, J. Soria, J. Catal. 194 (2000) 385.

[152] G. Balducci, M.S. Islam, J. Kaspar, P. Fornasiero, M. Graziani, Chem. Mater. 12 (2000) 677.

[153] S. Bernal, G. Blanco, G.A. Cifredo, J.J. Delgado, D. Finol, J.M. Gatica, J.M. Rodriguez-Izquierdo, H. Vidal, Chem. Mater. 14 (2002) 844.

[154] T. Ozaki, T. Masui, K. Machida, G. Adachi, T. Sakata, H. Mori, Chem. Mater. 12 (2000) 643.

[155] Z.Y. Pu, J.Q. Lu, M.F. Luo, Y.L. Xie, J. Phys. Chem. C 111 (2007**)** 18695.

[156] G. Stefanic, S. Music, R. Trojko, J. Alloys Comp. 388 (2005) 126.

[157] M. Villanueva-Ibanez, C. Le Luyer, S. Parola, O. Marty, J. Mugnier, Rev. Adv. Mater. Sci. 5 (2003) 296.

[158] H. Fujimori, M. Yashima, S. Sasaki, M. Kakihana, T. Mori, M. Tana Yoshimura, Chem. Phys. Lett. 346 (2001) 217.

[159] R.D. Robinson, J. Tang, M.L. Steigerwald, L.E. Brus, I.P. Herman, Phys. Rev. B 71 (2005) 115408.

[160] C. Bozo, F. Gaillard, N. Guilhaume, Appl. Catal. A: Gen. 220 (2001) 69.

[161] B.M. Reddy, P. Lakshmanan, P. Bharali, P. Saikia, G. Thrimurthulu, M. Muhler, W. Grünert, J. Phys. Chem. C 111 (2007) 10478.

[162] D.E. Keller, S.M.K. Airaksinen, A.O. Krause, B.M. Weckhuysen, D.C. Koningsberger, J. Am. Chem. Soc. 129 (2007) 3189.

Chapter 2

This chapter presents the experimental details pertaining to the preparative methodologies employed to obtain the nanosized composite oxides and the techniques related to BET surface area, thermogravimetry, X-ray diffraction, Raman spectroscopy, UV-vis diffuse reflectance spectroscopy, X-ray photoelectron spectroscopy, ion scattering spectroscopy, and temperature programmed reduction with necessary theoretical background.

EXPERIMENTAL SECTION

2.1 Preparations

2.1.1 Preparation of Ceria-hafnia Nanocomposite oxide

Ceria–hafnia (CH, 8:2 mole ratio based on oxides) composite oxide was prepared by adopting a coprecipitation method using ammonium cerium(IV) nitrate (Loba Chemie, GR grade) and hafnium(IV) chloride (Aldrich, AR grade), respectively. The required amounts of precursors were dissolved separately in deionised water under mild stirring conditions and mixed together. Upon complete mixing, excess ammonium hydroxide was added dropwise until the precipitation was complete (pH = ~8.5). The resulting slurry was filtered off and thoroughly washed with distilled water until free from anion impurities. The mixed hydroxide paste was allowed to dry overnight in a hood. It was then oven dried at 393 K for 12 h. Finally, it was calcined at 773 K for 5 h in air atmosphere to remove water and any residual precursors remaining from the coprecipitation step. Some portions of the catalyst were further calcined at 873, 973, and 1073 K, respectively for 5 h in air atmosphere. After cooling, the solid residues were ground using a ceramic mortar and pestle until fine powders were obtained. The rate of heating as well as cooling was always maintained at 5 K min^{-1}. For comparison purpose, CeO_2–ZrO_2 composite oxide was also prepared from ammonium cerium(IV) nitrate (Loba Chemie, GR grade) and zirconium(IV) nitrate (Fluka, AR grade) by similar precipitation method using dilute aqueous ammonia solution and calcined at 773 to 1073 K for 5 h in air atmosphere.

2.1.2 Preparation of Supported Ceria-hafnia Nanocomposite Oxides

The following supported ceria-hafnia nanocomposite oxides were prepared in this investigation:

CeO_2–HfO_2/SiO_2 (CHS)

CeO_2–HfO_2/TiO_2 (CHT)

CeO_2–HfO_2/Al_2O_3 (CHA)

The nanosized ceria-hafnia composite oxides over SiO_2, TiO_2, and Al_2O_3 supports (CeO_2: HfO_2: support oxide = 8:2:10 mole ratio based on oxides) were synthesized by a deposition coprecipitation method using dilute aqueous ammonia solution as the precipitating agent. The precursors employed were $(NH_4)_2Ce(NO_3)_6$, $HfCl_4$, colloidal SiO_2 (Ludox, 40 wt.%, Aldrich), TiO_2-anatase (EU consortium, SA 49 $m^2\ g^{-1}$), and γ-Al_2O_3 (Harshaw, SA 127 $m^2\ g^{-1}$), respectively. At first, cerium and hafnium precursors were dissolved separately in deionized water and mixed together in an appropriate quantity. The supporting oxides were dispersed separately in deionized water, stirred vigorously and then mixed with the ceria-hafnia precursor solutions together. The mixture solution was further diluted with deionized water and kept in stirring condition for another 1 h. Aqueous NH_3 solution was added dropwise to the mixture solution under vigorous stirring until the pH reached ~8.5. The obtained precipitates were filtered off, washed with deionized water until free from anion impurities and oven dried at 393 K for 12 h, and subsequently calcined at 773 K for 5 h in air atmosphere to remove water and any residual precursors remaining from the precipitation step. Some portions of the 773 K calcined sample were further treated at 873, 973 and 1073 K for 5 h in air atmosphere. The rate of heating as well as cooling was always maintained at 5 K min^{-1}.

2.2 Catalyst Characterization

In the present investigation the following spectroscopic and non-spectroscopic techniques were employed to characterize various composite oxide catalysts:

1. Specific Surface Area by BET Method
2. Thermal Analysis (TGA/DTA)
3. X-ray Diffraction Studies (XRD)
4. Temperature Programmed Reduction (TPR)
5. Scanning Electron Microscopy (SEM)
6. Transmission Electron Microscopy (TEM)
7. UV-vis Diffuse Reflectance Spectroscopy (UV-vis DRS)
8. Laser Raman Spectroscopy (LRS)
9. X-ray Photoelectron Spectroscopy (XPS)
10. Ion Scattering Spectroscopy (ISS)

2.2.1 Specific Surface Area: BET Method

The Brunauer-Emmett-Teller (BET) method is the most acceptable procedure for measuring surface areas of various materials by physical adsorption of gases at their boiling temperatures. In principle the amount of adsorbate (nitrogen) required to form a monolayer of molecules over the surface of catalyst is given by the following BET equation [1–3].

$$\frac{P}{V_a (P_0 - P)} = \frac{1}{V_m C} + \frac{C - 1}{V_m C} \frac{P}{P_0} \qquad (2.1)$$

Where,

P is the pressure,

P_0 is the saturation vapor pressure,

V_a is the amount of gas adsorbed at the relative pressure P/P_0,

V_m is the monolayer capacity, and

C is a BET constant.

A plot of $P/V_a (P_0-P)$ versus relative pressure of P/P_0 is a straight line with a slope of $(C–1)/(V_mC)$ and intercept of $1/(V_mC)$, respectively. Knowing slope and intercept permits calculation of V_m. Subsequently the specific surface area of the sample can be determined by the following equation.

$$\text{Specific Surface Area } (m^2 g^{-1}) = \frac{V_m \text{ X } L \text{ X } A_m}{W \text{ X } V_0} \qquad (2.2)$$

Where,

L is the Avagodro constant ($6.023 \text{ X } 10^{23}$ molecules mol^{-1})

A_m is cross sectional area of adsorbate molecule, (N_2) 0.162 nm^2 at 77 K

W is the weight of the sample

V_0 is 22414 mL mol^{-1}

In the present investigation, the BET surface areas were determined by N_2 adsorption using a Micromeritics Gemini 2360 Instrument. Prior to analysis, the samples were oven dried at 393 K for 12 h under vacuum and flushed with Argon gas for 2 h. All the BET values in this study were measured within the precision of ± 5%.

2.2.2 Thermal Analysis

When a substance is subjected to a programmed heating and cooling, it normally undergoes physical, chemical or mechanical changes. The gain or loss in weight of a sample as a function of temperature is measured by thermogravimetry (TG). It is a very useful technique for the study of solid-gas systems. Most physical, chemical or physicochemical phenomena are characterized by variations in the masses of reactive samples when these samples are subjected to various environments, such as temperature, atmosphere, vacuum, and pressure. As the main parameter is often the temperature, thus the common name of thermogravimetry. The measuring instrument is comprised of an ultra sensitive weighing device. The changes in the mass of the sample clearly imply evolution or uptake of matter by the sample. This method works well for compact samples [4]. All the TGA curves represented in this thesis were obtained on a Mettler Toledo TGA/SDTA 851^e instrument. The samples were heated from ambient temperature to 1273 K under a nitrogen flow at flow rate of 20 mL min^{-1} and heating rate of 10 K min^{-1}.

2.2.3 X-ray Diffraction Studies

X-ray diffraction (XRD) was used to investigate the bulk phases present in the sample and to determine the calcination induced solid-solid phase transformations if any. X-rays are energetic enough to penetrate into the material and their wavelengths are of the same order of magnitude as interatomic distances in solids. Thus, a collimated beam of X-rays is diffracted by the crystalline phases in the sample according to Bragg's Law [5–7]. Powder diffraction profiles are obtained by measuring the angles at which an X-ray beam of wavelength λ is diffracted by the sample. Position, intensity, shape and width of the diffraction lines give information about the sample.

The spacing between two planes (*hkl*) *d* is related to the diffraction angle 2θ by the Bragg law:

$$n\lambda = 2d \sin \theta \qquad (2.3)$$

Where,

λ is the wavelength of the X-rays,

d is the distance between two atomic planes in the crystalline phase,

n is the order of the diffraction, and

θ the incoming diffraction angle.

Phase identification is based on the comparison of the set of reflections of the specimen with that of pure reference phases, or with a database. The *powder diffraction file* (PDF) [8] distributed by the International Centre for Diffraction Data (ICDD) (formerly ASTM then JCPDS) is the base most commonly used. It is a collection of single phase X-ray powder diffraction patterns in the form of tables of characteristic interplanar spacings and corresponding relative intensities along with crystallographic properties. All powder X-ray diffraction (XRD) patterns presented in this thesis, were recorded on a Rigaku Multiflex diffractometer using nickel-filtered Cu Kα (0.15418 nm) radiation source and a scintillation counter detector. The intensity data were collected over a 2θ range of 2–80° with a 0.02° step size and using a counting time of 1 s per point. Diffraction patterns were assigned using the PDF database supplied by the International Centre for Diffraction Data.

Crystallite Size Determination

The average crystallite size in various samples was estimated with the help of Scherrer equation using the XRD data of all prominent lines. Diffraction lines should, in principle, be very narrow; however, when the crystallite size of a polycrystalline material falls below 1000 Å, broadening of the diffraction lines is observed. Instrumental limitations and lattice strain can also cause line broadening.

The relation between line broadening and crystallite size for a stress free material, is given by Scherrer formula:

$$< L >_{hkl} = \frac{K\lambda}{\beta_{hkl} \text{Cos } \theta} \qquad (2.4)$$

Where K is a constant that depends on the definition of β [FWHM value of a particular hkl plane, in degrees (a Polar co-ordinate), needs to be converted into radians (a Cartesian co-ordinate), since, crystallite size measures in length units] used and the crystal geometry. The constant K varies from 0.98 to 1.39, but because of experimental uncertainties, the constant is often set equal to 1. When β is defined as the integral breadth, <L> is a volume average crystallite size [5].

Cell Parameter Estimation

The cell parameter 'a' was calculated by standard cubic indexation method using the intensity of the most prominent XRD lines (111) of $Ce_{0.8}Hf_{0.2}O_2$ and $Ce_{0.75}Zr_{0.25}O_2$ phases in respective samples. For calculation of the unit cell parameters, the cubic relationship of d_{hkl} and the cell parameters was assumed for all the samples as per the equation given below [9,10]:

$$1/d^2_{hkl} = (h^2 + k^2 + l^2) / a^2 \qquad (2.5)$$

2.2.4 Temperature Programmed Reduction

Temperature programmed reduction (TPR) using hydrogen (H_2) or carbon monoxide (CO) as reducing agent is a widely used technique for the characterization of reducible solids and catalysts. In TPR, a reducible catalyst or catalyst precursor is exposed to a flow of a reducing gas mixture (typically a few vol.% of H_2 or CO in an inert gas) while the temperature is linearly increased. The rate of reduction is continuously followed by measuring the composition (H_2 or CO content) of the reducing gas mixture at the outlet of the reactor. The experiment permits the determination of the total amount of H_2 or CO consumed, from which the degree of reduction and thus, the average oxidation state of the solid after reduction can be calculated. A detailed description of the underlying

physical principles of the TPR method is presented in pertinent reviews and papers [11–15].

The present investigation involves the use of both CO and H_2 as reducing agent for the TPR measurements. For the H_2-TPR runs, about 100 mg of catalyst sample was loaded in an isothermal zone of the reactor and heated at a rate of 10 K min^{-1} to 473 K in 30 mL min^{-1} helium gas which facilitated desorption of the physically adsorbed water. After the sample was cooled to room temperature, the helium was switched to 20 mL min^{-1} of reducing gas consisting of 5% H_2/Ar and the temperature was increased to 1073 K at heating rate of 5 K min^{-1}. The reactor effluent gas was passed through a molecular sieve trap to remove the produced water and was analyzed by gas chromatograph (GC) using a thermal conductivity detector (TCD). On the other hand for CO-TPR runs, the concentration of CO, flow rate and the heating rate were balanced with the amount of catalyst (100–150 mg) for TPR experiments as per literature. Measurements were made using 9.98% CO/Ar gas mixture at a flow rate of 20 mL min^{-1} and up to 873 K maximum temperature with a heating rate of 5 K min^{-1}. Before measurements, the catalysts were pretreated at 773 K for 1 h in 10.2% O_2/Ar gas mixture, using a heating rate of 10 K min^{-1}. The oxidized sample was then purged in argon and cooled to the desired starting temperature. The CO and CO_2 gas concentrations were measured using an Uras 14 infrared analyzer module, and the O_2 concentration was measured using a Magnos 16 analyzer (Hartmann & Braun).

2.2.5 Scanning Electron Microscopy

Because of its versatility and the wide range of information scanning electron microscopy (SEM) can provide, the scanning electron microscope is often the preferred starting tool for analytic microscopy. With SEM, a focused beam of high-energy electrons is scanned over the surface of a material. The electron beam interacts with the material, causing a variety of signals; secondary electrons, backscattered electrons, X-rays, photons, etc. each of which may be used to characterize a material with respect to specific properties. To study the surface topography and to assess the surface dispersion of the active components, SEM analyses were carried out with a JEOL JSM 5410 microscope, operating with an accelerating voltage of 15 kV. SEM micrographs were taken after coating by gold sputtering.

2.2.6 Transmission Electron Microscopy

Heterogeneous catalysts usually consist of highly divided solid phases that are closely interconnected and thus difficult to characterize. Transmission electron microscopy (TEM) offers the unique advantage of allowing the direct observation of catalyst morphology with a resolution tuneable in the range 10^{-4}–10^{-10} m and of obtaining structural information by lattice imaging and microdiffraction techniques. The technique of high-resolution electron microscopy (HREM) is performed with axial illumination using an objective aperture, which allows several diffracted beams to be combined with the axial transmitted beam to form the image. The HREM images can be directly related with the atomic structure of the material. From images it is possible to obtain data on the shape and size of particles belonging to supports as well as active phases and to unravel how they are distributed with respect to each other. Structural information such as symmetry and unit cell parameters of crystallites, crystal orientations (e.g. epitaxial relationship between support and active phase), lattice defects can be obtained by electron diffraction and lattice imaging techniques [16–19]. Specimen preparation is a critical step in electron microscopy because image quality is highly dependent on how the different solid phases are dispersed on the microscope grid and on their thickness. The thickness of solid phases should be less than 50-100 nm to allow sufficient transmittance. Thinner the samples better the resolution and better contrast. Another important factor is the stability of the preparation. Specimens have to be deposited on 2/3 mm diameter copper grids (100–400 mesh) covered with a thin amorphous carbon film. The easiest way is to ultrasonically disperse a few milligram of the powder in a few milliliter of ethanol (EtOH), take a drop of the suspension deposit it on a carbon coated grid and let the liquid evaporate. In this study, the electron microscopic investigations were carried on a JEM-2010 (JEOL) instrument equipped with a slow-scan CCD camera and at an accelerating voltage of 200 kV.

2.2.7 UV-vis Diffuse Reflectance Spectroscopy

The absorption bands occurring in the visible and near-UV regions are used to obtain information on the electronic structure of catalyst and support. Most heterogeneous catalysts are opaque powdered samples from which light is reflected and not transmitted. The radiation reflected from a powdered crystalline surface consists of two components:

the specular component that is reflected from the surface without transmission (mirror reflection) and the diffuse component that is absorbed into the material and reappears at the surface after multiple scattering. Commercial spectrophotometers are designed to minimize the specular component and the term reflectance is used for diffusely reflected radiation [20–23].

In a diffuse reflectance spectrum (DRS), the ratio of the light scattered from a (2-3 mm) thick layer of sample and an ideal non-absorbing reference sample is measured as a function of wavelength λ (i.e. $F_{SKM}(R\infty)$ vs λ in nm). The relation between the diffuse reflectance of the sample ($R\infty$), absorption (K), and scattering (S) coefficients are related by the Schuster-Kubelka-Munk (SKM) remission function [21,22]:

$$F(R_\infty) = (1- R_\infty)^2/2 R_\infty = K/S \qquad (2.6)$$

The samples were diluted in a KBr matrix by pelletization. The spectra were obtained over the wavelength range λ = 200–800 nm using a GBS-Cintra 10e UV-Vis NIR spectrophotometer with the integration sphere diffuse reflectance attachment. The corresponding diluent (KBr) was used as baseline standard. The DRS spectra were processed with SPECTRAL 1.70 software, consisting of calculation of $F(R_\infty)$ from the absorbance.

2.2.8 Laser Raman Spectroscopy

Raman spectroscopy is one of the most useful techniques for characterization of catalytic materials and to gather information on both M–O bond arrangement and lattice defects. Raman spectra of the fluorite type oxides are dominated by oxygen lattice vibrations, which are sensitive to the crystal symmetry, being thus a potential tool to obtain additional structural information. It can discriminate between the different chemical states of the metal oxides because each state possesses a unique vibrational spectrum that is related to its structure. Therefore, Raman spectroscopy provides direct information about the structure of each state. It is well reported in the literature that the intensity of Raman bands may vary depending on the laser source used. Recently, a study was reported on the investigation of the surface and bulk properties of fluorite-type oxide materials with four different excitation lasers by Raman spectroscopy [24]. On the basis of the fact that

the laser with shorter wavelength is closer to the electronic adsorption of samples, it is reported that the Raman information detected by excitation laser with shorter wavelength is more sensitive to the surface region of samples.

In the present investigation, the Raman spectra were recorded with two different spectrometers. UV-RS were recorded with a LabRam HR800UV Raman spectrometer (Horiba Jobin-Yvon) equipped with a confocal microscope and liquid-nitrogen cooled charge-coupled device (CCD) detector. The emission line at 325 nm from He-Cd laser (Melles Griot Laser) was focused on the sample under the microscope, with the diameter of the analyzed spot being ~1 μm. The vis-RS were recorded with a LabRam HR spectrometer (Horiba Jobin-Yvon) equipped with a CCD detector. The emission line at 514.53 nm from an Ar^+-Kr^+ ion RM2018 laser (Spectra Physics) was focused on the sample under the microscope, with the diameter of the analyzed spot being ~1μm. The power of the incident beam on the sample was typically 0.5mW. The time of acquisition in both the cases was adjusted according to the intensity of the Raman scattering. The wave number values reported from the spectra are accurate to within 1 cm^{-1}. In order to ascertain the homogeneity of the samples, spectra were recorded at various points and compared. All samples were found to be highly homogeneous [25–27].

2.2.9 X-ray Photoelectron Spectroscopy

X-ray photoelectron spectroscopy (XPS) is a well-known surface technique, also known as Electron Spectroscopy for Chemical Analysis (ESCA). It is now a widely used analytical technique for investigating the chemical composition of solid surfaces with its attenuation depth of 20 Å. XPS is accompanied by irradiating a sample with monoenergetic soft X-rays and energy analyzing the electrons emitted. Mg Kα (1253.6 eV) or Al Kα (1486.6 eV) X-rays are ordinarily used. These photons have limited penetrating power in a solid, of the order of 1-10 micrometers. They interact with atoms in this surface region by the photoelectric effect, causing electrons to be emitted. The emitted electrons have kinetic energy (KE) given by:

$$KE = h\upsilon - BE - \varphi_s \qquad (2.7)$$

Where,

$h\upsilon$ is the energy of photon

BE is the binding energy of atomic orbital from which the electron originates

φ_s is the spectrometer work function

The binding energy may be regarded as ionization energy of the atom for the particular shell involved. Since there are a variety of possible ions from each type of atom, there is a corresponding variety of kinetic energies of the emitted electrons.

The XP spectra of all the samples were recorded on a Shimadzu (ESCA 3400) spectrometer by using Mg Kα (1253.6 eV) radiation as the excitation source. Charging of catalyst samples was corrected by setting the binding energy of the adventitious carbon (C 1s) at 284.6 eV. The XPS analysis was done at ambient temperature and pressures typically in the order of less than 10^{-6} Pa. Prior to analysis, the samples were out-gassed in a vacuum oven overnight. All binding energies quoted in this study were measured within a precision of ±0.1 eV [28,29].

Atomic Ratio Estimations

Quantification of atomic ratios was achieved by determining the elemental peak areas, following a Shirley background subtraction and correcting by using atomic sensitivity factors supplied by the instrument manufacturer [28,29].

2.2.10 Ion Scattering Spectroscopy

If a beam of ions is directed at a sample surface, then a certain number will be elastically reflected. The intensity of the scattered ions as a function of emission provides information regarding the surface crystallographic structure. The variation in the intensity of the scattered beam is partly due to shadowing the substrate atoms. Bye use of scattering theory, knowledge the sites that the surface atoms occupy can be derived. The technique is called Ion Scattering Spectroscopy (ISS) [30]. The term encompasses actually several techniques depending on the energy of the primary ion beam. LEIS (Low Energy Ion Scattering) spectroscopy is referred to primary energies in the range of 100 eV to 10 keV, Often the LEIS technique is called ISS. ISS provides information on the atomic

composition of the outer surface, when noble gas ions are used as projectiles. In ISS experiments, low-energy noble gas ions are scattered by atoms in the exposed surface. According to the laws of conservation of energy and momentum, the energy spectrum of the backscattered ions is equivalent to the mass spectrum of the target atoms. The information depth of ISS is limited to one atomic layer because of the high neutralization probability of the noble gas ions.

The process can be considered as a series of elastic collisions with the atoms in the top layers. In this (kilovolt) energy range one can assume that the collisions are binary and the atoms are free, so that the ion-atom interaction is described by repulsion interatomic potentials only. According to the classical mechanics, the energy of scattered particle is given by

$$E_1/E_o = \{\pm(M_2^2-M_1^2\sin^2\theta_1)^{1/2} + M_1\cos\theta_1] / (M_1+M_2)\}^2 \qquad (2.8)$$

(both signs hold for $M_1>M_2$ and only the positive signs otherwise), where E_o is the initial energy, θ_1 is the scattering angle, M_1 and M_2 are the ion and target atom mass respectively [30,31]. This equation directly relates the energy of the scattered particle to the mass of the target. It can be used also to evaluate the energy after two, three or more collisions. Low energy ion scattering is attractive as a surface-specific technique. Spectra are usually obtained using noble gas ion beams from 0.5 to 5 keV.

In the present investigation, IS spectra were measured in a Leybold surface analysis system equipped with X-ray and ion sources and an EA 10/100 electron (ion) analyzer with multichannel detection (Specs). The samples were pretreated in flowing synthetic air (20% O_2/N_2) at 573 K for 30 min before they were introduced into the spectrometer vacuum without further contact with the ambient humid atmosphere (in situ treatment). The measurements were done with 3000 eV Ar^+ ions and recorded with the analyzer in pass-energy mode (pass energy 84.5 eV). The surface charge was removed with a flood gun. The source and the flood gun were allowed to stabilize with the sample withdrawn from the measurement position. Signal intensities were estimated assuming the background to be linear.

2.3 Catalytic Activity Studies

The composite oxides prepared and characterized by different spectroscopic and non-spectroscopic techniques in the present investigation were evaluated for their usefulness in various catalytic reactions:

1. Potential Oxygen Storage Capacity (OSC)
2. CO Oxidation Reaction
3. Soot Oxidation Reaction
4. Dehydration of 4-methylpentan-2-ol

2.3.1 Potential Oxygen Storage Capacity

Potential catalytic performance was tested by oxygen release characteristics of powders under dry air at temperatures of 573–1073 K. The change of weight of the sample was monitored by thermogravimetry (TG) measurement under cyclic heat treatment in flowing air. TG/DTA analyzer (Netzsch, Luxx, Germany) was employed to evaluate the oxygen storage characteristics of the investigated samples. The heat cycle consisted of a first heating to 1073 K, cooling to 423 K, and a second heating to 1073 K. All heating and cooling rates were 5 K min^{-1}. The weight loss of samples in the second heating TG data was used as a measure of oxygen release properties of the composite powders between 573 and 1073 K. The heat treatment temperature maxima (1073 K) correspond to the moderate thermal condition of practical automotive exhaust gases. This technique of OSC evaluation is essentially similar to that described previously [32,33].

2.3.2 CO Oxidation Reaction

CO oxidation is one of the key steps in the overall process of the TWCs, and therefore it has frequently been used as a probe reaction over ceria-based materials to evaluate different catalyst formulations and investigate mechanistic issues [34–39]. The catalytic activity was evaluated for oxidation of CO at normal atmospheric pressure and temperatures in the range of 300–773 K in a fixed bed micro-reactor at a heating ramp of 5 K min^{-1}. About 100 mg catalyst sample (250–355 μm sieve fraction) diluted with quartz particles of the same sieve fraction was placed in a quartz reactor for evaluation.

Temperature was measured directly at the catalyst bed, using a thermocouple placed in the hollow shaft of the reactor. The following gases and gas mixtures were used (supplied by Air Liquide): argon (>99.999% purity), 9.98% CO in argon (CO purity, >99.997%; argon purity, >99.99%), and 10.2% O_2 in argon (oxygen purity, >99.995%). The total flow rates maintained by three mass flow controllers were in the range of 50–100 NmL min^{-1} (milliliters normalized to 273.15 K and 1 atm.). The CO and CO_2 gas concentrations were measured using an Uras 14 infrared analyzer module, and the O_2 concentration was measured using a Magnos 16 analyzer (Hartmann & Braun). Prior to oxidation of CO, the catalysts were heated to 773 K in 10.2% O_2/Ar gas mixture, using a heating ramp of 10 K min^{-1}, and kept at the final temperature for 1 h. The oxidized sample was then purged in argon and cooled to the desired starting temperature. The CO/O_2 reactant feed ratio was 1, and partial pressures of CO and O_2 were in the range of 10 mbar.

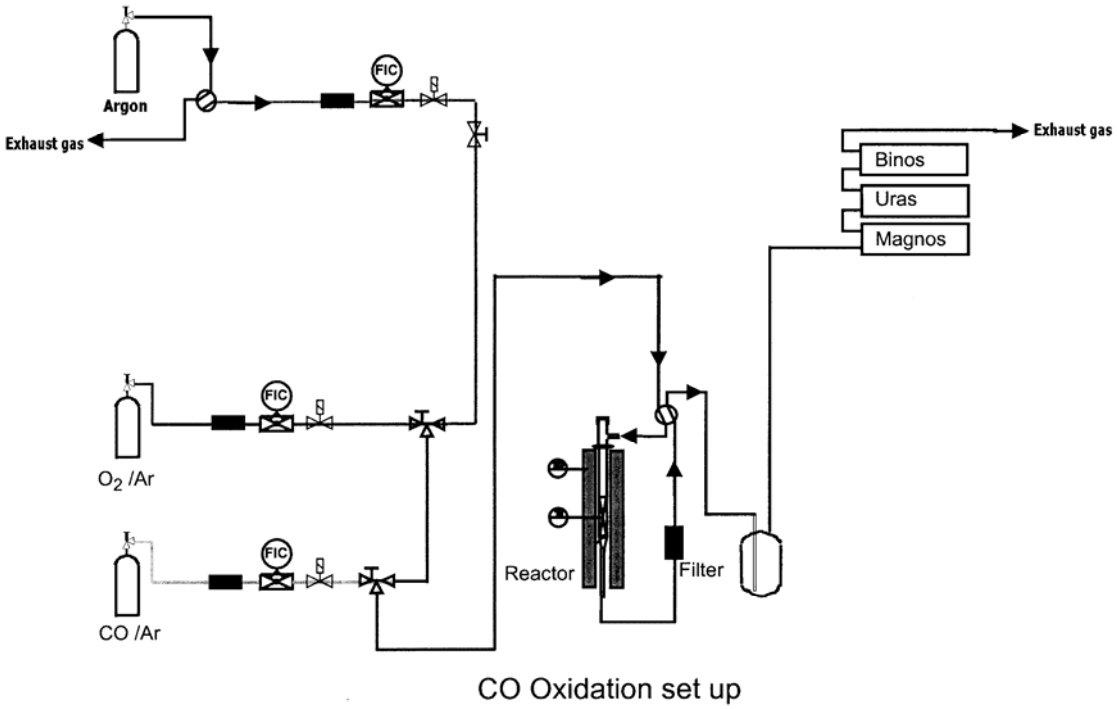

Figure 2.1: Simplified experimental set up for CO oxidation showing different gases used, reactor and analyzer (FIC – Mass flow controllers).

The simplified experimental set-up used for the oxidation of CO under normal atmospheric pressure using 9.98 % CO/Ar and 10.2 % O_2/Ar in the present study is presented in the Figure 2.1.

The conversion of CO and O_2 and yield of CO_2 were calculated as follows:

$$\text{Conversion of CO (\%)} = \frac{[CO]^{in} - [CO]^{out}}{[CO]^{in}} \times 100$$

$$\text{Conversion of } O_2 \text{ (\%)} = \frac{[O_2]^{in} - [O_2]^{out}}{[O_2]^{in}} \times 100$$

$$\text{Yield of } CO_2 \text{ (\%)} = \frac{[CO_2]^{out} - [CO_2]^{in}}{[CO]^{in}} \times 100$$

where $[CO]^{in}$ is the inlet concentration of CO,
$[CO]^{out}$ is the outlet concentration of CO,
$[O_2]^{in}$ is the inlet concentration of O_2,
$[O_2]^{out}$ is the outlet concentration of O_2,
$[CO_2]^{in}$ is the inlet concentration of CO_2,
$[CO_2]^{out}$ is the outlet concentration of CO_2.

2.3.3 Soot Oxidation Reaction

The incomplete combustion that occurs in the diesel engines leads to huge emissions of atmospheric pollutants as soot particulates and toxic gases. Among several techniques that have been developed for reducing the emissions from diesel engines, filtering followed by catalytic oxidation is one of the most promising options. This approach is based on the application of a catalyst to achieve the onset of regeneration at a significantly lower temperature [40]. Pertaining to the mechanism involved in the oxidation of soot, several authors have pointed out the significance of redox properties of the catalysts, and the use of cerium oxide materials which confer interesting properties to soot combustion catalysts [40–42]. Catalysts typically employed for soot oxidation should decrease the oxidation temperature (light-off temperature, $T_{1/2}$) and maintain a high activity for longer working periods. The $T_{1/2}$ strongly depends on the contact between the

soot and the catalyst and on the specific surface area of the catalytic material [42,43]. The growth of oxide particles (sintering) during soot oxidation is therefore detrimental to the catalytic activity. It has been reported that gas phase O_2 replenishes the lattice oxygen of ceria creating highly active oxygen, which reacts with soot [44,45]. Incorporation of La^{3+} significantly improved the catalytic activity of CeO_2 for soot oxidation and this improvement was correlated to an increase in the BET surface area and enhanced redox properties.

In this present investigation soot oxidation measurements were carried out by using thermogravimetry method. For the activity measurements in 'loose contact' (mixed by spatula) condition with catalyst-soot mixtures in 4:1 wt/wt ratio, a Cahn TG/DTA coupled with quadruple mass spectrometer (QMS) is used. On the other hand, the activity measurements in 'tight contact' (ground in agate mortar) condition with catalyst-soot mixtures in 4:1 wt/wt ratio is performed in a Mettler Toledo, TGA/SDTA 851^e instrument [41,46]. The model soot, Printex U, used in this work was provided by Degussa. A weighed amount of the sample was placed in a TGA crucible and heated to 1,273 K in 60−100 mL min^{-1} helium or air and the heating rate was 10 K min^{-1}.

2.3.4 Dehydration of 4-methylpentan-2-ol

The conversion of 4-methylpentan-2-ol produces mainly 4-methylpent-1-ene and 4-methylpent-2-ene with trace amounts of C_6 alkenes as dehydration products. Besides dehydration, dehydrogenation of the reactant alcohol gives rise to 4-methylpentan-2-one and higher ketones (in very low amounts) [47−50]. The catalytic activity for vapor phase dehydration of 4-methylpentan-2-ol was investigated in a down-flow fixed-bed microreactor at different temperatures under normal atmospheric pressure. In a typical experiment *ca*. 0.5 g catalyst was placed at the centre of the reactor between two plugs of quartz wool (pyrex glass tube, o.d. 1 cm and i.d. 0.8 cm), and above the catalyst bed filled with glass chips in order to act as preheating zone. The reactor was placed vertically inside a tubular furnace, which can be heated electrically. The reactor temperature was monitored by a thermocouple with its tip located near the catalyst bed and connected to a temperature indicator-controller. The catalyst was preheated using CO_2-free airflow at 773 K for 5 h, prior to the reaction. The 4-methylpentan-2-ol was fed with N_2 stream, into the

vaporizer at a flow rate of 1.5 mL h^{-1} from a motorized syringe pump (Perfusor Secura FT, Germany) into the vaporizer. The flow rate of dry N_2 was maintained at 60–70 mL min^{-1}.

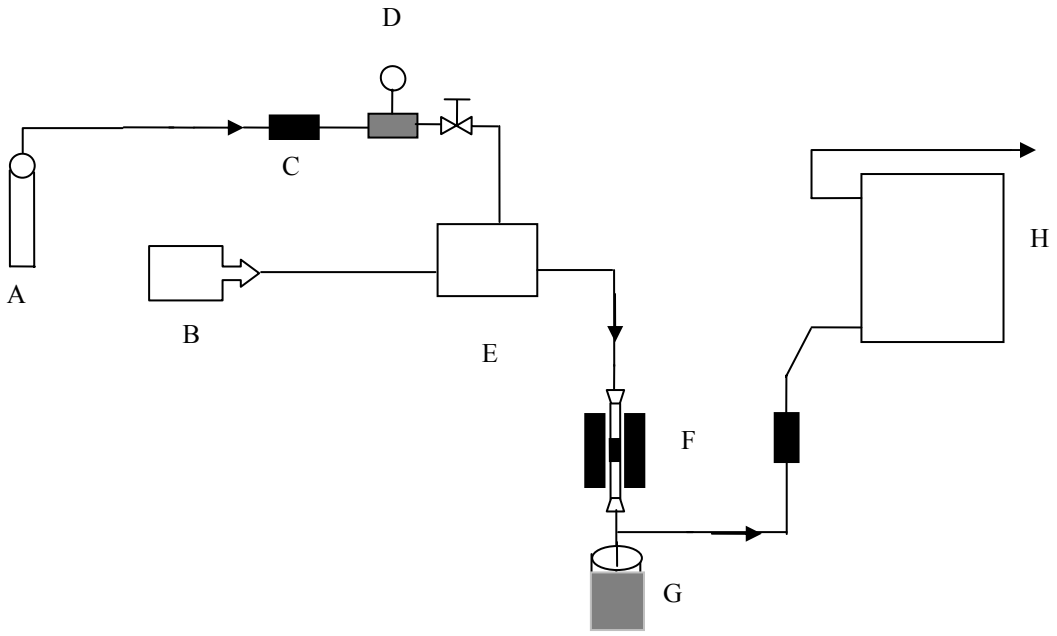

Figure 2.2: Simplified experimental set up for dehydration of 4-methylpentan-2-ol; A – Nitrogen; B – Alcohol syringe pump; C – Filter; D – Mass flow controller; E – Saturator; F – Reactor; G – Freezing trap; H – GC.

The liquid products were collected in ice-cold freezing traps and were analyzed by a gas chromatograph with flame ionization detector (FID). The qualitative analysis of the products was performed with the help of NMR and Mass spectrometry techniques. The activity data was collected under steady state conditions. The conversions and product selectivity were calculated as per the procedure described elsewhere [49,50]. The condensed reaction products were analyzed with a CIC 2011 gas chromatograph equipped with a flame ionization detector and a capillary column (BPX5, 50 m x 0.32mm).

The simplified experimental set-up used for the dehydration of 4-methylpentan-2-ol under normal atmospheric pressure using nitrogen in this study is presented in the Figure 2.2. The main products obtained were 4-methylpent-1-ene, 4-methylpent-2-ene, and 4-methylpentan-2-one, along with some traces of unidentified products. The activity data was collected under steady state conditions.

2.4 References

[1] S. Brunauer, P.H. Emmett, E. Teller, J. Am. Chem. Soc. 60 (1938) 309.

[2] H. Emmett, Catalysis, vol. 1, Reinhold, New York (1954).

[3] J.R. Anderson and K.C. Pratt, Introduction to the Characterization and Testing of Catalysts. 1985, Academic press, Sydney.

[4] A. Auroux in Catalyst Characterization: Physical Techniques for Solid Materials (Eds., B. Imelik, J.C. Vedrine), Plenum Press, New York, 1994, Chapter 22.

[5] H.P. Klug, L.E. Alexander, X-Ray Diffraction Procedures for Polycrystalline and Amorphous Material, 2nd ed., Wiley, New York, 1974.

[6] P. Gallezot in Catalysis, Science and Technology (Eds: J.R. Anderson, M. Boudart), Springer, Berlin, 1984, Vol. 5, p. 221-273.

[7] G. Bergeret, P. Gallezot in Catalyst Characterization: Physical Techniques for Solid Materials (Eds: B. Imelik, J.C. Vedrine), Plenum Press, New York, 1994, Chapter 15.

[8] International Centre for Diffraction Data, 12 Campus Boulevard, Newton Square, PA 19073-3273, USA.

[9] A. Bozo, F. Gaillard, N. Guilhaume, Appl. Catal. A: Gen. 220 (2001) 69.

[10] G. Colon, M. Pijolat, F. Valdivieso, H. Vidal, J. Kaspar, E. Finocchio, M. Daturi, C. Binet, J.C. Lavalley, R.T. Baker, S. Bernal, J. Chem. Soc. Faraday Trans. 94 (1998) 3717.

[11] N.W. Hurst, S.J. Gentry, A. Jones, B.D. McNicol, Catal. Rev. Sci. Eng. 24 (1982) 233.

[12] D.A.M. Monti, A. Baiker, J. Catal. 83 (1983) 323.

[13] A. Jones, B. McNicol, Temperature-Programmed Reduction for Solid Materials Characterization in Chemical Industries, Vol. 25, Marcel Dekker, New York, 1986.

[14] P. Malet, A. Caballero, J. Chem. Soc., Faraday Trans. 84 (1988) 2369.

[15] G. Ertl, H. Knözinger, J. Weitkamp (Eds.), Handbook of Heterogeneous Catalysis, Vol. 2, VCH, Weinheim, 1997, S. 681 ff.

[16] G. Thomas and M.J. Goring, Transmission Electron Microscopy of Materials, John Wiley, New York (1979).

[17] J.C.H. Spence, Experimental High Resolution Electron Microscopy, Clarendon, Oxford (1981).

[18] T. Baird, Catalysis 5 (1981) 172.

[19] J.V. Sanders, Catalysis Science and Technology, Vol. 7 (J.R. Anderson and M. Boudart, eds.), Springer-Verlag, Berlin (1985) p. 51.

[20] B.M. Weckhuysen, R.A. Schoonheydt, Catal. Today 49 (1999) 441.

[21] G. Kortum, Reflectance Spectroscopy: Principles, Methods and Applications, Springler Verlag, Berlin, 1969.

[22] W.N. Delgass. G.L. Haller, R. Kellerman, J.H. Lunsford, Spectroscopy in Heterogeneous Catalysis, Academic Press, New York.

[23] X. Gao, I.E. Wachs, J. Phys. Chem. B 104 (2000) 1261.

[24] M.-F. Luo, Z.-L. Yan, L.-Y. Jin, M. He, J. Phys. Chem. B 110 (2006) 13068.

[25] H. Knözinger in Fundamental Aspects of Heterogeneous Catalysis Studies by Particle Beams (Eds: H.H. Brongersma, R.A. van Santen), Plenum Press, New York, 1991, 167.

[26] J.M. Stencel, Raman Spectroscopy for Catalysis, van Nostrand Reinhold, New York, 1990.

[27] E. Garbowski, G. Coudurier in Catalyst Characterization: Physical Techniques for Solid Materials (Eds: B. Imelik, J.C. Vedrine), Plenum Press, New York, 1994, Chapter 3.

[28] A. Briggs, M.P. Seah, Eds. Practical Surface Analysis, 2nd ed.; Auger and X - Ray Photoelectron Spectroscopy, Wiley, New York, 1990; Vol. 1.

[29] C.D. Wagner, W.M. Riggs, L.E. Davis, J.F. Moulder, in: G.E. Muilenberg, Ed. Handbook of X-Ray Photoelectron Spectroscopy, Perkin-Elmer Corporation, Minnesota (1978).

[30] J.V. Sanders, in: Catalysis Science and Technology, J.R. Anderson, M. Boudart, Eds., Springer-Verlag, Berlin,1985, Vol. 7, p. 51.

[31] D. G. Swartzfager, Anal. Chem. 56 (1984) 55.

[32] M. Ozawa, C.K. Loong, Catal. Today 50 (1999) 329.

[33] A.D. Logan, M. Shelef, J. Mater. Res. 9 (1994) 468.

[34] A. Trovarelli, Catal. Rev.-Sci. Eng. 38 (1996) 439.

[35] E. Aneggi, J. Llorca, M. Boaro, A. Trovarelli, J. Catal. 234 (2005) 88.

[36] M.F. Milkes, P. Hayden, A.K. Bhattacharya, J. Catal. 219 (2003) 295.

[37] W. Liu, M. Flytzani-Stephanopoulos, J. Catal. 153 (1995) 304.

[38] Y. Madier, C. Descorme, A.M. LeGovic, D. Duprez, J. Phys. Chem. B 103 (1999) 10999.

[39] R.H. Nibbelke, A.J.H. Nievergeld, J.H.B.H. Hoebnik, G.B. Marin, Appl. Catal. B: Environ. 19 (1998) 245.

[40] L. Zhua, J. Yu, X. Wang, J. Hazardous Mater. 140 (2007) 205.

[41] J. Liu, Z. Zhao, C. Xu, A. Duan, L. Wang, S. Zhang, Catal. Commun. 8 (2007) 220.

[42] J. Neeft, M. Makkee, J. Moulijn, Chem. Eng. J. 64 (1996) 295.

[43] A. Bueno-Lopez, K. Krishna, M. Makkee, J.A. Moulijn, J. Catal. 230 (2005) 237.

[44] A. Bueno-Lopez, K. Krishna, M. Makkee, J.A. Moulijn, Catal. Lett. 99 (2005) 203.

[45] I. Atribak, A. Bueno-Lopez, A. Garcia-Garcia, Catal. Commun. 9 (2008) 250.

[46] K. Krishna, A. Bueno-Lopez, M. Makkee, J.A. Moulijn, Top. Catal. 44- 45 (2007) 221.

[47] M.G. Cutrufello, I. Ferino, V. Solinas, A. Primavera, A. Trovarelli, A. Auroux, C. Picciau, Phys. Chem. Chem. Phys. 1 (1999) 3369.

[48] M.G. Cutrufello, I. Ferino, R. Monaci, E. Rombi, V. Solinas, Top. Catal. 19 (2002) 225.

[49] V. Solinas, E. Rombi, I. Ferino, M.G. Cutrufello, G. Colon, J.A. Navio, J. Mol. Catal. A: Chem. 204-205 (2003) 629.

[50] B.M. Reddy, G. Thrimurthulu, P. Saikia, P. Bharali, J. Mol. Catal. A: Chem. 275 (2007) 167.

Chapter 3

This chapter presents the results and discussion pertaining to the structural characteristics of the nanosized composite oxides of CeO_2–HfO_2 and CeO_2–ZrO_2 systems by various spectroscopic and non-spectroscopic techniques.

STUDIES on CeO_2–HfO_2 COMPOSITE OXIDE CATALYST

3.1 Introduction

Ceria (CeO_2) has attracted considerable interest in recent years due to its diverse applications. It is a candidate material for a wide variety of applications ranging from catalysis to ceramic biomaterials, fuel cell technologies, electrochemical applications, optical glass-polishing, gas sensors, and so on. Although disagreements remain about the mechanism that ceria plays in many of these applications, it is clear that redox properties of ceria or doped ceria or ceria solid solutions are very important [1–5]. Owing to the facile redox couple (Ce^{4+}/Ce^{3+}) and elevated oxygen ion migration ability, it has been used for years as one of the components of catalytic automobile exhaust converters. Catalytic converters, which convert the three primary pollutants in automobile exhaust-gas, namely, CO, NO*x*, and hydrocarbons, into nontoxic products are referred to as three-way catalysts (TWC). Improvements in such features are currently in demand for designing better catalytic cartridges for new-generation cleaner cars [6]. The conversion efficiency of TWC is highly dependent upon the air-to-fuel (A/F) ratio, which has to be maintained at the stoichiometric level (~14.6) [7]. To maintain this level the catalyst must possess oxygen storage capacity (OSC) so that it can provide oxygen to the gas mixture during fuel-rich conditions and absorb oxygen in fuel-lean conditions. Hence, the redox chemistry of ceria is a critical parameter in the efficiency of the multifunctional and multicomponent three-way catalysts [8]. The release and uptake of oxygen in ceria occurs owing to the following reversible reaction [9].

$$CeO_2 \Leftrightarrow CeO_{2-x} + x/2O_2 \ (0 \le x \le 0.5)$$

However, for direct automotive applications, the OSC and thermal durability of pure ceria are insufficient [10,11]. Also, it is an established fact that ceria exhibits a cubic fluorite structure and sinters equally three dimensionally. Therefore, many studies have been carried out in this direction to increase the thermal stability and the OSC of ceria [12–15]. The mixed metal oxides have played an important role recently in many areas of chemistry, physics, material science, and geochemistry. Obviously, the chemical behavior of mixed metal oxides may differ from that of single metal oxides. The combination of two

metal oxides in an oxide matrix can lead to novel structural and electronic properties of the final oxide, favoring its catalytic activity. At structural levels, a dopant can facilitate defect formation within the oxide host by generating stress into the lattice. On the contrary, nontypical coordination modes of lattice host resulting in a deviation in the dopant's chemical nature may also be possible. As a result, metal-metal or metal-oxygen-metal interactions in mixed metal oxides lead to perturbed electronic states compared to single metal oxides. Although most of the recent literature concerning alternative materials for TWC applications deals with ceria-zirconia based systems, the redox properties and chemical activity of pure ceria can be enhanced by introducing different types of metals (Ca, Cu, Tb, Mn, etc.) into the oxide lattice other than zirconium [16–18]. However, it is not clear what type of second metal is useful to improve both the stability at high temperature and the chemical activity by introducing O vacancies in the ceria. For example, Zr mixing improved the thermal stability of ceria nanoparticles but showed no significant O vacancies, whereas Ca mixing introduced a lot of O vacancies in the host structure, but the mixed metal oxide bears a relatively low stability and phase segregation into CeO_2 and CaO occurs at temperatures close to 973 K [19,20]. Therefore, it was interesting to investigate the effect of substitution of a new dopant with a smaller ionic radius than zirconium into the ceria lattice.

It is already realized in heterogeneous catalysis that catalytic activity scales with surface area. Hence, maximum dispersion of the particles is of extraordinary importance, which makes the production of nanoscaled catalysts very tempting. The nanoparticle configurations are interesting from a practical viewpoint also as most of the applications are surface-sensitive, and a high surface-to-volume ratio in addition to improved redox properties, related to oxygen vacancy generation, can be reached by using nanosized materials. In a recent communication, we have demonstrated the efficiency of Hf^{4+} (ionic radius 0.78 Å) on the OSC and CO oxidation activity of ceria when incorporated even in smaller quantities than Zr^{4+} (ionic radius 0.84 Å) [21]. Against this background, an extensive characterization of the ceria-hafnia solid solution was carried out and presented here. The structural evolution has been investigated using thermal analysis (TG-DTA), X-ray diffraction (XRD), temperature programmed reduction (TPR), scanning electron microscopy (SEM), transmission electron microscopy TEM), UV-visible diffuse reflectance spectroscopy (UV-vis DRS), Laser Raman spectroscopy (LRS), X-ray photoelectron spectroscopy (XPS), ion scattering spectroscopy (ISS), and BET surface area (BET SA)

techniques. Given the importance of ceria and particularly of ceria-zirconia solid solutions, and further to help resolve some of the apparent discrepancies between the Ce-Hf and Ce-Zr mixed oxides, a reference ceria-zirconia solid solution was also examined for comparison purposes.

3.2 Experimental

The CeO_2–HfO_2 (CH; 8:2 mole ratio based on oxides) composite oxide was prepared by a modified coprecipitation method as per the procedure described in the chapter 2. The obtained CeO_2–HfO_2 catalyst was subjected to thermal treatments from 773 to 1073 K in order to understand the thermal stability, and the physicochemical properties of these materials. These effects have been investigated by means of TG-DTA, BET SA, XRD, TPR, SEM, TEM, UV-vis DRS, LRS, XPS, ISS and other techniques. For comparison purpose, CeO_2–ZrO_2 (CZ; 1:1 mole ratio based on oxides) composite oxide was also prepared by similar procedure and characterized by various techniques mentioned above.

3.3 Results and Discussion

3.3.1 Thermal Measurements

The CeO_2–HfO_2 and CeO_2–ZrO_2 composite oxide were subjected to TG-DTA analysis before calcination. The thermograms obtained between ambient temperature and 1273 K are shown in Figures 3.1a and 3.1.b, respectively. The TG-DTA analysis provided some evidence about the decomposition and sintering behavior of the composite oxides. As presented in Figures 3.1a and 3.1.b, both the samples exhibited one major and two minor weight loss peaks. The major low temperature peak in the range 309 – 473 K is primarily due to the loss of non-dissociative adsorbed water as well as water held on the surface by hydrogen bonding. The minor weight loss peaks at high temperatures are due to loss of water held in the micropores of the gels and dehydroxylation of the surface, respectively. The weight loss from ambient to 625 K is about 10% and from 625 to 840 K is 1.5%. However, the weight loss between 840 and 1273 K is only about 0.5%. It indicates that over the temperature range between 840 and 1273 K, the CeO_2–HfO_2 composite oxide is quite stable in terms of phases and chemical composition.

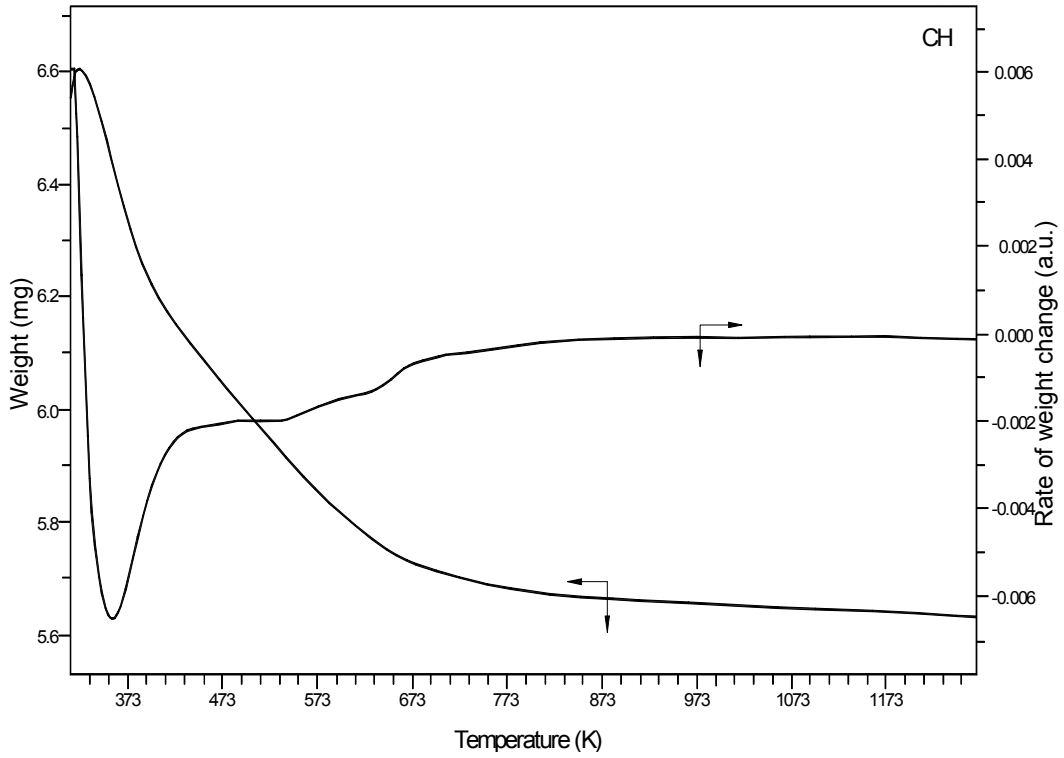

Figure 3.1a: TGA profile of CeO_2–HfO_2 (CH) sample before calcination.

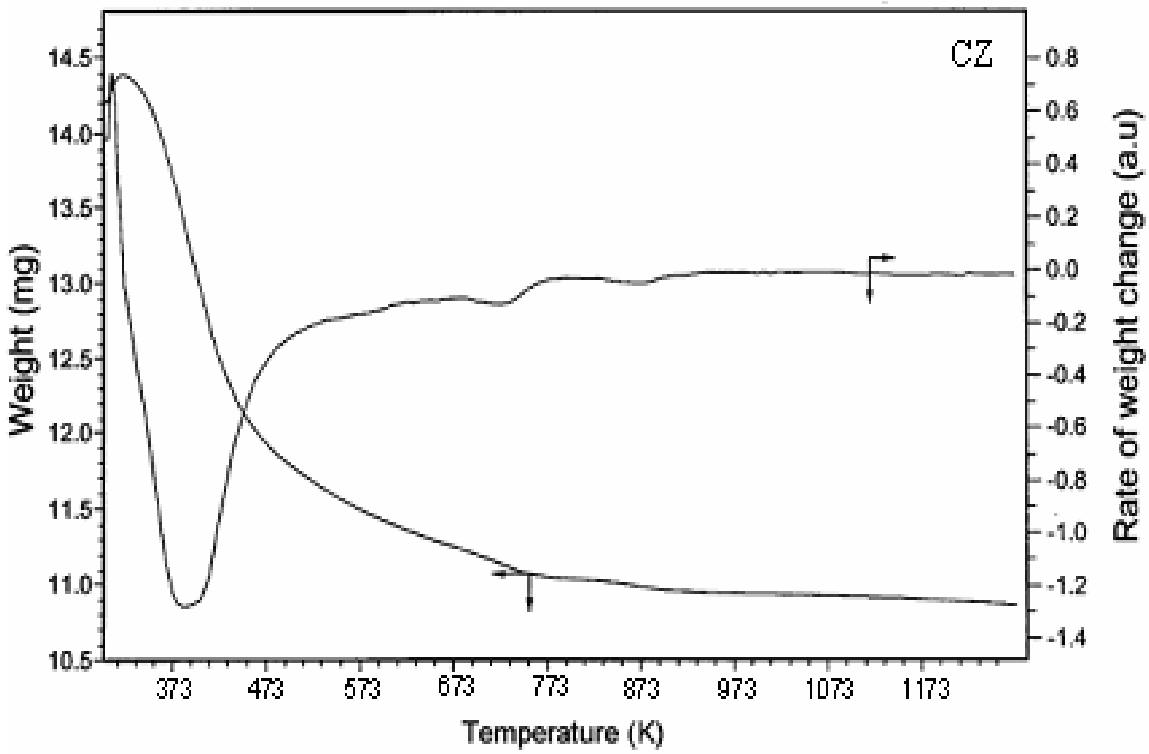

Figure 3.1b: TGA profile of CeO_2–ZrO_2 (CZ) sample before calcination.

3.3.2 BET Surface Area Measurements

The N_2 BET surface area pertaining to CeO_2–HfO_2 (CH) and CeO_2–ZrO_2 (CZ) samples calcined at different temperatures are presented in Table 3.1. The BET results indicate reasonably high specific surface areas for both the samples. The CH and CZ samples calcined at 773 K bear a specific surface area of 78 and 84 m^2g^{-1}, respectively. Pure CeO_2 prepared by a similar method possessed a specific surface area of 41 m^2g^{-1} [22]. This observation indicates that the incorporation of Hf^{4+} and Zr^{4+} into ceria lattice induces an increase in the surface area. It is generally known that the mixed oxides with highest possible specific surface area are of great interest in view of their practical utility. As can be seen from the Table 3.1, thermal treatments at higher temperatures cause gradual sintering and crystallite growth resulting in the loss of surface area. However, the resistance to thermal sintering of these mixed oxides is remarkable in comparison to pure ceria [22].

3.3.3 X-ray Diffraction Studies

The XRD patterns pertaining to the CeO_2–HfO_2 (CH) and CeO_2–ZrO_2 (CZ) samples samples calcined at 773 – 1073 K are presented in Figure 3.2a and 3.2b, respectively. These results reveal the formation of solid solutions with typical cubic fluorite phases of the composition $Ce_{0.8}Hf_{0.2}O_2$ (PDF-ICDD 04-006-1933) and $Ce_{0.75}Zr_{0.25}O_2$ (PDF-ICDD 28-0271), respectively for 773 K calcined samples. Upon increasing calcinations temperature up to 1073 K, the same monophasic composition is retained for CH sample but phase segregation into $Ce_{0.75}Zr_{0.25}O_2$ and $Ce_{0.6}Zr_{0.4}O_2$ (PDF-ICDD 38-1439) were observed for CZ sample. As could be seen from Fig. 3a,b, the CH and CZ samples are indexed to (111), (200), (220), (311), (222), (400), (331), and (420) crystallographic faces of ceria-hafnia and ceria-zirconia, respectively. No XRD lines pertaining to either HfO_2 or ZrO_2 were observed in the respective cases. Also gradual sharpening of the XRD peaks with increasing calcination temperature could be observed as a result of sintering phenomenon. The presence of a single-phase solid solution is always preferable compared to micro-domain or phase segregated non-homogeneous mixed oxides, as the former systems generally lead to better textural stability and redox properties [23,24]. XRD analysis reveals only cubic phase and any departure from the internal cubic symmetry can not be distinguished using XRD due to small atomic scattering factor of oxygen in

comparison to those of Zr, Hf, and Ce, which dominate the diffractograms [25–27]. It has been reported previously that ceria-zirconia solid solutions with intermediate compositions can form metastable tetragonal phases that are difficult to distinguish from a true cubic phase using XRD alone [28]. This might indeed be the case for the present $Ce_xZr_{1-x}O_2$ and $Ce_xHf_{1-x}O_2$ composite oxides, given that the widths of the diffraction peaks made it impossible to distinguish between cubic and tetragonal phases [5]. Therefore, other techniques, particularly Raman spectral analysis, were used as a complementary study.

Table 3.1: BET surface area, FWHM, crystallite size and cell parameter measurements of CeO_2–HfO_2 (CH) and CeO_2–ZrO_2 (CZ) samples calcined at various temperatures

Sample/Calcination Temp. (K)	Surface Area ($m^2 g^{-1}$)	FWHM ($2\theta^o$)	Crystallite Size[a] (nm)	Cell Parameter (Å)
CeO_2–HfO_2				
773	78	1.76	4.6	5.34
873	62	1.29	6.3	5.34
973	40	1.08	7.2	5.34
1073	36	0.92	13.1	5.34
CeO_2–ZrO_2				
773	84	1.55	4.7	5.35
873	67	1.54	4.8	5.33
973	51	1.50	5.0	5.30
1073	36	1.35	5.5	5.27

[a] From the XRD measurements

The crystallite sizes (D_{XRD}) pertaining to the CeO_2–HfO_2 (CH) and CeO_2–ZrO_2 (CZ) samples calcined at 773 – 1073 K calculated using Scherrer equation are shown in Table 3.1. As shown in the table, mixed oxide particles of both samples are in the nanometer range. The 773 K calcined samples bear a crystallite size of *ca.* 5 nm, which increases slightly at higher temperatures. There is a significant influence of Hf^{4+} and Zr^{4+} cations in the ceria lattice to decrease the particle sizes compared to pure CeO_2 [22]. The higher values of crystallite size of the mixed oxides after high temperature treatment is due to the effect of sintering [21,22].

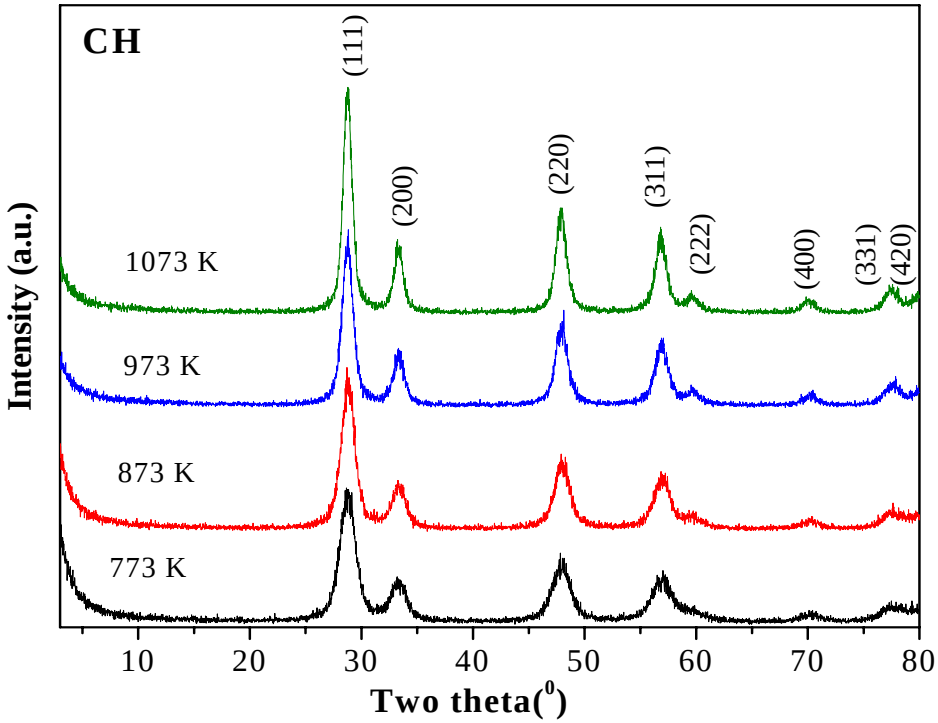

Figure 3.2a: Powder XRD patterns of CeO_2–HfO_2 (CH) samples calcined at different temperatures.

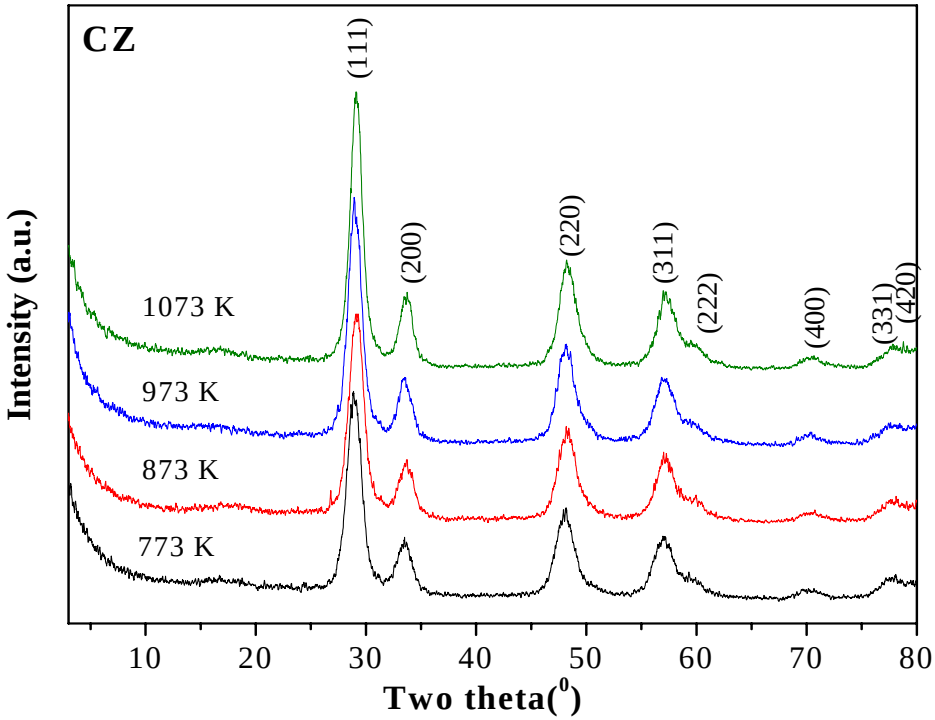

Figure 3.2b: Powder XRD patterns of CeO_2–ZrO_2 (CZ) samples calcined at different temperatures.

The lattice parameter calculations for both Hf^{4+} and Zr^{4+} incorporated ceria mixed oxides are presented in Table 3.1. The observed change in the cell 'a' parameter values of all the samples indicate penetration of Hf^{4+} and Zr^{4+} cations into the ceria cubic lattice resulting in the formation of solid solutions. Relative to pure ceria (5.41 Å) the cell 'a' parameter values of CH and CZ samples decreased to 5.34 and 5.35 Å, respectively for the 773 K calcined samples [21]. At higher temperatures the cell parameter values decreased slightly for CZ samples, while no such changes were observed for CH sample. This observation may be attributed to the further shrinkage of ceria lattice due to the replacement of Ce^{4+} (0.97 Å) ions with smaller cations of Zr^{4+} (0.84 Å), caused by phase segregation of the Ce-Zr oxide phases, especially at higher temperatures. This fact has been elaborated in the subsequent sections.

3.3.4 Temperature Programmed Reduction Studies

TPR has been studied for both the CH and CZ catalysts using H_2 and CO as reducing gas, respectively. Figure 3.3 shows the typical H_2-TPR profiles of CH and CZ samples calcined at 773 K. The quantification of H_2 consumption is estimated using CuO as the standard for TPR analysis. As could be seen in the TPR patterns, there is only one temperature maxima for both the samples. In general, the reduction peak is well resolved for CH in comparison to CZ. Earlier research has reported that the there is two peaks observed in the TPR patterns of some ceria-based catalysts and are assigned as, (i) the reduction of the most easily reducible surface oxygen of highly dispersed ceria species and (ii) the removal of oxygen from bulk ceria. In case of ceria-zirconia mixed oxides, however, only one broad peak is observed and many researchers suggest that surface and bulk reduction cannot be distinguished by the conventional TPR technique since both processes occur almost simultaneously during TPR measurement [29,30]. In line with earlier findings we also observed only one TPR peak for both the samples. However there is a small hump observed at lower temperature region for CH sample. The temperature maxima for the reduction of CH is around 845 K with a small hump around 700 K. On the other hand CZ undergoes reduction at around 843 K. The separation of TPR peaks in the CH sample infers about better reducibility of the system. This further reveal that Hf^{4+} could be more efficient to reduce ceria in comparison to Zr^{4+} incorporated CeO_2. Moreover, it could be seen from the TPR profiles that there is more consumption of H_2 in the case of CH compared to CZ. The H_2 consumption values calculated from the peak area under the

reduction peaks over the complete temperature range for the CH and CZ samples are 649 and 628 μmol g^{-1} of the catalyst, respectively. This shows that the degree of reduction of CeO_2 is enhanced to more extent after the incorporation of Hf^{4+} in CeO_2 lattice compared to Zr^{4+}.

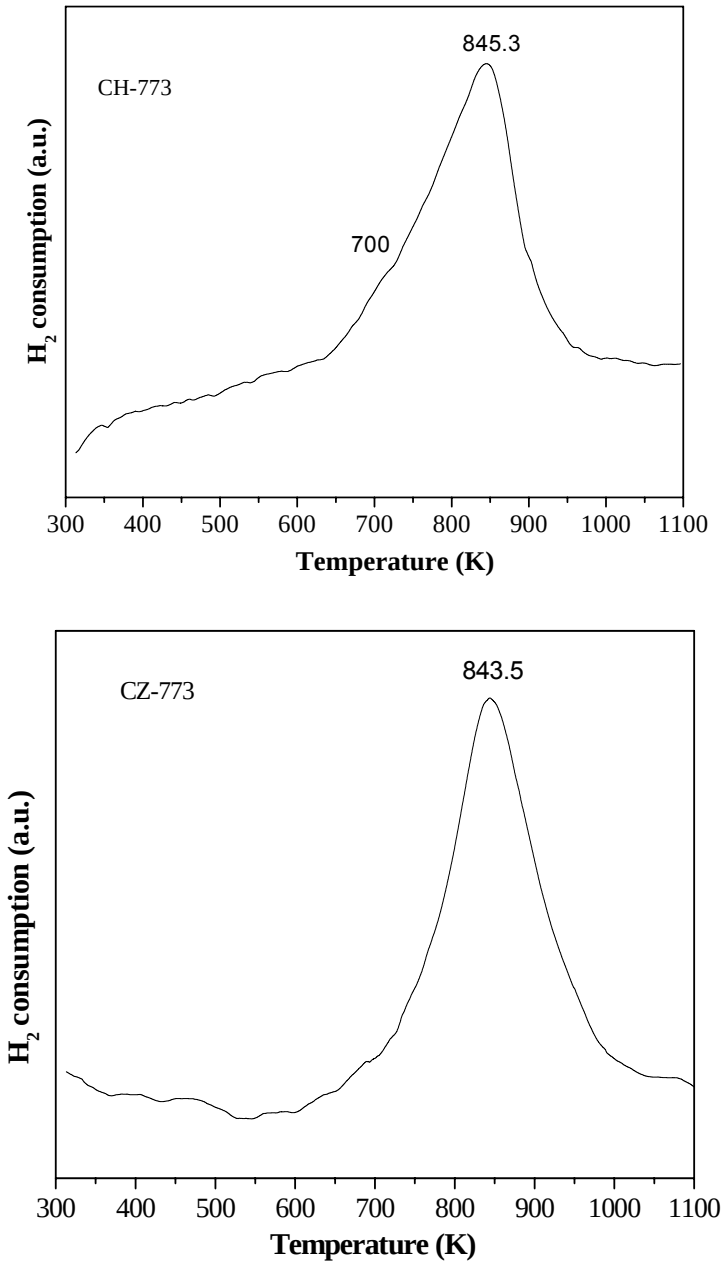

Figure 3.3: The H_2-TPR profiles of CeO_2–HfO_2 (CH) and CeO_2–ZrO_2 (CZ) samples calcined at 773 K.

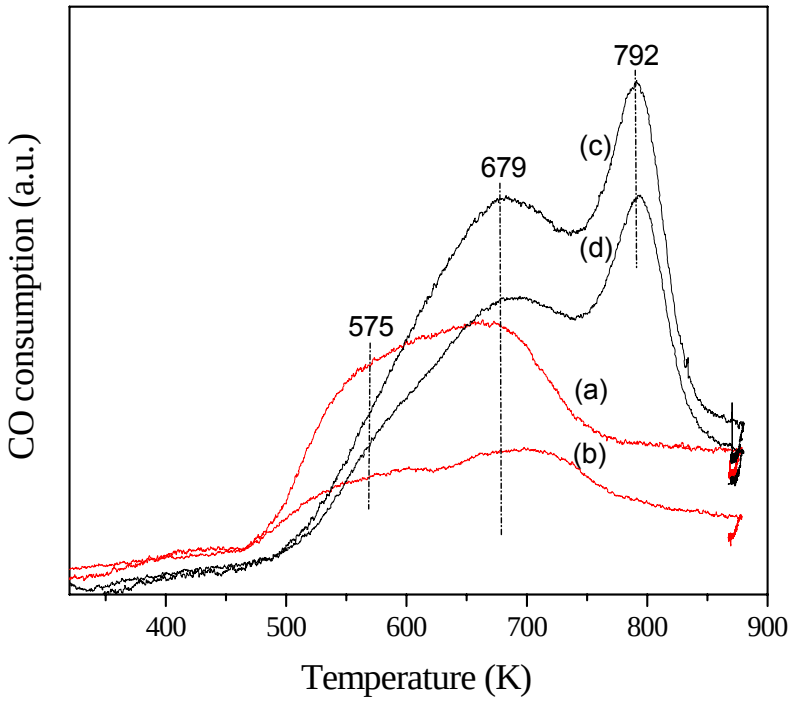

Figure 3.4: The CO-TPR profiles of CeO_2–HfO_2 (CH) and CeO_2–ZrO_2 (CZ) samples calcined at 773 and 1073 K; (a) CH-773, (b) CH-1073, (c) CZ-773, and (d) CZ-1073, respectively.

On the other hand the CO-TPR profiles of CH and CZ samples show clearly that there are two reduction peaks. The CO-TPR profiles (not to scale) of CZ and CH samples calcined at 773 and 1073 K are shown in Figure 3.4, which reveal a combination of two broad peaks for both the samples. The presence of these two peaks is associated with a stepwise reduction of the samples. The high temperature reduction feature is mainly due to bulk oxygen removal while the low temperature reduction feature has been related to most easily reducible surface capping oxygen of ceria [31]. The temperature maxima of TPR for CH samples are centered on ~579 and ~679 K, respectively, while for CZ the peaks are observed around 679 and 792 K, respectively. Very interestingly, the surface reduction of CH sample is taking place at a lower temperature than that of CZ sample. The decrease in the reduction temperature of CH sample could be attributed to increased oxygen mobility in the defective fluorite structure generated by introduction of the smaller Hf^{4+} cations (0.78 Å), in comparison to Zr^{4+} (0.84 Å), into the ceria core lattice.

3.3.5 Scanning Electron Microscopy Studies

SEM measurements were performed to assess the external morphologies of the mixed oxides. The micrographs corresponding to the CH series of samples calcined at 773 and 1073 K, respectively are shown in Figure 3.5a,b.

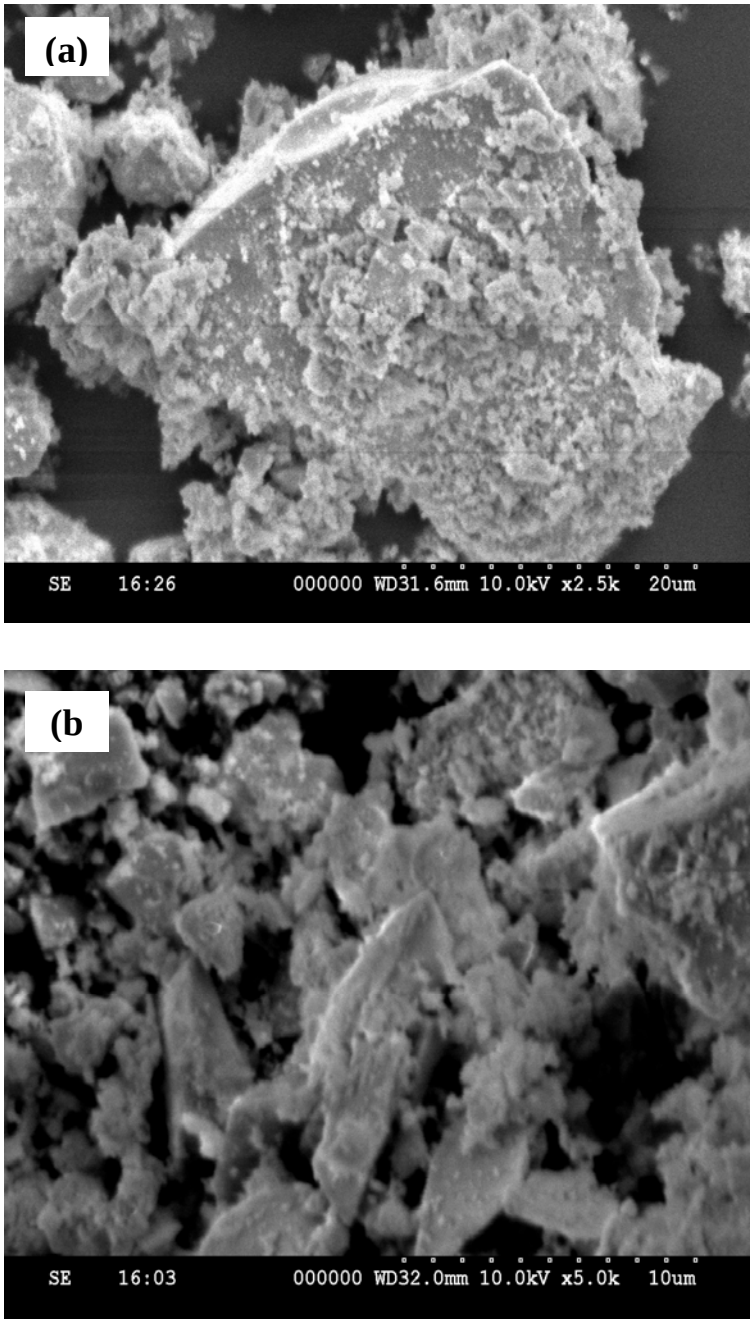

Figure 3.5: SEM micrographs of CeO_2–HfO_2 (CH) samples calcined at (a) 773 and (b) 1073 K.

As observed from the SEM images, the samples consist of typical agglomerates of homogeneous morphology of nearly equal particle distribution within the narrow size range. The 773 K calcined samples exhibited more amorphous features and densely packed agglomerates of smaller crystallites. At higher calcination temperature (1073 K) the agglomerated homogeneous structures have collapsed due to better crystallization of mixed oxide particles. Interestingly, both the samples possess amorphous features and densely packed agglomerates of crystallites.

3.3.6 Transmission Electron Microscopy Studies

In order to ascertain the results obtained from XRD and SEM measurements and to explore the structural evolution at atomic scale, conventional TEM and HREM studies were performed on some selected CH and CZ samples. The TEM-HREM images revealed nanometer sized particles and most of them are uniform in size. The representative micrographs of 773 and 1073 K calcined CH samples are presented in Figures 3.6 and 3.7, respectively. The obtained micrographs reveal agglomerated microstructures. However, plain faces of crystallites could not be seen in the figure, which suggests that a large part of the material is still amorphous. The average particle sizes observed from the TEM and HREM images (Fig. 3.6) of the 773 K calcined CH samples were about 5 nm and in fair agreement with the calculated values from XRD technique (Table 3.1). A gradual increase in the crystallite size after heat treatment at 1073 K is evident from the micrographs. The grain size increased from ~5 to ~10 nm for the CH sample (Fig. 3.7) with increasing treatment temperature from 773 to 1073 K. These results differ slightly with crystallite size data obtained from XRD with use of the Scherrer equation (Table 3.1). It should be remembered that the particle size estimations of solid solutions are subject to uncertainties due to compositional nonuniformity. Because, while using the Scherrer equation, one assumes that the particle size effects are the only source of peak broadening. A distribution of different hafnium concentrations within individual particles as well as between particles would lead to a distribution of two-θ values and thus broader peaks which would be interpreted as reduced particles with use of the Scherrer equation [25,26]. The micrographs, on the whole, represent the cubic structure of the as-prepared and high temperature calcined CH samples. The representative TEM-HREM micrographs of 773 and 1073 K calcined CZ samples are presented in Figures 3.8 and 3.9, respectively. The obtained micrographs also reveal

(a)

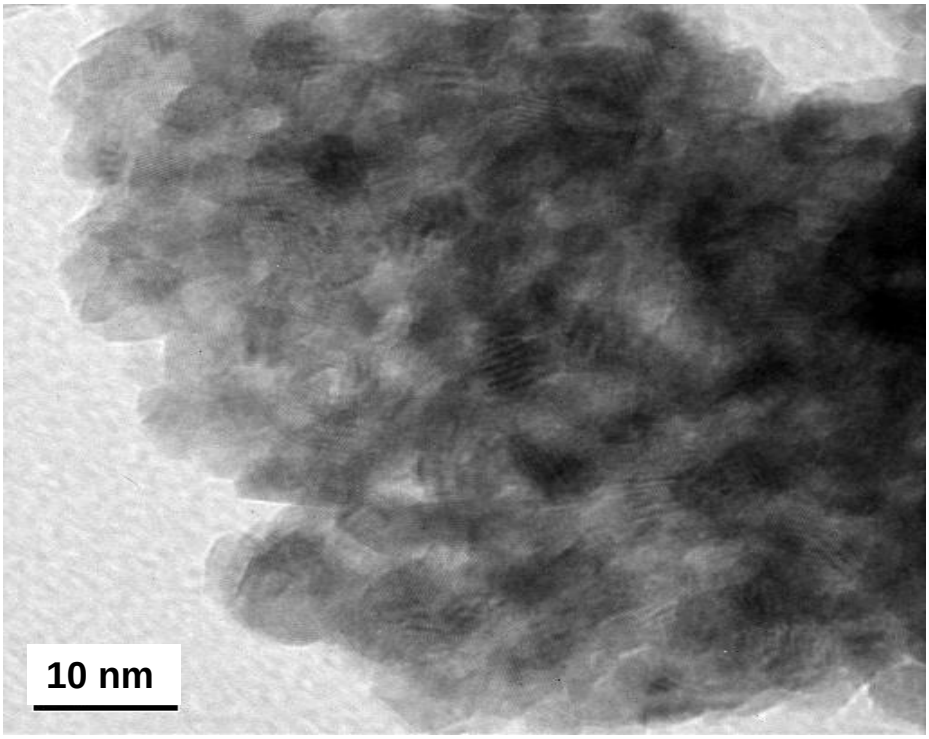

(b)

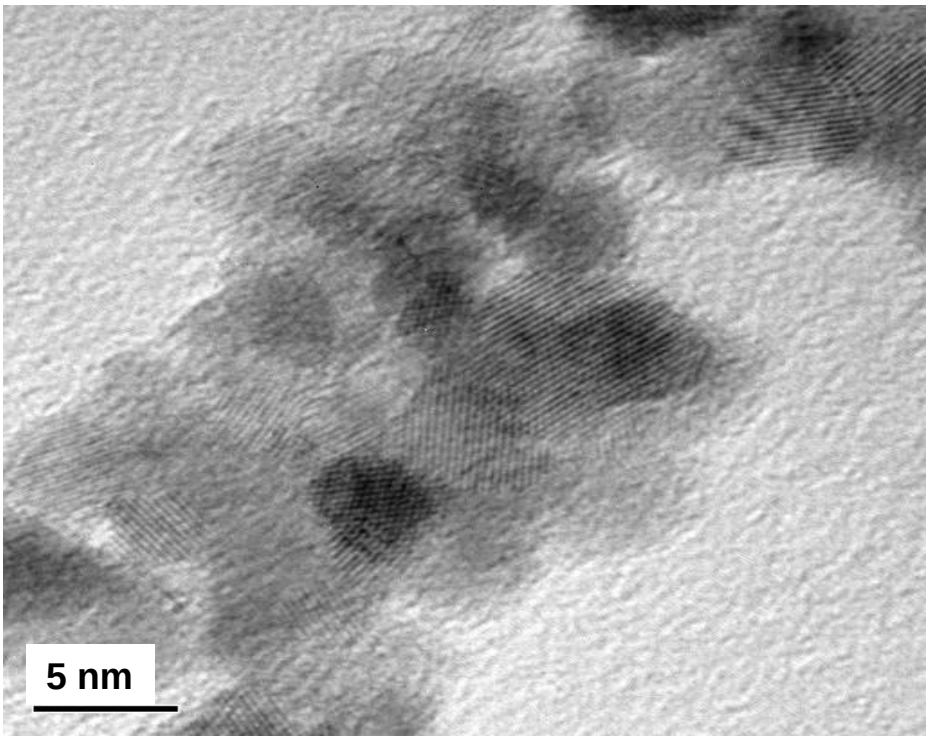

Figure 3.6: (a) TEM and (b) HREM micrographs of CeO_2–HfO_2 (CH) samples calcined at 773 K.

(a)

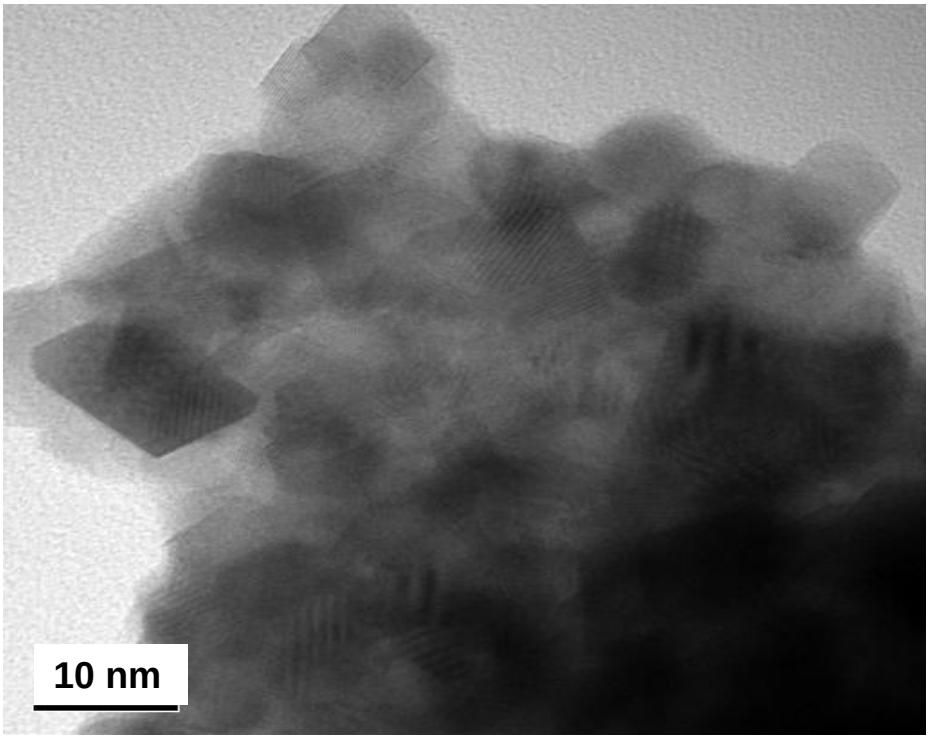

(b)

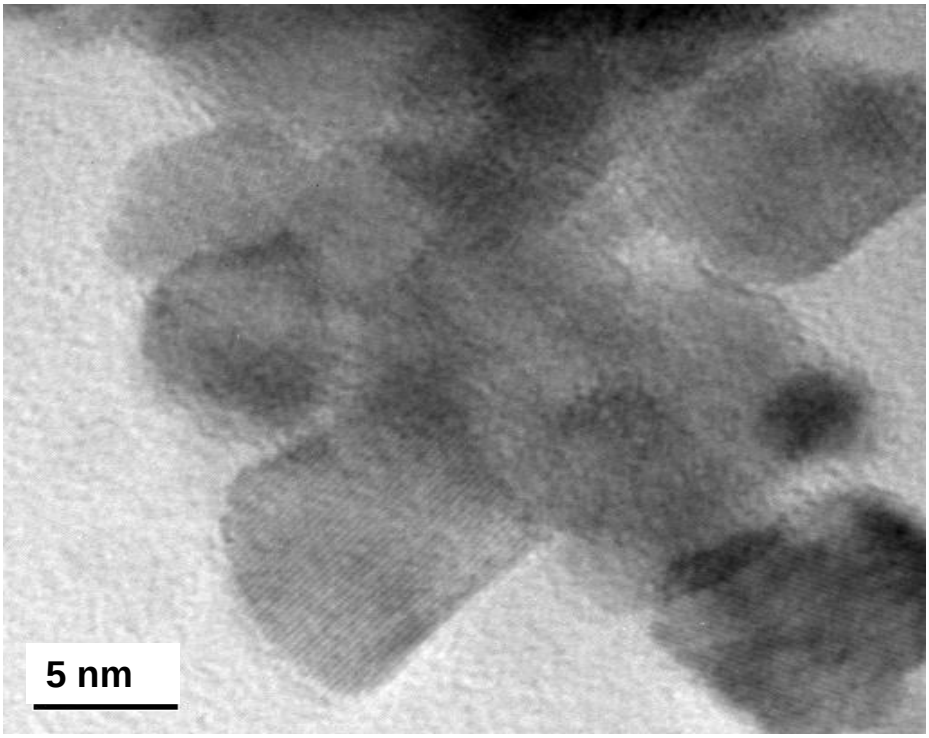

Figure 3.7: (a) TEM and (b) HREM micrographs of CeO_2–HfO_2 (CH) samples calcined at 1073 K.

(a)

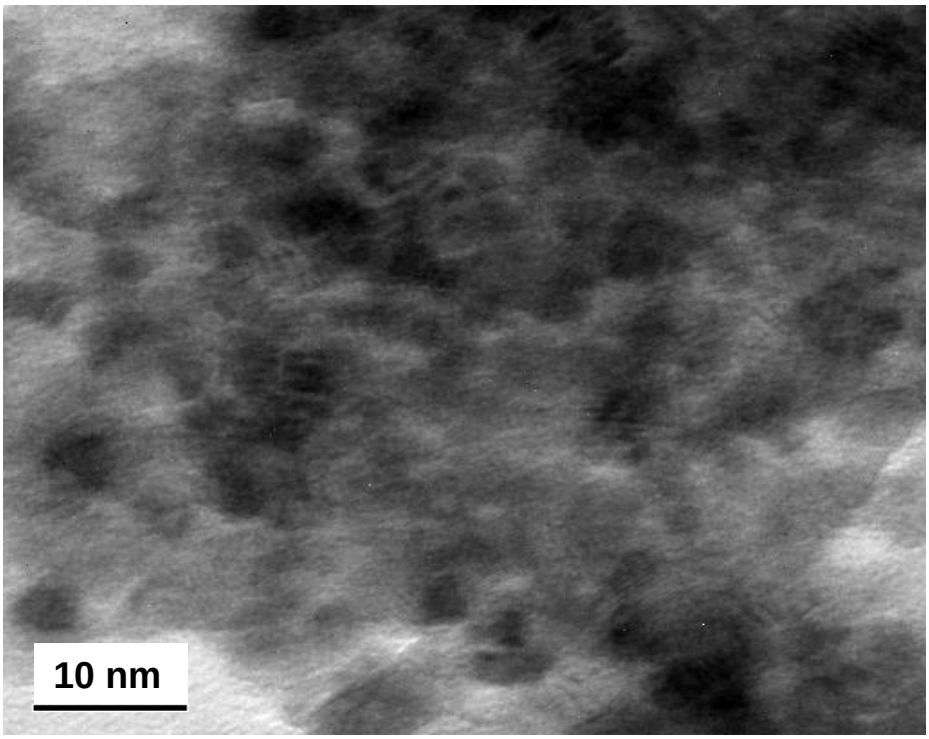

(b)

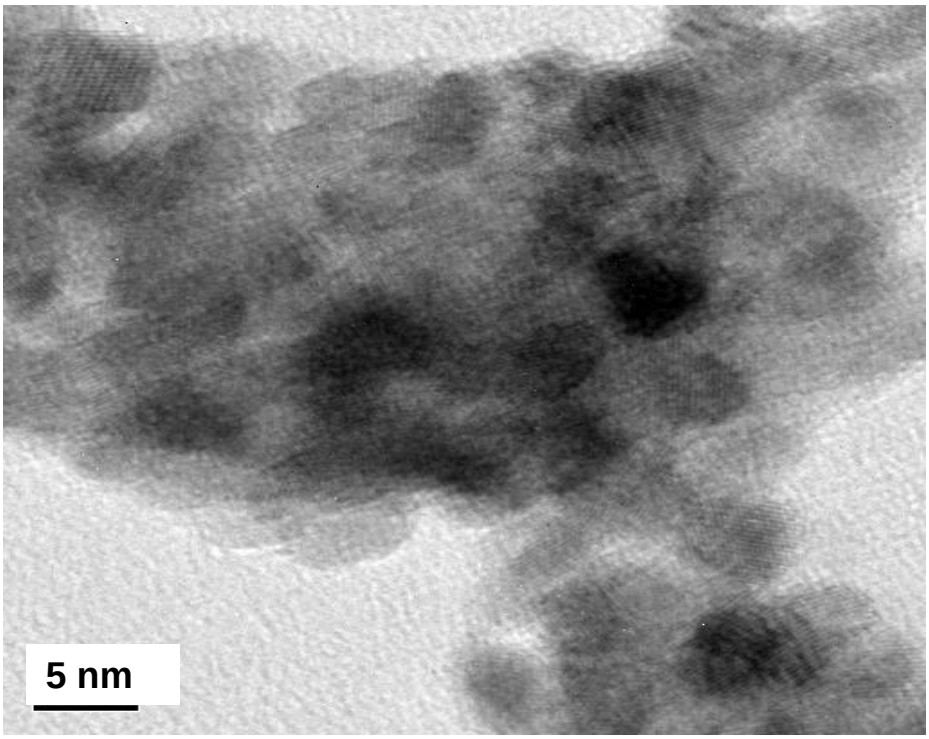

Figure 3.8: (a) TEM and (b) HREM micrographs of CeO_2–ZrO_2 (CZ) samples calcined at 773 K.

(a)

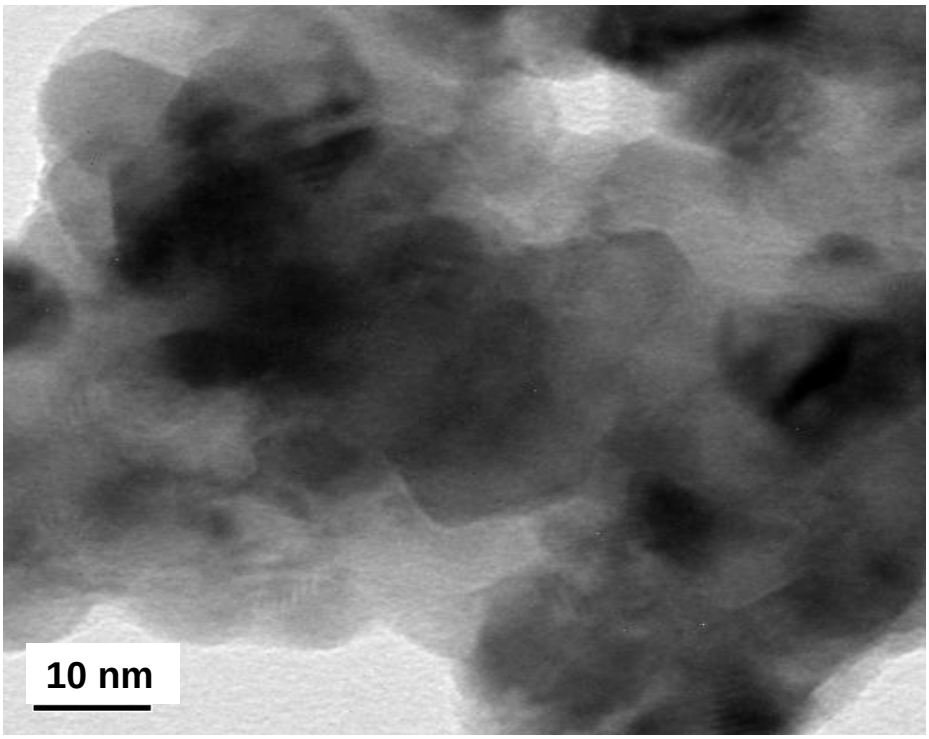

(b)

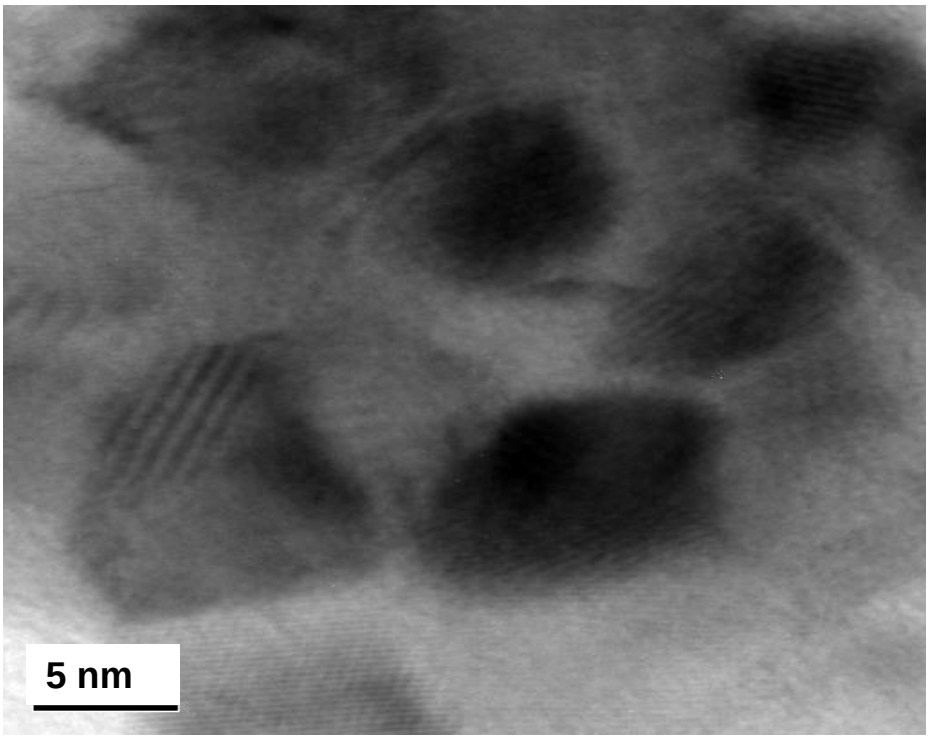

Figure 3.9: (a) TEM and (b) HREM micrographs of CeO_2–ZrO_2 (CZ) samples calcined at 1073 K.

agglomerated microstructures. In this case also plain faces of crystallites could not be seen in the figure, which suggests that a large part of the material is still amorphous. The average particle sizes observed from the TEM and HREM images (Fig. 3.8) of the 773 K calcined CZ samples were about 5 nm and in fair agreement with the calculated values from XRD technique (Table 3.1). The mixed oxide samples show an increase in particle size with increasing calcination temperature. As revealed by TEM and HREM images (Fig. 3.9), the particle sizes increase to ~8 nm for CZ samples calcined at 1073 K. On the whole, the micrographs represent the cubic structure of the as-prepared and high temperature calcined CZ samples. The shapes of the particles observed were almost similar to those usually seen in previous works for ceria or ceria–zirconia specimens [22].

The cuboctahedral shapes were clearly dominant in both the 1073 K calcined CH and CZ samples. Interestingly, from the TEM-HREM images of 1073 K calcined samples of CH and CZ (Figs. 3.7 and 3.9), very few near-rectangular shapes could also be seen. This may be due to the occurrence of (100)-plane terminations. It is known that for CeO_2, the most stable exposed surfaces are (111) and (110) [32], while the (100) surface needs a substantial number of anion vacancies to be stabilized. It may be possible that the number of vacancies present during the high temperature treatment allow such surfaces to stabilize leading to the observed particle shapes. This should be taken into account when surface reactivity of these materials is analyzed, which may become modified to some extent if the crystal plane that is preferentially exposed changes. However, from XRD analysis, no information regarding the stabilization of the (100) surface in case of 1073 K calcined samples could be obtained. The HREM images of CH and CZ (Figs. 3.7b and 3.9b) show some overlapping regions of the mixed oxide particles, which are very important from the catalytic point view.

3.3.7 UV-visible Diffuse Reflectance Spectroscopy Studies

Despite the difficulties in interpreting large bandwidths and specular reflectance often observed, UV-vis DRS has been used to study various metal oxides to obtain information on surface co-ordination and different oxidation states of the metal ions by measuring d-d, f-d transitions and oxygen–metal ion charge transfer bands [33]. It is reported that the wavelength corresponding to the UV absorption edge of a semiconductive powder such as CeO_2 can be safely used to probe the presence of nano-

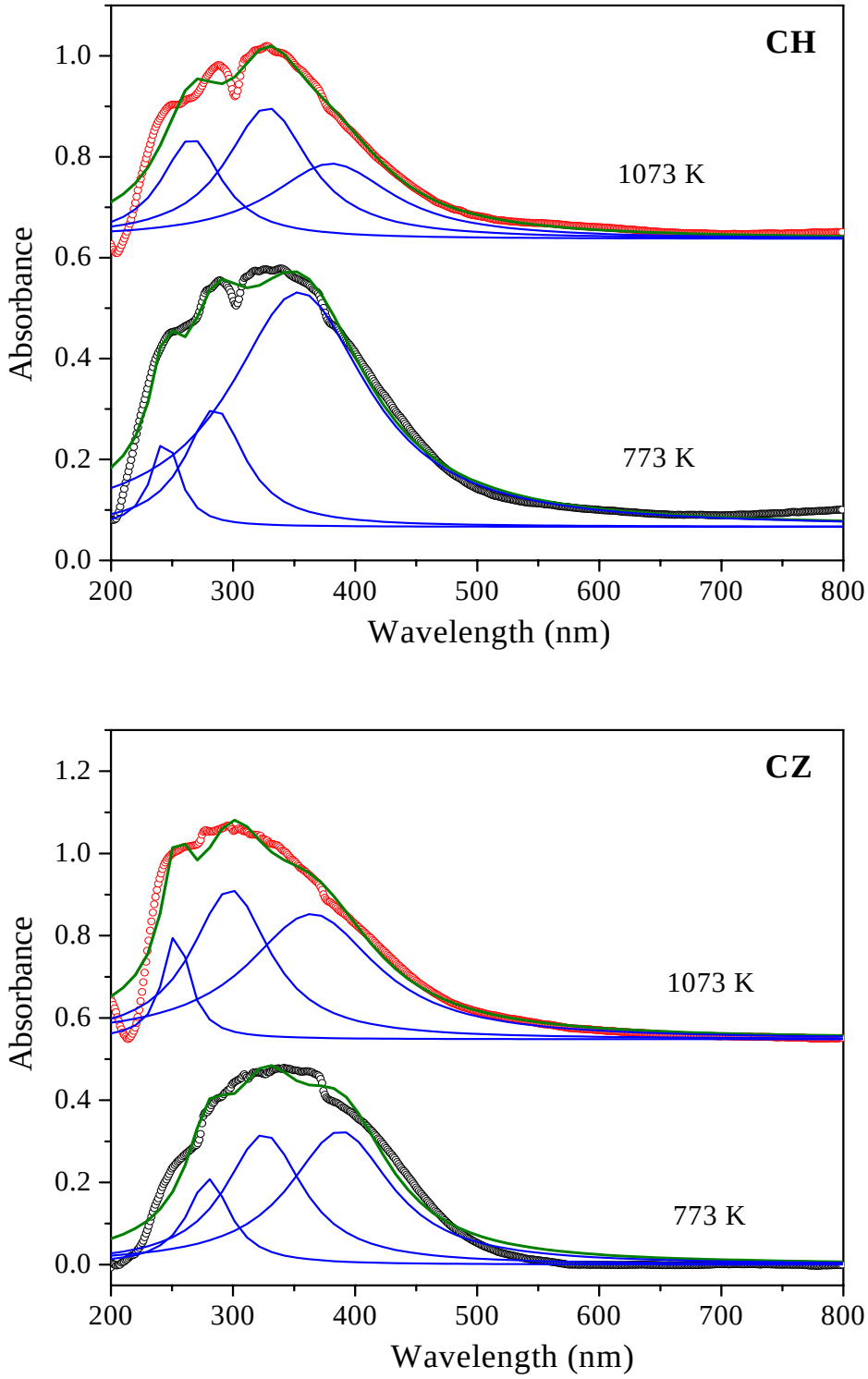

Figure 3.10: UV-vis DRS spectra of CeO_2–HfO_2 (CH) and CeO_2–ZrO_2 (CZ) samples calcined at 773 and 1073 K.

crystallites (<5 nm), which cannot be detected by XRD [34]. Pure CeO_2 exhibits three absorption maxima centered at ~255, 285, and 340 nm in its DR spectra. The latter two absorption maxima are ascribed to $Ce^{4+} \leftarrow O^{2-}$ charge transfer and inter-band transitions respectively [35]. The poorly resolved former maxima correspond to $Ce^{3+} \leftarrow O^{2-}$ charge transfer transitions [34]. As revealed by Figure 3.10, there are slight shifts towards higher wavelengths in the absorption edges of CH and CZ samples. Substitution of Hf^{4+} or Zr^{4+} into the CeO_2 lattice leads to lowering of symmetry and consequent strain development at the cerium sites. This may cause the observed shift towards higher wavelengths [22]. The absorption bands, which correspond to different charge transfer transitions, are poorly resolved in CZ, while the absorption edges are relatively sharp in the case of CH sample. Moreover, the band at ~255 nm, which has been characterized as $Ce^{3+} \leftarrow O^{2-}$ charge transfer transition, is well resolved in CH compared CZ samples with slight blue-shifted towards lower wavelength. The occurrence of oxygen vacancy defects as noticed from Raman spectroscopy studies support the $Ce^{3+} \leftarrow O^{2-}$ transitions, which is more prominent in the CH sample. There is no evidence for the presence of different phases like ZrO_2 or HfO_2 from DRS study in agreement with XRD measurements.

3.3.8 Raman Spectroscopy Studies

Raman spectroscopy is a good technique for the elucidation of structures of complex metal oxides present either as bulk phases or as two-dimensional supported phases. Therefore this technique has been successfully used to discriminate between different structures on oxide surfaces. In general, the spectra measured at the two types of wavelengths (UV and Visible) are more or less similar in terms of vibrational bands observed. However, depending on the nature and condition of the samples, Raman shift and intensity of patterns may change. We have used both UV excitation laser (He-Cd laser with wavelength 325 nm) and visible excitation laser (Ar^+-Kr^+ laser with wavelength 514.53 nm) in the present investigation. The UV-Raman spectra of the CH samples calcined at different temperatures and CZ samples calcined at 773 and 1073 K are presented in Figures 3.11 and 3.12, respectively. For the space group *Fm*3*m*, the only Raman active mode (F_{2g}) is centered at around 460 cm^{-1} [22]. The UV–Raman spectrum of the pure CeO_2 shows intense peak at 469 cm^{-1} corresponding to the F_{2g} mode. Before analysis, the sample was not dehydrated. So there is a possibility that a small degree of

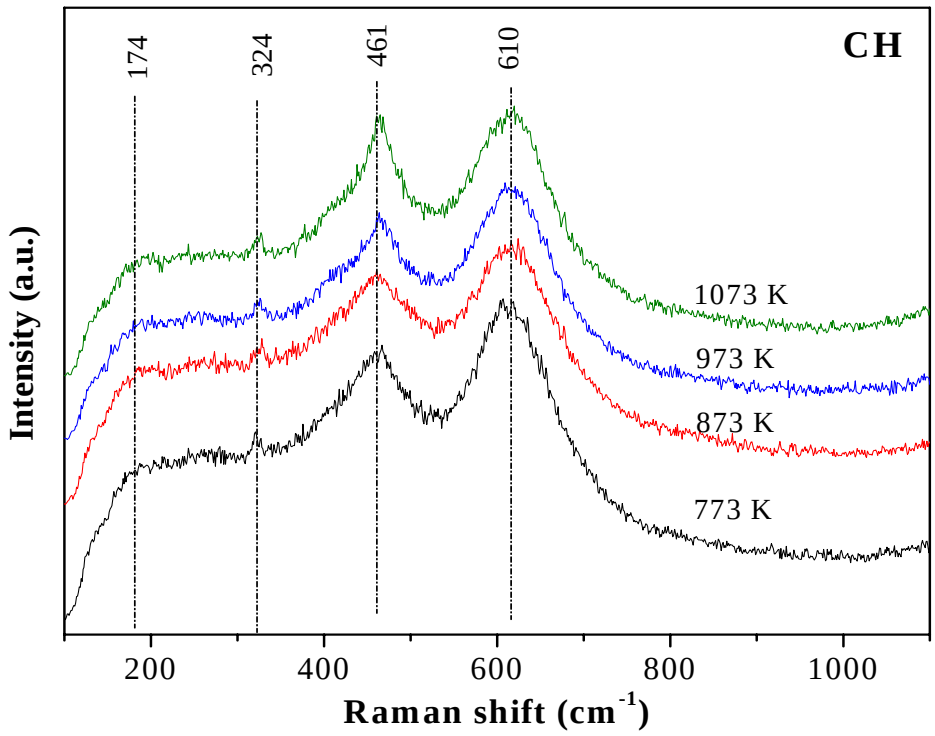

Figure 3.11: UV-Raman spectra of CeO_2–HfO_2 (CH) samples calcined at different temperatures.

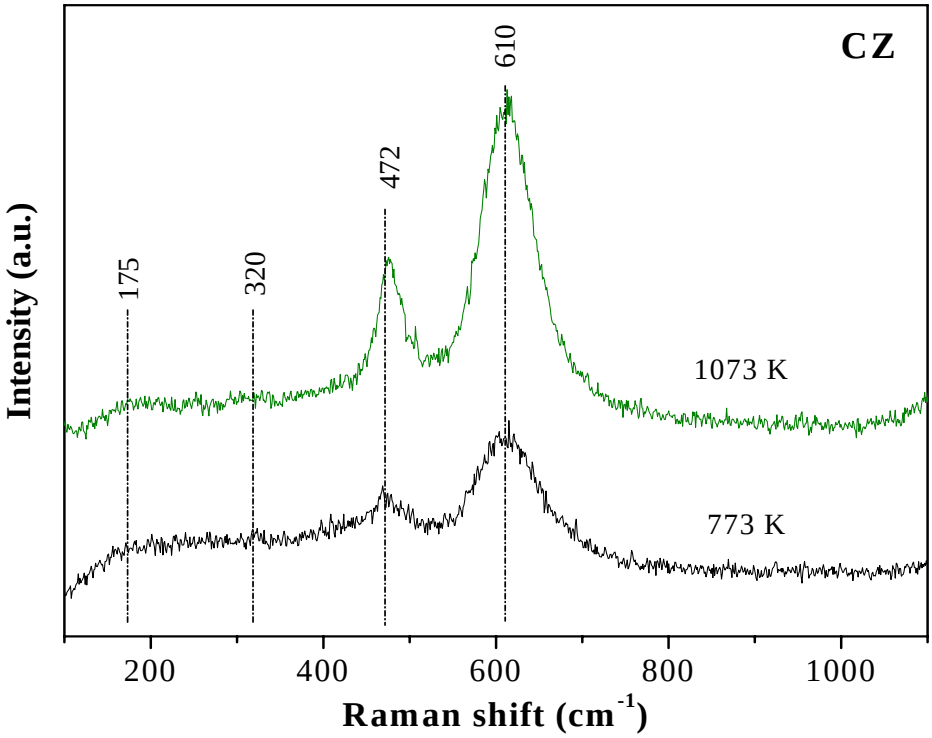

Figure 3.12: UV-Raman spectra of CeO_2–ZrO_2 (CZ) samples calcined at 773 and 1073 K.

hydration causes this band shift [36,37]. Additionally, a weak band at ~260 cm^{-1} and a shoulder at ~610 cm^{-1} are observed, which can be attributed respectively to the Raman inactive (but IR active) transverse and longitudinal optical phonon modes at the Brillouin zone centre [38,39]. The presence of these peaks is normally attributed to the perturbation of the fluorite structure. As could be observed from the Fig. 3.11, the CH samples calcined at different temperatures exhibit four bands in the wave number range 100 to 1100 cm^{-1}. The band positions are centred around 174, 324, 461, and 610 cm^{-1}, respectively for all the samples. The band at 461 cm^{-1} is due to the Raman active F_{2g} mode of ceria. The weak bands observed at around 174 and 324 cm^{-1} could be attributed to formation of oxygen vacancy and displacement of oxygen atoms from their ideal fluorite lattice positions [40]. Interestingly, for all CH samples, the peak at ~610 cm^{-1} is relatively more pronounced, which reveal some structural changes in the cubic fluorite structure of ceria after incorporation of hafnium into its lattice. This band is also linked to the oxygen vacancies in the CeO_2 lattice [41,42]. The nature of the pattern may be due to resonance enhancement of the Raman scattering cross section under UV excitation [36]. It is also known that depending on the system under study, there is a possibility for the resonance Raman scattering to be largely quenched due to a short lifetime for the electronically excited state [36]. Therefore, we may observe the low intensity of the F_{2g} band in case of the mixed oxide samples. There is no appreciable change in the intensity of the peak patterns with increasing calcination temperatures up to 1073 K. No shifts in band positions or emergence of new bands are noted for all the samples implying the homogeneous nature of the samples even after high thermal treatment. Fig. 3.12 shows the UV-Raman spectrum of CZ samples calcined at 773 and 1073 K, which exhibit four bands in the wave number range 100 to 1100 cm^{-1}. The band positions are centred around 175, 320, 472, and 610 cm^{-1}, respectively. The band at 472 cm^{-1} due to the Raman active F_{2g} mode of ceria is shifted to higher wave number compared to CH samples. The bands around 175 and 320 cm^{-1} are weaker compared to CH samples, also could be attributed to formation of oxygen vacancy and displacement of oxygen atoms from their ideal fluorite lattice positions [40]. Interestingly, in this case also the peak at ~610 cm^{-1} is relatively more pronounced. This band is also linked to the oxygen vacancies in the CeO_2 lattice [41,42]. Compared to CH, the relative intensity of ~610 cm^{-1} band in the case of CZ is more pronounced. A slight increase in the intensity of the peak patterns are noticed due to better crystallization of the mixed oxides at higher calcination temperature [40].

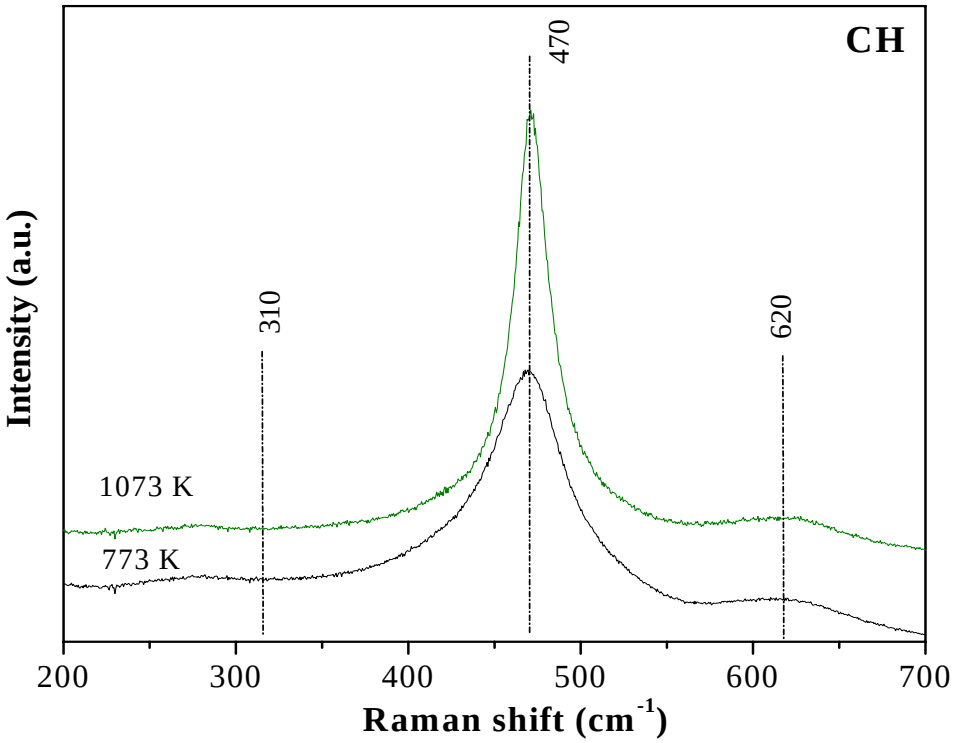

Figure 3.13: Visible-Raman spectra of CeO_2–HfO_2 (CH) samples calcined at 773 and 1073 K.

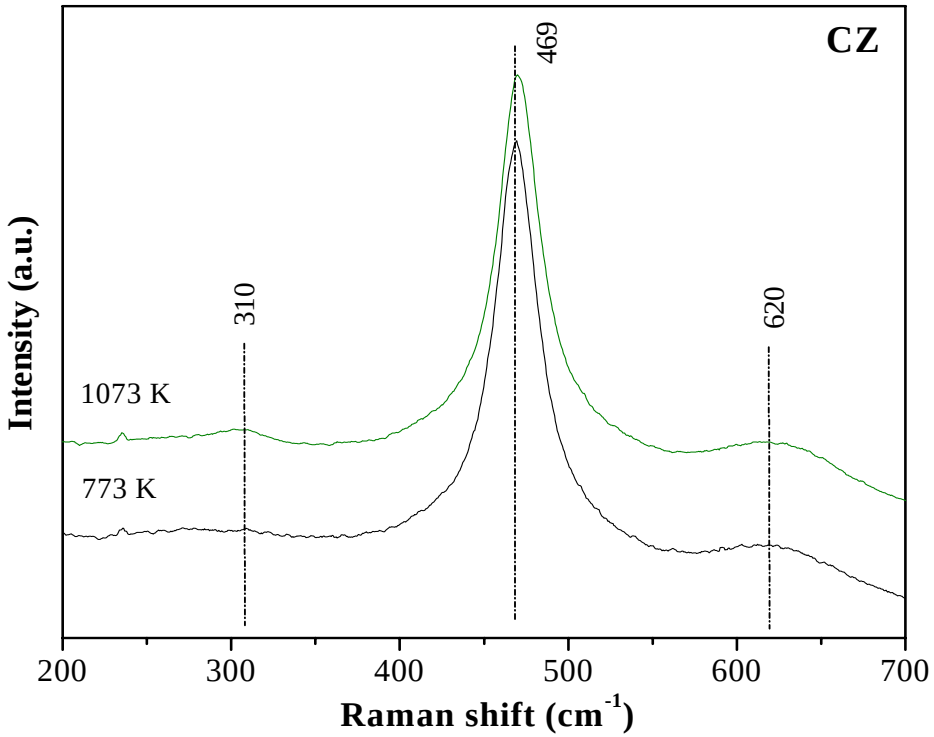

Figure 3.14: Visible-Raman spectra of CeO_2–ZrO_2 (CZ) samples calcined at 773 and 1073 K.

The visible-Raman spectra of CH and CZ samples calcined at 773 and 1073 K are shown in Figures 3.13 and 3.14, respectively. The Raman spectra of CH and CZ samples reveal a weak band at ~310 cm^{-1} and a shoulder at ~620 cm^{-1}, in addition to the most intense peaks at 470/471 and 469/470 cm^{-1}, respectively. The most intense peaks are due to F_{2g} vibration of the fluorite type lattice. Pure ceria exhibited prominent peaks at 462 and 464 cm^{-1} for 773 and 1073 K calcined samples, respectively, which are due to the F_{2g} mode of the cubic fluorite structure [22,43,44]. No other features existed in the spectra indicating no defects in the CeO_2 crystal lattice. The shift in the peak positions, in the case of CH and CZ samples, to higher wave numbers signifies changes in bond energies as a consequence of bond lengths as evidenced by lattice parameter estimations. Doping of lighter atoms such as Hf and Zr and subsequent contraction of the ceria unit cell may induce an increase in the F_{2g} band position. In line with XRD results, no Raman features pertaining to HfO_2 and ZrO_2 were noted. As can be observed from Figures 3.13 and 3.14, the Raman spectra are broad, which could be attributed to the reduction of phonon lifetime in the nanocrystalline regime [45–48]. This observation also gives a clue for predicting changes in the grain size and morphology of the prepared samples [49]. The broad band at ~620 cm^{-1} corresponds to the nondegenerate Longitudinal Optical (LO) mode of ceria, [45–50] arising due to relaxation of symmetry rules which is again linked to oxygen vacancies in the ceria lattice [25,51–53]. This is ascribed to a localized substitution defect vibration [54]. The weak bands observed at around 310 cm^{-1} could be attributed to displacement of oxygen atoms from their ideal fluorite lattice positions [55]. The above observations also predict the possibility of the existence of a t'' phase in the mixed oxide systems [54,56]. With increasing calcination temperature from 773 to 1073 K, in both cases, the main Raman band is sharpened with a small shift. This is due to better crystallization of the samples at higher calcination temperatures in line with XRD results [23].

3.3.9 X-ray Photoelectron Spectroscopy Studies

The ceria-hafnia and ceria-zirconia composite oxides calcined at different temperatures have been investigated with XPS technique. The photoelectron peaks of O 1s, Ce 3d, Hf 4f, Hf 4d and Zr 3d are depicted in Figures 3.15–3.18, respectively. The corresponding binding energy (eV) values and Ce/Hf and Ce/Zr atomic ratios are

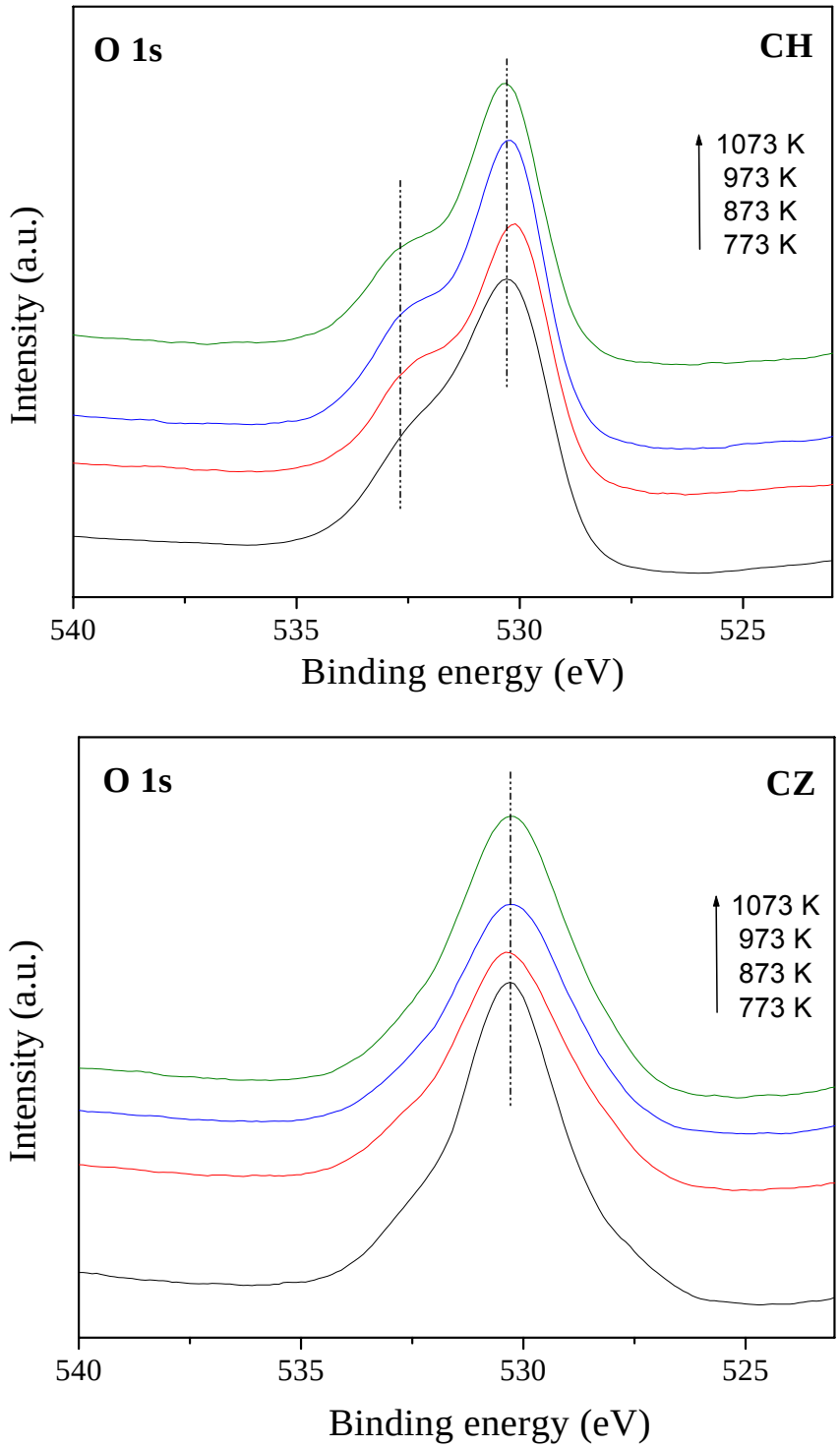

Figure 3.15: O 1s XP spectra of CeO_2–HfO_2 (CH) and CeO_2–ZrO_2 (CZ) samples calcined at different temperatures.

presented in the Tables 3.2 and 3.3, respectively. All the figures, binding energy, and atomic ratio values provided in the Tables 3.2 and 3.3 clearly indicate that the XPS bands and the corresponding BE values are sensitive to the calcination temperature and to the composition of the samples.

The O 1s core level XPS profiles of CH and CZ samples calcined at different temperatures are presented in Fig. 3.15.The position of the primary O 1s feature (ca. 530.3 eV) is attributed to the lattice oxygen associated with the CH and CZ metal oxides. When only one peak is observed for CZ samples, one very small additional peak along with the main peak is present in CH samples (Fig. 3.15). The peak at about 530.3 eV shown in the figure corresponds to O 1s, while the small peak at about 532.6 eV may be attributed to the adsorbed oxygen possibly from absorbed water and/or carbonates [57,58].

XPS was employed to investigate the oxidation state of Ce in the mixed oxides. The Ce 3d core level peak of ceria is known to be complicated by the hybridization of the O 2p valence band with the Ce 4f level [59,60]. This includes several final states for the Ce emission which are seen in the spectra. In the case of two possible cerium oxidation states (3+ and 4+) as many as 10 different features could be found in the Ce 3d region. The interpretation is performed by the following notations used previously [22]. The XP spectra of CH and CZ samples calcined at different temperatures are shown in Figure 3.16, in which assignment of the features in the spectra can be seen. Peaks labeled as 'v' correspond to Ce $3d_{5/2}$ contributions and those labeled as 'u' represent the Ce $3d_{3/2}$ contributions. The bands u_0 and u are the main Ce $3d_{3/2}$ lines, and the bands v_0 and v are the main Ce $3d_{5/2}$ lines of Ce^{3+} and Ce^{4+}, respectively. The band labeled as v' is a satellite to the Ce^{3+} $3d_{5/2}$ main line v_0, whereas v'' and v''' are related to Ce^{4+} (main line v). Analogous assignments are valid for the corresponding 'u' features. The relative intensity of the u''' feature, which is well separated from the remaining signals, is often used to assess the reduction degree of the Ce ions in the surface region. It should be kept in mind that partial reduction of cerium-zirconium mixed oxides can occur during XPS measurements. This has been noticed by many authors [61,62] and must be taken into account when discussing quantitatively the oxidation states of surface species of the samples. Besides the X-ray dose, several factors may lead to such partial reduction like secondary electrons from the X-ray source, sample charging, temperature, vacuum, etc.

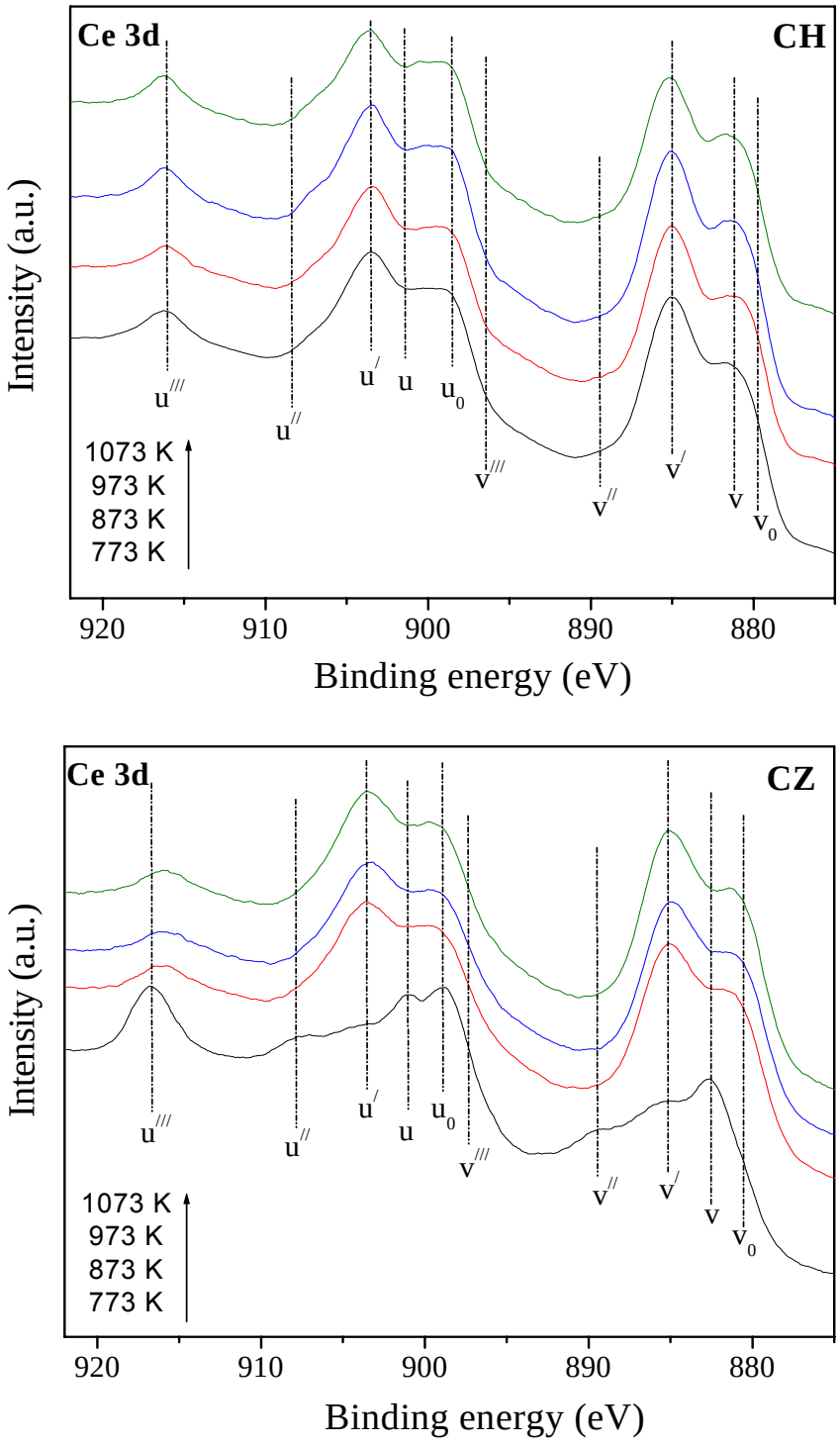

Figure 3.16: Ce 3d XP spectra of CeO_2–HfO_2 (CH) and CeO_2–ZrO_2 (CZ) samples calcined at different temperatures.

[63]. In the present study, the peaks at about 898.5 and 880.7 eV are the principal binding energies of Ce $3d_{3/2}$ and Ce $3d_{5/2}$, respectively. This is significantly lower than the values

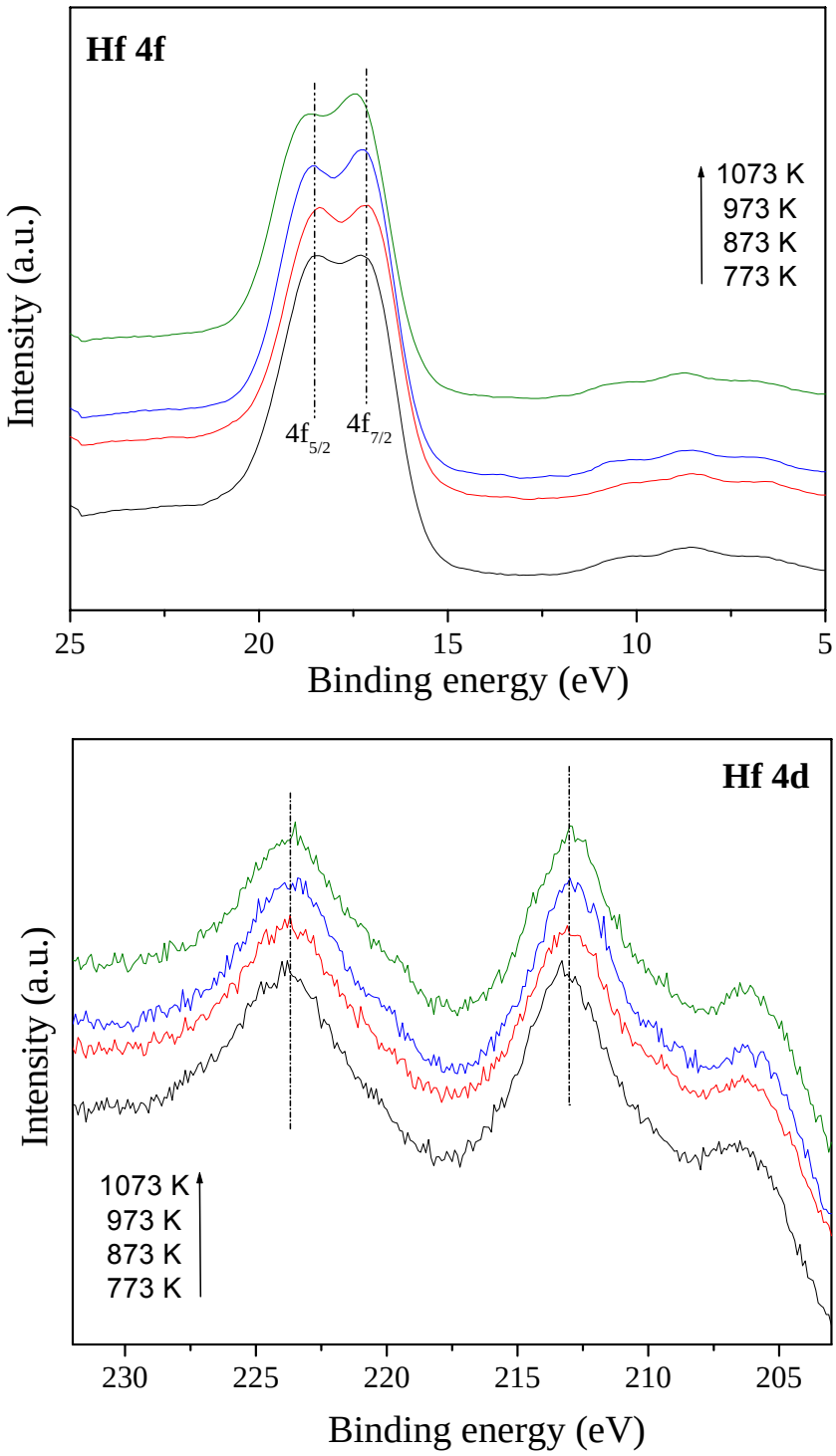

Figure 3.17: Hf 4f and Hf 4d XP spectra of CeO_2–HfO_2 (CH) samples calcined at different temperatures.

typical for Ce^{4+} (900.2–900.6 and 881.7–882.0 eV, respectively) [64] which suggests a significant concentration of Ce^{3+} ions in the surface region. This is supported by the low intensity of the u''' feature in all samples except CZ after calcination at 773 K. Obviously, the surface region of our samples was strongly reduced, with the ceria present predominantly in the 3+ state, only in the surface region of CZ after calcination at 773 K were Ce^{3+} and Ce^{4+} present in comparable concentrations.

Figure 3.17 shows the core level XP spectra of Hf 4f and Hf 4d corresponding to the CH samples calcined at different temperatures. As could be observed from the XP spectra of Hf 4f, there are two features at about 17.2 and 18.6 eV, respectively. It is reported that the Hf 4f spectrum consists of two components, the $4f_{7/2}$ part at 16.79 ± 0.08 eV and the $4f_{5/2}$ part at 18.54 ± 0.10 eV [65]. The peak positions of Hf 4f photoelectrons are known to be very sensitive to the binding states of the hafnium species [57,66]. According to a database, the metallic hafnium species reveals the Hf $4f_{7/2}$ peak at 14.3–14.4 eV, while HfO_2 shows it at 16.7 eV. Lee et al. investigated HfO_2 films on a silicon substrate by synchrotron XPS and found the binding energies of Hf $4f_{7/2}$ and Hf $4f_{5/2}$ at 17.55 and 19.26 eV, respectively [67].

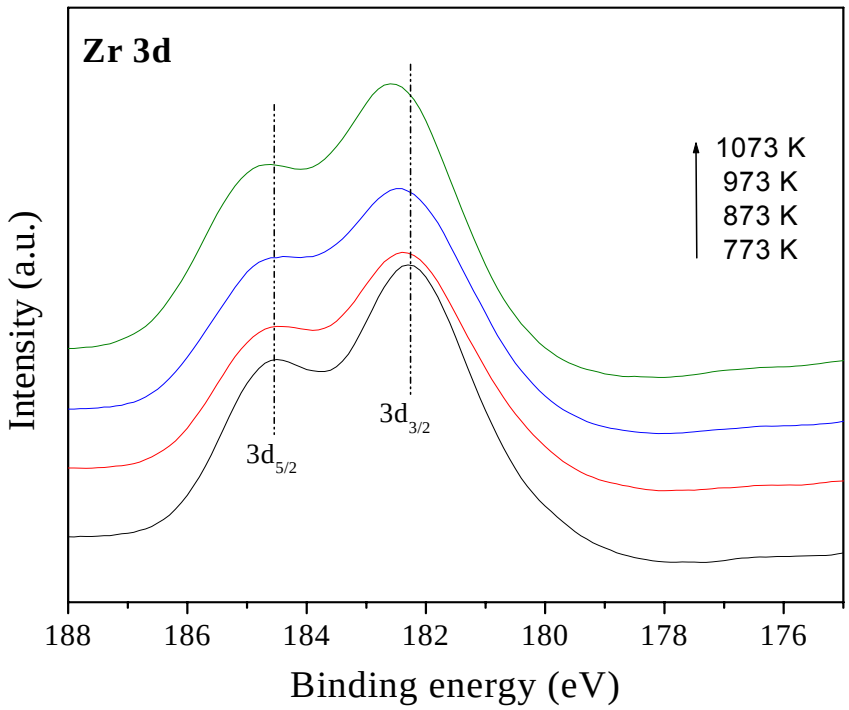

Figure 3.18: Zr 3d XP spectra of CeO_2–ZrO_2 (CZ) samples calcined at different temperatures.

However, the difference of about 1.4 eV in the binding energies between the Hf $4f_{7/2}$ and Hf $4f_{5/2}$ in the present investigation is in line with the reported values [57]. On the other hand, the XP spectra of Hf 4d photoelectron peak in relatively very scarce in the literature. As observed the spectra consists of two features in the binding energy values of ~223.8 and ~213.3 eV, respectively, which are in good agreement with the data presented in 'The Handbook of X-ray Photoelectron Spectroscopy'. On the whole, from the XP spectra of Hf 4f and Hf 4d, it is observed that Hf is mainly in 4+ oxidation state.

The core level XP spectra of Zr 3d corresponding to the CZ samples calcined at different temperatures are presented in Figure 3.18. As could be seen from the figure, a progressive broadening along with shift towards higher binding energy from 182.2 to 182.6 eV with increasing calcination temperature indicating the formation of solid solutions between ceria and zirconia in different stoichiometric combinations as envisaged earlier [57,68,69]. The overlapping peaks at 182.2 and 184.6 eV correspond to Zr $3d_{5/2}$ and Zr $3d_{3/2}$, respectively. The difference in the binding energies between the Zr $3d_{5/2}$ and Zr $3d_{3/2}$ photoemission feature is 2.4 eV, which is in agreement with the literature [57,70]. The shift towards higher binding energy as a function of calcination temperature signifies the enrichment of Zr and account for the emergence of $Ce_{0.6}Zr_{0.4}O_2$ phase at higher calcination temperatures. The XPS studies indicate that zirconium is mainly present in 4+ oxidation state.

Table 3.2: XPS core level electron binding energies (eV) of the CeO_2–HfO_2 (CH) and CeO_2–ZrO_2 (CZ) samples calcined at different temperatures

Calcination Temp. (K)	Binding Energy (eV)				
	O 1s	Ce 3d	Zr 3d	Hf 4f	Hf 4d
CeO_2–HfO_2					
773	530.1	880.7	–	18.4 (17.2)	223.8 (213.3)
873	530.2	880.9	–	18.4 (17.2)	223.7 (213.1)
973	530.2	881.0	–	18.5 (17.3)	223.6 (213.0)
1073	530.3	881.1	–	18.7 (17.5)	223.5 (213.0)
CeO_2–ZrO_2					
773	530.1	882.5	182.2	–	–
873	530.2	881.5	182.3	–	–
973	530.3	881.5	182.5	–	–
1073	530.3	881.3	182.6	–	–

Table 3.3: XPS atomic ratio of the CeO_2–HfO_2 (CH) and CeO_2–ZrO_2 (CZ) samples calcined at different temperatures

Calcination Temperature (K)	Atomic Ratio	
	Ce/Hf	Ce/Zr
CeO_2–HfO_2		
773	4.87	–
873	4.86	–
973	4.65	–
1073	4.65	–
CeO_2–ZrO_2		
773	–	3.91
873	–	2.80
973	–	2.24
1073	–	1.85

The Ce/Hf and Ce/Zr atomic ratios as determined by XPS are presented in Table 3.3. As observed there is a meager decrease in the Ce/Hf atomic ratios of the CH samples, as a function of calcination temperature and the decrease can be attributed to the incorporation of Hf^{4+} cations into the ceria lattice at higher calcination temperatures, thereby increasing the surface content of Hf^{4+} ions. In the case of CZ samples, the Ce/ Zr atomic ratios are found to decrease with increasing calcination temperature, thus supporting the surface enrichment of zirconia due to the formation of zirconium rich $Ce_{0.6}Zr_{0.4}O_2$ phase over the surface. The atomic ratios among different systems were found to be far from the theoretical estimations due to the complex nature of the systems envisaged and also the amount of error involved in the XPS quantifications [68,69]. However, the trends observed in a given system (as a function of calcination temperature) provide valuable information on the surface composition of the sample and fairly support the conclusions drawn from XRD and Raman techniques.

3.3.10 Ion Scattering Spectroscopy Studies

To examine the surface structure of the mixed oxides, ISS measurements were carried out as ISS allows the analysis of the extreme periphery of the powder particles. The intensity (cps) versus kinetic energy (eV) plots of the 773 and 1073 K calcined CH

samples and 773 K calcined CZ sample after definite scans are presented in Figures 3.19 and 3.20, respectively.

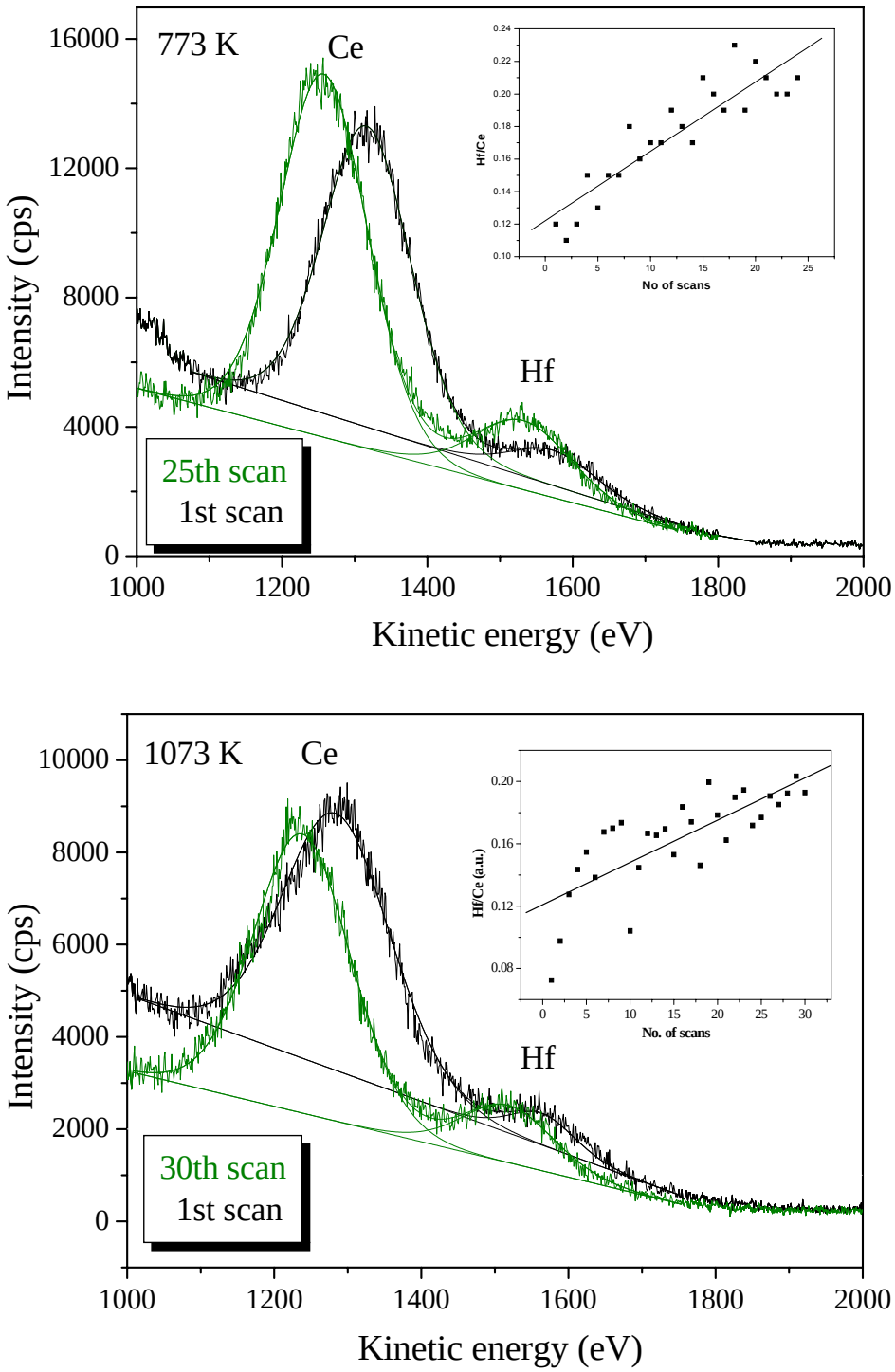

Figure 3.19: ISS spectra of CeO_2–HfO_2 (CH) sample calcined at 773 and 1073 K after definite scans. Inset: plot of Hf/Ce intensity ratio.

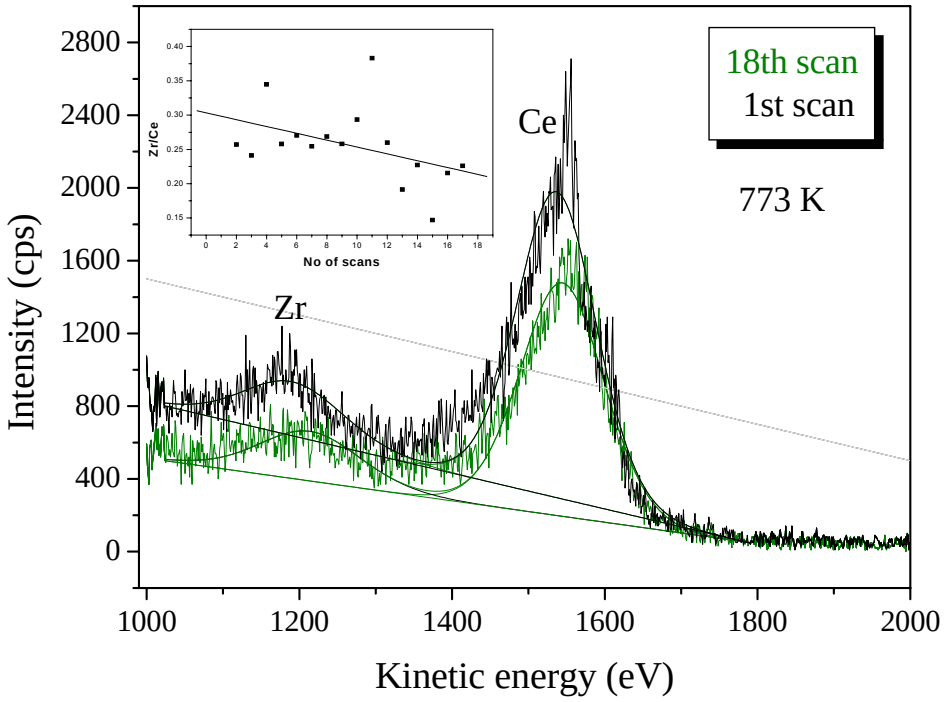

Figure 3.20: ISS spectra of CeO_2–ZrO_2 (CZ) sample calcined at 773 K after definite scans. Inset: plot of Zr/Ce intensity ratio.

The insets show the development of the intensity ratios between Hf and Ce, and Zr and Ce, respectively. The shifts of the signal positions in Figure 3.19 and to a smaller extent in Figure 3.20 are due to instability of the kinetic energy scale, i.e., an instrumental problem encountered in heavy-ion ISS with the spectrometer used. It can be observed from Figure 3.19 that there is a linear increase in the Hf/Ce intensity ratio during the sputter series, i.e., the Ce is enriched at the external surface of the mixed oxide. Both the CH samples calcined at 773 and 1073 K followed similar trend. In the CZ sample, a strong surface enrichment cannot be detected. There is a slight decrease of the Zr/Ce intensity ratio during the sputter series, but the trend is hardly significant given the rather large scatter of the experimental data. The slight surface enrichment of cerium in the CH samples, which is responsible for showing the reducible property, is expected to facilitate easy reducibility of the mixed oxide at lower temperatures. Accordingly, one can expect better activity for the CH samples compared to that of the CZ sample [71].

3.3 Conclusions

The structural characteristics of ceria-zirconia and ceria-hafnia nanosized composite oxides have been systematically investigated. These catalysts were synthesized by adopting a modified coprecipitation method and thermally treated up to 1073 K to study the temperature stability. The mixed oxides exhibit high specific surface area and show resistance to thermal sintering. XRD results infer the monophasic composition ($Ce_{0.8}Hf_{0.2}O_2$) for CH even up to 1073 K, while phase segregation into $Ce_{0.75}Zr_{0.25}O_2$ and $Ce_{0.6}Zr_{0.4}O_2$ was noted for the CZ sample at 1073 K. The TEM images confirmed the nanometer-sized particles of the prepared catalysts with almost uniform size (~5 nm). A marginal increase in crystallite size (up to ~10 nm) after heat treatment at 1073 K was noticed. UV-vis DRS measurements gave information on different oxygen to metal charge transfer transitions. The lowering of symmetry and consequent strain development at the cerium sites is also revealed by UV-vis DRS measurements. Raman spectroscopy measurements revealed the changes in the grain size and morphology of the catalyst, and defective fluorite structure leading to oxygen vacancy formation. The XPS measurements revealed the presence of both Ce^{3+} and Ce^{4+} states, which are sensitive to calcination temperature and the nature of the mixed oxide. ISS studies indicated surface enrichment of cerium in the case of the CH sample, which might be responsible for the observed better reducibility and catalytic activity of this sample. Thus the use of various spectroscopic and non-spectroscopic techniques provided interesting information regarding the physicochemical characteristics of ceria-hafnia and ceria-zirconia composite oxides.

3.4 References

[1] S.D. Park, J. M. Vohs, R.J. Gorte, Nature 404 (2000) 265.

[2] C.W. Xu, P.K. Shen, J. Power Sources 142 (2005) 27.

[3] P. Bance, N.P. Brandon, B. Girvan, P. Holbeche, S. O'Dea, S. B.C.H. Steele, J. Power Sources 131 (2004) 86.

[4] S.V. Chavan, A.K. Tyagi, Mater. Sci. Eng. A 433 (2006) 203.

[5] T. Kim, J.M. Vohs, R.J. Gorte, Ind. Eng. Chem. Res. 45 (2006) 5561.

[6] S. Bernal, G. Blanco, M.A. Cauqui, P. Corchado, J.M. Pintado, J.M. Rodriguez-Izquierdo, Chem. Commun. (1997) 1545.

[7] T. Masui, T. Ozaki, K. Machida, G. Adachi, J. Alloys Compd. 303–304 (2000) 49.

[8] B.M. Reddy, In Metal Oxides: Chemistry and Applications; J.L.G. Fierro, Ed.; Taylor & Francis: New York, 2006, Chapter 8; pp 215.

[9] A. Trovarelli, Catal. Rev. Sci. Eng. 38 (1996) 439.

[10] H.J. Shinjoh, J. Alloys Compd. 408–412 (2006) 1061.

[11] M. Sugiura, Catal. Surv. Asia 7 (2003) 77.

[12] B.M. Reddy, A. Khan, P. Lakshmanan, M. Aouine, S. Loridant, J.C. Volta, J. Phys. Chem. B 109 (2005) 3355.

[13] R.K. Usmen, G.W. Graham, W.L.H. Watkins, R.W. McCabe, Catal. Lett. 30 (1995) 53.

[14] M.Y. Sinev, G.W. Graham, L.P. Haach, M. Shelef, J. Mater. Res. 11 (1996) 1960.

[15] M. Ozawa, K. Matuda, S. Suzuki, J. Alloys Compd. 303–304 (2000) 56.

[16] M. Fernandez-Garcia, A. Martinez-Arias, A. Iglesius-Juez, C. Belver, A.B. Hungria, J.C. Conesa, J. Soria, J. Catal. 194 (2000) 385.

[17] G. Balducci, M.S. Islam, J. Kaspar, P. Fornasiero, M. Graziani, Chem. Mater. 12 (2000) 677.

[18] S. Bernal, G. Blanco, G.A. Cifredo, J.J. Delgado, D. Finol, J.M. Gatica, J.M. Rodriguez-Izquierdo, H. Vidal, Chem. Mater. 14 (2002) 844.

[19] X. Wang, J.C. Hanson, G. Liu, J.A. Rodriguez, A. Iglesius-Juez, M. Fernandez-Garcia, J. Chem. Phys. 107 (2004) 5434.

[20] J.A. Rodriguez, J.C. Hanson, J.-Y. Kim, G. Liu, A. Iglesius-Juez, M. Fernandez-Garcia, J. Phys. Chem. B 107 (2003) 3535.

[21] B.M. Reddy, P. Bharali, P. Saikia, A. Khan, S. Loridant, M. Muhler, W. Grunert, J. Phys. Chem. C 111 (2007) 1878.

[22] B.M. Reddy, A. Khan, Catal. Surv. Asia 9 (2005) 155.

[23] R.D. Monte, J. Kaspar, J. Mater. Chem. 15 (2005) 633.

[24] S. Bernal, J. Kaspar, A. Trovarelli, Recent Progress in Catalysis by Ceria and Related Compounds. Catal. Today 50 (1999) 173.

[25] B.M. Reddy, A. Khan, Y. Yamada, T. Kobayashi, S. Loridant, J.C. Volta, Langmuir 19 (2003) 3025.

[26] K. Kenevey, F. Valdivieso, M. Soustelle, M. Pijolat, Appl. Catal. B: Environ. 29 (2001) 93.

[27] M. Yashima, K. Morimoto, N. Ishizawa, M.J. Yoshimura, J. Am. Ceram. Soc. 76 (1993) 1745.

[28] J. Kaspar, P. Fornasiero, G. Balducci, R.D. Monte, N. Hickey, V. Sergo, Inorg. Chim. Acta 349 (2003) 217.

[29] F. Fally, V. Perrichon, H. Vidal, J. Kaspar, G. Blanco, J.M. Pintado, S. Bernal, G. Colon, M. Daturi, J.C. Lavalley, Catal. Today 59 (2000) 373.

[30] P. Vidmar, J. Kaspar, P. Fornasiero, M. Graziani, J. Phys. Chem. B 102 (1998) 557.

[31] M. Boaro, M. Vicario, C. de Leitenburg, G. Dolcetti, A. Trovarelli, Catal. Today 77 (2003) 407.

[32] T.X.T. Sayle, S.C. Parker, C.R.A. Catlow, J. Chem. Soc. Chem. Commun. (1992) 977.

[33] B.M. Weckhuysen, R.A. Schoonheydt, Catal. Today 49 (1999) 441.

[34] A. Bensalem, F.B. Verduraz, M. Delamar. G. Bugli, Appl. Catal. 121 (1995) 81.

[35] A. Bensalem, J.C. Muller, F.B. Verduraz., J. Chem. Soc. Faraday Trans. 88 (1992) 153.

[36] Y.T. Chua, P.C. Stair, I.E. Wachs, J. Phys. Chem. B 105 (2001) 8600.

[37] B.M. Reddy, P. Saikia, P. Bharali, Y. Yamada, T. Kobayashi, M. Muhler, W. Grunert, J. Phys. Chem. C 112 (2008) 16393.

[38] P.K. Dutta, R.E. Zaykoski, Zeolites 8 (1988) 179.

[39] B.M. Reddy, P. Saikia, P. Bharali, S.-E. Park, M. Muhler, W. Grunert, J. Phys. Chem. C 113 (2009) 2452.

[40] B.M. Reddy, K.N. Rao, G.K. Reddy, A. Khan, S.-E. Park, J. Phys. Chem. C 111 (2007) 18751.

[41] B.M. Reddy, P. Lakshmanan, P. Bharali, P. Saikia, G. Thrimurthulu, M. Muhler, W. Grünert, J. Phys. Chem. C 111 (2007) 10478.

[42] J.-M. Jehng, J. Phys. Chem. B 102 (1998) 5816.

[43] A. Martinez-Arias, M. Fernandez-Garcia, L.N. Salamanca, R.X. Valenzuela, J.C. Conesa, J. Soria, J. Phys. Chem. B 104 (2000) 4038.

[44] J.Z. Shyu, W.H. Weber, H.S. Gandhi, J. Phys. Chem. 92 (1988) 4964.

[45] W.H. Weber, K.C. Hass, J.R. McBride, Phys. Rev. B 48 (1993) 178.

[46] P. Parayanthal, F.H. Pollak, Phys. Rev. Lett. 52 (1984) 1822.

[47] H. Richter, Z.P. Wang, L. Ley, Solid State Commun. 39 (1981) 625.

[48] M. Fujii, S. Hayashi, K. Yamamoto, Appl. Phys. Lett. 57 (1990) 2692.

[49] J.E. Spanier, R.D. Robinson, F. Zhang, S.-W. Chan, I.P. Herman, Phys. Rev. B 64 (2001) 245407.

[50] X.-M. Lin, L.-P. Li, G.-S. Li, W.-H. Su, Mater. Chem. Phys. 69 (2001) 236.

[51] B.M. Reddy, P. Lakshmanan, A. Khan, S. Loridant, C.L. Cartes, T.C. Rojas, A. Fernandez, J. Phys. Chem. B 109 (2005) 13545.

[52] J.R. McBride, K.C. Hass, B.D. Poindexter, W.H. Weber, J. Appl. Phys. 76 (1994) 2435.

[53] A.B. Hungria, A. Martinez-Arias, M. Fernandez-Garcia, A. Iglesius-Juez, G.A. Ruiz, J.J. Calvino, J.C. Conesa, J. Soria, Chem. Mater. 15 (2003) 4309.

[54] M. Yashima, H. Arashi, M. Kakihana, M. Yoshimura, J. Am. Ceram. Soc. 77 (1994) 1067.

[55] V.S. Escribano, E.F. Lopez, M. Panizza, C. Resini, J.M.G. Amores, G. Busca, Solid State Sci. 5 (2003) 1369.

[56] G. Vlaic, P. Fornasiero, S. Geremia, J. Kaspar, M. Graziani, J. Catal. 268 (1997) 386.

[57] C.D. Wagner, W.M. Riggs, L.E. Davis, J.F. Moulder, in: Handbook of X-ray Photoelectron Spectroscopy, G.E. Muilenberg, Ed., Perkin-Elmer Corporation, Eden Prairie, MN, 1978.

[58] F. Guodong, F. Changgen, Z. Zhao, J. Rare Earths 25 (2007) 42.

[59] F.L. Normand, J.E. Fallah, L. Hilaire, P. Legare, A. Kotani, J.C. Parlebas, Solid State Commun. 71 (1989) 885.

[60] D.R. Mullins, S.H. Overbury, D.R. Huntley, Surf. Sci. 409 (1997) 307.

[61] A.E. Hughes, J.D. Gorman, P.J.K. Patterson, R. Carter, Surf. Interface Anal. 24 (1996) 634.

[62] K. Bak, L. Hilaire, Appl. Surf. Sci. 70–71 (1995) 191.

[63] L. Hilaire, M. Romeo, J.E. Fallah, F.L.J. Normand, Electron Spectrosc. Relat. Phenom. 73 (1995) 89.

[64] A.E. Nelson, K.H. Schulz, Appl. Surf. Sci. 210 (2003) 206.

[65] T. Brezesinski, B. Smarsly, K.-I. Iimura, D. Grosso, C. Boissiere, H. Amenitsch, M. Antonietti, C. Sanchez, Small 8–9 (2005) 889.

[66] V. Cosnier, M. Olivier, G. Theret, A. Andre, J. Vac. Sci. Technol. A 19 (2001) 2267.

[67] J.C. Lee, S.J. Oh, M. Cho, C.S. Hwang, R. Jung, Appl. Phys. Lett. 84 (2004) 1305.

[68] B.M. Reddy, A. Khan, Y. Yamada, T. Kobayashi, S. Loridant, J.C. Volta, J. Phys. Chem. B 107 (2003) 11475.

[69] D. Briggs and M.P. Seah, (eds.), Practical Surface Analysis, 2nd edn.; Auger and X - Ray Photoelectron Spectroscopy, vol. 1 (Wiley, New York, 1990).

[70] S.-P. Wang, X.-C. Zheng, X.-Y. Wang, X.-R. Wang, S.-M. Zhang, L.-H. Yu, W.-P. Huang, S.-H. Wu, Catal. Lett. 105 (2005) 163.

[71] B.M. Reddy, P. Bharali, P. Saikia, S.-E. Park, M.W.E. van den Berg, M. Muhler, W. Grünert, J. Phys. Chem. C 112 (2008) 11729.

Chapter 4

This chapter presents the results and discussion pertaining to the structural characteristics of the nanosized composite oxides of CeO_2–HfO_2/SiO_2 system by various spectroscopic and non-spectroscopic techniques.

STUDIES on CeO_2–HfO_2/SiO_2 COMPOSITE OXIDE CATALYST

4.1 Introduction

Numerous technological applications in several fields such as catalysis, electrochemistry, biomaterials, photochemistry and materials science have made ceria (CeO_2) a unique material of great significance [1−14]. In recent years, environmental protection has been considered very seriously and the case of automotive exhaust gas is highlighted as one of the most important subjects. A well-tuned automotive engine even produces many pollutants by incomplete combustion of the fuel. Therefore, the development of new technologies for controlling the emission of gaseous pollutants into the atmosphere is intriguing. In this context, three-way-catalysts (TWCs) are of great importance. Cerium oxide, due to very low redox potential of the Ce^{3+}/Ce^{4+} couple (E = 1.7 V), can take up oxygen from lean fuel gas and release it during fuel-rich operation and can regulate oxygen storage and release properties, which is the most important and remarkable feature of three-way catalysts [15]. Primarily, ceria was recognized as a promising material, because it keeps a cubic crystal structure even during the alternate storage and release of oxygen and its volume change is small. However, OSC and thermal durability of CeO_2 were both insufficient for automotive use. In order to overcome the problems associated with pure ceria, it was stabilized by combining with other metal oxides like ZrO_2, TbO_2, HfO_2 etc. Ceria-based composite oxides show better redox properties and thermal stability relative to pure ceria [1,2]. In spite of this, these unsupported oxides are susceptible to a fall in the surface area and a decrease in the stability of the structure during high temperature applications [3,4]. The design of nanocomposite oxides where the CeO_2-based composite oxide phase is dispersed over a stable inert support could represent a suitable way to improve thermal and structural stability of these systems. Silica is a well-known support, which exhibits good chemical resistance, high thermal stability, and high surface area. It is extensively used as a support in the reparation of supported metal catalysts because of its inert character, which allows investigation of the effect of the metal, minimizing the effect of the metal-support interaction. For example, the weak interaction between SiO_2 surfaces and Au particles makes silica supports very convenient for studying the size effect of the gold nanoparticles on their catalytic activity, minimizing the disturbance of the support interaction [1]. Colloidal silica was used as a precursor for SiO_2 in the present investigation. There are

certain advantages associated with colloidal dispersions. First is the fact that the colloidal dispersion is much less reactive towards the catalytic material, and as a consequence, solid-state reactions are slightly less likely to occur with the colloidal materials than with the coprecipitated materials from soluble salts. Second the particles of the colloid are larger than the particles of the coprecipitated salt. This has the feature of making larger pores and a more open structure for the final catalyst. Against the aforesaid background, the present investigation was undertaken to understand the physicochemical characteristics and nanostructural evolution of CeO_2-HfO_2/SiO_2 composite oxide catalyst where ceria-hafnia composite oxide acts as the active phase and silica as thermally stable inert support.

4.2 Experimental

Silica supported ceria-hafnia sample (CHS; 8:2:10 mole ratio based on oxides) was prepared by adopting a deposition coprecipitation method as per the procedure described in Chapter 2. The obtained catalysts were subjected to thermal treatments from 773 to 1073 K in order to understand the thermal stability, and the physicochemical properties of these materials. These effects have been investigated by means of TG-DTA, BET SA, XRD, TPR, SEM, TEM, UV-vis DRS, LRS, XPS, ISS and other techniques.

4.3 Results and Discussion

4.3.1 Thermal Measurements

The synthesized CHS composite oxide was subjected to TG/DTA analysis before calcination. The obtained thermogram between ambient temperature and 1273 K is shown in Figure 4.1. The analysis provided some interesting information about the role of support in retarding the sintering and decomposition behavior of ceria-hafnia solid solution. The TGA profiles of the CHS sample revealed one major and one minor weight loss peaks. The low temperature broad weight loss peak corresponds to the loss of non-dissociative adsorbed water and the loss of water held in the micropores of the gel. The other minor weight loss peak observed at higher temperature region is due to dehydroxylation of the surface. This observation indicates that the weight loss of samples from ambient to ~840

K was about 10.5% whereas from 840 to 1273 K it was about 1.4% only, which revealed that the silica supported ceria-hafnia composite oxide is thermally quite stable.

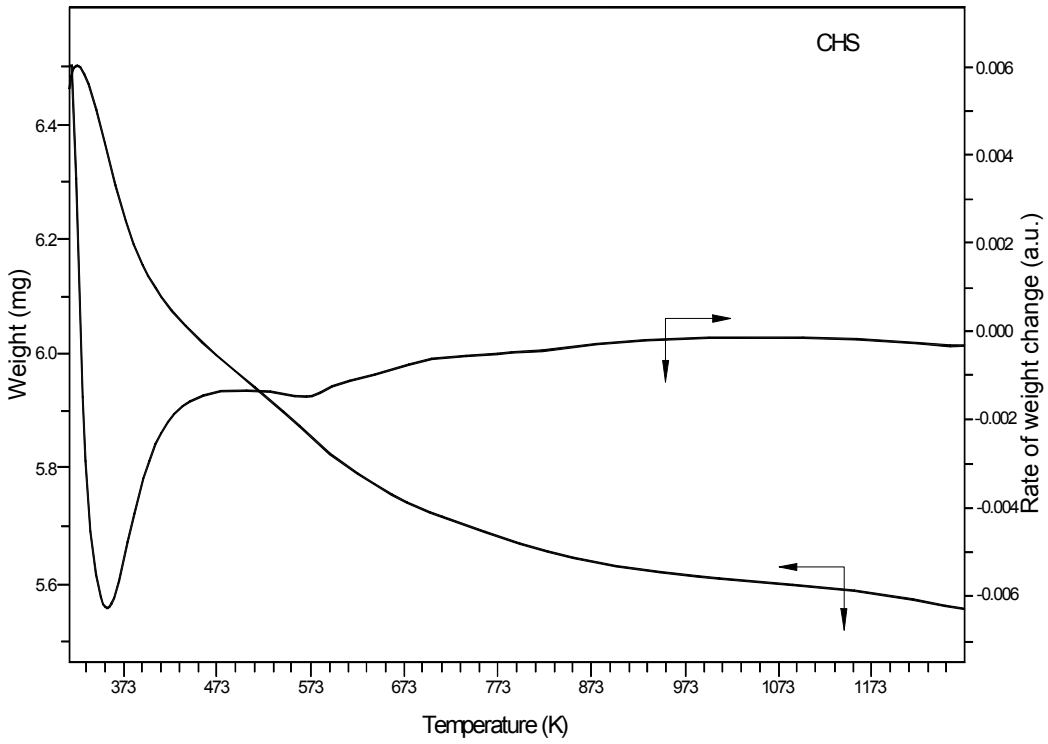

Figure 4.1: TGA profile of CeO_2–HfO_2/SiO_2 (CHS) sample before calcination.

4.3.2 BET Surface Area Measurements

The N_2 BET surface areas of various samples calcined at different temperatures are presented in Table 4.1. The 773 K calcined CHS sample exhibited a very high surface area of 168 $m^2\ g^{-1}$. With increase in calcination temperature from 773 to 1073 K, the specific surface area of the CHS sample showed a gradual decrease. However, even after calcination at 1073 K, a fairly high surface area of 116 $m^2\ g^{-1}$ was obtained. Retaining a high surface area even after calcination at 1073 K is a remarkable observation. It is also important that the surface area of the supported ceria-hafnia samples and their resistance against thermal sintering strongly depends on the synthetic methodology. The preparation method that was adopted in this study was found to be highly effective in stabilizing the surface area of the supported ceria-hafnia nanocomposite oxides.

Table 4.1: BET surface area, FWHM values, crystallite size and lattice parameter measurements of CeO_2–HfO_2/SiO_2 (CHS) samples calcined at different temperatures

Calcination Temp. (K)	S.A. ($m^2 g^{-1}$)	FWHM[a] ($2\theta^o$)	Crystallite Size[b] (nm)	Cell parameter (Å)
773	168	2.3	3.5	5.36
873	142	2.1	3.9	5.36
973	128	2.0	4.0	5.36
1073	116	1.9	4.3	5.35

[a] From most prominent XRD (111) peak;

[b] Crystallite size from Scherrer equation.

4.3.3 X-ray Diffraction Studies

The powder XRD patterns of the CHS samples calcined at different temperatures are presented in Figure 4.2. The broad nature of the peaks distinctly indicated the nanocrystalline nature of the samples in general. A cubic fluorite type phase with the composition $Ce_{0.8}Hf_{0.2}O_2$ (PDF-ICDD 04-006-1933) was identified from the diffraction patterns of the CHS samples calcined at different temperatures. As could be seen from Fig. 4.2, the CHS samples are indexed to (111), (200), (220), (311), (222), (400), (331), and (420) crystallographic faces of ceria-hafnia. With increasing calcination temperature, there is no appreciable change in the in the intensity of the lines without any distinct shift in the peak positions was observed. At lower calcination temperatures the crystallite size is usually small and the surface area is large (Table 4.1). Hence the surface energy makes a large contribution to the total energy of the system. As sintering proceeds and surface area decreases, the surface energy contribution becomes smaller. In this situation, the evolution of different phases leading to phase segregation is likely to occur [16]. The phase segregation phenomenon is considered to be surface energy driven and the solid solutions will be stable as long as the crystallite size does not exceed a critical size, above which the surface energy contribution to the total energy of the system becomes too small to allow its stabilization thereby leading to the phase segregation [16,17]. Very interestingly, no phase segregation is observed in the present investigation. The XRD investigation also provided an interesting information that there is no further compound formation between various component oxides (CeO_2, HfO_2, and SiO_2) of the sample such as $Ce_{9.33}(SiO_4)_6O_2$, and $CeSiO_4$ as reported in the literature [18,19]. This

could be attributed to various factors such as strong interaction between the cerium and hafnium oxides to form solid solutions, use of inert colloidal silica as the support, and lower calcination temperatures employed [16]. Within the detection limits of the XRD technique, there was no evidence about the presence of hafnia phases in either of the investigated systems. Additionally, the XRD features of silica were also not apparent, indicating amorphous nature of the support.

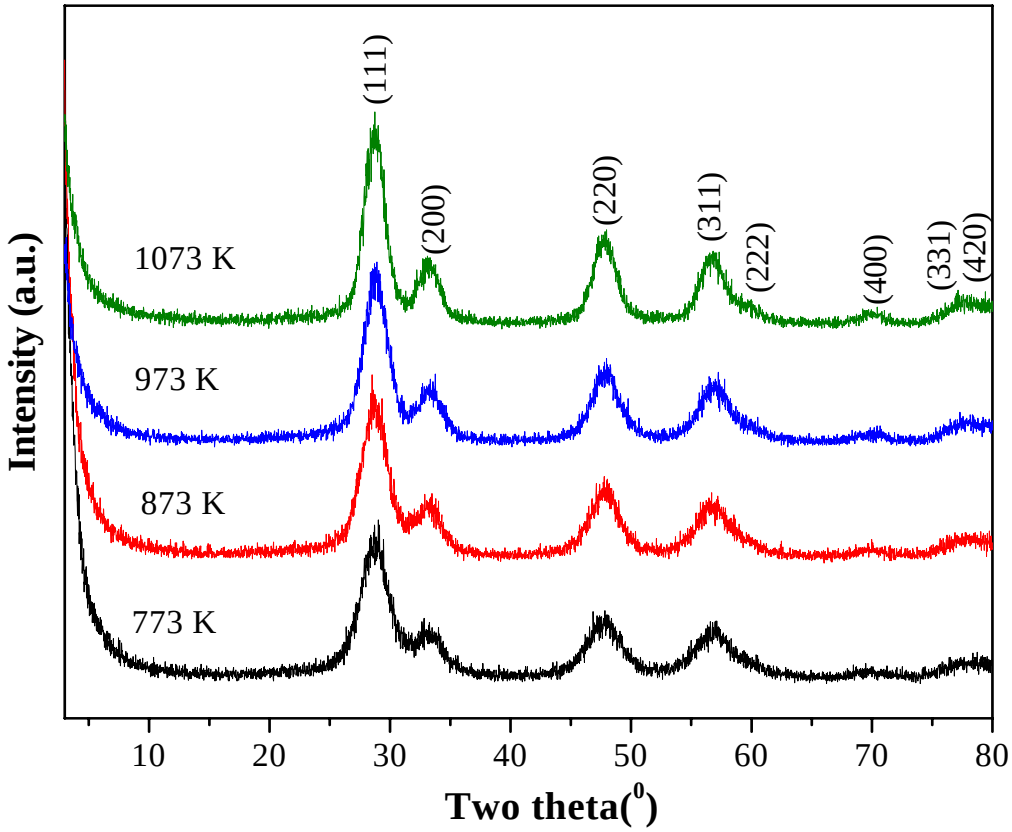

Figure 4.2: Powder XRD patterns of CeO_2–HfO_2/SiO_2 (CHS) samples calcined at different temperatures.

Using the most intense line (111) of the XRD patterns, calculation of 'a' cell parameters was carried out [20,21]. The evolved values of 'a' cell parameter for various samples as a function of calcination temperature are summarized in Table 4.1. As shown in the table, there was no apparent change in the cell 'a' parameter values after increasing calcination temperature, indicating the stable nature of the compound. However, the size of the unit cell decreases after incorporation of hafnium ions in to the ceria lattice in agreement with Vegard's law, which states that the lattice parameter of a solid solution is directly proportional to the atomic percent of the solute present [22–24]. Hafnium is

reported to have ionic radius of 0.78 Å for Hf^{4+} [25]. This implies that Hf^{4+} has a smaller ionic radius than Ce^{4+} (0.97 Å). This would result in a reduction and enhancement of the lattice parameter of the crystalline system when Ce^{4+} ions are substituted solely by Hf^{4+} ions. The calculated lattice parameter values reveal that Hf is present in only as Hf^{4+}.

The average crystallite sizes (D_{XRD}) of $Ce_{0.8}Hf_{0.2}O_2$ phases in various samples as a function of calcination temperature are also summarized in Table 4.1. It is apparent from the table that crystallization of ceria-hafnia solid solutions primarily depends on the nature of support and the calcination temperature. As a result, a meager increase in the crystallite size was observed with increasing calcination temperature. Due to the very broad nature of the XRD peaks, the crystallite size estimation, particularly for high temperature treated samples, are ambiguous. Because, if any new phase results in from phase segregation at higher temperature, there may be overlapping of diffraction peaks originated for different phases. Therefore, these values are not considered as absolute values for this type of samples and TEM-HREM techniques are used to get a clear picture.

4.3.4 Temperature Programmed Reduction Studies

TPR has been performed for the CHS samples calcined at 773 K using both H_2 and CO as reducing gas. Figure 4.3 shows the typical H_2-TPR profile of CHS sample calcined at 773 K. The quantification of H_2 consumption is estimated using CuO as the standard for TPR analysis. As could be seen in the TPR pattern, there is only one temperature maxima for the CHS sample. Earlier research has shown that the there is two peaks observed in the TPR patterns of some ceria-based catalysts and are assigned as, (i) the reduction of the most easily reducible surface oxygen of highly dispersed ceria species and (ii) the removal of oxygen from bulk ceria. In case of ceria-zirconia mixed oxides, however, only one broad peak is observed and many researchers suggest that surface and bulk reduction cannot be distinguished by the conventional TPR technique since both processes occur almost simultaneously during TPR measurement [26,27]. In line with earlier findings we also observed only one TPR peak for the sample. The reduction feature was started at ~650 K and centered ~864 K. Moreover, the reduction peak is too broad to distinguish two separate reduction features in the sample. However, in comparison to ceria-zirconia and ceria-hafnia, higher amount of H_2 consumption was

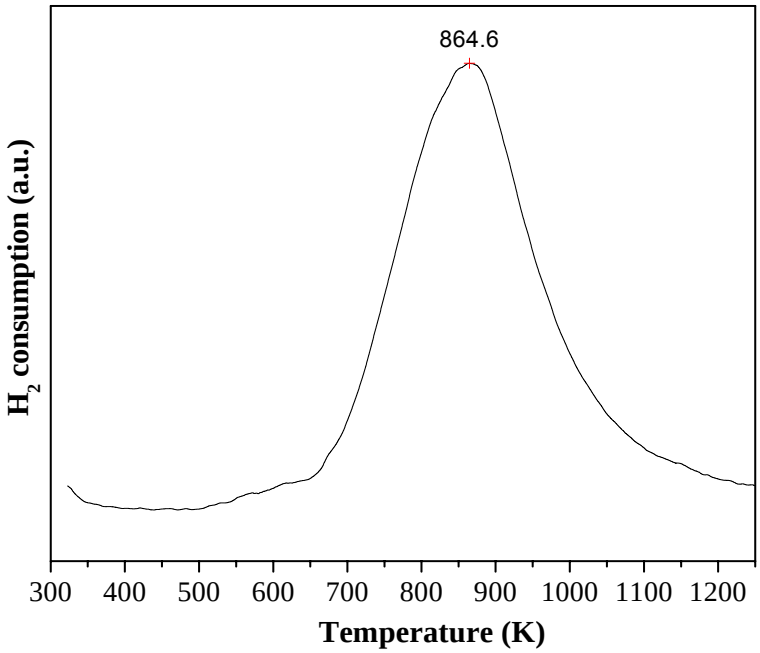

Figure 4.3: The H_2-TPR profile of CeO_2–HfO_2/SiO_2 (CHS) sample calcined at 773 K.

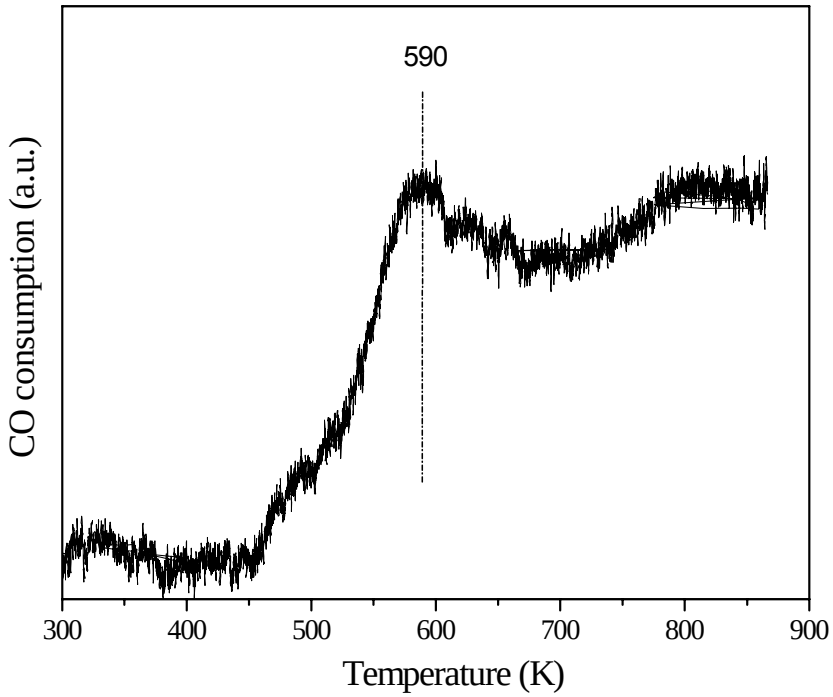

Figure 4.4: The CO-TPR profile of CeO_2–HfO_2/SiO_2 (CHS) sample calcined at 773 K.

observed as could be seen from the TPR profile. The H_2 consumption calculated from the peak area under the reduction peak over the complete temperature range for the CHS sample is 1329 μmol g^{-1} of the catalyst which is higher compared to ceria-zirconia and ceria-hafnia (Fig. 3.3, chapter 1). This shows that the degree of reduction of CeO_2-HfO_2 is enhanced to more extent after silica was used as support. Similarly, the CO-TPR profile of CHS sample calcined at 773 K also showed only one reduction peak. The CO-TPR profile (not to scale) of CHS sample calcined at 773 is shown in Figure 4.4, which reveal a broad reduction feature. However, there is a possibility of the overlapping of the two reduction peaks in the sample. In literature it has been reported that the reduction of ceria-based materials associated with a stepwise reduction with two peaks observed for some samples. The high temperature reduction feature is mainly due to bulk oxygen removal while the low temperature reduction feature has been related to most easily reducible surface capping oxygen of ceria [28]. But in the present case the sample showed only one TPR peak, from which we can not distinguish the stepwise reduction processes. However, the reduction feature is similar to the unsupported ceria-hafnia (Fig. 3.4, chapter 1). As could be seen from the Fig. 4.4, the temperature maxima for the CHS sample is centered around 590 K. The temperature range for the reduction of the sample is similar to that of unsupported ceria-hafnia. Though we have not quantified the amount of CO consumption in the sample, it could be observed that compared to ceria-hafnia, higher amount of CO was consumed by the CHS sample, which infers about the usefulness of silica as support.

4.3.5 Scanning Electron Microscopy Studies

SEM measurements were performed to assess the external morphologies of the mixed oxides. The micrographs corresponding to the CHS series of samples calcined at 773 and 1073 K, respectively are shown in Figure 4.5a,b. As observed from the SEM images, the samples consist of typical agglomerates of homogeneous morphology of nearly equal particle distribution within the narrow size range. The 773 K calcined samples exhibited more amorphous features and densely packed agglomerates of smaller crystallites. At higher calcination temperature (1073 K) the densely packed homogeneous structures have collapsed due to better crystallization of mixed oxide particles with the formation of bigger particles. Interestingly, both the samples exhibit amorphous features and densely packed agglomerates of crystallites.

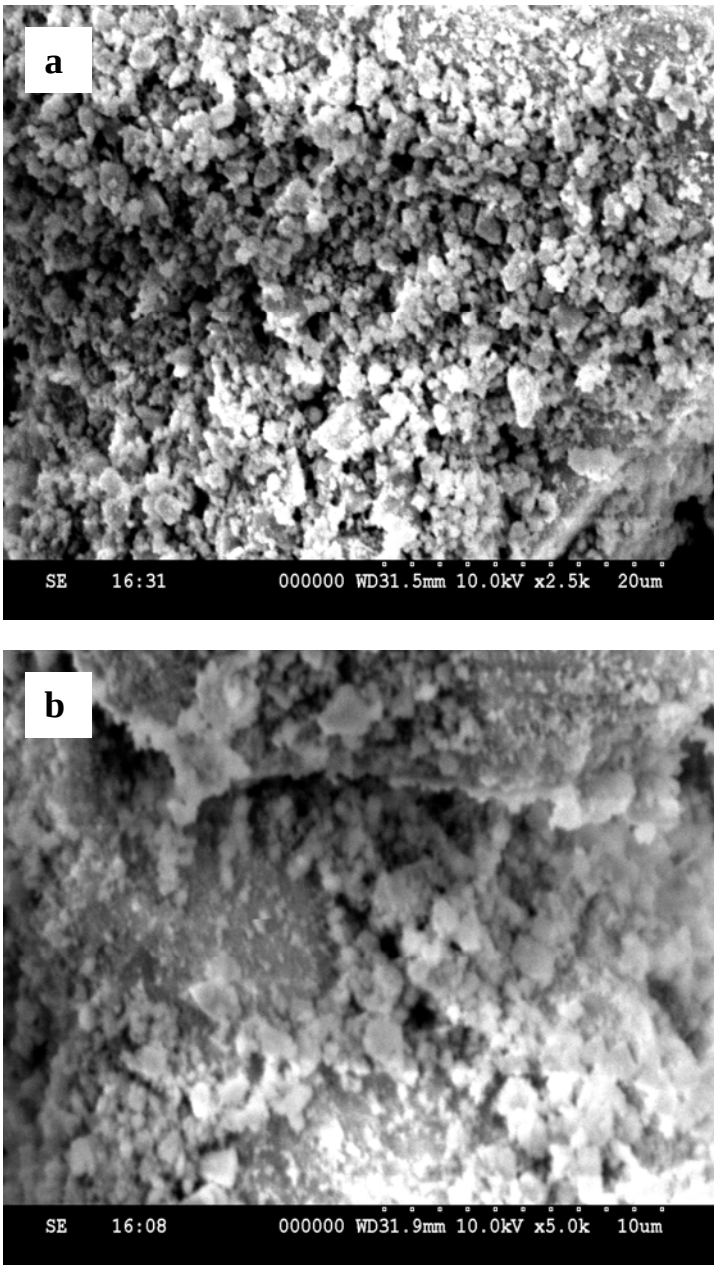

Figure 4.5: SEM micrographs of CeO_2–HfO_2/SiO_2 (CHS) samples calcined at (a) 773 and (b) 1073 K.

4.3.6 Transmission Electron Microscopy Studies

To investigate the structural aspects at atomic scale, the electron microscopic studies were performed, which on the other hand, can compliment the results obtained from XRD and SEM. Figure 4.6 represents the TEM global pictures of the CHS samples

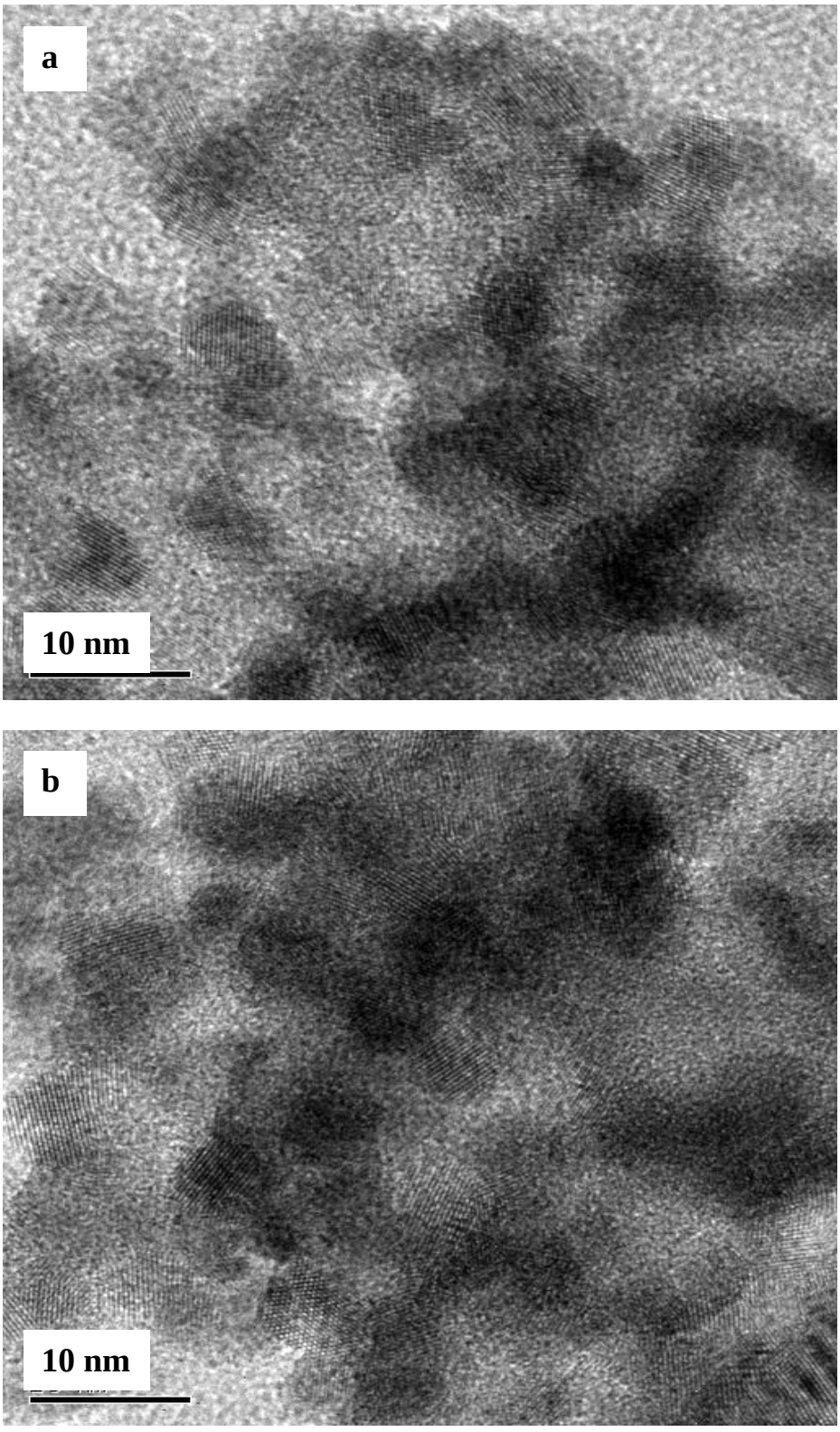

Figure 4.6: TEM global pictures of (a) 773 K and (b) 1073 K calcined CeO_2–HfO_2/SiO_2 (CHS) samples.

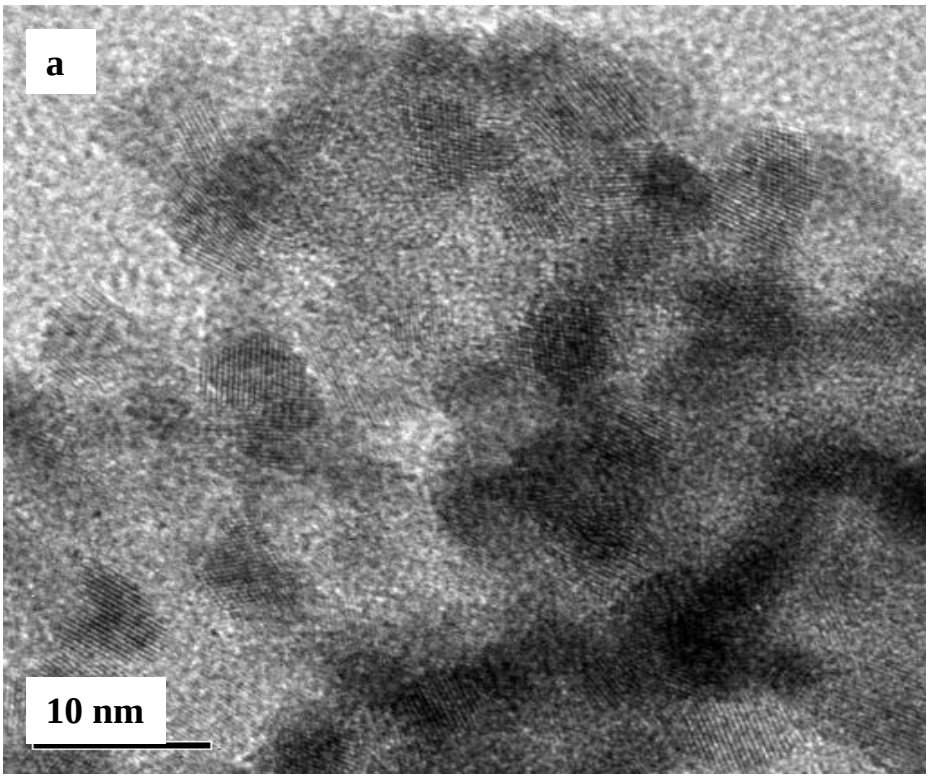

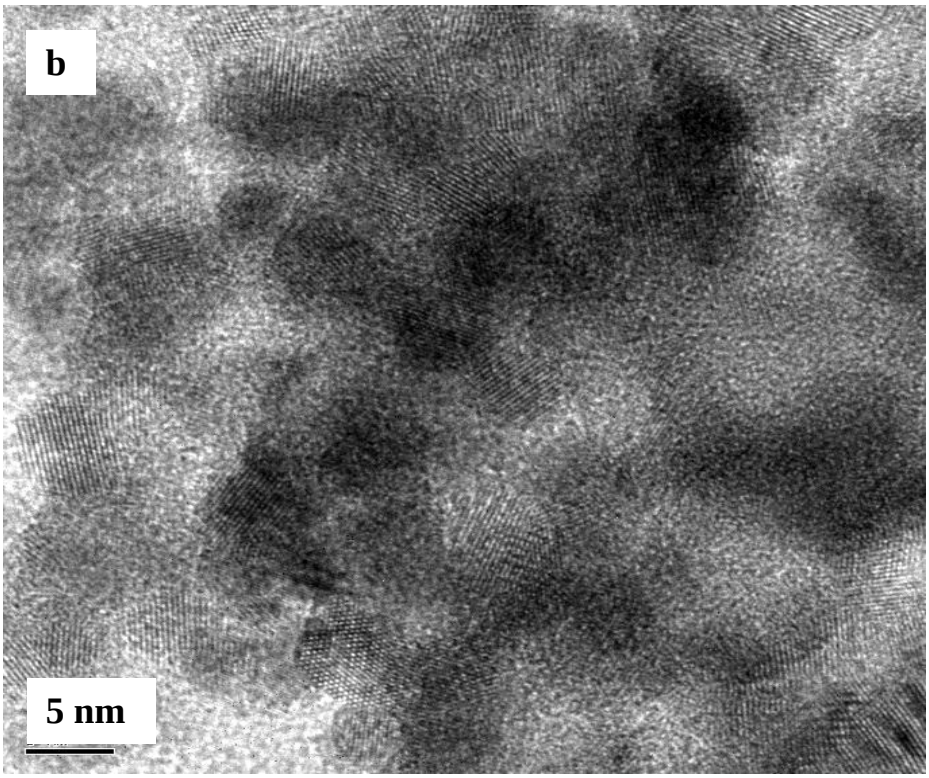

Figure 4.7: HREM images of (a) 773 K and (b) 1073 K calcined CeO_2–HfO_2/SiO_2 (CHS) samples.

calcined at 773 and 1073 K. To have better idea of the size and shape of the particles HREM analysis was carried out. Figure 4.7 shows the HREM images pertaining to CHS samples calcined at 773 and 1073 K. These images disclose the existence of small crystals (~3–4 nm) dispersed over an amorphous matrix. The obtained micrographs reveal agglomerated microstructures. Plain faces of crystallites in the figure are very rare, which suggests that a large part of the material is in amorphous state. The composite oxide samples showed a very nominal increase in particle size with temperature increase. As revealed by Figure 4.7, the particle sizes increase to ~5 nm after calcination at 1073 K. The shapes of the particles observed were almost similar to those usually seen in previous works for ceria or ceria–zirconia specimens [5].

4.3.7 UV-visible Diffuse Reflectance Spectroscopy Studies

UV-vis DRS measurement is a very interesting method to have information on surface coordination and different oxidation states of the metal ions by measuring d-d, f-d transitions and oxygen–metal ion charge transfer bands, despite difficulty in interpreting large bandwidths and specular reflectance often observed in the spectra [29].

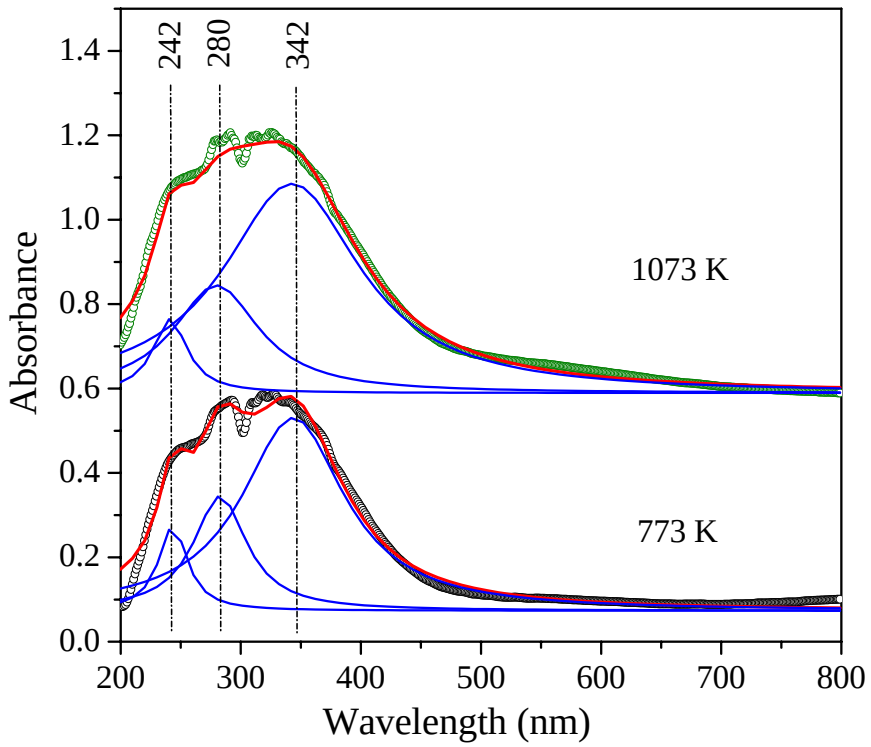

Figure 4.8: UV–vis DRS spectra of CeO_2–HfO_2/SiO_2 (CHS) samples calcined at different temperatures.

Nanocrystalline nature of ceria (< 5 nm), which can not be detected by XRD, could be identified with the help of this technique [30,31]. DR spectra for CHS sample calcined at 773 and 1073 K are shown in Figure 4.8. The band at ~280 nm can be ascribed to $Ce^{4+} \leftarrow O^{2-}$ charge transfer whereas the band at ~342 nm is pertaining to inter-band transitions [32]. The poorly resolved band maxima near ~242 nm correspond to $Ce^{3+} \leftarrow O^{2-}$ charge transfer transitions [30]. Importantly, the absorption edges are blue-shifted towards lower wavelengths in comparison to pure ceria [33]. The occurrence of the $Ce^{3+} \leftarrow O^{2-}$ transitions hints the oxygen vacancy defects generation. There is no evidence for the presence of other phases like HfO_2 or SiO_2 from this study in line with XRD results.

4.3.8 Raman Spectroscopy Studies

Raman spectroscopy has been extensively employed to discriminate between different structures on oxide surfaces. On the basis of the fact that the laser with shorter wavelength is closer to the electronic adsorption of samples, it is reported that the Raman information detected by excitation laser with shorter wavelength is more sensitive to the surface region of samples. We have used both UV excitation laser (He-Cd laser with

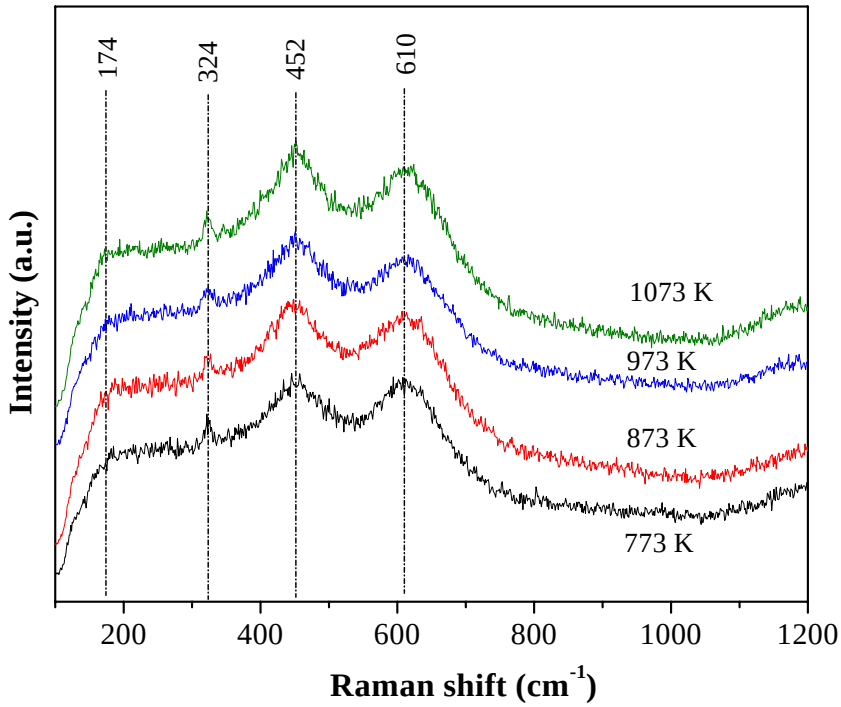

Figure 4.9: UV-Raman spectral patterns of CeO_2–HfO_2/SiO_2 (CHS) samples calcined at different temperatures.

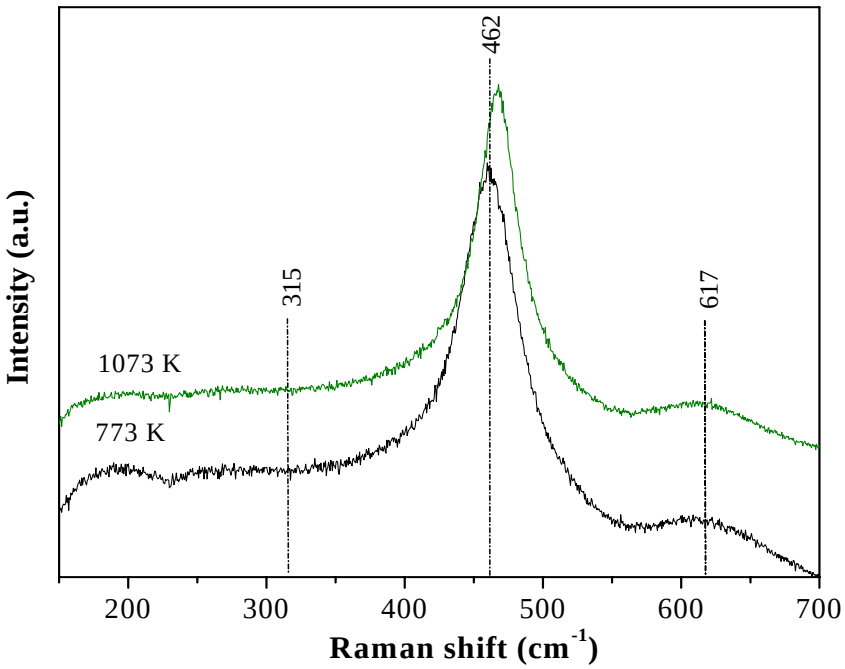

Figure 4.10: Visible-Raman spectral patterns of CeO_2–HfO_2/SiO_2 (CHS) samples calcined at 773 and 1073 K.

wavelength 325 nm) and visible excitation laser (Ar^+-Kr^+ laser with wavelength 514.53 nm) in the present investigation. The UV- and visible-Raman spectra of the CHS samples calcined at different temperatures are presented in Figures 4.9 and 4.10, respectively. Figure 4.9 shows the UV-Raman spectra of CHS samples calcined at different temperatures. For the space group *Fm*3*m*, the only Raman active mode (F_{2g}) is centered at around 460 cm^{-1} [34]. The UV–Raman spectrum of pure CeO_2 shows Raman active (F_{2g} mode) peak at 469 cm^{-1} [35]. Most probably, a small degree of hydration causes this band shift [36]. However, for CHS samples the F_{2g} band is blue-shifted. The peak observed at ~452 cm^{-1} in all CHS samples is consistent with the presence of a cubic $Ce_xHf_{1-x}O_2$ phase. The emergence of additional prominent bands at 324 and 610 cm^{-1} indicates some distortion of the oxygen sublattice. Another very weak peak observed at around 174 cm^{-1}. Interestingly, the intensity of the peak at ~610 cm^{-1} is comparable to the Raman active F_{2g} band. The nature of the patterns may be due to the resonance enhancement of the Raman scattering cross section under UV excitation [36]. No Raman lines due to hafnia or silica were observed corroborating with the XRD results. The band at ~452 cm^{-1} is due to symmetric O–Ce–O stretching mode [37]. As can be observed from

the figure, the relative intensity of the F_{2g} band increased with increasing calcination temperature due to better crystallization of ceria-hafnia solid solution at higher calcination temperatures. The broadness of Raman peaks is due to small particle size and the presence of SiO_2 support. It is known that the intensity of the Raman band depends on several factors including grain size and morphology [38]. It is also known from literature that sintering of sample under high temperature conditions leads to the formation of oxygen vacancies, which perturb the local M–O bond symmetry leading to relaxation of symmetry selection rules [34]. The presence of the strong prominent broad band at ~610 cm^{-1} was attributed to a non-degenerate Raman inactive longitudinal optical mode of ceria which arises due to relaxation of symmetry rules [34,39]. In particular, the substitution of hafnium into the ceria lattice with an increase in calcination temperature gives rise to oxygen vacancies, which are responsible for the emergence of this band [40]. The appearance of a weak band at ~324 cm^{-1} was accounted for the displacement of oxygen atoms from their normal lattice positions [37]. Interestingly, these bands gained intensity after calcination at 1073 K, indicating a high disorder of the oxygen sublattice in the fluorite structure. Silica did not exhibit any Raman features in line with the results reported in the literature [41]. This gave an impression that silica forms part of the substrate support on which ceria-hafnia solid solution is dispersed. The absence of any other Raman features provided one more inference that silica is not forming any compound with cerium and hafnium oxides.

The visible-Raman spectra of CHS samples calcined at 773 and 1073 K is shown in Figure 4.10. The Raman spectra of CHS samples reveal a weak band at ~315 cm^{-1} and a shoulder at ~617 cm^{-1}, in addition to the most intense peaks at 462 cm^{-1}. The most intense peak is due to F_{2g} vibration of the fluorite type lattice. Pure ceria exhibited prominent peaks at 462 and 464 cm^{-1} for 773 and 1073 K calcined samples, respectively, which are due to the F_{2g} mode of the cubic fluorite structure [42,43,44]. No other features existed in the spectra indicating no defects in the CeO_2 crystal lattice. The slight shift in the peak position at higher temperatures to higher wave number signifies changes in bond energies as a consequence of bond lengths as evidenced by lattice parameter estimations. Doping of lighter atom such as Hf subsequent contraction of the ceria unit cell may induce an increase in the F_{2g} band position. In line with XRD results, no Raman features pertaining to HfO_2 and SiO_2 were noted. As can be observed from Figure 4.10, the Raman spectra are broad, which could be attributed to the reduction of phonon lifetime in the nanocrystalline regime [39,45–47]. This observation also gives a clue for

predicting changes in the grain size and morphology of the prepared samples [38]. The broad band at ~617 cm^{-1} corresponds to the nondegenerate Longitudinal Optical (LO) mode of ceria, [34,38,39,45–47] arising due to relaxation of symmetry rules which is again linked to oxygen vacancies in the ceria lattice [16,25,40]. This is ascribed to a localized substitution defect vibration [37]. The weak bands observed at around 315 cm^{-1} could be attributed to displacement of oxygen atoms from their ideal fluorite lattice positions [48]. With increasing calcination temperature from 773 to 1073 K, the main Raman band is sharpened with a small shift. This is due to better crystallization of the samples at higher calcination temperatures in line with XRD results [23].

4.3.9 X-ray Photoelectron Spectroscopy Studies

The CHS samples calcined at different temperatures have been investigated with XPS technique. The photoelectron peaks of O 1s, Ce 3d, Hf 4f, Hf 4d, and Si 2p are depicted in Figures 4.11–4.15, respectively. The corresponding binding energy (eV) values and atomic ratios of Ce/Hf and Ce/Si are presented in Tables 4.2 and 4.3, respectively. The interactions in the nanostructured systems are quite complex and depend on a number of factors including synthetic methodology adopted.

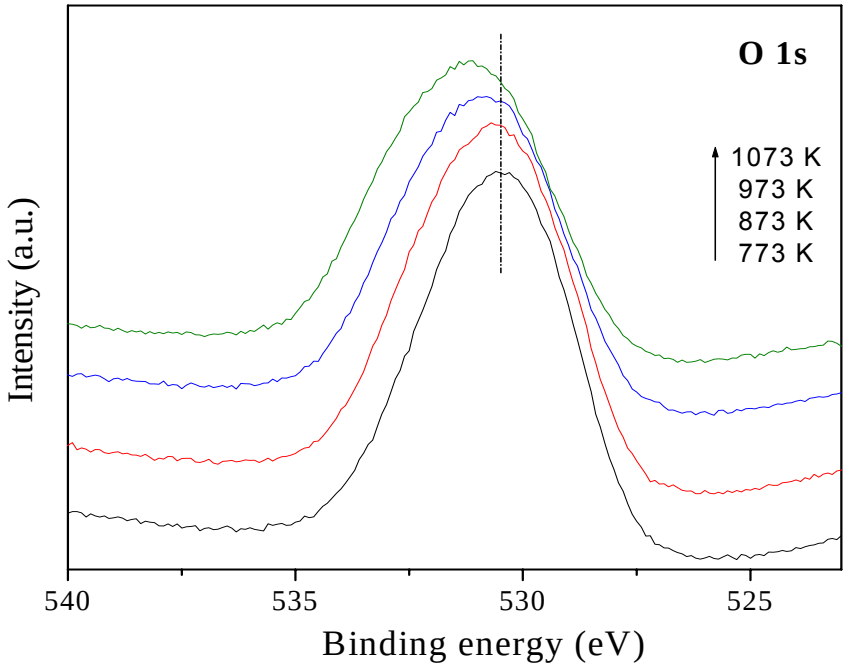

Figure 4.11: O 1s XP spectra of CeO_2–HfO_2/SiO_2 (CHS) samples calcined at different temperatures.

All figures and binding energy values provided in the table clearly indicated that the XPS bands and the corresponding binding energy values are highly sensitive to the calcination temperature and to the composition of the samples. The O 1s profiles as shown in Figure 4.11 are, in general, more complicated due to the overlapping contribution of oxygen from ceria, hafnia, and the supporting oxide silica. The binding energy of the most intense O 1s peak was observed at about 530.6 eV for 773 K calcined sample, which could be attributed to the O 1s ionization of oxygen associated with $Ce_{0.8}Hf_{0.2}O_2$ solid solution. The O 1s binding energy values shows that there is no apparent change with increasing calcination temperature. The profiles subjected to different thermal treatments also showed that with increasing the calcination temperature, the O 1s line becomes sharp. This is due to better crystallization of the composite oxides in higher calcination temperatures. From this it can be inferred that there is no compound formation between the component oxides after 773 K.

Figure 4.12 shows the Ce 3d spectra of CHS samples calcined at different temperatures. The complexity of the Ce 3d photoelectron spectra is well-known and can be rationalized in terms of hybridization between the partially occupied 4f levels of the Ce and 2p states of oxygen [30]. The Ce 3d spectra pertaining to various samples as presented in Figure 4.12 are analyzed by following the labeling previously used by Burroughs et al. [49]. The peaks labeled as 'v' correspond to Ce $3d_{5/2}$ contributions and those of labeled as 'u' represents the Ce $3d_{3/2}$ contributions. Specifically, the bands u_0 and u are due to Ce $3d_{3/2}$ ionization, and bands v_0 and v are for Ce $3d_{5/2}$ ionizations for Ce^{3+} and Ce^{4+}, respectively. The bands labeled as v', v'', and v''' are satellites arising from the $3d_{5/2}$ ionization, while the bands u', u'', and u''' represent Ce $3d_{3/2}$ ionization. As can be seen from the figure, very complicated Ce 3d spectra showed a typical peak shape indicating the presence of both Ce^{3+} and Ce^{4+} oxidation states. The u''' peak is the most convenient feature to follow the progressive Ce reduction, since it does not overlap with others. Particularly, a progressive reduction of Ce^{4+} into Ce^{3+} oxidation state results in a decrease in the intensity of the structures due to $4f^0$ (v''' and u'''), and an increase in v' and u' at the expense of v'' and u''. As the calcination temperature increases, the intensity of v, v'' and v''', u, u'' and u''' disappeared progressively. This observation indicated that there is an increase in the surface content of Ce^{3+}. There is a probability that the Ce^{3+} has been formed due to the reduction of Ce^{4+} under the conditions of ultra high vacuum during XPS measurements in conformity with the earlier reports in the literature [50,51].

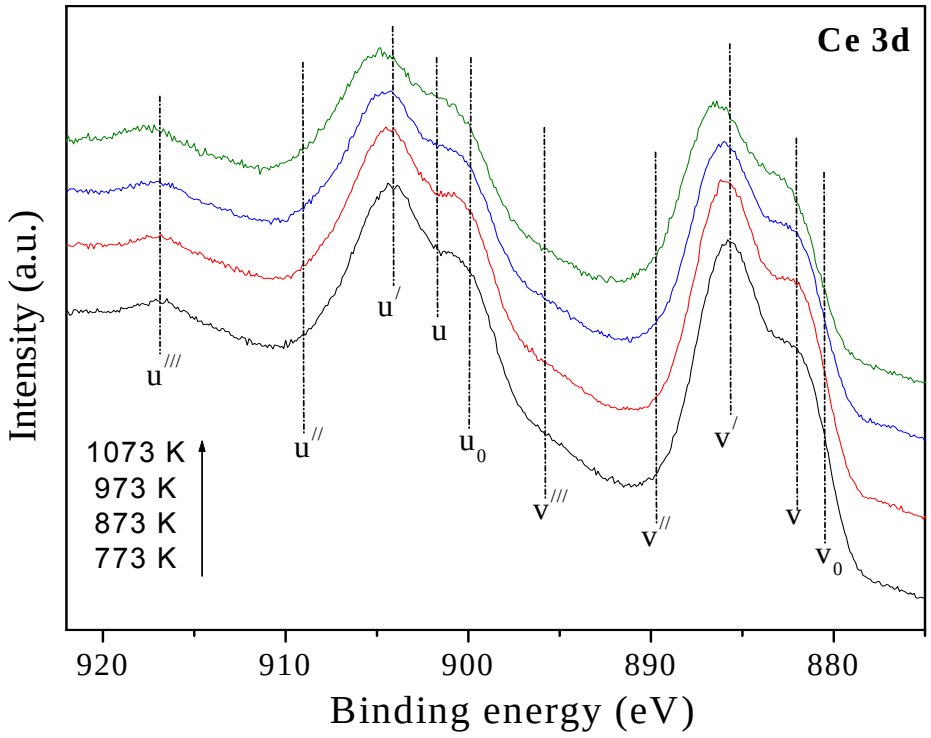

Figure 4.12: Ce 3d XP spectra of CeO_2–HfO_2/SiO_2 (CHS) samples calcined at different temperatures.

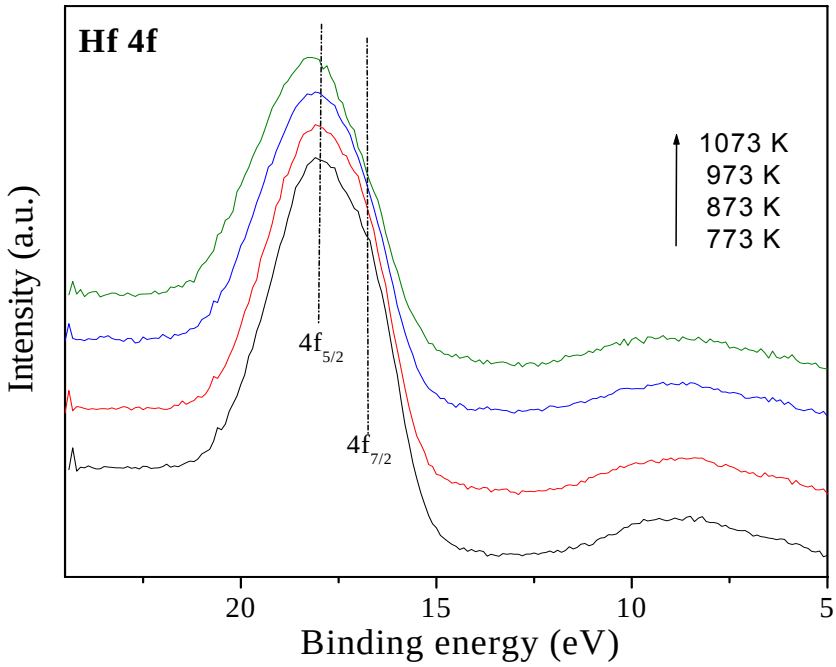

Figure 4.13: Hf 4f XP spectra of CeO_2–HfO_2/SiO_2 (CHS) samples calcined at different temperatures.

Figures 4.13 and 4.14 show the core level XP spectra of Hf 4f and Hf 4d, respectively corresponding to the CHS samples calcined at different temperatures. As could be observed from the XP spectra of Hf 4f (Fig. 4.13), there are two features at about 16.7 and 18.1 eV, respectively. It is reported that the Hf 4f spectrum consists of two components, the $4f_{7/2}$ part at 16.79 ± 0.08 eV and the $4f_{5/2}$ part at 18.54 ± 0.10 eV [52]. The peak positions of Hf 4f photoelectrons are known to be very sensitive to the binding states of the hafnium species [53,54]. According to a database, the metallic hafnium species reveals the Hf $4f_{7/2}$ peak at 14.3–14.4 eV, while HfO_2 shows it at 16.7 eV. Lee et al. investigated HfO_2 films on a silicon substrate by synchrotron XPS and found the binding energies of Hf $4f_{7/2}$ and Hf $4f_{5/2}$ at 17.55 and 19.26 eV, respectively [55]. However, the difference of about 1.4 eV in the binding energies between the Hf $4f_{7/2}$ and Hf $4f_{5/2}$ in the present investigation is in line with the reported values [53]. On the other hand, the XP spectra of Hf 4d photoelectron peak in relatively very scarce in the literature. As observed the spectra consists of two features in the binding energy values of ~224.2 and ~213.2 eV, respectively, which are in good agreement with the data presented in 'The Handbook of X-ray Photoelectron Spectroscopy' [53]. On the whole, from the XP spectra of Hf 4f and Hf 4d, it is observed that Hf is mainly in 4+ oxidation state.

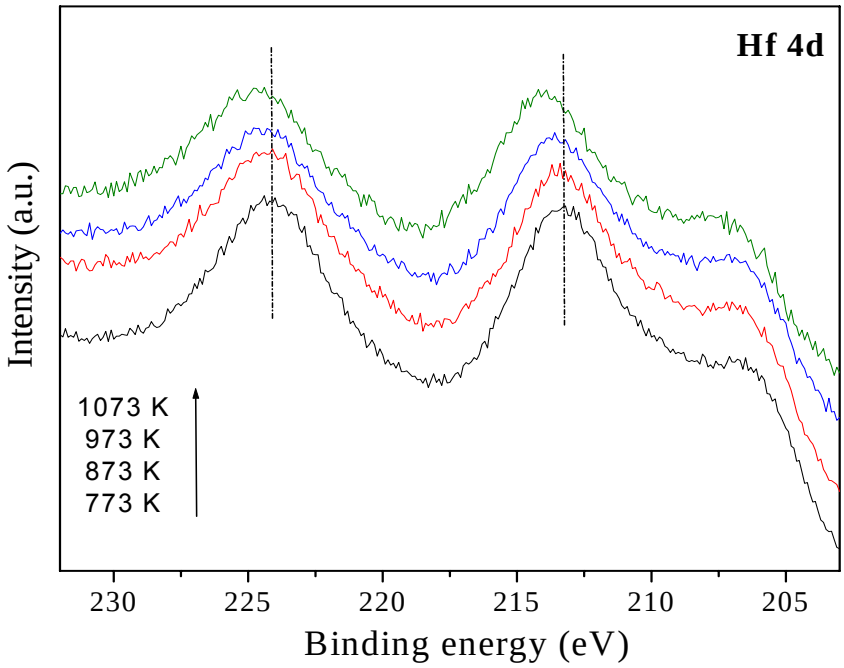

Figure 4.14: Hf 4d XP spectra of CeO_2–HfO_2/SiO_2 (CHS) samples calcined at different temperatures.

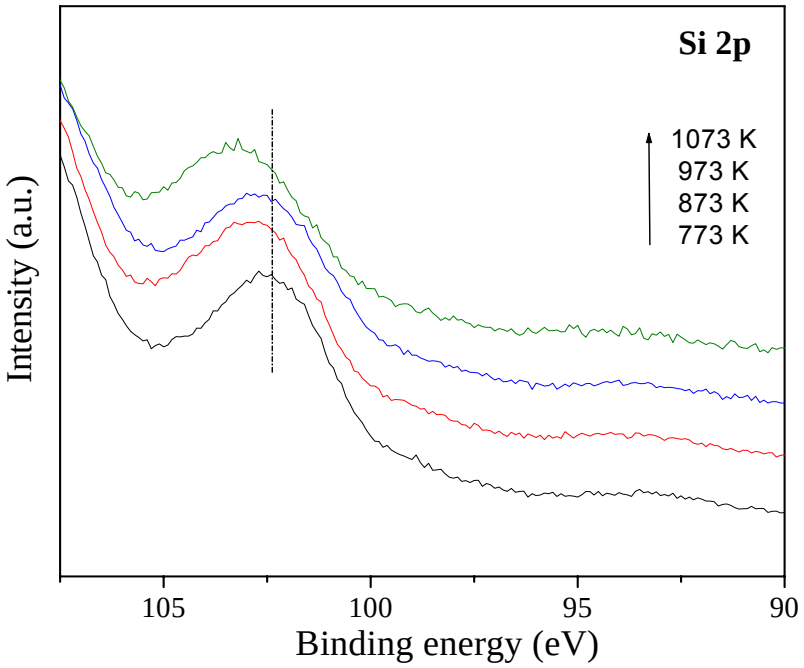

Figure 4.15: Si 2p XP spectra of CeO_2–HfO_2/SiO_2 (CHS) samples calcined at different temperatures.

Figure 4.15 shows the core level Si 2p XPS spectra pertaining to CHS samples calcined at different temperatures. The binding energy of the Si 2p photoelectron peaks for the samples agree well with the values reported in the literature [53,56]. However, the poor intensity of the spectra with large peak widths indicated that SiO_2 is not easily accessible at the surface due to the presence of Ce-Hf-oxide over-layers. The presence of oxidized silicon has been abundantly described in the literature, sometimes as CeO_{2-x}/SiO_2 [57,58] or as an amorphous silicate layer [59,60], where partial reduction of Ce^{4+} to Ce^{3+} occurs together with partial oxidation of Si. There is no formation of $CeSiO_4$ which could be identified by the Si 2p binding energy value of 101 eV [61].

Table 4.2: XPS core level electron binding energies (eV) of the CeO_2–HfO_2/SiO_2 (CHS) samples calcined at different temperatures

Calcination Temp. (K)	Binding Energy (eV)				
	O 1s	Ce 3d	Hf 4f	Hf 4d	Si 2p
773	530.6	882.0	18.1 (16.7)	224.3 (213.2)	102.7
873	530.7	882.0	18.1 (16.7)	224.2 (213.4)	102.8
973	530.8	882.1	18.1 (16.7)	224.4 (213.6)	103.0
1073	531.1	882.2	18.1 (16.7)	224.4 (214.2)	103.2

Table 4.3: XPS atomic ratio of the CeO_2–HfO_2/SiO_2 (CHS) samples calcined at different temperatures

Calcination Temperature (K)	Atomic Ratio	
	Ce/Hf	Ce/Si
773	4.84	0.484
873	4.84	0.461
973	4.39	0.444
1073	4.31	0.425

As presented in Table 4.3, the atomic ratios for Ce/Hf and Ce/Si did not change considerably when the temperature was increased from 773 to 1073 K. The meager decrease in the atomic ratios implies the lower amount of surface content of cerium in the samples at higher temperatures. However, the results distinctly show that there is no change of composition.

4.3.10 Ion Scattering Spectroscopy Studies

To examine the surface structure of the composite oxides, ISS measurements were carried out as ISS allows the analysis of the extreme periphery of the powder particles. The intensity (cps) versus kinetic energy (eV) plots of the CHS samples calcined at 773 and 1073 K after definite scans are presented in Figure 4.16a,b, respectively. The insets show the development of the intensity ratios between Hf and Ce in both the 773 and 1073 K calcined samples, respectively. The shifts of the signal positions in Figure 4.16a and, to a smaller extent in Figure 4.16b is due to instability of the kinetic energy scale, i.e. an instrumental problem encountered in heavy-ion ISS with the spectrometer used. It can be observed from Figure 4.16a that there is a linear increase in the Hf/Ce intensity ratio during the sputter series, i.e., the Ce is enriched at the external surface of the composite oxide. In the CHS sample calcined at 1073 K, a strong surface enrichment cannot be detected. There is a slight decrease of the Hf/Ce intensity ratio during the sputter series, but the trend is hardly significant given the rather large scatter of the experimental data. The slight surface enrichment of cerium in CHS sample calcined at 773 K, which is responsible for showing reducible property, is expected to facilitate easy reducibility of the composite oxide at lower temperatures. Accordingly, one can expect better activity for CHS sample calcined at 773 K compared to that of 1073 K calcined CHS sample.

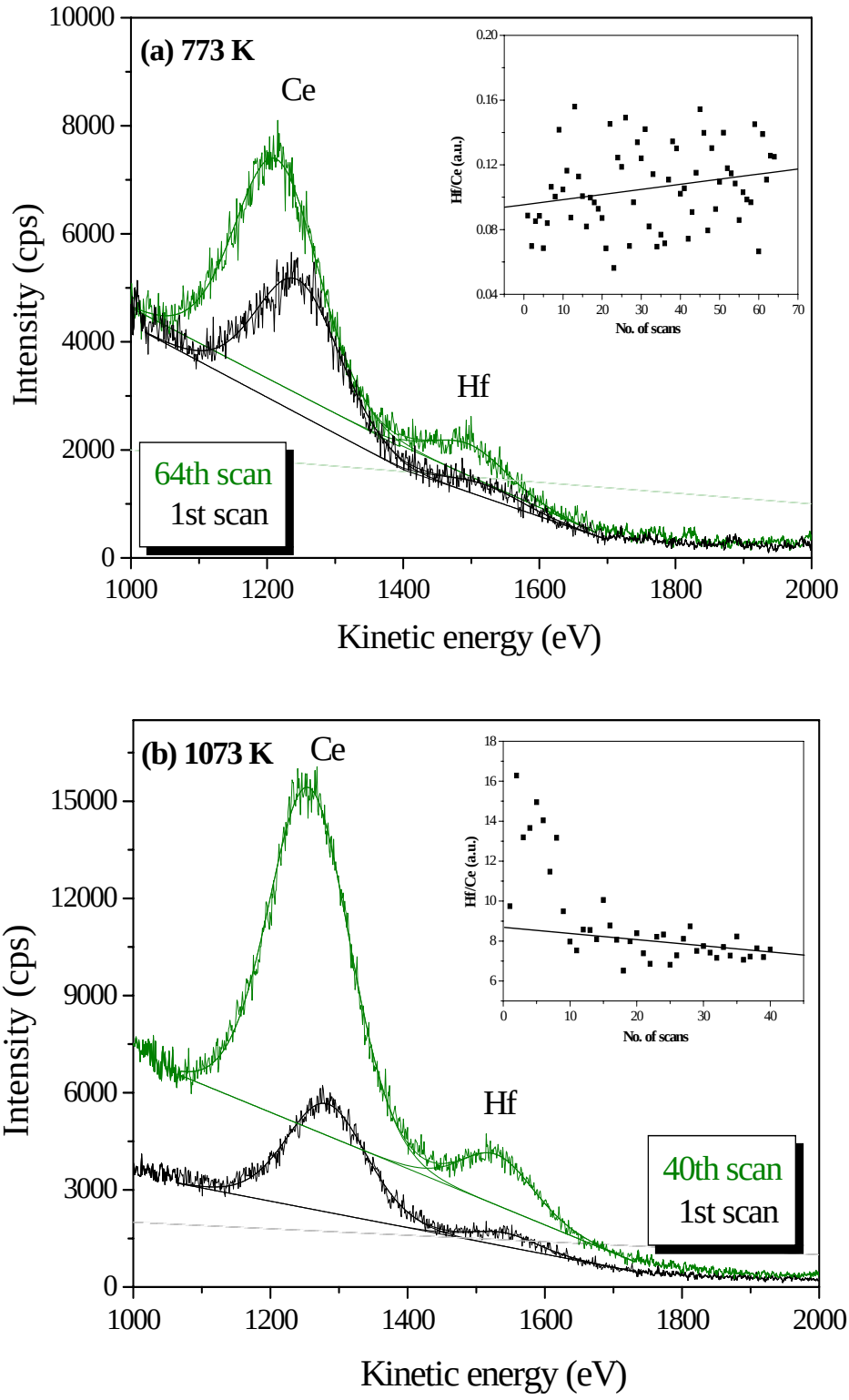

Figure 4.16: ISS spectra of CeO_2–HfO_2/SiO_2 (CHS) sample calcined at (a) 773 K and (b) 1073 K, after definite scans. Inset: plot of Hf/Ce intensity ratio.

4.4 Conclusions

Thermally stable, high surface area, nanostructured ceria-hafnia solid solutions over silica support could be synthesized by a soft chemical route adopting deposition coprecipitation method. The XRD measurements indicate the presence of only cubic $Ce_{0.8}Hf_{0.2}O_2$ phase up to the treatment temperature of 1073 K for the samples. This reveals that there is no more incorporation of hafnium into the ceria lattice at higher calcination temperature. There is no indication of compound formation between silica and cerium, and hafnium oxides. TEM-HREM results indicate a well-dispersed nanosized $Ce_xHf_{1-x}O_2$ (~3 nm) over the surface of amorphous silica. No significant increase in crystallite size is noted with increase of calcination temperature from 773 to 1073 K. This clearly establishes the significance of the support and the preparation method adopted. UV-vis DRS measurements gave information on different oxygen to metal charge transfer transitions. The lowering of symmetry and consequent strain development at the cerium sites is also revealed by UV-vis DRS measurements. In line with XRD results, Raman measurements show that silica is not forming any compound with cerium and hafnium oxides. Further, Raman studies suggest the generation of prominent lattice defects and thereby oxygen vacancy formation in ceria cubic lattice. XPS measurements indicate the presence of cerium in both 4+ and 3+ oxidation states. At high calcination temperature an increase in the surface content of Ce^{3+} is noted. ISS studies indicated surface enrichment of cerium in the case 773 K calcined CHS sample, which might be responsible for the observed better reducibility of this sample. Thus the use of various spectroscopic and non-spectroscopic techniques provided interesting information regarding the physicochemical characteristics of silica supported nanosized ceria-hafnia composite oxides.

4.5 References

[1] R. Zanella, A. Sandoval, P. Santiago, V. A. Basiuk, J.M. Saniger, J. Phys. Chem. B 110 (2006) 8559.

[2] A. Trovarelli, in: Catalysis by Ceria and Related Materials, G.J. Hutchings, Ed., Catalytic Science Series, Imperial College Press, London, 2002, Vol. 2.

[3] A. Trovarelli, Catal. Rev. Sci. Eng. 38 (1996) 439.

[4] M. Fernandez-Garcia, A. Martinez-Arias, J.C. Hanson, J.A. Rodriguez, Chem. Rev. 104 (2004) 4063.

[5] B.M. Reddy, P. Saikia, P. Bharali, Catal. Surv. Asia 12 (2008) 214.

[6] B.M. Reddy, P. Bharali, P. Saikia, A. Khan, S. Loridant, M. Muhler, W. Grünert, J. Phys. Chem. C 111 (2007) 1878.

[7] B.M. Reddy, P. Lakshmanan, P. Bharali, P. Saikia, G. Thrimurthulu, M. Muhler, W. Grünert, J. Phys. Chem. C 111 (2007) 10478.

[8] K. Klabunde, in: Nanoscale Materials in Chemistry, Wiley-Interscience, New York, 2001.

[9] M.M. Natile, G. Boccaletti, A. Glisenti, Chem. Mater. 17 (2005) 6272.

[10] B.M. Reddy, in: Metal Oxides: Chemistry and Applications, J.L.G. Fierro, Ed., CRC Press, Florida, 2006, Ch. 8, p. 215.

[11] A. Trovarelli, C. de Leitenburg, G. Dolcetti, Chem. Tech. 27 (1997) 32.

[12] Q. Fu, H. Saltsburg, M.F. Stephanopoulos, Science 301 (2003) 935.

[13] S. Park, J.M. Vohs, R.J. Gorte, Nature 404 (2000) 265.

[14] G.A. Deluga, S.R. Salge, L.D. Schmidt, X.E. Verykios, Science 303 (2004) 993.

[15] F. Deganello, A. Martorana, J. Solid State Chem. 163 (2002) 527.

[16] B.M. Reddy, P. Lakshmanan, A. Khan, S. Loridant, C.L. Cartes, T.C. Rojas, A. Fernández, J. Phys. Chem. B 109 (2005) 13545.

[17] K. Kenevey, F. Valdivieso, M. Soustelle, M. Pijolat, Appl. Catal. B: Environ. 2 (2001) 93.

[18] E. Rocchini, A. Trovarelli, J. Liorca, G.W. Graham, W.H. Weber, M. Maciejewski, A. Baiker, J. Catal. 194 (2000) 461.

[19] B. Kucharczyk, W. Tylus, L. Kepinski. Appl. Catal. B: Environ. 49 (2004) 27.

[20] C. Bozo, F. Gaillard, N. Guilhaume, Appl. Catal. A: Gen. 220 (2001) 69.

[21] G. Colon, M. Pijolat, F. Valdivieso, H. Vidal, J. Kaspar, E. Finocchio, M. Daturi, C. Binet, J.C. Lavalley, R.T. Baker, S. Bernal, J. Chem. Soc. Faraday Trans. 94 (1998) 3717.

[22] R.D. Shannon, Acta Crystallogr. A 32 (1976) 751.

[23] S. Meriani, G. Spinolo, Powder Diffract. 2 (1987) 255.

[24] B.D. Cullity, in: Elements of X-ray Diffraction, Addison-Wesley, Reading, MA, 1956.

[25] A.B. Hungria, A. Martinez-Arias, M. Fernandez-Garcia, A. Iglesius-Juez, A. G. Ruiz, J.J. Calvino, J.C. Conesa, J. Soria, Chem. Mater. 15 (2003) 4309.

[26] F. Fally, V. Perrichon, H. Vidal, J. Kaspar, G. Blanco, J.M. Pintado, S. Bernal, G. Colon, M. Daturi, J.C. Lavalley, Catal. Today 59 (2000) 373.

[27] P. Vidmar, J. Kaspar, P. Fornasiero, M. Graziani, J. Phys. Chem. B 102 (1998) 557.

[28] M. Boaro, M. Vicario, C. de Leitenburg, G. Dolcetti, A. Trovarelli, Catal. Today 77 (2003) 407.

[29] B.M. Weckhuysen, R.A. Schoonheydt, Catal. Today 49 (1999) 441.

[30] A. Bensalem, F.B. Verduraz, M. Delamar, G. Bugli, Appl. Catal. A: Gen. 121 (1995) 81.

[31] M.I. Zaki, G.A.M. Hussein, S.A.A. Mansour, H.M. Ismail, G.A.H. Mekhemer, Coll. Surf. A: Physico. Chem. Eng. Asp. 127 (1997) 47.

[32] A. Bensalem, J.C. Muller, F.B. Verduraz., J. Chem. Soc. Faraday Trans. 88 (1992) 153.

[33] B.M. Reddy, P. Bharali, G. Thrimurthulu, P. Saikia, L. Katta, S.-E. Park, Catal. Lett. 123 (2008) 327.

[34] X.-M. Lin, L.-P. Li, G.-S. Li, W.-H. Su. Mater. Chem. Phys. 69 (2001) 236.

[35] B.M. Reddy, P. Saikia, P. Bharali, Y. Yamada, T. Kobayashi, M. Muhler, W. Grünert J. Phys. Chem. C 112 (2008) 16393.

[36] Y.T. Chua, P.C. Stair, I.E. Wachs, J. Phys. Chem. B 105 (2001) 8600.

[37] M. Yashima, H. Arashi, M. Kakihana, M. Yoshimura, J. Am. Ceram. Soc. 77 (1994) 1067.

[38] J.E. Spanier, R.D. Robinson, F. Zhang, S.W. Chan, I.P. Herman, Phys. Rev. B 64 (2001) 245407.

[39] W.H. Weber, K.C. Hass, J.R. McBride, Phys. Rev. B. 48 (1993) 178.

[40] J.R. McBride, K.C. Hass, B.D. Poindexter, W.H. Weber, J. Appl. Phys. 76 (1994) 2435.

[41] I.E. Wachs, F.D. Hardcastle, S.S. Chan, Spectroscopy 1(1986) 30.

[42] B.M. Reddy, A. Khan, Catal. Surv. Asia 9 (2005) 155.

[43] A. Martinez-Arias, M. Fernandez-Garcia, L.N. Salamanca, R.X. Valenzuela, J.C. Conesa, J. Soria, J. Phys. Chem. B 104 (2000) 4038.

[44] J.Z. Shyu, W.H. Weber, H.S. Gandhi, J. Phys. Chem. 92 (1988) 4964.

[45] P. Parayanthal, F.H. Pollak, Phys. Rev. Lett. 52 (1984) 1822.

[46] H. Richter, Z.P. Wang, L. Ley, Solid State Commun. 39 (1981) 625.

[47] M. Fujii, S. Hayashi, K. Yamamoto, Appl. Phys. Lett. 57 (1990) 2692.

[48] V.S. Escribano, E.F. Lopez, M. Panizza, C. Resini, J.M.G. Amores, G. Busca, Solid State Sci. 5 (2003) 1369.

[49] A. Burroughs, A. Hamnett, A.F. Orchard, G. Thornton, J. Chem. Soc., Dalton Trans. 1 (1976) 1686.

[50] J.S. Albero, F.R. Reinoso, A.S. Escribano, J. Catal. 210 (2002) 127.

[51] M. Daturi, C. Binet, J. Lavalley, A. Galtayries, R. Sporken. Phys. Chem. Chem. Phys. 1 (1999) 5717.

[52] T. Brezesinski, B. Smarsly, K.-I. Iimura, D. Grosso, C. Boissiere, H. Amenitsch, M. Antonietti, C. Sanchez, Small 8−9 (2005) 889.

[53] C.D. Wagner, W.M. Riggs, L.E. Davis, J.F. Moulder, in: Handbook of X-ray Photoelectron Spectroscopy, G.E. Muilenberg, Ed., Perkin-Elmer Corporation, Eden Prairie, MN, 1978.

[54] V. Cosnier, M. Olivier, G. Theret, A. Andre, J. Vac. Sci. Technol. A 19 (2001) 2267.

[55] J.C. Lee, S.J. Oh, M. Cho, C.S. Hwang, R. Jung, Appl. Phys. Lett. 84 (2004) 1305.

[56] D. Briggs, M.P. Seah, in: Auger and X- ray Photoelectron Spectroscopy, Practical Surface Analysis, Wiley, New York, 1990, 2nd ed. Vol. 1.

[57] A. Galtayries, M. Crucifix, G. Blanchard, G. Terwagne, R. Sporken, Appl. Surf. Sci. 142 (1999) 159.

[58] H. Nagata, M. Yoshimoto, T. Tsukahara, S. Gonda, H. Koinuma, Mater. Res. Soc. Symp. Proc. 202 (1991) 445.

[59] T. Inoue, Y. Yamamoto, M. Satoh, A. Ide, S. Katsumata, Thin Solid Films 281 (1996) 24.

[60] F. Sanchez, M. Varela, C. Ferrater, M.V.G. Cuenca, R. Aguiar, J.L. Morenza, Appl. Surf. Sci. 70 (1993) 94.

[61] H. Behner, J. Wecker, T. Mathee, K. Samwer, Surf. Interf. Anal. 18 (1992) 685.

Chapter 5

This chapter presents the results and discussion pertaining to the structural characteristics of the nanosized composite oxides of CeO_2–HfO_2/TiO_2 system by various spectroscopic and non-spectroscopic techniques.

STUDIES on CeO_2–HfO_2/TiO_2 COMPOSITE OXIDE CATALYST

5.1 Introduction

Titania (TiO_2) has been widely studied because of its unique optical and chemical properties in catalysis, photocatalysis, sensitivity to humidity and gas, nonlinear optics, photoluminescence, and so on [1,2,3]. Titania, as a catalyst exhibits a number of attractive characteristics such as chemical stability, non-toxicity, low cost, and highest oxidation rate of many active metal oxides investigated. The unique physiochemical properties of TiO_2 also offer an exciting spectrum of applications having the additional advantage of being biocompatible, environmentally friendly, and readily available material [1,3–5]. Additionally, TiO_2 has also been used as an oxygen sensor to monitor automobile engine performance [3]. TiO_2 crystallizes as three different natural phases namely, orthorhombic brookite, tetragonal anatase, and tetragonal rutile [6]. Some properties of TiO_2 are very sensitive to its structure. Anatase phase is chemically and optically active making it suitable for catalysts and supports. Rutile phase is known to bear highest refractive index and UV-absorptivity for which it finds uses in paints, pigments and UV-absorbents [6]. For most commercial selective catalytic reduction (SCR) and selective oxidation applications, TiO_2 has been employed as the support on which the active chemical species including V_2O_5, WO_3, and MoO_3 were impregnated [7,8]. Since anatase is a metastable TiO_2 polymorph, it tends to transform into rutile phase decreasing its surface area thereby inducing a loss of catalytic activity [7]. The anatase to rutile transformation has been reported to be a major cause of deactivation in TiO_2-based catalysts [9]. Recently, TiO_2 in combination with ceria-zirconia has been tested for oxygen sensing applications [10]. Unlike conventional oxygen sensors used in monitoring exhaust gas emissions, in which one side of the sensor must be directly exposed to the air reference, the new sensor employs a ternary mixed oxide of CeO_2–ZrO_2–TiO_2 (CZT) as the reference. The sensor consists of yttria-stabilized zirconia (YSZ) electrolyte and CZT reference layers with platinum coating as electrodes. The response of the sensor was investigated and an interesting behavior was noticed not observed in air-referenced structures. Furthermore, recent investigations reveal that the reducibility of pure ceria can be enhanced due to the presence of Ti^{4+} ions [11].

It is a well-known support material in various commercial processes. For instance, V_2O_5/TiO_2 is the basic component of industrial catalysts for SCR of nitrogen oxides,

selective oxidation of various hydrocarbons, and ammoxidation of N-heteroaromatic compounds [12–15]. Ceria-titania compositions find applications in low temperature CO oxidation [16], coating for electrochromic devices [17,18], and adsorbents for fuel cell applications [19]. Motivated by the favorable characteristics of both ceria-based composite oxide and TiO_2, and to overcome the disadvantages associated with unsupported ceria-hafnia composite oxide solid solutions, preparation and intensive characterization of CeO_2-HfO_2/TiO_2 was undertaken in the present investigation.

5.2 Experimental

Titania supported ceria-hafnia sample (CHT; 8:2:10 mole ratio based on oxides) was prepared by adopting a deposition coprecipitation method as per the procedure described in Chapter 2. The obtained catalysts were subjected to thermal treatments from 773 to 1073 K in order to understand the thermal stability, and the physicochemical properties of these materials. These effects have been investigated by means of TG-DTA, BET SA, XRD, TPR, SEM, TEM, UV-vis DRS, LRS, XPS and other techniques.

5.3 Results and Discussion

5.3.1 Thermal Analysis

The TG/DTA analysis of the TiO_2-supported $Ce_xHf_{1-x}O_2$ (CHT) sample before calcination was performed to gain some evidences about the role of TiO_2 in retarding the decomposition and sintering behavior of $Ce_xHf_{1-x}O_2$. As presented in Figure 5.1, the sample exhibited one major and two minor weight loss peaks. The major low temperature peak in the range 309–473 K is primarily due to the loss of nondissociative adsorbed water as well as water held on the surface by hydrogen bonding. The minor weight loss peaks at high temperatures are due to loss of water held in the micropores of the gels and dehydroxylation of the surface, respectively. It is observed that the weight loss from ambient to 840 K is about 7.4%. However, the weight loss between 840 and 1273 K is only about 0.8%. It indicates that over the temperature range between 840 and 1273 K, the CHT composite oxide sample is thermally quite stable in terms of phases and chemical composition.

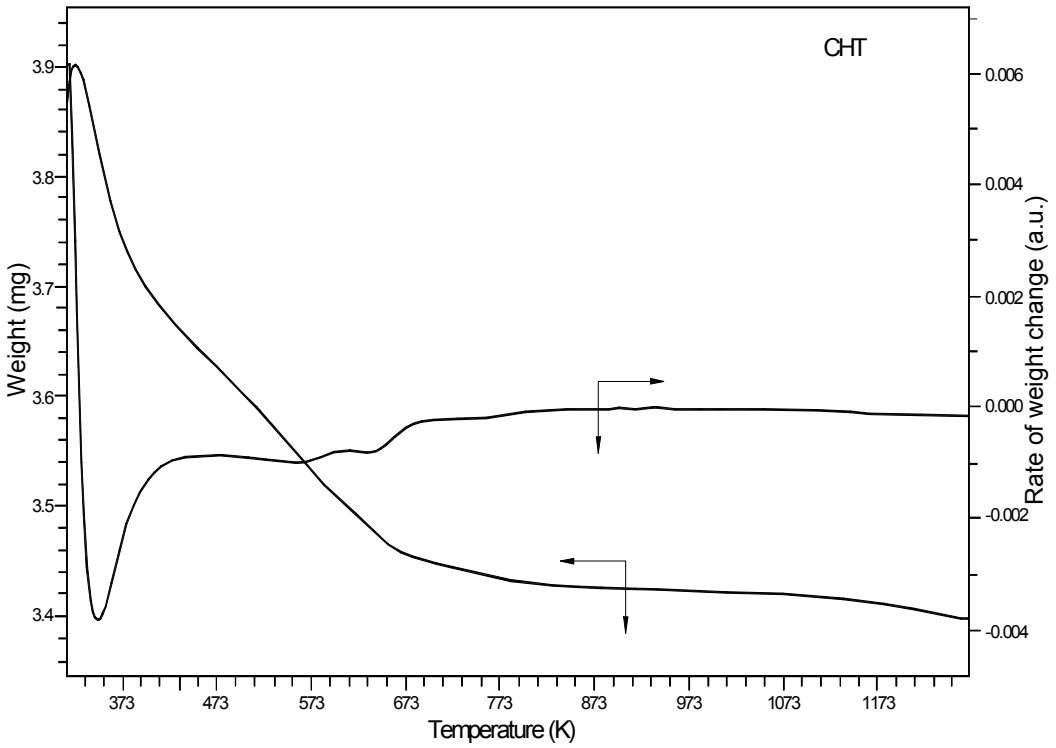

Figure 5.1: TGA profile of CeO_2–HfO_2/TiO_2 (CHT) sample before calcination.

Table 5.1: BET surface area, FWHM values, crystallite size and lattice parameter measurements of CeO_2–HfO_2/TiO_2 (CHT) samples calcined at different temperatures

Calcination Temp. (K)	S.A. ($m^2 g^{-1}$)	FWHM[a] (2θ °)		Crystallite Size[b] (nm)		Cell parameter (Å)
		CH	TiO_2-anatase	CH	TiO_2-anatase	
773	112	1.48	0.41	5.55	20.31	5.36
873	97	1.28	0.41	6.42	20.31	5.36
973	78	1.23	0.40	6.68	20.84	5.36
1073	48	0.52	0.29	16.0	29.38	5.35

[a] From most prominent XRD (111) peak of ceria-hafnia and (101) peak of TiO_2-anatase

[b] Crystallite size from Scherrer equation.

5.3.2 BET Surface Area Measurements

The N_2 BET surface areas of CHT samples calcined at 773 to 1073 K are presented in Table 5.1. All the samples exhibit reasonably high specific surface areas. It is clear from the table that dispersion of CH on TiO_2 support enhances the surface area of

CH. The CH bears a surface area of 78 $m^2 g^{-1}$ at 773 K, which decreases to 26 $m^2 g^{-1}$ when the treatment temperature is increased to 1073 K. On the contrary, 773 and 1073 K calcined CHT samples exhibit surface areas of 112 $m^2 g^{-1}$ and 48 $m^2 g^{-1}$, respectively. In general, the decrease in the surface area at higher temperatures is a normal phenomenon due to sintering of the samples. It is well-known that for certain technological applications, materials with high specific surface area are essential. As observed, TiO_2 supported CH composite oxides retained high surface area even after thermal treatment at 1073 K in comparison to unsupported one.

5.3.3 X-ray Diffraction Studies

The XRD patterns of CHT samples calcined at 773 to 1073 K are presented in Figure 5.2. As can be noted from the figure, the samples are poorly crystalline and broad diffraction lines corresponding to $Ce_{0.8}Hf_{0.2}O_2$ (PDF-ICDD 04-006-1933) solid solutions along with distinct peaks due to TiO_2-anatase phase could be observed. The broad nature of the peaks pertaining to ceria-hafnia solid solutions does not allow us to predict about the phase segregation phenomenon, if happens, within the studied temperature range. The Ce-Hf composite oxide planes could be indexed to (111), (200), (220), (311), (222), (400), (331), and (420) crystallographic faces as depicted in the figure. Literature reveals that under certain circumstances, ceria-titania solid solution formation is also quite possible [20,21]. However, the methods adopted for preparation of Ce-Ti solid solution are either sol-gel or solution combustion method [20,21]. Reddy et al. reported that there is no solid solution formation between ceria and titania in case of ceria-titania and ceria-zirconia/titania systems when prepared via coprecipitation or deposition coprecipitation methods [22,23]. The intensity of the XRD peaks get sharpened as the calcination temperature was increased. As reported by Preuss and Gruehn, formation of different Ce-Ti-O phases namely Ce_2TiO_5, $Ce_2Ti_2O_7$, and $Ce_4Ti_9O_{24}$ are possible at 1523 K [24]. But there is no such phases could be observed, which may be due to the different preparation method adopted or lower calcination temperature employed in the present investigation. It should be noted that there is no anatase to rutile phase transformation in the present study. It is known that the transformation of TiO_2-anatase to rutile is thermodynamically feasible beyond 873 K in impurity free TiO_2 samples [2,14]. However, there is no evidence regarding the formation of rutile phase even up to 1073 K in this case. The anatase to rutile phase transformation is inhibited in the CHT system due to the stabilization of

anatase by the surrounding cerium/hafnium ions as envisaged for TiO_2–SiO_2 and other mixed oxides in the literature [25,26]. This is an interesting observation from catalytic standpoint.

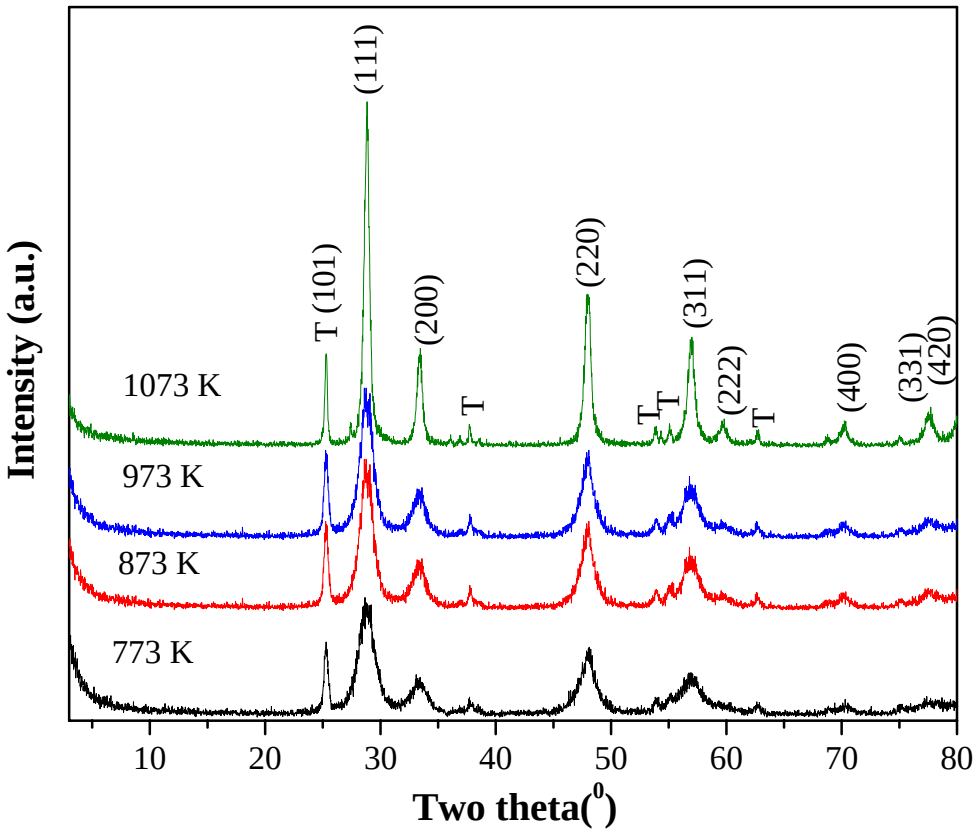

Figure 5.2: Powder XRD patterns of CeO_2–HfO_2/TiO_2 (CHT) samples calcined at different temperatures. Peak legend 'T' corresponds to TiO_2-anatase.

Using the most intense line (111) of the $Ce_{0.8}Hf_{0.2}O_2$ pattern, cubic indexation and calculation of cell parameters have been carried out. The calculated 'a' cell parameter values as presented in Table 5.1, for the CHT composite oxides reveals incorporation of hafnium cation into the ceria lattice as the cell dimensions are lower than pure ceria (unit cell constant a = 5.410 Å). Hf^{4+} has an ionic radius lower than that of Ce^{4+} (the ionic radii values for Ce^{4+} and Hf^{4+} are 0.97 and 0.78 Å, respectively) [27,28]. Interestingly, the lattice parameters of the titania supported CH composite oxides are slightly larger than that of the unsupported CH composite oxides. However, the lattice cell parameter values for the composite oxides (both supported and unsupported) are smaller than ceria. This observation opens up another possibility of incorporation of Ti^{4+} cations with cationic

radius of 0.64 Å in to the ceria lattice other than Hf^{4+}. The cell parameter values change negligibly with temperature (Table 5.1) showing comparatively small value in case of 1073 K calcined sample. So there is a possibility that the amount of Hf^{4+} is slightly high in this sample. There is also a possibility that all hafnia may not be fully incorporated in the process of composite oxide formation. However, from XRD results the presence of segregated hafnia in crystalline form could not be observed. But we cannot rule out the possibility of the presence of hafnia in amorphous state. As shown, the crystallization of $Ce_xHf_{1-x}O_2$ solid solution primarily depends on the calcination temperature as well as on the presence of TiO_2-anatase.

The broadened XRD line shapes indicate the presence of very small particles of nanometer size. The average crystallite sizes of the Ce–Hf composite oxides and TiO_2-anatase phase calculated using Scherrer equation are presented in Table 5.1. For 773 K calcined Ce–Hf composite oxide sample the crystallize size was found to be ~5.5 nm which is gradually increased to ~16 nm after heat treatment at 1073 K. Gradual sharpening of the XRD peaks with increasing calcination temperature could be noted as a result of sintering. With corresponding increase in crystallite size, decrease in specific surface area after calcination at 873–1073 K is also clearly observed (Table 5.1). It is expected that TiO_2 support stabilizes the Ce-Hf-oxide nanoparticles over its surface and inhibits the coagulation or grain growth (sintering) of the particles to an extent.

5.3.4 Temperature Programmed Reduction Studies

TPR has been performed for the CHT samples using both H_2 and CO as reducing gas. Figure 5.3 shows the typical H_2-TPR profile of CHT sample calcined at 773 K. The quantification of H_2 consumption is estimated using CuO as the standard for TPR analysis. As could be seen in the TPR pattern, there is only one temperature maxima with a shoulder for the CHT sample. Earlier research has shown that the there is two peaks observed in the TPR patterns of some ceria-based catalysts and are assigned as, (i) the reduction of the most easily reducible surface oxygen of highly dispersed ceria species and (ii) the removal of oxygen from bulk ceria. In case of ceria-zirconia mixed oxides, however, only one broad peak is observed and many researchers suggest that surface and bulk reduction cannot be distinguished by the conventional TPR technique since both processes occur almost simultaneously during TPR measurement [29,30]. In line with earlier findings we also observed only one TPR peak with a broad shoulder for the

sample. The reduction feature was started at ~650 K and centered ~830 K with the shoulder peak at around 700 K. However, in comparison to ceria-zirconia and ceria-hafnia, higher amount of H_2 consumption was observed as could be seen from the TPR profile. The H_2 consumption calculated from the peak area under the reduction peak over the complete temperature range for the CHT sample is 723 μmol g^{-1} of the catalyst which is higher compared to ceria-zirconia and ceria-hafnia (Fig. 3.3, chapter 1). This shows that the degree of reduction of CeO_2-HfO_2 is enhanced to more extent after TiO_2 was used as support.

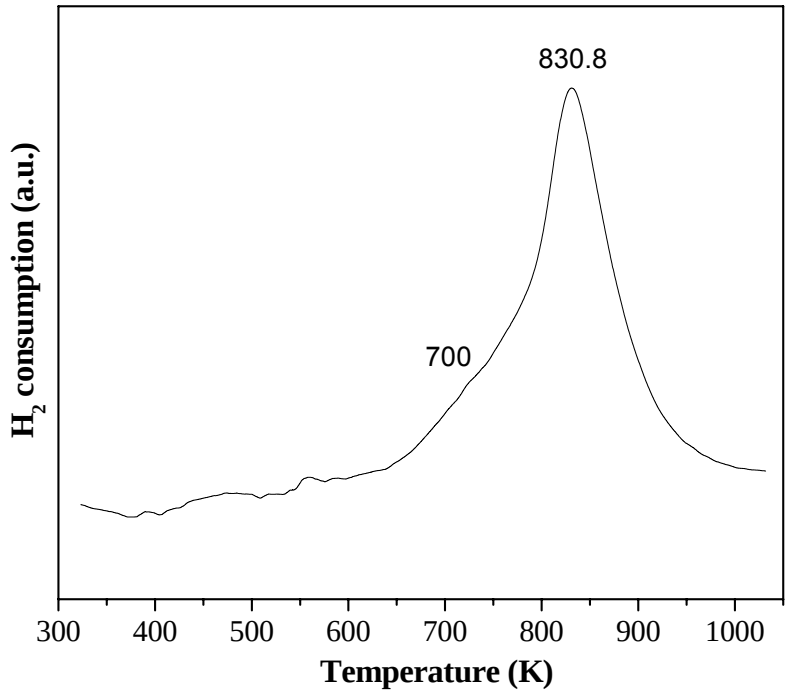

Figure 5.3: The H_2-TPR profile of CeO_2–HfO_2/TiO_2 (CHT) sample calcined at 773 K.

The CO-TPR profiles (not to scale) of CHT sample calcined at 773 and 1073 K are shown in Figure 5.4, which reveal two broad reduction features. In literature it has been reported that the reduction of ceria-based materials associated with a stepwise reduction with two peaks observed for some samples. The high temperature reduction feature is mainly due to bulk oxygen removal while the low temperature reduction feature has been related to most easily reducible surface capping oxygen of ceria [31]. The reduction features are similar to that of unsupported ceria-hafnia (Fig. 3.4, chapter 1). As could be seen from the Fig. 5.4, the temperature maxima for the CHT samples (calcined

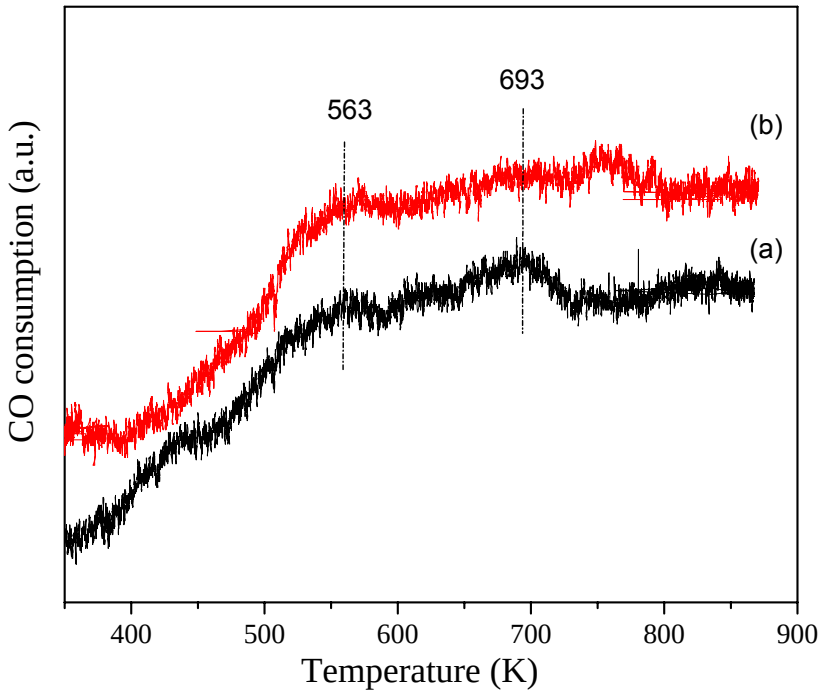

Figure 5.4: The CO-TPR profile of CeO_2–HfO_2/TiO_2 (CHT) sample calcined at (a) 773 and (b) 1073 K.

at 773 and 1073 K) are centered around 560 and 690 K. The temperature range for the reduction of the sample is similar to that of unsupported ceria-hafnia. Though we have not quantified the amount of CO consumption in the sample, it could be observed that compared to ceria-hafnia, higher amount of CO was consumed by the CHT sample, which infers about the usefulness of TiO_2 as support.

5.3.5 Scanning Electron Microscopy Studies

SEM measurements were performed to assess the external morphologies of the composite oxides. The micrographs corresponding to the CHT series of samples calcined at 773 and 1073 K, respectively are shown in Figure 5.5a,b. As observed from the SEM images, the samples consist of typical agglomerates of homogeneous morphology of nearly equal particle distribution within the narrow size range. The 773 K calcined samples exhibited more amorphous features and densely packed agglomerates of smaller crystallites. At higher calcination temperature (1073 K) the densely packed homogeneous structures have collapsed due to better crystallization of composite oxide particles with the

formation of bigger composite oxides particles. Interestingly, it could be observed from the SEM images that there are different smaller crystallites over bigger particles. It is due to the formation of composite oxides of ceria-hafnia over bigger crystals of TiO_2. However, the exact growth of different particles could not be confirmed from SEM analysis, so TEM-HREM analysis has been performed and described in the next subheadings.

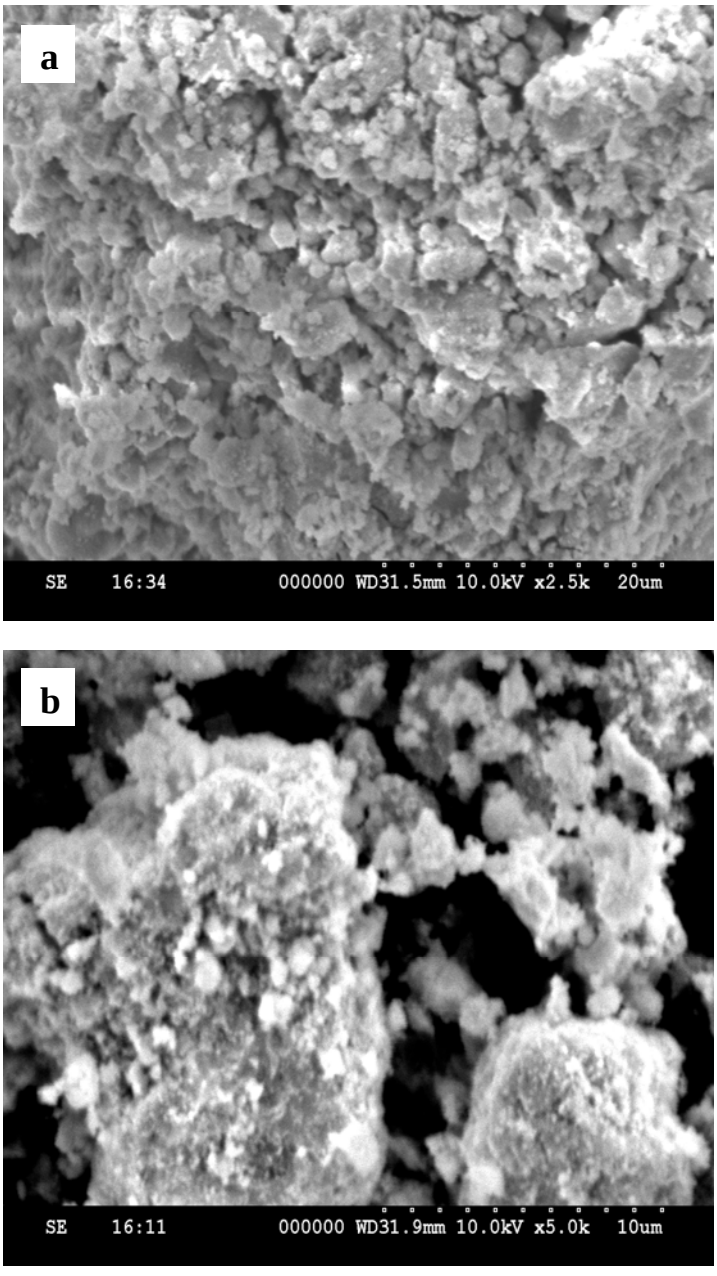

Figure 5.5: SEM micrographs of CeO_2–HfO_2/TiO_2 (CHT) samples calcined at (a) 773 and (b) 1073 K.

5.3.6 Transmission Electron Microscopy Studies

The TEM-HREM measurements were performed to ascertain the crystallite growth and morphology of ceria-hafnia composite oxides over the surface of titania.

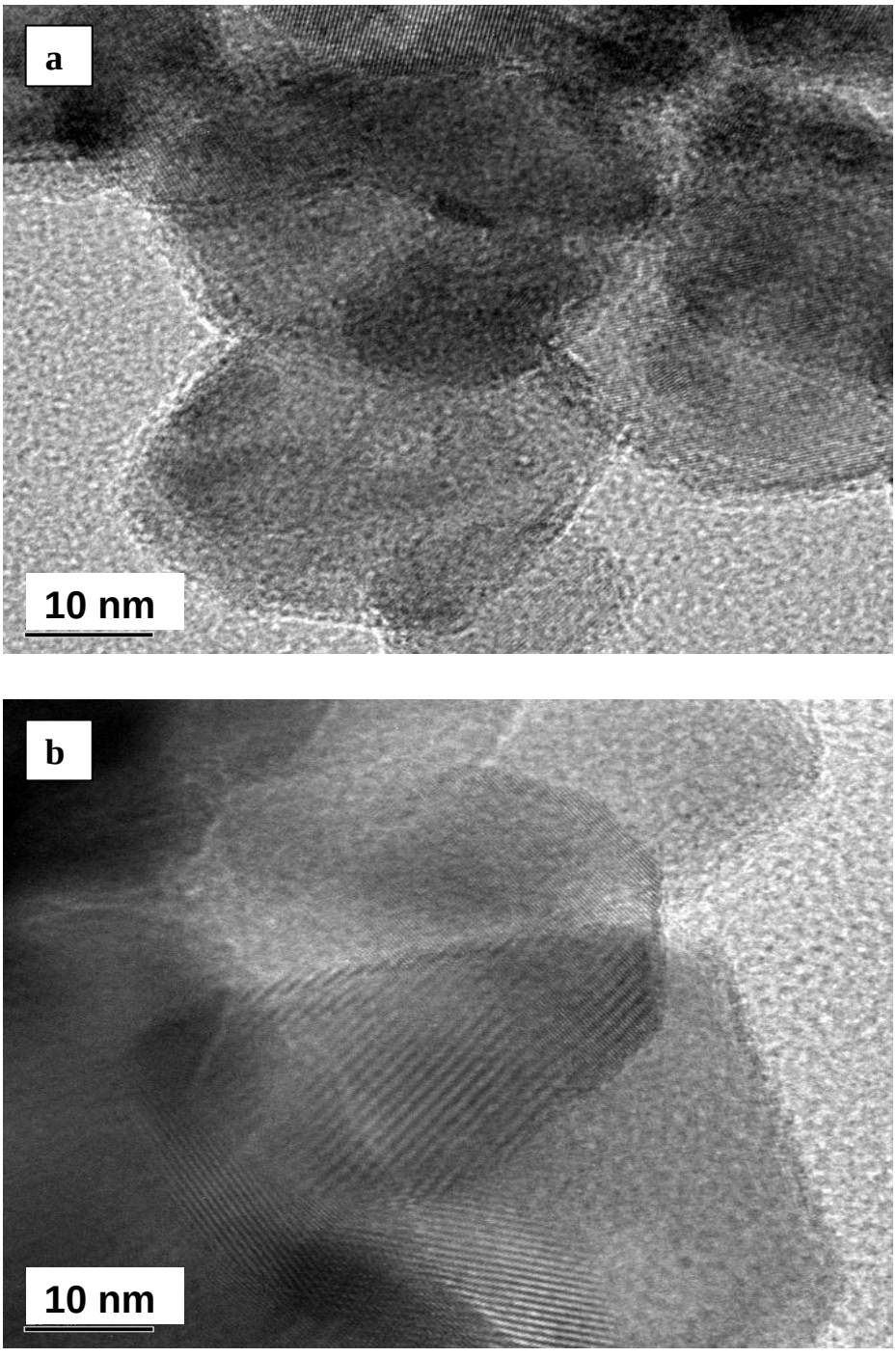

Figure 5.6: TEM global pictures of CeO_2–HfO_2/TiO_2 (CHT) samples calcined at (a) 773 K and (b) 1073 K.

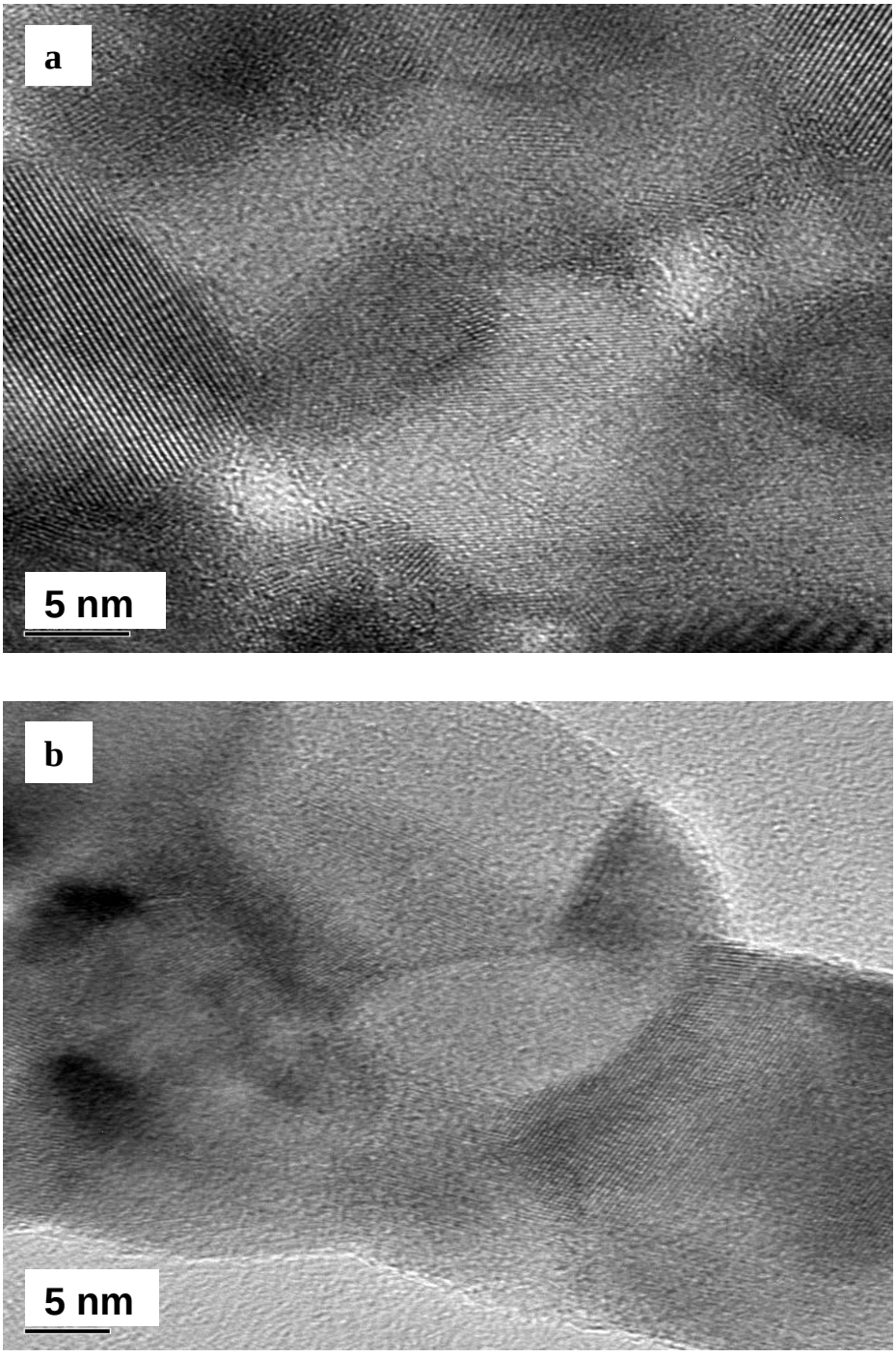

Figure 5.7: HREM images of CeO_2–HfO_2/TiO_2 (CHT) samples calcined at (a) 773 K and (b) 1073 K.

The representative TEM global pictures of CHT sample calcined at 773 and 1073 K are presented in Figure 5.6. The corresponding HREM images are shown in the Figure 5.7.

As could be observed from Figures 5.3a and 5.7a, CHT sample calcined at 773 K crystallizes in cubic structure with an average ceria-hafnia particle sizes in the range ~5–6 nm over bigger crystals of TiO_2-anatase of particle size ca. 20 nm. The closer view of the micrographs (Figs. 5.6b and 5.7b) clearly shows that the growth of the cubic structure of ceria-hafnia composite oxide particles took place over the bigger crystals of TiO_2-anatase. The increase of ceria-hafnia particles from ~5 to ~16 nm under the effect of heat treatment could be observed from the HREM images which is due to the crystallite growth and agglomeration of smaller particles at higher temperatures. Figures 5.6b and 5.7b show some superimposed contrasts arising from different types of phases due to some overlapping regions of crystal planes that constitute the catalyst. The existence of such overlapping regions in the composite oxide particles is very important from catalysis point of view which may offer better catalytic activity. The digital diffraction patterns (not shown) with the *d* spacings of 3.1 and 2.7 Å observed in the corresponding HREM images may be assigned to (111) and (002) planes of cubic Ce-Hf-oxide, respectively. Thus, TEM-HREM results fairly corroborate with the conclusions drawn from XRD data.

5.3.7 UV-visible Diffuse Reflectance Spectroscopy Studies

UV-vis DRS is a very useful technique to study the surface coordination and different oxidation states of the metal ions in metal oxides. The DR spectra of CHT sample calcined at 773 and 1073 K are presented in Figure 5.8. The DR spectra of pure CeO_2 exhibits three absorption maxima centered at ~255, 285, and 340 nm. The latter two well-resolved absorption maxima may be caused by $Ce^{4+} \leftarrow O^{2-}$ charge transfer (285 nm) and inter-band (340 nm) transitions [32,33], whereas the poorly resolved former maxima correspond to $Ce^{3+} \leftarrow O^{2-}$ charge transfer transitions [34]. As presented in Figure 5.8, in case of the CHT sample calcined at 773 and 1073 K, the absorption edges are in good agreement with the bands observed for pure CeO_2 with a slight blue-shift in the 1st band irrespective of calcination temperatures. At both 773 and 1073 K, the CHT samples exhibit the absorption bands at ~242, ~285, and ~350 nm, respectively. This infers that TiO_2-anatase has influence on the lowering of absorption edges towards lower wavelengths to some extent. In case of ceria-hafnia system, the substitution of Hf^{4+} into the CeO_2 lattice and consequent strain development at the cerium sites due to lowering of symmetry, caused the shift towards higher wavelengths compared to pure CeO_2 as already described in the chapter 3 [35]. Interestingly, the band at ~242 nm, which has been

characterized as $Ce^{3+} \leftarrow O^{2-}$ charge transfer transition, is well-resolved in CHT compared to CH samples with slight shift towards lower wavelength. The occurrence of oxygen vacancy defects supports the $Ce^{3+} \leftarrow O^{2-}$ transitions, which is very prominent in the case of CHT samples [32,33].

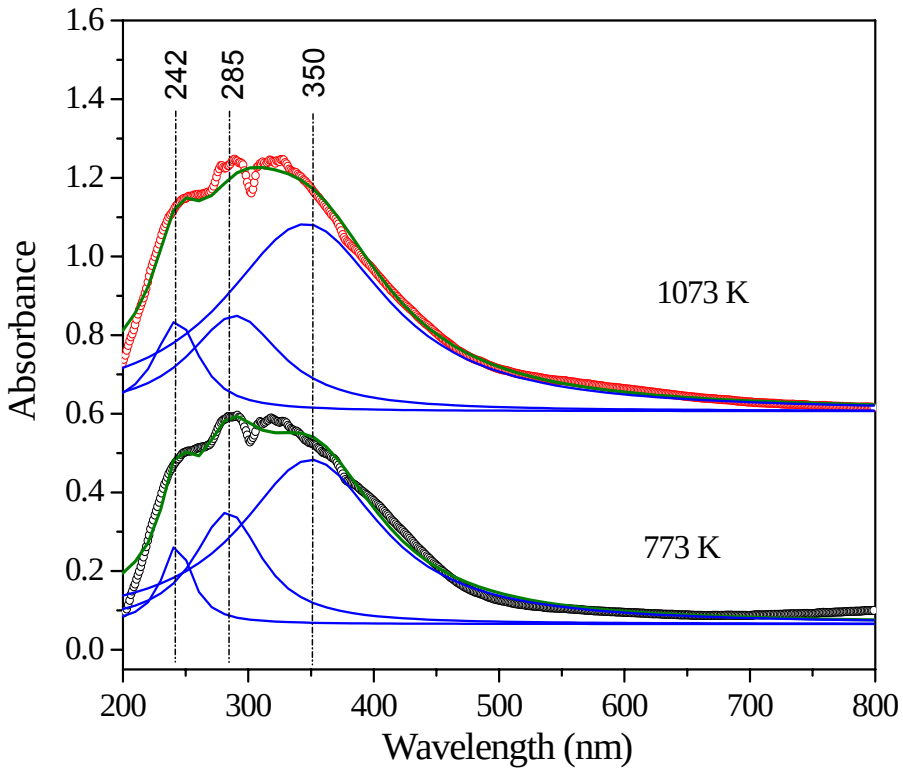

Figure 5.8: UV-vis DRS spectra of CeO_2–HfO_2/TiO_2 (CHT) samples calcined at 773 and 1073 K.

5.3.8 Raman Spectroscopy Studies

Raman spectroscopy is very useful technique to characterize the structures on oxide surfaces. Raman results give useful information the M–O bond arrangements in oxide materials. It is well reported that the Raman information detected by excitation laser with shorter wavelength is more sensitive to the surface region of samples as the laser with shorter wavelength is closer to the electronic adsorption of samples [36]. We have used two different lasers, UV excitation laser (He-Cd laser with wavelength 325 nm) and visible excitation laser (Ar^+-Kr^+ laser with wavelength 514.53 nm) in the present investigation. The UV- and visible-Raman spectra of the CHT samples calcined at

different temperatures are presented in Figures 5.9 and 5.10, respectively. Figure 5.9 shows the UV-Raman spectra of CHT samples calcined at different temperatures. As presented in Figure 5.9, the UV-Raman spectra of CHT samples show typical spectra of TiO_2-anatase phase (space group *$I4_1/amd$*) with the appearance of prominent Raman bands at ca. 152, 202, 400, 520, and 635 cm^{-1}, which agree well with the literature reports [37,38]. The observed Raman band at ~467 cm^{-1} can be attributed to the F_{2g} vibration of the fluorite type lattice. It can be viewed as a symmetric breathing mode of the oxygen atoms around cerium ions [38]. The other weak band observed at around 324 cm^{-1} could be attributed to displacement of oxygen atoms from their ideal fluorite lattice positions [39]. No Raman lines due to either hafnia or TiO_2-rutile phase (band at ~144, 148, and 611 cm^{-1}) are observed in line with XRD measurements.

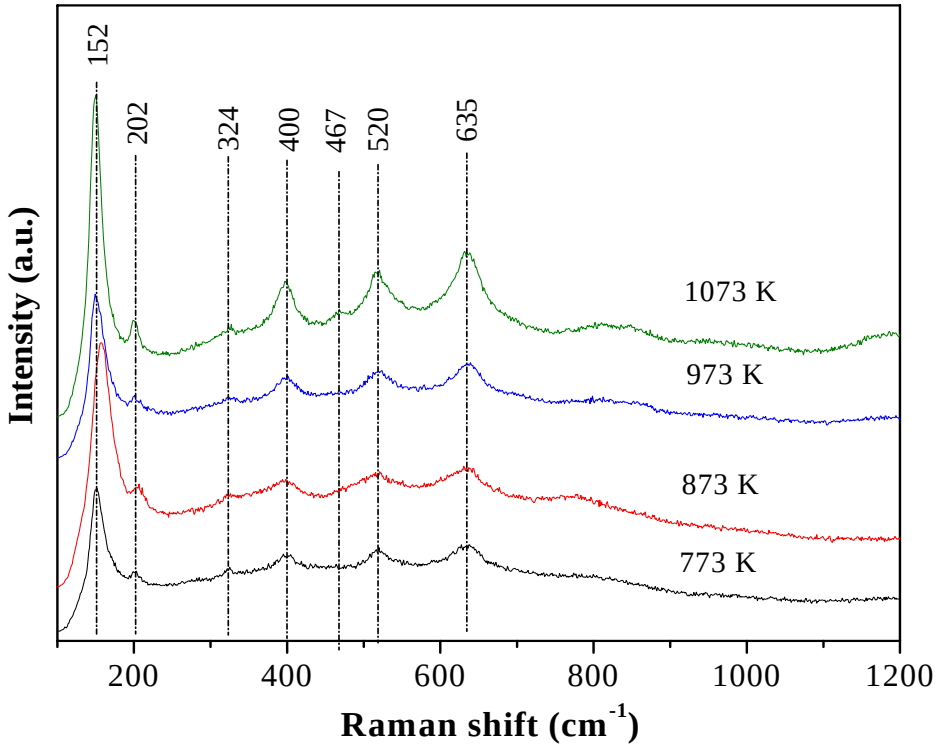

Figure 5.9: UV-Raman spectra of CeO_2–HfO_2/TiO_2 (CHT) samples calcined at different temperatures.

The visible-Raman spectra of CHT sample calcined at 773 K (Fig. 5.10) also show typical spectra of TiO_2-anatase phase (space group *$I4_1/amd$*) with the appearance of prominent Raman bands at ca. 196, 396, 515, and 640 cm^{-1}, which agree well with the literature reports [37,38]. The observed Raman band at ~466 cm^{-1} can be attributed to the

F_{2g} vibration of the fluorite type lattice. It can be viewed as a symmetric breathing mode of the oxygen atoms around cerium ions [38]. Interestingly, emergence of three new additional Raman bands could be observed for the 1073 K calcined CHT sample (Fig. 5.10). The new bands are observed around 238, 450, and 612 cm^{-1} are attributed to the formation of rutile phase by the transformation of TiO_2-anatase at 1073 K. Though this observation was not detected by XRD and UV-Raman spectra, the prominent Raman bands in the visible-Raman spectra conform about the stabilization of rutile phase along with the anatase phase of TiO_2 at higher temperatures. It was found that the results of UV-Raman spectra are different from those of visible-Raman spectra. The anatase phase of TiO_2 at the surface region can remain at relatively higher temperatures than that in the bulk at elevated calcination temperatures; namely, the anatase phase in the inner region of the agglomerated TiO_2 particles turns out to change into the rutile phase more easily than that in the outer surface region of the agglomerated TiO_2 particles [40].

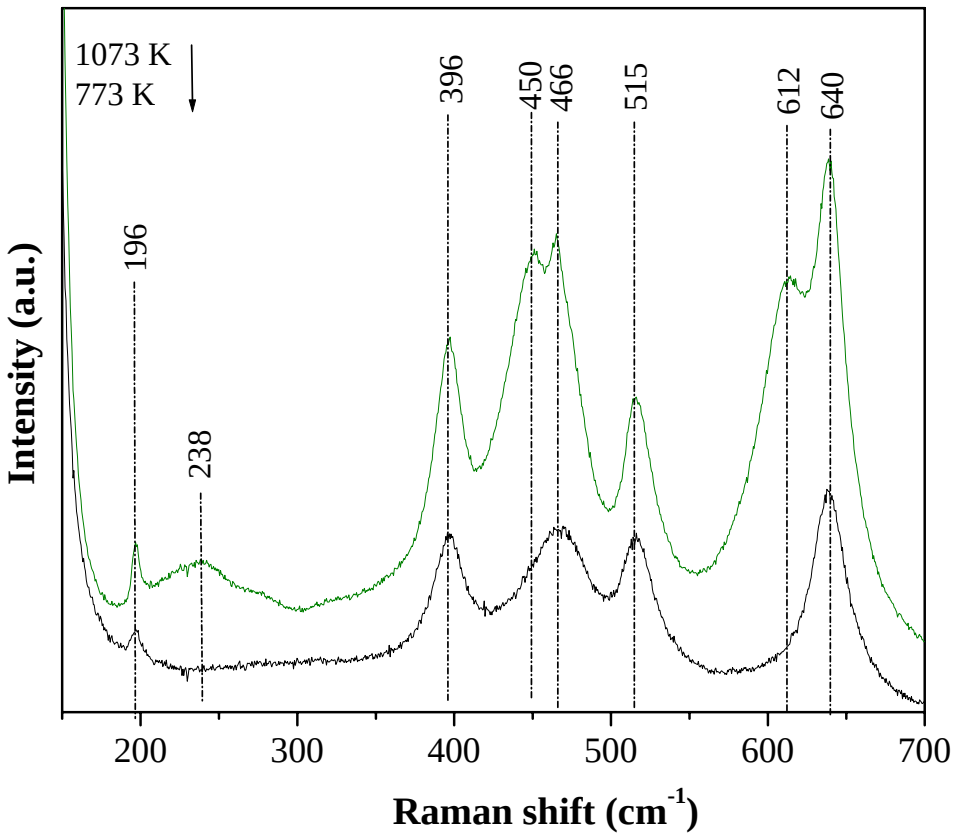

Figure 5.10: Visible-Raman spectra of CeO_2–HfO_2/TiO_2 (CHT) samples calcined at 773 and 1073 K.

5.3.9 X-ray Photoelectron Spectroscopy Studies

XPS measurements have been performed to study the effect of interaction between the metal ions and to acquire the information of oxidation states in the catalytic system. The effect of calcination temperature on the photoelectron peaks of O 1s, Hf 4f, Hf 4d, Ti 2p, and Ce 3d for CHT samples are presented in Figures 5.11–5.15, respectively. The corresponding binding energy (eV) values and XPS atomic ratios (Ce/Hf and Ce/Ti) are presented in Tables 5.2 and 5.3, respectively. The interactions between the components in the nanostructured systems are quite complicated and depend on several factors, which include thermal treatment temperature, synthesis procedure etc. As could be observed from all the figures, the XPS bands and the corresponding binding energy values are highly sensitive to the calcination temperature and to the composition of the samples. Figure 5.11 displays the O 1s XP spectra of CHT composite oxide samples calcined at different temperatures.

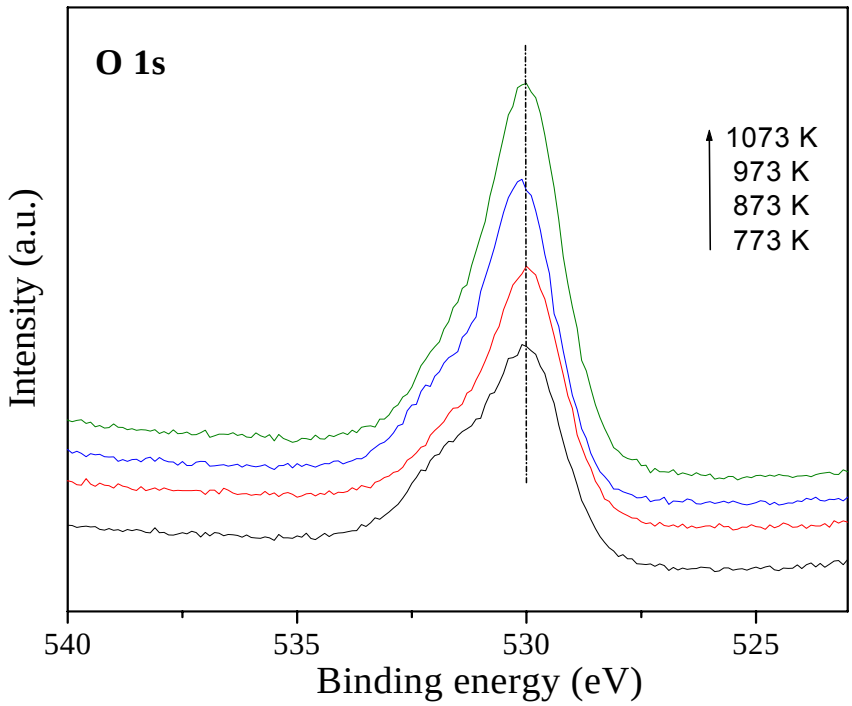

Figure 5.11: O 1s XP spectra of CeO_2–HfO_2/TiO_2 (CHT) samples calcined at different temperatures.

The O 1s profiles are generally complicated due to the overlapping contribution of oxide ions from ceria, hafnia, and titania in the respective cases. As reported earlier, the O ions

in pure CeO_2 exhibit intense peaks at 528.6, 528.8, 529.6, and 530.1 eV, respectively [41–43]. The O 1s binding energy value reported for TiO_2 is 530.0 eV [43–46]. The O 1s profile of the CHT samples showed that with increasing calcination temperature, the O 1s lines become sharp. The binding energy of most intense O 1s peak in these cases were observed at around 530.0 eV, mainly belonging to the oxygen ions that are bound to $Ce_{0.8}Hf_{0.2}O_2$ solid solution [41,42]. The slight shift in the binding energy value for the 1073 K calcined sample inferred that some changes in the chemical environment around O atoms have occurred.

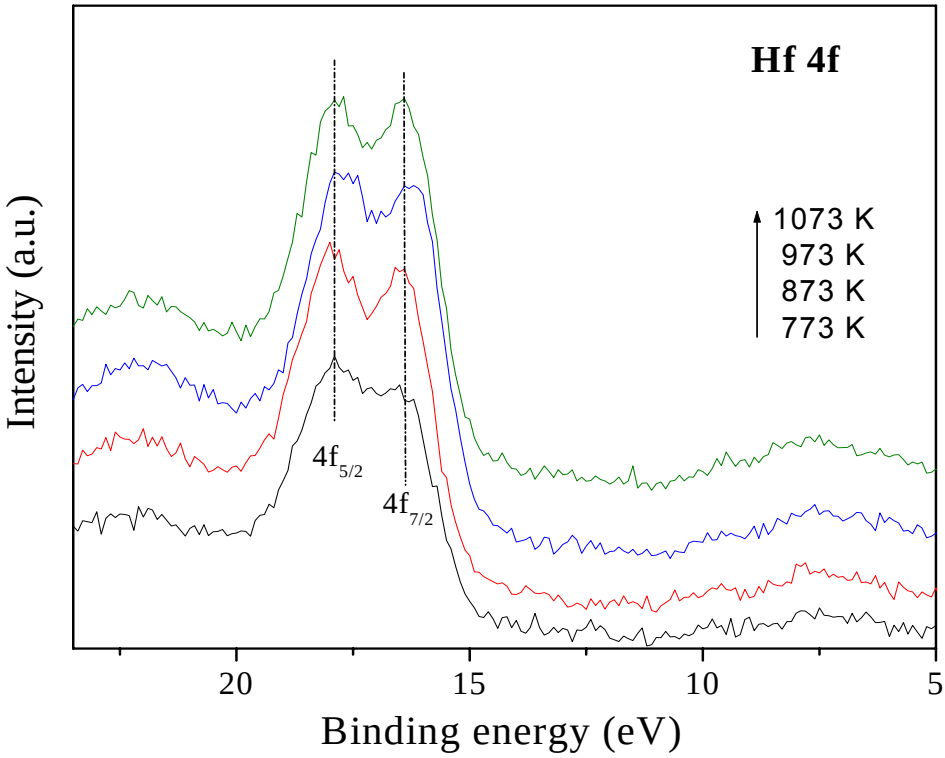

Figure 5.12: Hf 4f XP spectra of CeO_2–HfO_2/TiO_2 (CHT) samples calcined at different temperatures.

Figures 5.12 and 5.13 show the core level XP spectra of Hf 4f and Hf 4d, respectively corresponding to the CHT samples calcined at different temperatures. As could be observed from the XP spectra of Hf 4f (Fig. 5.12), there are two features at about 16.4 and 18.0 eV, respectively. It is reported that the Hf 4f spectrum consists of two components, the $4f_{7/2}$ part at 16.79 ± 0.08 eV and the $4f_{5/2}$ part at 18.54 ± 0.10 eV [47]. The peak positions of Hf 4f photoelectrons are known to be very sensitive to the binding states of the hafnium species [41,48]. According to a database, the metallic hafnium species reveals the Hf $4f_{7/2}$ peak at 14.3–14.4 eV, while HfO_2 shows it at 16.7 eV. Lee et al.

investigated HfO_2 films on a silicon substrate by synchrotron XPS and found the binding energies of Hf $4f_{7/2}$ and Hf $4f_{5/2}$ at 17.55 and 19.26 eV, respectively [49]. However, the difference of about 1.4 eV in the binding energies between the Hf $4f_{7/2}$ and Hf $4f_{5/2}$ in the present investigation is in line with the reported values [41]. On the other hand, the XP spectra of Hf 4d photoelectron peak in relatively very scarce in the literature. As observed the spectra consists of two features in the binding energy values of ~224.2 and ~213.0 eV, respectively, which are in good agreement with the data presented in 'The Handbook of X-ray Photoelectron Spectroscopy' [41]. On the whole, from the XP spectra of Hf 4f and Hf 4d, it is observed that Hf is mainly in 4+ oxidation state.

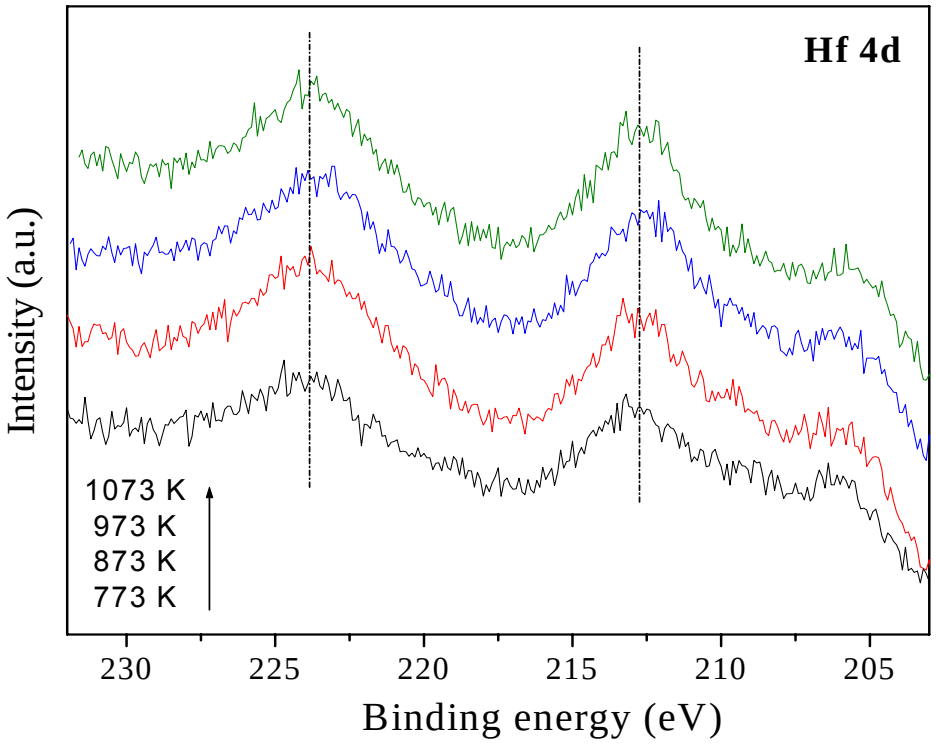

Figure 5.13: Hf 4d XP spectra of CeO_2–HfO_2/TiO_2 (CHT) samples calcined at different temperatures.

The Ti 2p photoelectron spectra of the CHT samples are shown in Figure 5.14, which exhibited typical XPS peaks of 458.5 eV for Ti $2p_{3/2}$ [45,46]. The intensity of the Ti 2p core level spectra showed slight increase with increasing treatment temperature due to better crystallization of TiO_2. It could be inferred from the XPS results that titanium is mostly confined to its highest, i.e. 4+ oxidation state.

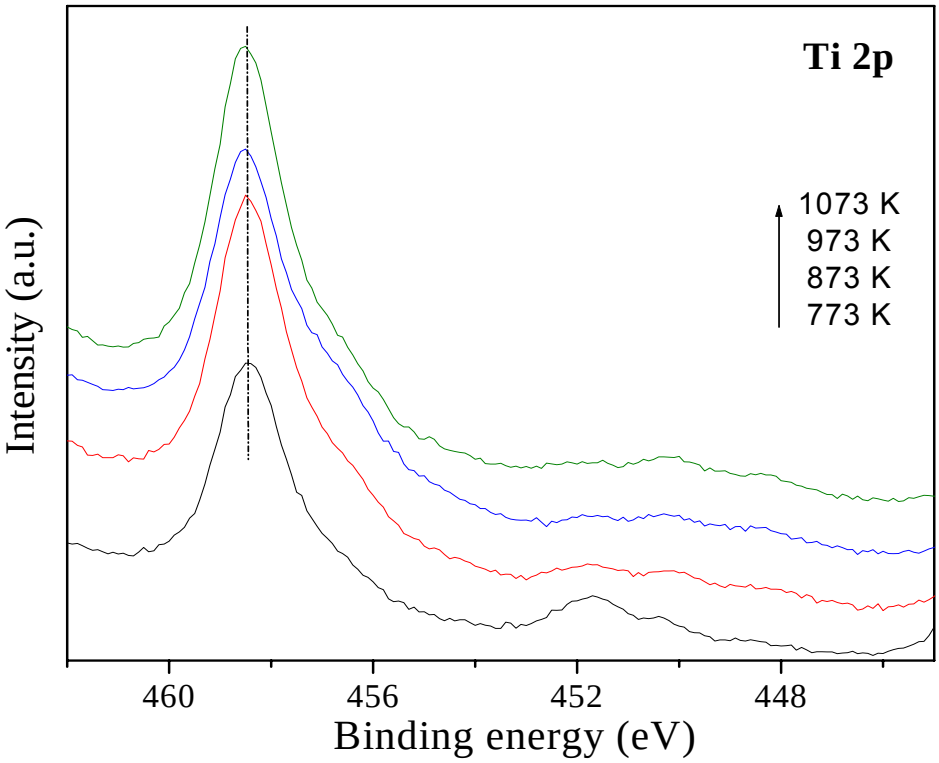

Figure 5.14: Ti 2p XP spectra of CeO_2–HfO_2/TiO_2 (CHT) samples calcined at different temperatures.

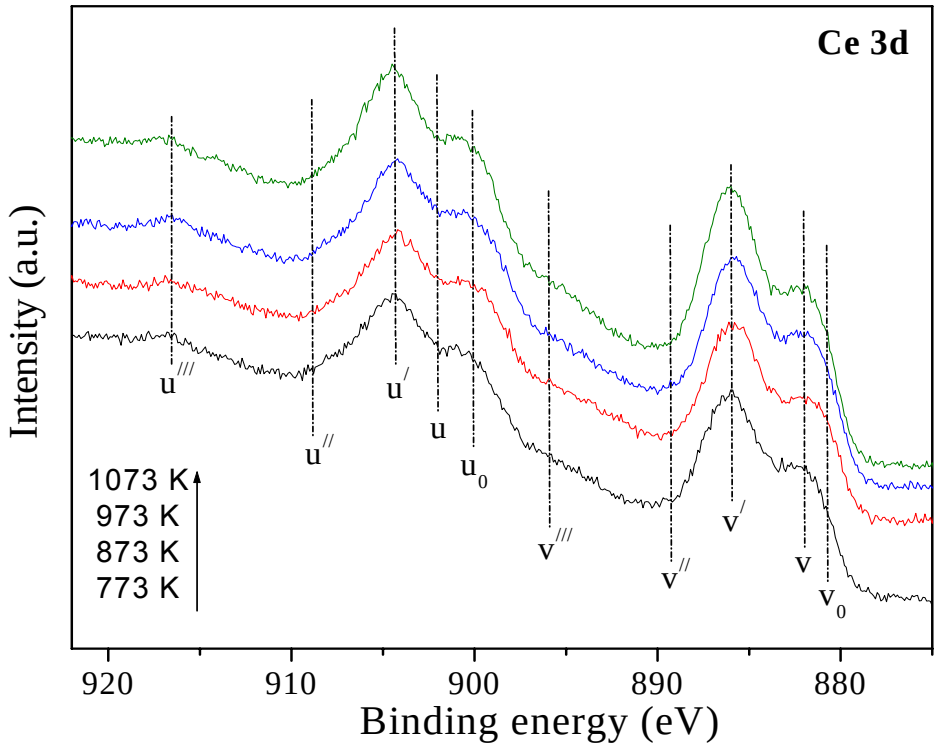

Figure 5.15: Ce 3d XP spectra of CeO_2–HfO_2/TiO_2 (CHT) samples calcined at different temperatures.

The XP spectra of Ce 3d core electron levels for CHT samples are presented in Figure 5.15. There are six peaks corresponding to the three pairs of spin-orbit doublets of oxidized CeO_2 and four peaks corresponding to the two doublets of Ce_2O_3 [35,41–44,50]. For each doublet, $3d_{5/2}$ corresponds to the label 'v' and $3d_{3/2}$ to 'u'. Details pertaining to the explanation of the origin of each doublet could be found in literature [35,43,51]. The peaks labeled v/u, v''/u'', v'''/u''' have been assigned to Ce^{4+} and v'/u', v_0/u_0 to Ce^{3+}. Two main bands of $Ce3d_{5/2}$ at 880.6–882.5 eV (v) corresponding to Ce^{4+} and 884.5–885.1 eV (v') corresponding to Ce^{3+}; were observed for all samples (Fig. 5.15) [44]. Thus cerium is present in both Ce^{4+} and Ce^{3+} oxidation states. The presence of Ce^{3+} could be mainly attributed to removal of surface hydroxyl groups and oxygen from CeO_2 surface during exposure of the samples to the X-ray in an ultrahigh vacuum chamber (UHV) as per earlier reports [35,43,52–54].

Table 5.2: XPS core level electron binding energies (eV) of the CeO_2–HfO_2/TiO_2 (CHT) samples calcined at different temperatures

Calcination Temp. (K)	Binding Energy (eV)				
	O 1s	Ce 3d	Hf 4f	Hf 4d	Ti 2p
773	530.0	882.0	18.0 (16.4)	224.2 (213.0)	458.5
873	530.0	882.0	18.0 (16.4)	224.2 (213.0)	458.5
973	530.1	882.2	17.9 (16.3)	224.1 (213.1)	458.5
1073	530.1	882.2	17.8 (16.4)	224.2 (213.2)	458.5

Table 5.3: XPS atomic ratio of the CeO_2–HfO_2/TiO_2 (CHT) samples calcined at different temperatures

Calcination Temperature (K)	Atomic Ratio	
	Ce/Hf	Ce/Ti
773	3.894	1.052
873	3.867	1.088
973	3.677	1.154
1073	3.427	1.164

The atomic ratios corresponding to the Ce/Hf and Ce/Ti as determined from XPS, are presented in Table 5.3. As could be observed from the table, the Ce/Hf atomic ratios decrease very meagerly with the increase in calcination temperature, whereas Ce/Ti atomic ratios did not change appreciably. The increase in the Ce/Hf atomic ratios infers about the surface enrichment of Hf at higher calcination temperatures.

5.4 Conclusions

The structural characteristics of nanostructured ceria-hafnia composite oxides supported over TiO_2 have been systematically investigated. The catalyst was synthesized by adopting a modified deposition coprecipitation method and thermally treated up to 1073 K to study the thermal stability. The composite oxides exhibit high specific surface area and show resistance to thermal sintering. XRD results infer the monophasic composition ($Ce_{0.8}Hf_{0.2}O_2$). The TEM images confirm the nano-meter sized particles of the prepared catalysts with size (~5 nm). An increase in crystallite size (up to ~16 nm) after heat treatment at 1073 K is noted. The lowering of symmetry and consequent strain development at the cerium sites is also revealed by UV-vis DRS measurements. Raman spectroscopy measurements revealed the arrangement of defective fluorite structure leading to oxygen vacancy formation. Especially, visible-Raman spectra gave information of the emergence of TiO_2-rutile phase at 1073 K. The XPS measurements revealed the presence of both Ce^{3+} and Ce^{4+} states, which are sensitive to calcination temperature. Thus the use of various spectroscopic and non-spectroscopic techniques provided interesting information regarding the physicochemical characteristics of titania supported nanosized ceria-hafnia composite oxides.

5.5 References

[1] J.E.G.J. Wijnhiven, W.L. Vos, Science 281 (1998) 802.

[2] K.I. Hadjiivanov, D.G. Klissurski, Chem. Soc. Rev. 25 (1996) 61.

[3] J. Whitehead, Titanium Compounds, Inorganic, in: Kirk-Othmer Encyclopedia of Chemical Technology, M. Grayson, Executive Ed., Wiley, New York, 1983, 3rd ed., Vol. 23, p.131.

[4] M. Wagemaker, G.J. Kearley, A.A. van Well, H. Mutka, F.M. Mulder, J. Am. Chem. Soc. 125 (2003) 840.

[5] D. Bersani, P.P. Lottici, X.Z. Ding, Appl. Phys. Lett. 72 (1998) 73.

[6] M.S.P. Francisco, V.R. Mastelaro, Chem. Mater. 14 (2002) 2514.

[7] J.M.G. Amores, V.S. Escribano, G. Busca, V. Lorezelli, J. Mater. Chem. 4 (1994) 965.

[8] S.T. Choo, S.D. Yim, I.S. Nam, S.W. Ham, J.B. Lee, Appl. Catal. B: Environ. 44 (2003) 237.

[9] R.Y. Saleh, I.E. Wachs, S.S. Chan, C.C. Chersich , J. Catal. 98 (1986) 102.

[10] N. Rajabbeigi, B. Elyassi, A.A. Khodadadi, S. Mohajerzadeh, Y. Mortazavi, M. Sahimi, Sensors and Actuators B: Chem. 108 (2005) 341

[11] T. Baidya, A. Gayen, M.S. Hegde, N. Ravishankar, L. Dupont, J. Phys. Chem. B 110 (2006) 5262.

[12] J.C. Vedrine, Ed.; Eurocat Oxide, Catal. Today 20 (1994) 1.

[13] H. Bosch, F. Janssen, Catal. Today 2 (1988) 369.

[14] G.C. Bond, S.F. Tahir, Appl. Catal. 71 (1991) 1.

[15] G. Deo, I.E. Wachs, J. Haber, Crit. Rev. Surf. Chem. 4 (1994) 141.

[16] H. Zhu, Z. Qin, W. Shan, J. Wang, J. Catal. 233 (2005) 41.

[17] A. Verma, S.B. Samantha, N.C. Mehra, A.K. Bakhshi, Solar Energy Mater. Solar Cells 86 (2005) 85.

[18] C.O. Avellaneda, L.O.S. Bulhoes, A. Pawlicka, Thins Solid Films 471 (2005) 100.

[19] S. Watanabe, X. Ma, C. Song, ACS National Meeting Book of Abstracts, 228 (1) p. Fuel-18, 2004.

[20] M. Luo, J. Chen, L. Chen, J. Lu, Z. Feng, C. Li, Chem. Mater. 13 (2001) 197.

[21] G. Dutta, U.V. Waghmare, T. Baidya, M.S. Hegde, K.R. Priolkar, P.R. Sarode, Chem. Mater. 18 (2006) 3249.

[22] B.M. Reddy, P. Lakshmanan, A. Khan, C.L. Cartes, T.C. Rojas, A. Fernandez, J. Phys. Chem. B 109 (2005) 1781.

[23] B.M. Reddy, A. Khan, P. Lakshmanan, M. Aouine, S. Loridant, J.C. Volta, J. Phys. Chem. B 109 (2005) 3355.

[24] A. Preuss, R. Gruehn, J. Solid State Chem. 110 (1994) 363.

[25] J. Lin, J.C. Yu, J. Photochem. Photobiol. A: Chem. 116 (1998) 63.

[26] B.M. Reddy, I. Ganesh, E.P. Reddy, J. Phys. Chem. B 101 (1997) 1769.

[27] D.M. Gruen, W.C. Koehler, J.J. Katz, J. Am. Chem. Soc. 73 (1951) 1475.

[28] A.B. Hungria, A. Martinez-Arias, M. Fernandez-Garcia, A. Iglesius-Juez, A.G. Ruiz, J.J. Calvino, J.C. Conesa, J. Soria, Chem. Mater. 15 (2003) 4309.

[29] F. Fally, V. Perrichon, H. Vidal, J. Kaspar, G. Blanco, J.M. Pintado, S. Bernal, G. Colon, M. Daturi, J.C. Lavalley, Catal. Today 59 (2000) 373.

[30] P. Vidmar, J. Kaspar, P. Fornasiero, M. Graziani, J. Phys. Chem. B 102 (1998) 557.

[31] M. Boaro, M. Vicario, C. de Leitenburg, G. Dolcetti, A. Trovarelli, Catal. Today 77 (2003) 407.

[32] A. Bensalem, J.C. Muller, F.B. Verduraz., J. Chem. Soc. Faraday Trans. 88 (1992) 153.

[33] B.M. Reddy, P. Bharali, G. Thrimurthulu, P. Saikia, L. Katta, S.-E. Park, Cat. Lett. 123 (2008) 327.

[34] A. Bensalem, F.B. Verduraz, M. Delamar. G. Bugli, Appl. Catal. 121 (1995) 81.

[35] B.M. Reddy, A. Khan, Catal. Surv. Asia. 9 (2005) 155.

[36] M.-F. Luo, Z.-L. Yan, L.-Y. Jin, M. He, J. Phys. Chem. B 110 (2006) 13068.

[37] M. Kosmulski, Adv. Colloid. Interf. Sci. 99 (2002) 255.

[38] X.M. Lin, L.P. Li, G.S. Li, W.H. Su, Mater. Chem. Phys. 69 (2001) 236.

[39] V.S. Escribano, E.F. Lopez, M. Panizza, C. Resini, J.M.G. Amores, G. Busca, Solid State Sci. 5 (2003) 1369.

[40] J. Zhang, M. Li, Z. Feng, J. Chen, C. Li, J. Phys. Chem. B 110 (2006) 927.

[41] C.D. Wagner, W.M. Riggs, L.E. Davis, J.F. Moulder, in: Handbook of X-ray Photoelectron Spectroscopy, G.E. Muilenberg, Ed., Perkin-Elmer Corporation, Eden Prairie, MN, 1978.

[42] D. Briggs, M.P. Seah, in: Auger and X- ray Photoelectron Spectroscopy, Practical Surface Analysis, Wiley, New York, 1990, 2nd ed., Vol. 1.

[43] B.M. Reddy, A. Khan, Y. Yamada, T. Kobayashi, S. Loridant, J.C. Volta, J. Phys. Chem. B 107 (2003) 11475.

[44] A. Galtayries, R. Sporken, J. Riga, G. Blanchard, R. Caudano, J. Electron Spectrosc. Relat. Phenom. 88-91 (1998) 951.

[45] J. Beiner, M. Baumer, J. Wang, R.J. Madrix, Surf. Sci. 450 (2000) 12.

[46] Q. Wang, R.J. Madrix, Surf. Sci. 474 (2001) L213.

[47] T. Brezesinski, B. Smarsly, K.-I. Iimura, D. Grosso, C. Boissiere, H. Amenitsch, M. Antonietti, C. Sanchez, Small 8−9 (2005) 889.

[48] V. Cosnier, M. Olivier, G. Theret, A. Andre, J. Vac. Sci. Technol. A 19 (2001) 2267.

[49] J.C. Lee, S.J. Oh, M. Cho, C.S. Hwang, R. Jung, Appl. Phys. Lett. 84 (2004) 1305.

[50] T. Yuzhakova, V. Rakic, C. Guimon, A. Auroux, Chem. Mater. 19 (2007) 2970.

[51] B.M. Reddy, K.N. Rao, G.K. Reddy, A. Khan, S.-E. Park, J. Phys. Chem. C 111 (2007) 18751.

[52] S. Damyanova, C.A. Perez, M. Schmal, J.M.C. Bueno, Appl. Catal. A: Gen. 234 (2002) 271.

[53] J.S. Albero, F.R. Reinoso, A.S. Escribano, J. Catal. 210 (2002) 127.

[54] M. Daturi, C. Binet, J.C. Lavalley, A. Galtayries, R. Sporken, Phys. Chem. Chem. Phys. 24 (1999) 5717.

Chapter 6

This chapter presents the results and discussion pertaining to the structural characteristics of the nanosized composite oxides of CeO_2–HfO_2/Al_2O_3 system by various spectroscopic and non-spectroscopic techniques.

STUDIES on CeO_2–HfO_2/Al_2O_3 COMPOSITE OXIDE CATALYST

6.1 Introduction

Regulations concerning automotive emissions are becoming more stringent in recent times and consequently more research efforts have directed toward lowering the environmental impact of pollutants emitted by vehicles and industries. In this context, the research focus has been aimed at the development of more efficient and highly resistant catalytic converters which could be able to maintain maximum durability while decreasing pollutant emissions to minimum levels. Three-way catalysts (TWCs) constitute the most satisfactory and efficient solution to reduce pollutant emissions from gasoline-engine-powered vehicles [1–4]. Automotive TWCs can convert exhausted carbon monoxide, hydrocarbon, and nitrogen oxides to environmentally friendly gases, respectively. In a typical design of a modern TWC, alumina is chosen to be a carrier because of its high surface area and relatively good thermal stability under the hydrothermal conditions of the exhausts [5]. Ceria-based materials have been recognized as an important component of the three-way catalysts because of their excellent oxygen storage capacity (OSC) [6,7]. The major role of ceria-based materials is the OSC, maintaining an air/fuel ratio around 14.6 during engine operation, and TWCs have high pollutant conversion efficiency under a narrow operation window [8]. After the high-temperature treatment, one of the major deactivation pathways for the TWCs is the sintering of the OSC promoter leading to a loss of OSC values. Therefore, the high thermal stability of the oxygen storage material is a requisite for developing advanced TWCs [9,10]. Because of the insufficient thermal stability of ceria, from 1995, ceria-zirconia composite oxides have gradually replaced pure ceria as OSC materials in TWCs [11]. Mixing methods of alumina and ceria-zirconia lead to differences in the interaction between alumina and ceria-zirconia, surface area, and bulk structures, which are important aspects of both the OSC behavior and the stability of alumina-ceria-zirconia materials [12–14]. At present, numerous literatures illustrate various mixing strategies with the aim to obtain ceria-zirconia and alumina materials of high thermal stability and superior redox properties [15,16]. Recently it was found that the homogeneous ceria-ziconia structure and strong interaction between alumina carriers and ceria-zirconia are excellent to obtain hydrothermal stability [17,18]. Morikawa et al. [19] testified that the introduction of alumina into $Ce_{1-x}Zr_xO_2$ primary particles can improve the

durability at high temperatures and velocity oxygen release of the materials. Against the above background, we have investigated the effect of γ-Al_2O_3 as chemically inert thermostable support for CeO_2–HfO_2 composite oxides prepared by a deposition coprecipitation method and thermally treated up to 1073 K. The thermal stability and dispersion behavior of the $Ce_xHf_{1-x}O_2$ composite oxides over Al_2O_3 support has been evaluated by different spectroscopic and non-spectroscopic techniques.

6.2 Experimental

Alumina supported ceria-hafnia (CHA; 8:2:10 mole ratio based on oxides) composite oxides was prepared by adopting a deposition coprecipitation method as per the procedure described in Chapter 2. The obtained catalysts were subjected to thermal treatments from 773 to 1073 K in order to understand the thermal stability, and the physicochemical properties of these materials. These effects have been investigated by means of TG-DTA, BET SA, XRD, TPR, SEM, TEM-HREM, UV-vis DRS, LRS, XPS, and other techniques.

6.3 Results and Discussion

6.3.1 Thermal Measurements

The CeO_2–HfO_2/Al_2O_3 composite oxide was subjected to TG/DTA analysis before calcination. The thermogram, obtained between 273 and 1273 K and at a ramp of 10 K/min, is shown in Figure 6.1. The thermal stability of the CHA sample was judged from the TG/DTA analysis. The temperatures suitable for calcination of the sample were also chosen on the basis of this analysis, at which the mass loss was stabilized. Three distinct features are observed in the TGA profile. One low temperature feature (at around 313–463 K) is due to the loss of molecularly absorbed water from the surface. The minor weight loss peaks at high temperatures, around 473–573 K and 573–673 K are due to loss of water held in the micropores of the gels and dehydroxylation of the surface, respectively. Above this temperature the weight loss was almost completely stabilized. On this basis, the primary calcination temperature for the catalyst sample was chosen to be 773 K. Up to 840 K, the total weight loss was calculated to be 13%, whereas from 840 to 1273 K, it was found to be only 0.8%. Thus thermogravimetric analysis clearly reveals that

the sample is thermally quite stable at high temperatures and could find use in high temperature applications.

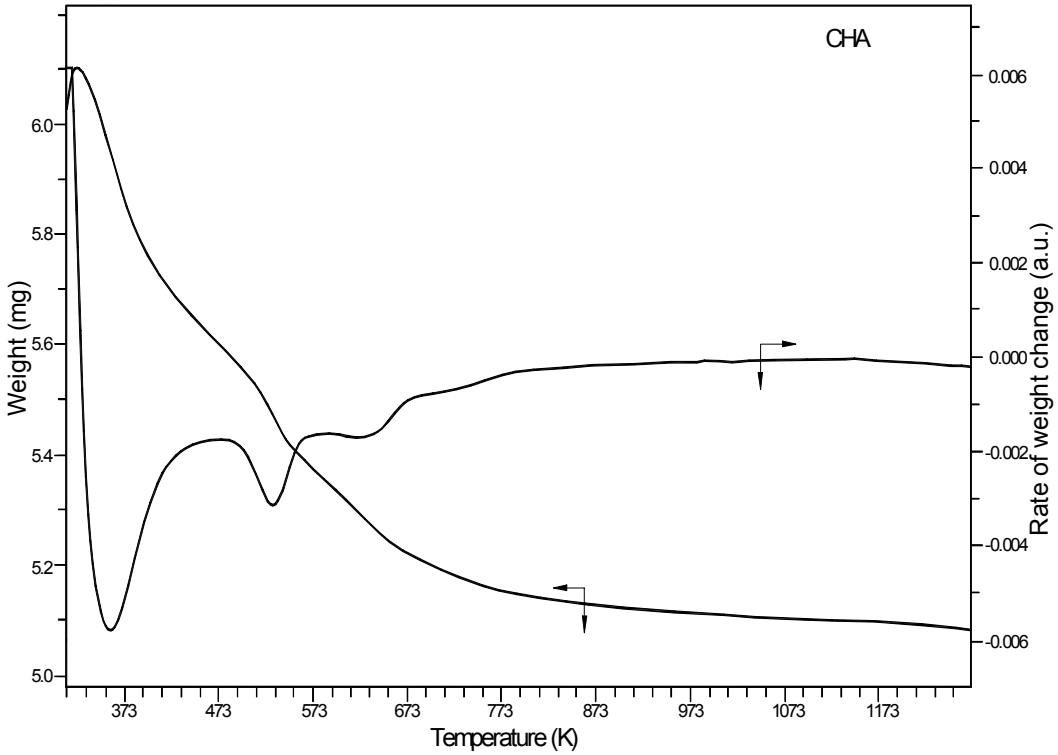

Figure 6.1: TGA profile of CeO_2–HfO_2/Al_2O_3 (CHA) sample before calcination.

6.3.2 BET Surface Area Measurements

The BET surface areas of the CeO_2–HfO_2/Al_2O_3 samples after treating at different temperatures (773–1073 K) are summarized in Table 6.1. As can be seen from the Table, all the samples reveal reasonably high BET surface areas. The 773 K calcined sample exhibits the surface area of 156 $m^2 g^{-1}$. With increase in calcination temperature from 773 to 1073 K the specific surface areas of the sample showed a gradual fall to 106 $m^2 g^{-1}$, showing only 32.0 % surface area loss. Thus the stabilization rendered by the alumina support is quite obvious. The decrease in the surface area with increasing calcination temperature is a general phenomenon due to sintering of the samples at high temperatures. However, it is observed that the sample exhibits sufficiently higher surface area after calcination at 1073 K, which shows the thermal stability of the system in terms of chemical composition.

Table 6.1: BET surface area, FWHM values, crystallite size and lattice parameter measurements of CeO_2–HfO_2/Al_2O_3 (CHA) samples calcined at different temperatures

Calcination Temp. (K)	S.A. ($m^2 g^{-1}$)	FWHM[a] ($2\theta^o$)	Crystallite Size[b] (nm)	Cell parameter (Å)
773	156	2.30	3.57	5.36
873	137	1.90	4.32	5.36
973	120	1.68	4.89	5.36
1073	106	1.13	7.28	5.35

[a] From most prominent XRD (111) peak;

[b] Crystallite size from Scherrer equation.

6.3.3 X-ray Diffraction Studies

X-ray diffraction data were collected for all the alumina supported Ce–Hf oxides after calcination in the temperature range from 773 to 1073 K and the patterns are shown in the Figure 6.2. The broad nature of the peaks distinctly indicated the nanocrystalline nature of the samples in general. A cubic fluorite type phase with the composition $Ce_{0.8}Hf_{0.2}O_2$ (PDF-ICDD 04-006-1933) was identified from the diffraction patterns of the CHA samples calcined at different temperatures. The formation of solid solution between ceria and hafnia is clearly noticed and no other species are detected. The diffraction peaks could be indexed to (111), (200), (220), (311), (222), (400), (331), and (420) crystal faces corresponding to a fluorite type structure of ceria–hafnia composite oxide. The broadened lines indicate the presence of smaller particles of nanometer size. The average crystallite sizes of the Ce–Hf composite oxides calculated using Scherrer equation are presented in Table 6.1. For 773 K calcined sample it was found to be ~3.57 nm which is gradually increased to ~7.2 nm after heat treatment at 1073 K. This observation is supported by the gradual sharpening of the XRD peaks with increasing calcination temperature which could be rationalized as a result of sintering. Thus, the observation indicates an improvement in the crystallinity with corresponding increase in crystallite size and decrease in specific surface area after calcination at 1073 K (Table 6.1).

The cell parameters of the supported composite oxides are slightly larger (5.35–5.36 Å) than that of the bulk composite oxide of the same nominal chemical composition (5.34 Å). This may indicate the presence of higher content of trivalent cations

(Ce^{3+}) in the lattice of the resultant supported oxide, which have cationic radius of 1.14 Å. Being Ce^{3+} cation bigger in size than the tetravalent Ce^{4+} (cationic radius of 0.97 Å), it can compensate for the contraction of the ceria lattice due to the presence of smaller Hf^{4+} (cationic radius of 0.78 Å). However, the lattice cell parameter values for the composite oxide samples are smaller than pure CeO_2 (cell parameter = 5.410 Å). This observation opens up another possibility of incorporation of Al^{3+} cations with cationic radius of 0.51 Å in to the ceria lattice other than Hf^{4+}. Literature shows that in case of ceria-alumina system, within the temperature range of 673–973 K, the reduction of ceria to non-stoichiometric CeO_{2-x} is favored and subsequently diffusion of Al^{3+} into the partially reduced ceria lattice may lead to the $CeAlO_3$ formation [20]. There is another possibility that all Hf may not be fully incorporated in the process of composite oxide formation with ceria and part of it may react with alumina counterpart. However, in the present case, as stated earlier, no evidence is available regarding the presence of any species other than ceria–hafnia solid solution within the investigated temperature range.

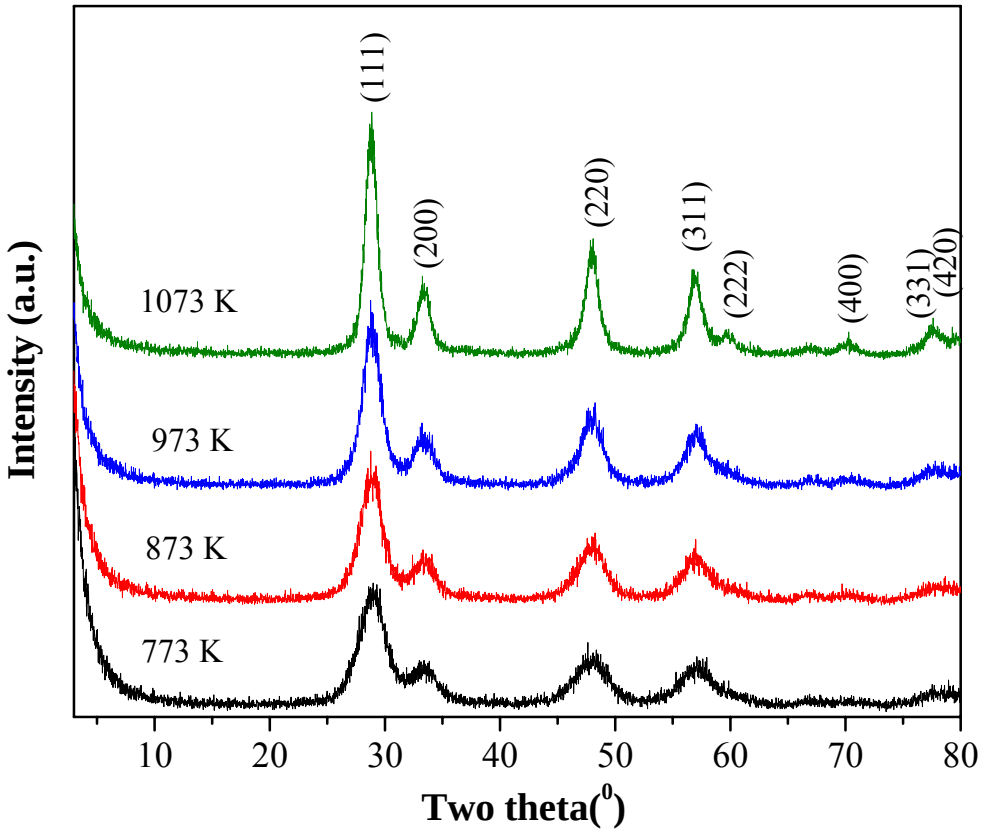

Figure 6.2: Powder XRD patterns of CeO_2–HfO_2/Al_2O_3 (CHA) samples calcined at different temperatures.

This is an important observation in terms of the catalytic activity of the sample. But we can not rule out the possibility of the presence of hafnia in amorphous state being beyond the limit of XRD detection. The XRD patterns on the whole reveal the single phase patterns for the Ce–Hf oxides without phase segregation even after calcination at 1073 K. However, the peak widths of the nanosized materials are relatively large and therefore it is not easy to draw an exact statement if small amounts of segregated phases are present.

6.3.4 Temperature Programmed Reduction Studies

TPR has been performed for the CHA samples using both H_2 and CO as reducing gas. Figure 6.3 shows the typical H_2-TPR profile of CHA sample calcined at 773 K. The quantification of H_2 consumption is estimated using CuO as the standard for TPR analysis. As could be seen in the TPR pattern, there is only one temperature maxima with broad nature for the CHA sample. Earlier research has shown that the there is two peaks observed in the TPR patterns of some ceria-based catalysts and are assigned as, (i) the reduction of the most easily reducible surface oxygen of highly dispersed ceria species and (ii) the removal of oxygen from bulk ceria. In case of ceria-zirconia composite oxides, however, only one broad peak is observed and many researchers suggest that surface and bulk reduction cannot be distinguished by the conventional TPR technique since both processes occur almost simultaneously during TPR measurement [21,22]. In line with earlier findings we also observed only one broad TPR peak for the sample. The reduction feature was started at ~650 K and centered ~872 K. However, in comparison to ceria-zirconia and ceria-hafnia, higher amount of H_2 consumption was observed as could be seen from the TPR profile. The H_2 consumption calculated from the peak area under the reduction peak over the complete temperature range for the CHA sample is 1173 μmol g^{-1} of the catalyst which is higher compared to ceria-zirconia and ceria-hafnia (Fig. 3.3, chapter 1). This shows that the degree of reduction of CeO_2-HfO_2 is enhanced to more extent after Al_2O_3 was used as support. The CO-TPR profiles (not to scale) of CHA sample calcined at 773 and 1073 K are shown in Figure 6.4, which reveal two broad reduction features. In literature it has been reported that the reduction of ceria-based materials associated with a stepwise reduction with two peaks observed for some samples. The high temperature reduction feature is mainly due to bulk oxygen removal while the low temperature reduction feature has been related to most easily reducible surface capping oxygen of ceria [23]. The reduction features are similar to that of

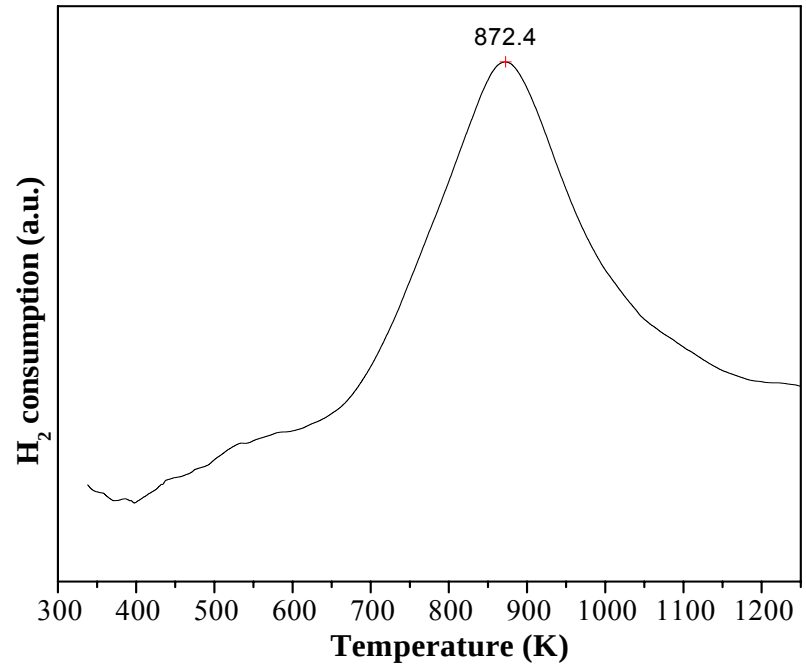

Figure 6.3: The H_2-TPR profile of CeO_2–HfO_2/Al_2O_3 (CHA) sample calcined at 773 K.

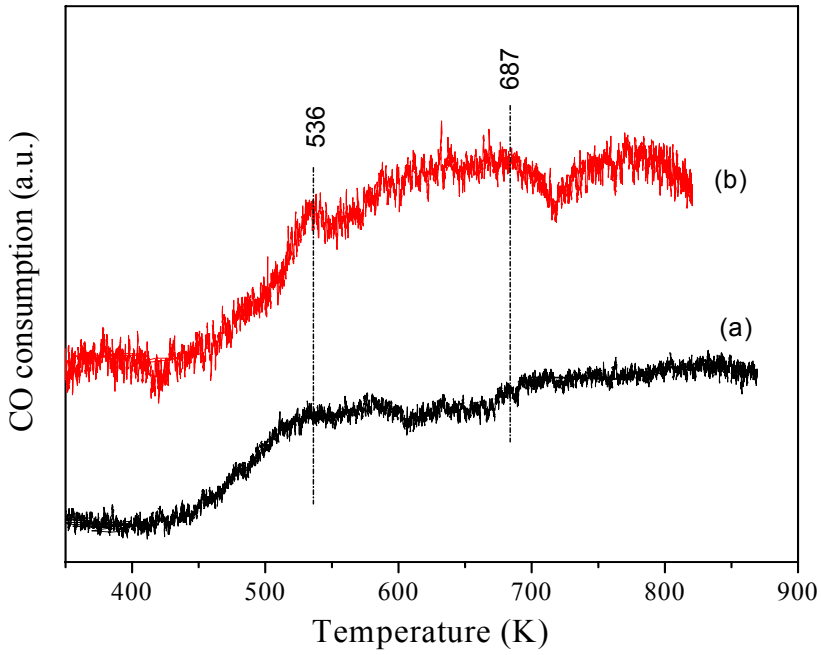

Figure 6.4: The CO-TPR profile of CeO_2–HfO_2/Al_2O_3 (CHA) sample calcined at (a) 773 and (b) 1073 K.

unsupported ceria-hafnia (Fig. 3.4, chapter 1). As could be seen from the Fig. 6.4, the temperature maxima for the CHA samples (calcined at 773 and 1073 K) are centered

around 536 and 687 K. The temperature range for the reduction of the sample is similar to that of unsupported ceria-hafnia.

6.3.5 Scanning Electron Microscopy Studies

SEM measurements were performed to assess the external morphologies of the composite oxides.

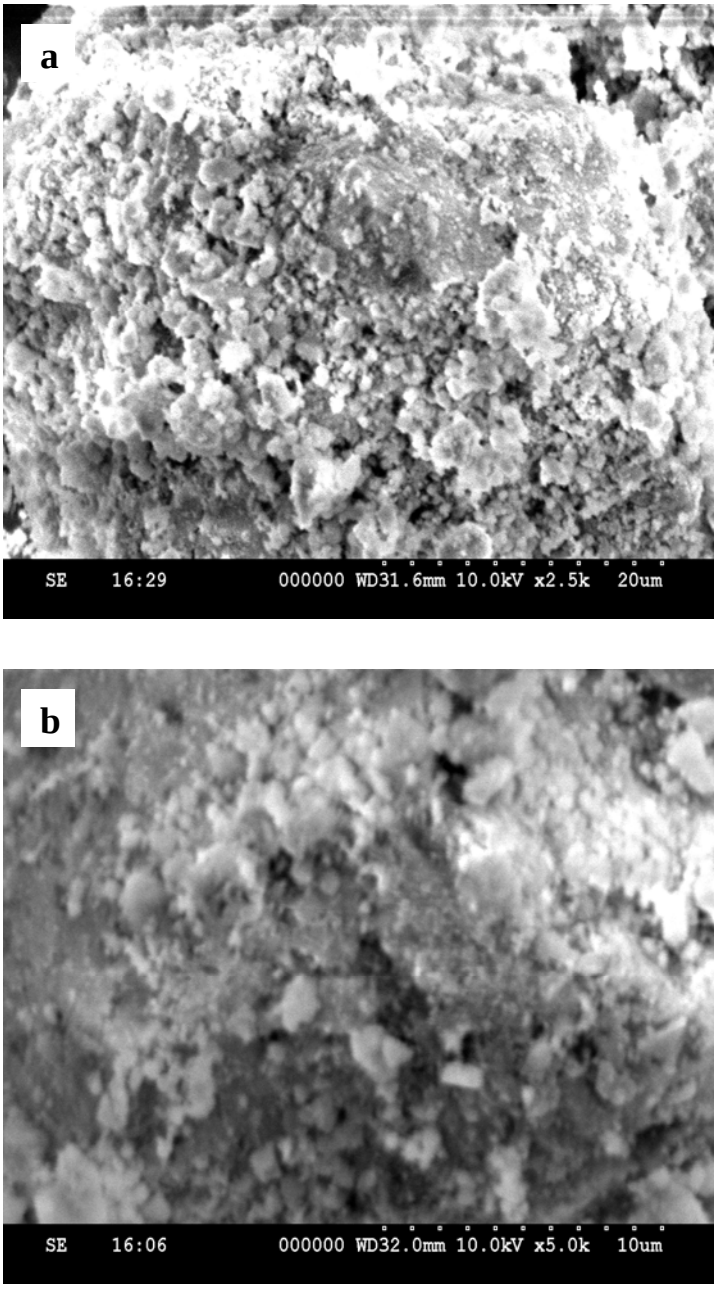

Figure 6.5: SEM micrographs of CeO_2–HfO_2/Al_2O_3 (CHA) samples calcined at (a) 773 and (b) 1073 K.

The micrographs corresponding to the CHA series of samples calcined at 773 and 1073 K, respectively are shown in Figure 6.5a,b. As observed from the SEM images, the samples consist of typical agglomerates of homogeneous morphology of nearly equal particle distribution within the narrow size range. The 773 K calcined samples exhibited more amorphous features and densely packed agglomerates of smaller crystallites. At higher calcination temperature (1073 K) the densely packed homogeneous structures have collapsed due to better crystallization of composite oxide particles with the formation of bigger composite oxides particles. Interestingly, it could be observed from the SEM image of 1073 K calcined sample (Fig. 6.5b) that smaller particles agglomerated to form bigger particles. However, the exact growth of particles could not be confirmed from SEM analysis, so TEM-HREM analysis has been performed and described in the next subheadings.

6.3.6 Transmission Electron Microscopy Studies

To have information on the nanometer sizes of the investigated composite oxides, TEM–HREM analysis was performed and some representative micrographs are included. The corresponding TEM and HREM micrographs for 773 and 1073 K calcined samples are presented in Figures 6.6a,b and 6.7a,b, respectively. In all the images, small, well faceted composite oxide particles deposited on the surface of an amorphous matrix are clearly visible. The particle size distribution of the composite oxide crystals seems to be well distributed on to the support, i.e. homogeneous in nature. It is a known fact that control of microstructure is an important factor for the improvement of OSC in such systems [24]. HREM micrographs give a better perception of the size and dispersion of these composite oxide particles. As observed, the composite oxide particles are agglomerated in nature. Plain faces representing the support could not be seen suggesting the amorphous nature of it. This observation is supported by the XRD results as well. The shapes of the particles are more or less cuboctahedral. Digital Diffraction pattern (DDP) for some selected particles show lattice spacings at 3.1 Å and 2.7 Å characteristics of the fluorite type structure with [110] orientation [25]. Some overlapping regions of the composite oxide particles are seen in the HREM images, which may be responsible for better catalytic activity. As can be seen from the Figures 6.6a and 6.7a, the 773 calcined composite oxide particles have the dimension of ~4–5 nm. Small

increase in particle size (up to ~7–8 nm) with temperature increase to 1073 K is revealed by Figures 6.6b and 6.7b, respectively.

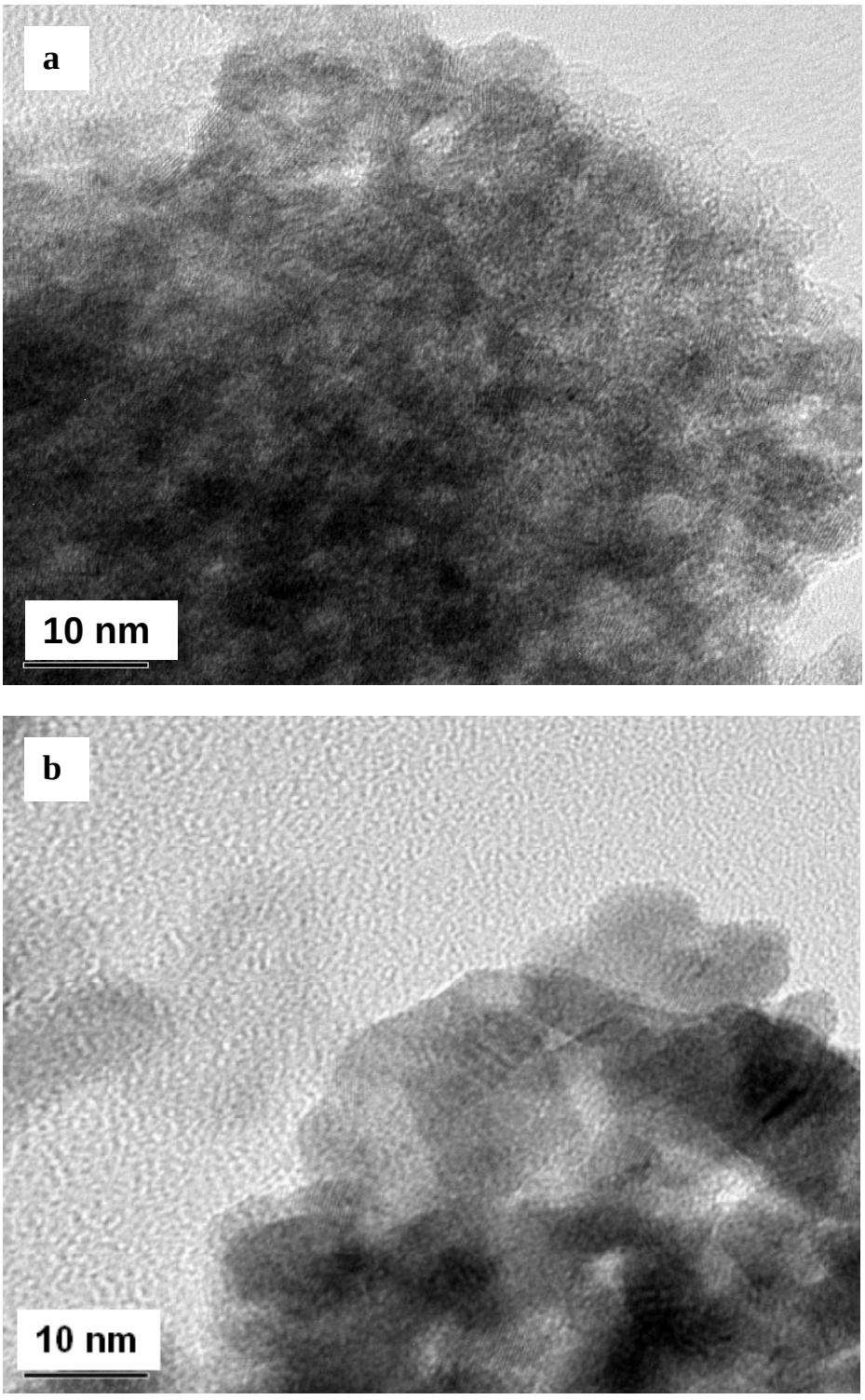

Figure 6.6: TEM micrographs of (a) 773 K and (b) 1073 K calcined CeO_2–HfO_2/Al_2O_3 (CHA) samples.

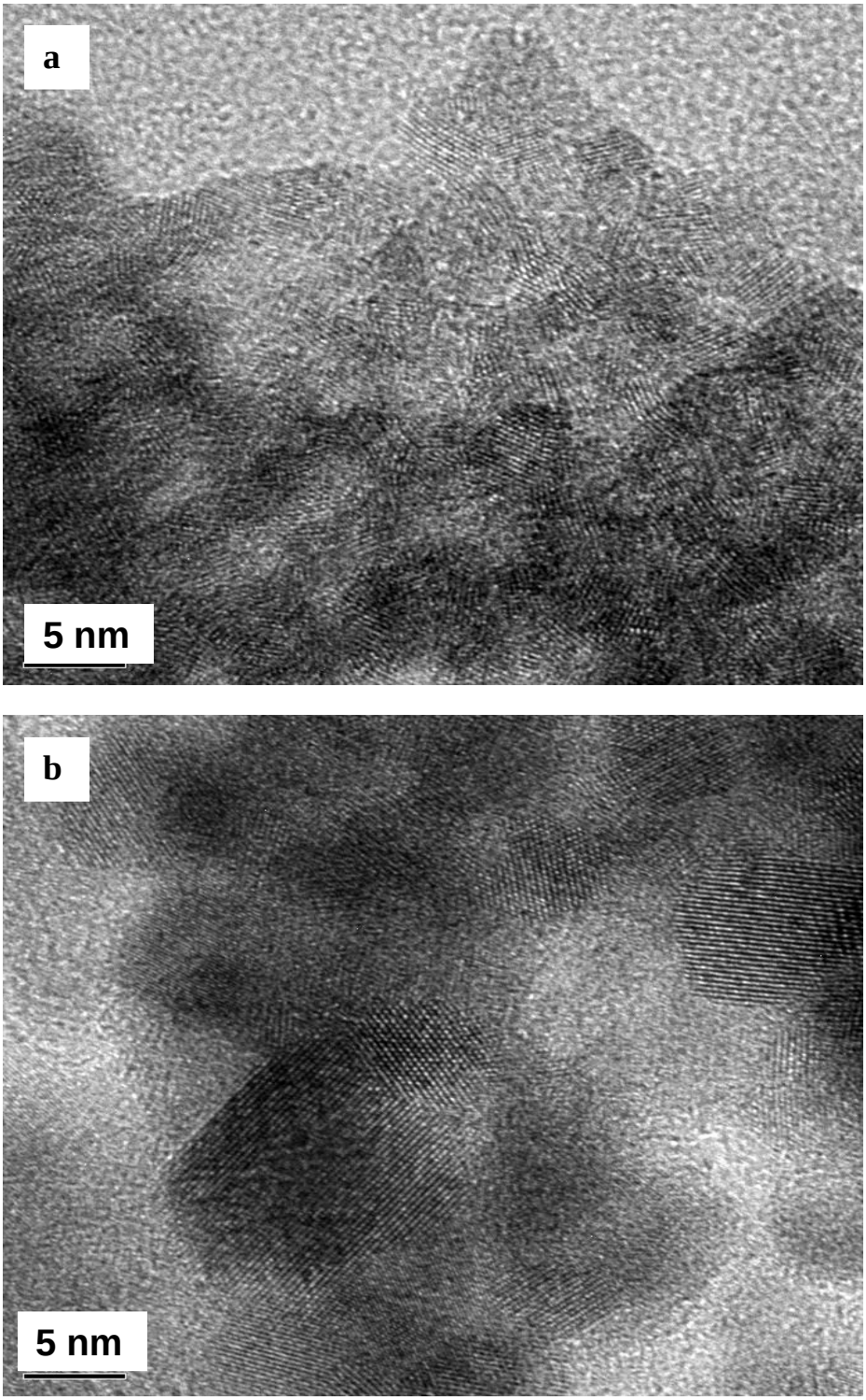

Figure 6.7: HREM micrographs of (a) 773 K and (b) 1073 K calcined CeO_2–HfO_2/Al_2O_3 (CHA) samples.

6.3.7 UV-visible Diffuse Reflectance Spectroscopy Studies

UV–vis DRS spectra of alumina supported ceria–hafnia samples calcined at 773 and 1073 K in the 200–800 nm range are shown in Figure 6.8. It is known that pure CeO_2 exhibits three absorption maxima centered at ~255, 285, and 340 nm in its DR spectra [26]. The latter two absorption maxima are ascribed to $Ce^{4+} \leftarrow O^{2-}$ charge transfer and inter-band transitions, respectively [27]. The former maxima corresponds to $Ce^{3+} \leftarrow O^{2-}$ charge transfer transitions [28]. Specular reflectance effects produced by the strong absorption of ceria in the UV range may lead to such nature of the patterns. Though it might affect the shape of the inter-band transition, the absorption edge position has not been modified remarkably. In the present case, the absorption edge is blue shifted (~247, 287, and 326 nm) with respect to ceria. This blue shift may be the result of decreasing particle size of ceria (quantum size effect) when hafnium is incorporated in to the ceria lattice as evidenced by XRD analysis [27,28].

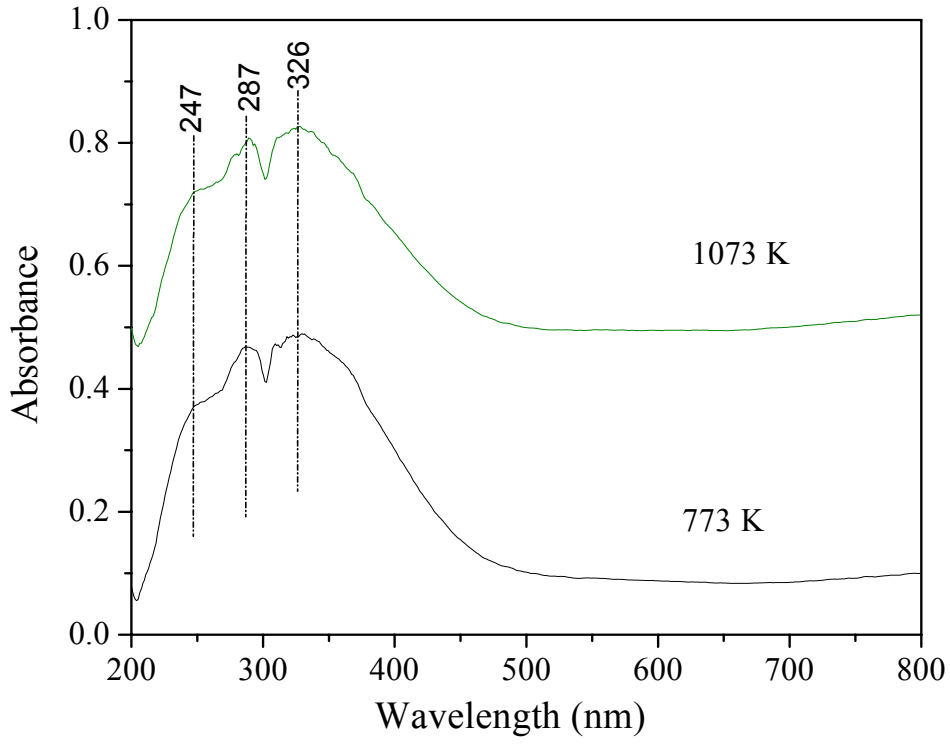

Figure 6.8: UV–vis DRS spectra of CeO_2–HfO_2/Al_2O_3 (CHA) sample calcined at 773 and 1073 K.

Also, it may be due to the increasing contribution of $Ce^{4+} \leftarrow O^{2-}$ charge transfer which is more prominent in case of small crystallites (localized effect). It is interesting to note that the band at ~247 nm, which has been characterized as $Ce^{3+} \leftarrow O^{2-}$ charge transfer transition, is also well resolved in case of both the samples investigated. This leads to the occurrence of oxygen vacancy defects in the samples. There is no clue for the presence of other phases like hafnia or alumina in agreement with XRD results.

6.3.8 Raman Spectroscopy Studies

Raman spectroscopy has some added advantages over IR spectroscopy when the supports used are specially γ-alumina and amorphous alumina, because they absorb strongly below 1000 cm^{-1} and thus the IR bands of the metal oxide species are generally masked by those bands. But Raman bands of these oxides support are very weak or Raman inactive in the same region [29]. Again, as the Raman spectrum of each molecular structure is unique, Raman spectroscopy can discriminate between different molecular structures of the supported metal oxides [30]. It is well reported that the Raman information detected by excitation laser with shorter wavelength is more sensitive to the surface region of samples as the laser with shorter wavelength is closer to the electronic adsorption of samples [31]. We have used two different lasers, UV excitation laser (He-Cd laser with wavelength 325 nm) and visible excitation laser (Ar^+-Kr^+ laser with wavelength 514.53 nm) in the present investigation. The UV- and visible-Raman spectra of the CHA samples calcined at different temperatures are presented in Figures 6.9 and 6.10, respectively. For the space group *Fm*3*m*, the only Raman active mode (F_{2g}) is centered at around 460 cm^{-1} [32]. The UV–Raman spectrum of pure CeO_2 shows Raman active (F_{2g} mode) peak at 469 cm^{-1} [33]. Most probably, a small degree of hydration causes this band shift [30]. However, for CHA samples the F_{2g} band is blue-shifted. The peak observed at ~461 cm^{-1} in all CHA samples is consistent with the presence of a cubic $Ce_xHf_{1-x}O_2$ phase. The emergence of additional prominent bands at 325 and 620 cm^{-1} indicates some distortion of the oxygen sublattice. Another very weak peak observed at around 174 cm^{-1}. Interestingly, the intensity of the Raman band at ~620 cm^{-1} is the highest intensity. The nature of the patterns may be due to the resonance enhancement of the Raman scattering cross section under UV excitation [30]. No Raman lines due to hafnia or alumina were observed corroborating with the XRD results. The band at ~461 cm^{-1} is due

to symmetric O–Ce–O stretching mode [34]. As can be observed from the figure, the relative intensity of the F_{2g} band increased with increasing calcination temperature due to better crystallization of ceria-hafnia solid solution at higher calcination temperatures. The broadness of Raman peaks is due to small particle size and the presence of Al_2O_3 support. It is known that the intensity of the Raman band depends on several factors including grain size and morphology [35]. It is also known from literature that sintering of sample under high temperature conditions leads to the formation of oxygen vacancies, which perturb the local M–O bond symmetry leading to relaxation of symmetry selection rules [36]. The presence of the strong prominent broad band at ~620 cm^{-1} is attributed to a non-degenerate Raman inactive longitudinal optical mode of ceria which arises due to relaxation of symmetry rules [36,37]. In particular, the substitution of hafnium into the ceria lattice with an increase in calcination temperature gives rise to oxygen vacancies, which are responsible for the emergence of this band [38]. The appearance of a weak band at ~325 cm^{-1} is accounted for the displacement of oxygen atoms from their normal lattice positions [34]. Interestingly, these bands gained intensity after calcination at 1073 K, indicating a high disorder of the oxygen sublattice in the fluorite structure. Alumina did not exhibit any Raman features. This gave an impression that alumina forms part of the substrate support on which ceria-hafnia solid solution is dispersed. The absence of any other Raman features provided one more inference that alumina is not forming any compound with cerium and hafnium oxides.

The visible-Raman spectra of CHA samples calcined at 773 and 1073 K is shown in Figure 6.10. The Raman spectra of CHA samples reveal a weak band at ~310 cm^{-1} and a shoulder at ~623 cm^{-1}, in addition to the most intense peaks at 464 cm^{-1}. The most intense peak is due to F_{2g} vibration of the fluorite type lattice. Pure ceria exhibited prominent peaks at 462 and 464 cm^{-1} for 773 and 1073 K calcined samples, respectively, which are due to the F_{2g} mode of the cubic fluorite structure [15,32,39]. No other features existed in the spectra indicating no defects in the CeO_2 crystal lattice. The slight shift in the peak position at higher temperatures to higher wave number signifies changes in bond energies as a consequence of bond lengths as evidenced by lattice parameter estimations. Doping of lighter atom such as Hf subsequent contraction of the ceria unit cell may induce an increase in the F_{2g} band position. In line with XRD results, no Raman features pertaining to HfO_2 and Al_2O_3 were noted. As can be observed from Figure 6.10, the Raman spectra are broad, which could be attributed to the reduction of phonon lifetime in the nanocrystalline regime [37,40–42]. This observation also gives a clue for

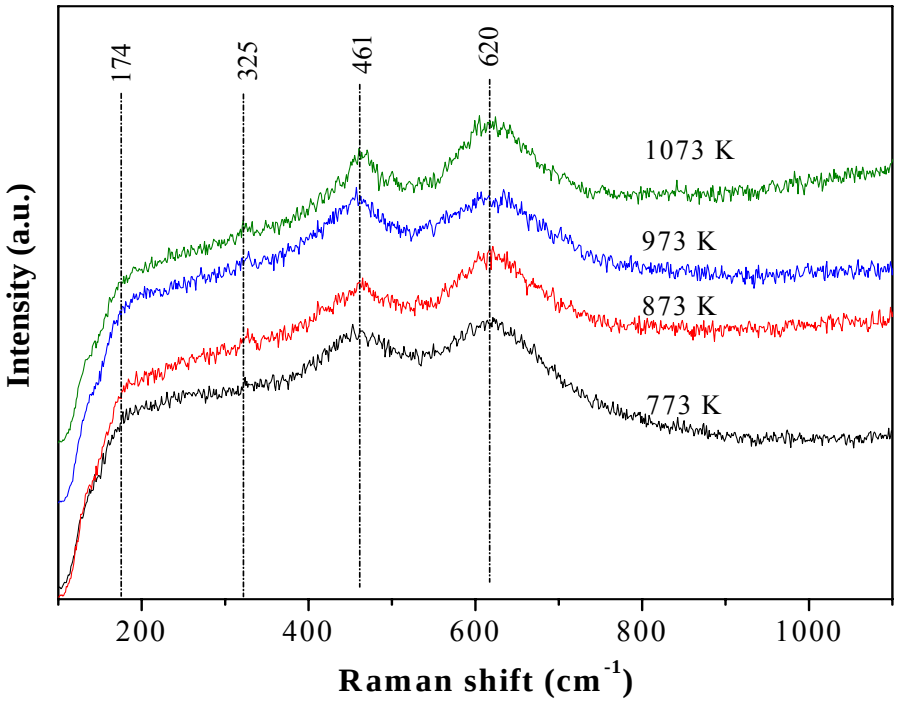

Figure 6.9: UV-Raman spectral patterns of CeO_2–HfO_2/Al_2O_3 (CHA) samples calcined at different temperatures.

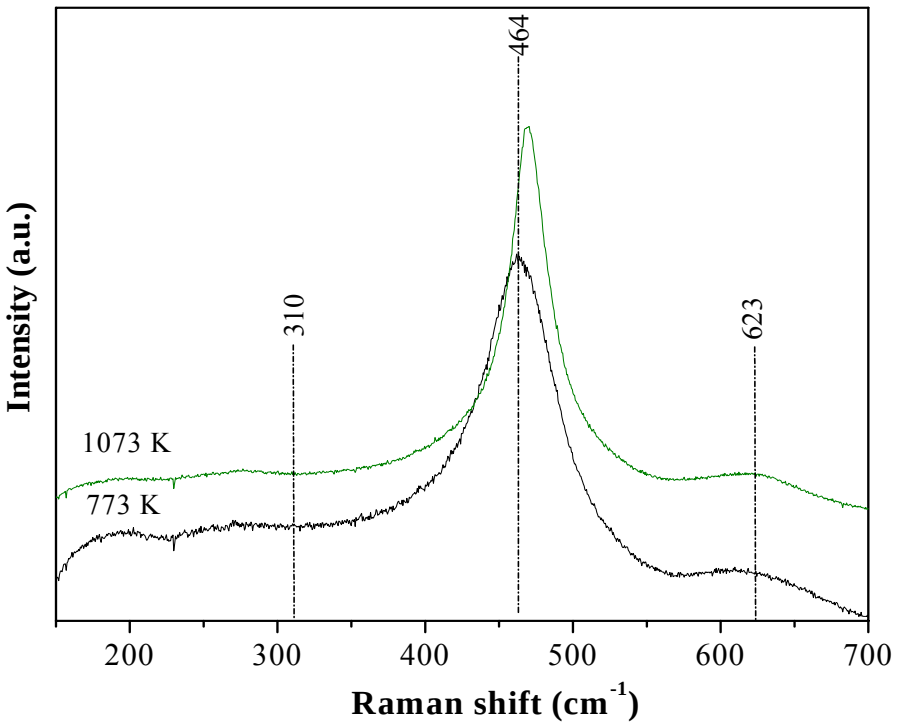

Figure 6.10: Visible-Raman spectral patterns of CeO_2–HfO_2/Al_2O_3 (CHA) samples calcined at 773 and 1073 K.

predicting changes in the grain size and morphology of the prepared samples [43]. The broad band at ~623 cm^{-1} corresponds to the nondegenerate Longitudinal Optical (LO) mode of ceria, [36,37,40–43] arising due to relaxation of symmetry rules which is again linked to oxygen vacancies in the ceria lattice [38,44,45]. This is ascribed to a localized substitution defect vibration [34]. The weak bands observed at around 310 cm^{-1} could be attributed to displacement of oxygen atoms from their ideal fluorite lattice positions [46]. With increasing calcination temperature from 773 to 1073 K, the main Raman band is sharpened with a small shift. This is due to better crystallization of the samples at higher calcination temperatures in line with XRD results [47].

6.3.9 X-ray Photoelectron Spectroscopy Studies

XPS measurements have been performed to acquire the information of oxidation states in the catalytic system. The effect of calcination temperature on the photoelectron peaks of O 1s, Ce 3d, Hf 4f, Hf 4d, and Al 2p for CHA samples are shown in Figures 6.11–6.15, respectively. The corresponding binding energy (eV) values and XPS atomic ratios (Ce/Hf and Ce/Al) are presented in Tables 6.2 and 6.3, respectively.

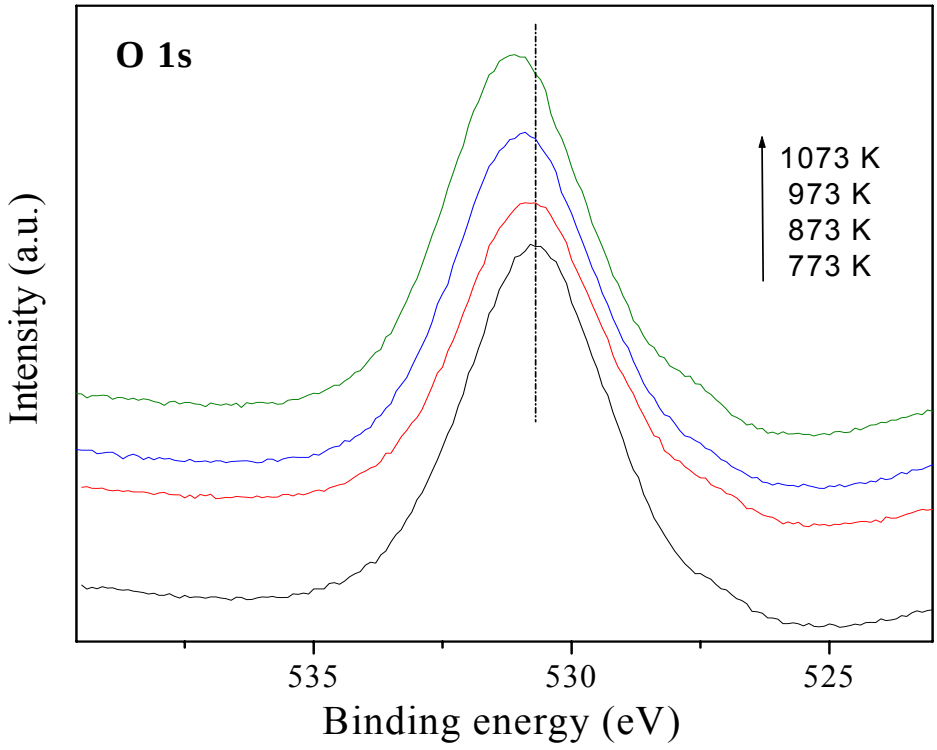

Figure 6.11: O 1s XP spectra of CeO_2–HfO_2/Al_2O_3 (CHA) samples calcined at different temperatures.

The XPS profiles of O 1s core electron level of CHA samples after thermal treatment at 773–1073 K are shown in the Figure 6.11. As can be observed, all the patterns consist of very broad peaks centered at 530.8 eV assigned to the lattice oxygens associated with the oxides. The asymmetric nature of the peaks can be attributed to the different environments for oxides of Ce, Hf, and Al. The very flat nature of the peaks may mask any probable shoulder towards the high binding energy side which is more likely to be present due to absorbed oxygen or to surface hydroxyl species and/or absorbed water present as contaminant at the surface [48]. As the temperature is increased, the peaks get sharpened due to the better crystallization of the samples. No appreciable change in binding energy maxima is noticed with temperature increase which indicates that the chemical state of the oxides remains unaltered.

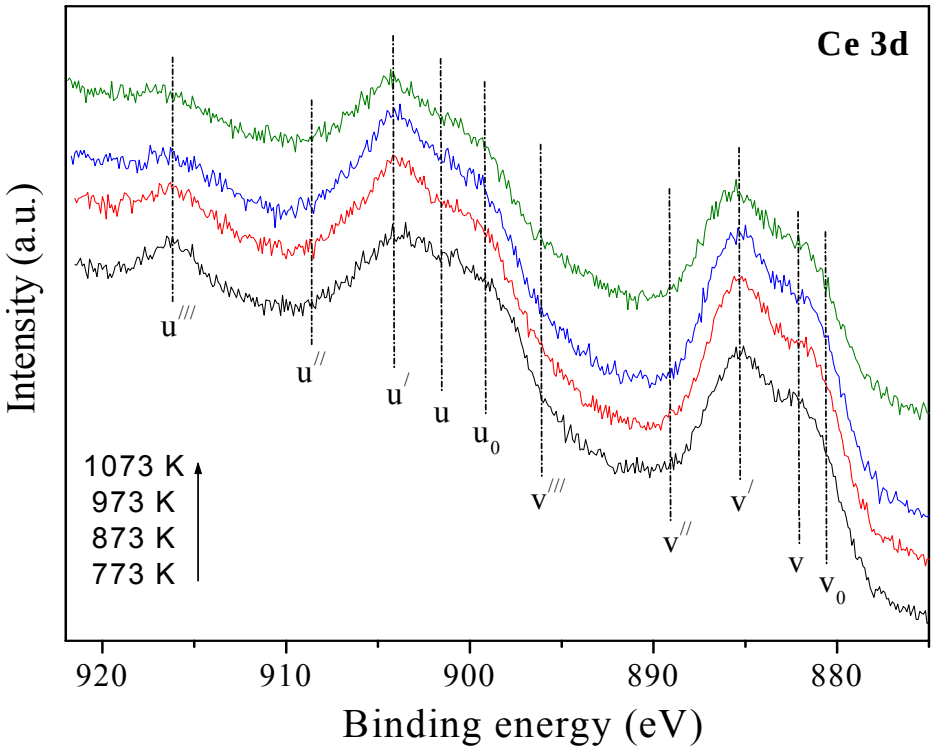

Figure 6.12: Ce 3d XP spectra of CeO_2–HfO_2/Al_2O_3 (CHA) samples calcined at different temperatures.

Due to the hybridization of the O 2p valence band with Ce 4f level, Ce 3d core level XPS pattern of ceria is very complicated resulting in several final states for cerium and a number of overlapping peaks [45,49]. As can be seen from the Figure 6.12, the Ce 3d spectra consists of two sets of spin-orbit multiplets featuring $3d_{3/2}$ and $3d_{5/2}$

(represented as 'u' and 'v' respectively) contributions. The peaks at ~882.1 eV (v) and 900.8 eV (u) are the main lines corresponding to Ce^{4+} state whereas features at 888.5 eV ($v^{//}$), 897.9 eV ($v^{///}$), 907.2 eV ($u^{//}$), and 916.8 eV ($u^{///}$) are satellites related to this state. The main signals of Ce^{3+} (v_0, u_0) are generally noticed at around 881 and 898 eV, respectively. Here, it can be seen that the latter peak is overlapping with $v^{///}$. The satellites to these features ($v^{/}$ and $u^{/}$) occur at 885.6 and 904.8 eV, respectively. It can be observed that the shoulder above 881 eV is made up of a mixture of v and v_0 features and the usual good separation between v and $v^{//}$ (characteristic of only Ce^{4+} state) is prevented by a significant intensity of $v^{/}$ indicating the presence of Ce^{3+} in the sample. Presence of Ce^{4+} state is supported by the considerable intensity of the $u^{///}$ peak. Thus, on the surface of the samples, concentration of both Ce^{4+} and Ce^{3+} are quite comparable. With increase in the calcination temperature, the intensity of the peaks at ~885 eV ($v^{/}$) and ~904 eV ($u^{/}$) increased and that of the peak at ~916 eV ($u^{///}$) decreased suggesting a higher amount of Ce^{3+} in the samples treated at higher temperatures.

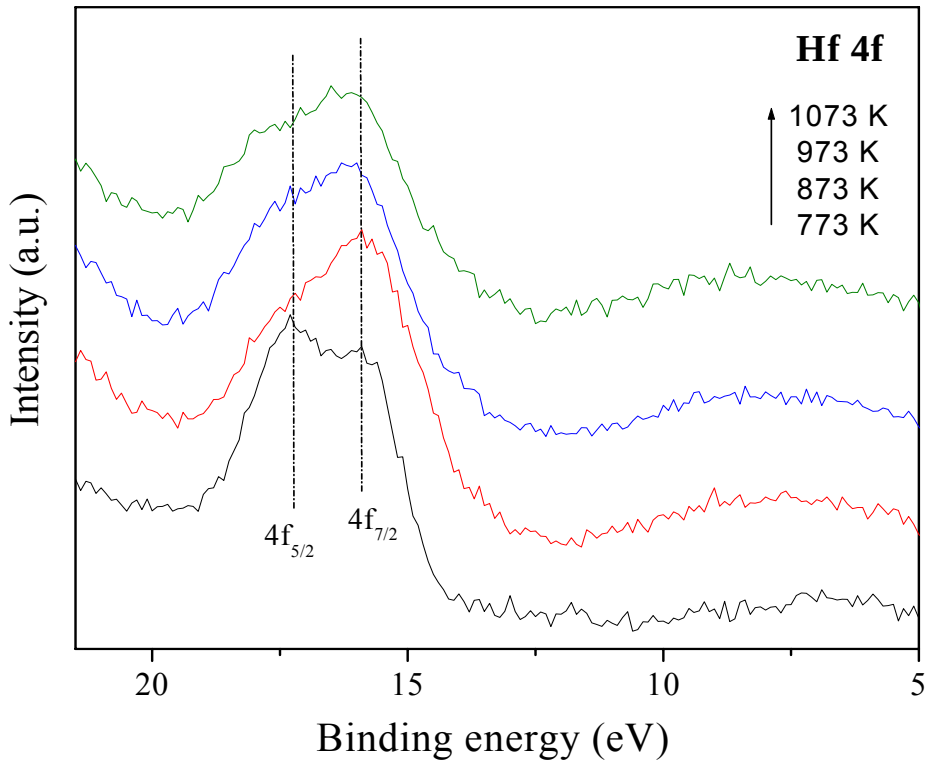

Figure 6.13: Hf 4f XP spectra of CeO_2–HfO_2/Al_2O_3 (CHA) samples calcined at different temperatures.

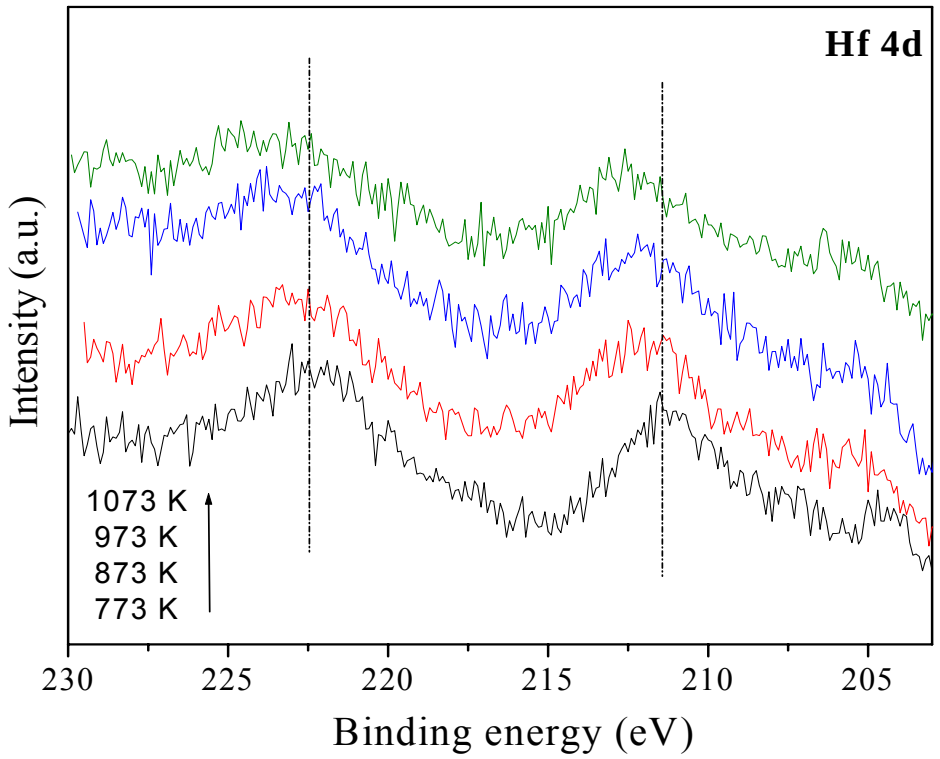

Figure 6.14: Hf 4d XP spectra of CeO_2–HfO_2/Al_2O_3 (CHA) samples calcined at different temperatures.

Figures 6.13 and 6.14 show the core level XP spectra of Hf 4f and Hf 4d, respectively corresponding to the CHA samples calcined at different temperatures. As could be observed from the XP spectra of Hf 4f (Fig. 6.13), there are two features at about 15.9 and 17.3 eV, respectively. It is reported that the Hf 4f spectrum consists of two components, the $4f_{7/2}$ part at 16.79 ± 0.08 eV and the $4f_{5/2}$ part at 18.54 ± 0.10 eV [50]. The peak positions of Hf 4f photoelectrons are known to be very sensitive to the binding states of the hafnium species [51,52]. According to a database, the metallic hafnium species reveals the Hf $4f_{7/2}$ peak at 14.3–14.4 eV, while HfO_2 shows it at 16.7 eV. Lee et al. investigated HfO_2 films on a silicon substrate by synchrotron XPS and found the binding energies of Hf $4f_{7/2}$ and Hf $4f_{5/2}$ at 17.55 and 19.26 eV, respectively [53]. However, the difference of about 1.4 eV in the binding energies between the Hf $4f_{7/2}$ and Hf $4f_{5/2}$ in the present investigation is in line with the reported values [51]. On the other hand, the XP spectra of Hf 4d photoelectron peak in relatively very scarce in the literature. As observed the spectra consists of two features in the binding energy values of ~224 and ~212 eV, respectively, which are in good agreement with the data presented in 'The Handbook of X-

ray Photoelectron Spectroscopy' [51]. On the whole, from the XP spectra of Hf 4f and Hf 4d, it is observed that Hf is mainly in 4+ oxidation state.

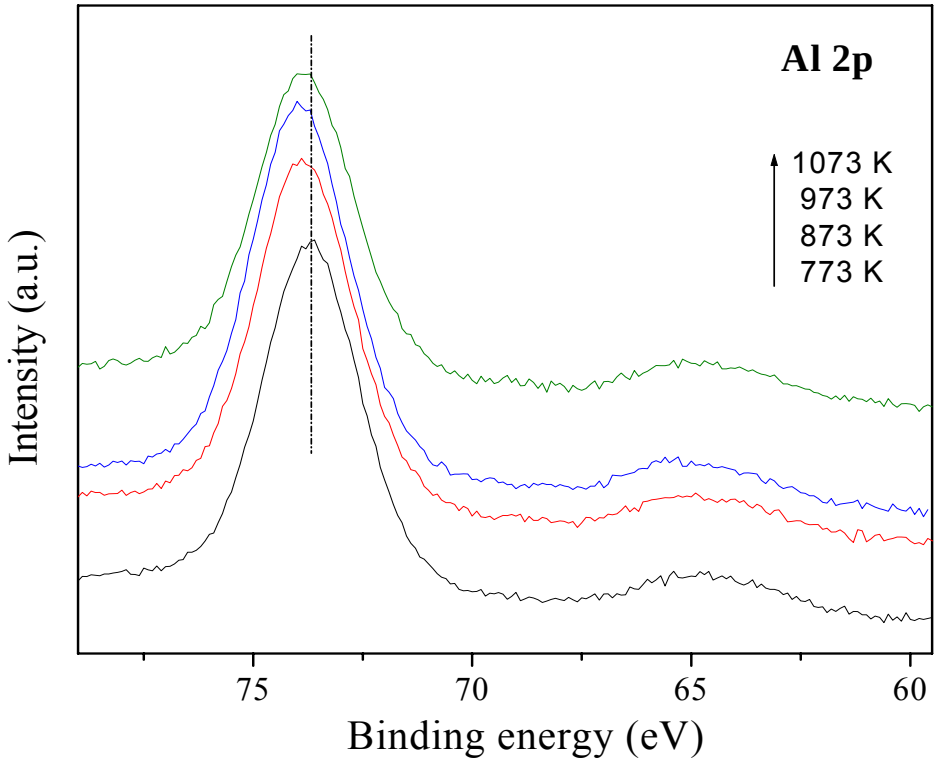

Figure 6.15: Al 2p XP spectra of CeO_2–HfO_2/Al_2O_3 (CHA) samples calcined at different temperatures.

The Al 2p core level patterns for the CHA samples are presented in the Figure 6.15. Dufresne et al. reported the binding energy of Al^{3+} in alumina (amorphous or γ-alumina) at 74.8 eV [54]. In the present case, it is observed at 73.6–74 eV. In the literature, however, large range of binding energies (73.7–74.8 eV) could be found for Al 2p core level of alumina [51,55]. As can be noticed from the figure, all the patterns look alike, intensity slightly enhancing with the temperature increase possibly due to better crystallization of the support. After this observation, it can be suggested that there is no formation of any composite oxide phases between alumina and ceria and/or hafnia, which has been already substantiated by XRD analysis.

As presented in Table 6.3, the atomic ratios for Ce/Hf and Ce/Al did not change considerably when the temperature was increased from 773 to 1073 K. This indicates that there is no change of composition or in other words, no further reaction occurred among the components within the temperature range of 773–1073 K.

Table 6.2: XPS core level electron binding energies (eV) of the CeO_2–HfO_2/Al_2O_3 (CHA) samples calcined at different temperatures

Calcination Temp. (K)	Binding Energy (eV)				
	O 1s	Ce 3d	Hf 4f	Hf 4d	Al 2p
773	530.8	881.2	17.3 (15.9)	223.0 (211.8)	73.6
873	530.9	881.2	17.3 (15.9)	223.3 (212.4)	73.9
973	530.9	881.3	17.4 (16.2)	223.8 (212.5)	74.0
1073	531.1	881.4	17.6 (16.2)	224.2 (212.6)	74.0

Table 6.3: XPS atomic ratio of the CeO_2–HfO_2/Al_2O_3 (CHA) samples calcined at different temperatures

Calcination Temperature (K)	Atomic Ratio	
	Ce/Hf	Ce/Al
773	2.964	0.203
873	2.851	0.202
973	2.729	0.191
1073	2.582	0.180

6.4 Conclusions

Ceria–hafnia composite oxides dispersed over Al_2O_3 support possessing high specific surface area and good thermal stability were successfully synthesized by a deposition coprecipitation method. The X-ray diffraction peaks revealed the crystal faces corresponding to a fluorite type structure of ceria-hafnia solid solution and there is no indication of formation of other compounds. The TEM–HREM studies showed that the particles of supported ceria–hafnia solid solutions have the dimension of ~4–8 nm within the investigated temperature range. The UV–vis DRS measurements indicated the lowering of symmetry and consequent strain development at the cerium sites. Raman spectroscopy studies show the formation of oxygen vacancies in the composite oxide lattice. The XPS analysis revealed the presence of Ce in both 3+ and 4+ oxidation states and Hf and Al in 4+ and 3+ oxidation states, respectively. There was no formation of any composite oxide phase between alumina and ceria and/or hafnia as supported by XRD analysis. Thus the use of various spectroscopic and non-spectroscopic techniques provided interesting information regarding the physicochemical characteristics of alumina supported nanosized ceria-hafnia composite oxides.

6.5. References

[1] A. Trovarelli, in: Catalysis by Ceria and Related Materials, Catalytic Science Series, Hutchings, G. J. Ed., Imperial College Press, London, 2002, Vol. 2.

[2] R. Wang, P.A. Crozier, R. Sharma, J.B. Adams, Nano Lett. 8 (2008) 962.

[3] M. Sugiura, Catal. Surv. Asia 7 (2003) 77.

[4] A. Iglesius-Juez, A. Martinez-Arias, M. Fernandez-Garcia, J. Catal. 221 (2004) 148.

[5] B.M. Reddy, P. Lakshmanan, P. Bharali, P. Saikia, G. Thrimurthulu, M. Muhler, W. Grünert, J. Phys. Chem. C 111 (2007) 10478.

[6] H.S. Gandhi, A.G. Piken, M. Shelef, R.G. Delosh, SAE Paper 760201 (1976) 55.

[7] X. Wu, X. Wu, Q. Liang, J. Fan, D.Z. Weng Xie, S. Wei, Solid State Sci. 9 (2007) 636.

[8] J. Kaspar, P. Fornasiero, N. Hickey, Catal. Today 77 (2003) 419.

[9] R.D. Monte, J. Kaspar, J. Mater. Chem. 15 (2005) 633.

[10] R. Si, Y.W. Zhang, L.M. Wang, S.J. Li, B.X. Lin, W.S. Chu, Z.Y. Wu, C.H. Yan, J. Phys. Chem. C 111 (2007) 787.

[11] J. Kaspar, P. Fornasiero, M. Graziani, Catal. Today 50 (1999) 285.

[12] M.W. Zhao, M.Q. Shen, J. Wang, J. Catal. 248 (2007) 258.

[13] B.M. Reddy, P. Bharali, P. Saikia, A. Khan, S. Loridant, M. Muhler, W. Grünert, J. Phys. Chem. C 111 (2007) 1878.

[14] O. Pozdnyakova-Tellinger, D. Teschner, J. Kroehnert, F.C. Jentoft, A. Knop-Gericke, R. Schlogl, A. Wootsch, J. Phys. Chem. C 111 (2007) 5426.

[15] J.Z. Shyu, W.H. Weber, H.S. Gandhi, J. Phys. Chem. 92 (1988) 4964.

[16] M.H. Yao, R.J. Baird, F.W. Kunz, T.E. Hoosty, J. Catal. 166 (1997) 67.

[17] R.D. Monte, P. Fornasiero, J. Kaspar, M. Graziani, J.M. Gatica, S. Bernal, H.A. Gomez, Chem. Commun. 21 (2000) 2167.

[18] R.D. Monte, P. Fornasiero, S. Desinan, J. Kaspar, J.M. Gatica, J.J. Calvino, E. Fonda, Chem. Mater. 16 (2004) 4273.

[19] M. Akira, S. Tadashi, K. Takaaki, K. Koichi, S. Akihiko, S. Hirofumi, Appl. Catal. B 78 (2007) 210.

[20] B.M. Reddy, K.N. Rao, G.K. Reddy, A. Khan, S.-E. Park, J. Phys. Chem. C 111 (2007) 18751.

[21] F. Fally, V. Perrichon, H. Vidal, J. Kaspar, G. Blanco, J.M. Pintado, S. Bernal, G. Colon, M. Daturi, J.C. Lavalley, Catal. Today 59 (2000) 373.

[22] P. Vidmar, J. Kaspar, P. Fornasiero, M. Graziani, J. Phys. Chem. B 102 (1998) 557.

[23] M. Boaro, M. Vicario, C. de Leitenburg, G. Dolcetti, A. Trovarelli, Catal. Today 77 (2003) 407.

[24] M. Ozawa, K. Matuda, S. Suzuki, J. Alloys Compd. 303–304 (2000) 56.

[25] A. Galtayries, G. Blanco, G.A. Cifredo, D. Finol, J.M. Pintado, H. Vidal, R. Sporken, S. Bernal, Surf. Interface Anal. 27 (1999) 941.

[26] B.M. Reddy, P. Bharali, G. Thrimurthulu, P. Saikia, L. Katta, S.-E. Park, Catal. Lett. 123 (2008) 327.

[27] A. Bensalem, J.C. Muller, F.B. Verduraz, J. Chem. Soc. Faraday Trans. 88 (1992) 153.

[28] A. Bensalem, F.B. Verduraz, M. Delamar, G. Bugli, Appl. Catal. 121 (1995) 81.

[29] I.E. Wachs, Catal. Today 27 (1996) 437.

[30] Y.T. Chua, P.C. Stair, I.E. Wachs, J. Phys. Chem. B 105 (2001) 8600.

[31] M.-F. Luo, Z.-L. Yan, L.-Y. Jin, M. He, J. Phys. Chem. B 110 (2006) 13068.

[32] B.M. Reddy, A. Khan, Catal. Surv. Asia 9 (2005) 155.

[33] B.M. Reddy, P. Saikia, P. Bharali, Y. Yamada, T. Kobayashi, M. Muhler, W. Grunert, J. Phys. Chem. C 112 (2008) 16393.

[34] M. Yashima, H. Arashi, M. Kakihana, M. Yoshimura, J. Am. Ceram. Soc. 77 (1994) 1067.

[35] J.E. Spanier, R.D. Robinson, F. Zhang, S.W. Chan, I.P. Herman, Phys. Rev. B 64 (2001) 245407.

[36] X.-M. Lin, L.-P. Li, G.-S. Li, W.-H. Su. Mater. Chem. Phys. 69 (2001) 236.

[37] W.H. Weber, K.C. Hass, J.R. McBride, Phys. Rev. B. 48 (1993) 178.

[38] J.R. McBride, K.C. Hass, B.D. Poindexter, W.H. Weber, J. Appl. Phys. 76 (1994) 2435.

[39] A. Martinez-Arias, M. Fernandez-Garcia, L.N. Salamanca, R.X. Valenzuela, J.C. Conesa, J. Soria, J. Phys. Chem. B 104 (2000) 4038.

[40] P. Parayanthal, F.H. Pollak, Phys. Rev. Lett. 52 (1984) 1822.

[41] H. Richter, Z.P. Wang, L. Ley, Solid State Commun. 39 (1981) 625.

[42] M. Fujii, S. Hayashi, K. Yamamoto, Appl. Phys. Lett. 57 (1990) 2692.

[43] J.E. Spanier, R.D. Robinson, F. Zhang, S.W. Chan, I.P. Herman, Phys. Rev. B 64 (2001) 245407.

[44] B.M. Reddy, P. Lakshmanan, A. Khan, S. Loridant, C.L. Cartes, T.C. Rojas, A. Fernández, J. Phys. Chem. B 109 (2005) 13545.

[45] A.B. Hungria, A. Martinez-Arias, M. Fernandez-Garcia, A. Iglesius-Juez, A. G. Ruiz, J.J. Calvino, J.C. Conesa, J. Soria, Chem. Mater. 15 (2003) 4309.

[46] V.S. Escribano, E.F. Lopez, M. Panizza, C. Resini, J.M.G. Amores, G. Busca, Solid State Sci. 5 (2003) 1369.

[47] S. Meriani, G. Spinolo, Powder Diffract. 2 (1987) 255.

[48] S. Damyanova, C.A. Perez, M. Schmal, J.M.C. Bueno, Appl. Catal. A Gen. 234 (2002) 271.

[49] F.L. Normand, J.E. Fallah, L. Hilaire, P. Legare, A. Kotani, J.C. Parlebas, Solid State Commun. 71 (1989) 885.

[50] T. Brezesinski, B. Smarsly, K.-I. Iimura, D. Grosso, C. Boissiere, H. Amenitsch, M. Antonietti, C. Sanchez, Small 8−9 (2005) 889.

[51] C.D. Wagner, W.M. Riggs, L.E. Davis, J.F. Moulder, in: Handbook of X-ray Photoelectron Spectroscopy, G.E. Muilenberg, Ed., Perkin-Elmer Corporation, Eden Prairie, MN, 1978.

[52] V. Cosnier, M. Olivier, G. Theret, A. Andre, J. Vac. Sci. Technol. A 19 (2001) 2267.

[53] J.C. Lee, S.J. Oh, M. Cho, C.S. Hwang, R. Jung, Appl. Phys. Lett. 84 (2004) 1305.

[54] P. Dufresne, E. Payen, J. Grimblot, J.P. Bonnelle, J. Phys. Chem. 85 (1981) 2344.

[55] A. Galtayries, G. Blanco, G.A. Cifredo, D. Finol, J.M. Pintado, H. Vidal, R. Sporken, S. Bernal, Surf. Interface Anal. 27 (1999) 941.

Chapter 7

This chapter presents the results and discussion pertaining to the activity studies of the synthesized catalyst systems for oxygen storage/release capacity, CO oxidation, soot oxidation, and selective dehydration of 4-methylpentan-2-ol, respectively.

CATALYTIC ACTIVITY STUDIES

7.1 Introduction

The results and discussion pertaining to the structural characteristics of unsupported CeO_2–HfO_2 and CeO_2–ZrO_2 and various supported CeO_2–HfO_2 catalytic systems were presented in chapters 3–6, respectively. The present chapter is compiled with the catalytic activity results obtained with the synthesized nanosized multicomponent composite oxides. Interestingly, the synthesized unsupported and supported ceria-hafnia composite oxides can be used as active catalysts as well as a novel composite oxide support in order to obtain different type of catalysts for several catalytic applications. It has been observed from the recent literature that these oxides are quite different from the conventional catalytic supports such as SiO_2, Al_2O_3, ZrO_2, and MgO, owing to their typical redox characteristics and the ability to influence the catalytic activity of noble metals and transition metals/metal oxides [1–4]. The oxygen storage capacity (OSC) is the most important characteristics of the ceria-based solid solutions and responsible for their extensive application in various catalytic applications, especially in three-way catalytic (TWC) applications. CO oxidation is one of the key steps in the overall process of the TWCs, and therefore it has frequently been used as a probe reaction over ceria-based materials to evaluate different catalyst formulations and investigate mechanistic issues [1,2,5–9]. Recently ceria-based composite oxides have attracted a lot of attention for oxidation of diesel soot particulates and reduction of toxic greenhouse gases [10–13]. In particular, the incomplete combustion that occurs in the diesel engines leads to huge emissions of atmospheric pollutants as soot particulates and toxic gases. Soot emission is a significant component of air pollution and is harmful for both human beings and the environment [14]. Among several techniques that have been developed for reducing the emissions from diesel engines, filtering followed by catalytic oxidation is one of the most promising options. This approach is based on the application of a catalyst to achieve the onset of regeneration at a significantly lower temperature [13]. Therefore, the synthesized unsupported CeO_2–HfO_2 and CeO_2–ZrO_2 and various supported CeO_2–HfO_2 composite oxides were tested for their OSC properties, CO oxidation, and soot oxidation activity. Metal oxides are used both for their acid-base and redox properties in heterogeneous catalysis [15]. To test the acid-base properties of the synthesized nanosized composite

oxides, some of the catalysts were also evaluated for the selective dehydration of 4-methylpentan-2-ol to 4-methylpent-1-ene.

7.2 Potential Oxygen Storage Capacity Measurement

The oxygen storage/release characteristics (OSC) of ceria-based solid solutions are a crucial requirement for the automotive three-way catalysts (TWCs) and especially oxidation reactions such as carbon monoxide and soot oxidation. Pure-CeO_2 has a relatively small oxygen storage capacity compared to the composite oxides of ceria, because only the surface oxygen is available for OSC [16]. Basically, the high OSC of CeO_2–HfO_2 and CeO_2–ZrO_2 solid solution comes from the contribution of dissolved HfO_2 or ZrO_2, which can release the oxygen inside the CeO_2 lattice at relatively low temperatures such as 773 K. The potential catalytic performance was tested by the oxygen release characteristics of the synthesized nanosized composite oxide powders under flow of dry air in the temperature range 573–1073 K. The change of weight of the sample was monitored by the thermogravimetric (TG) measurement under cyclic heat treatment in flowing air. A TGA/DTA analyzer was employed to evaluate the oxygen storage characteristics of the investigated samples. The heat treatment cycle consisted of a first run up to 1073 K, cooling to 423 K, and a second heating treatment to 1073 K again. All the heating and cooling rates were 5 K min^{-1}. The weight loss of sample in the second heating TG data was used as a measure of oxygen release properties of the composite powders between 573 and 1073 K. The heat treatment temperature maxima (1073 K) correspond to the moderate thermal condition of practical automotive exhaust gases. This technique of OSC evaluation is essentially similar to that described previously [17,18].

Depending on the temperature at oxygen partial pressure P_{O_2} = 0.2 atm., a part of cerium ion (Ce^{4+}) in ceria changes to Ce^{3+}. The reaction of oxygen release from CeO_2 is described in equation 7.1.

$$CeO_2 \rightarrow Ce_2O_3 + 1/2\ O_2 \qquad (7.1)$$

Since the value of oxygen vacancy content is relatively meager, while writing the equation for Ce-Hf oxide solid solutions, both the vacancy content 'δ' and structural change

considerations must be taken into account. The equation for ceria-hafnia solid solutions is as follows.

$$Ce^{4+}_{1-x}\, Hf_xO_2 \rightarrow (Ce^{4+}_{1-2\delta}\, Ce^{3+}_{2\delta})_{1-x}\, Hf_xO_{2-\delta} + \delta/2O_2 \qquad (7.2)$$

When oxygen is removed, the crystal acquires overall positive charge, in order to keep the crystal neutral, two electrons have to be introduced per oxygen ion removed. These are associated with two cerium atoms that will change charge from +4 to +3. The equation 7.2 clearly indicates that for every 'δ' unit oxygen loss, 2δ units of cerous ions are formed in the system.

Table 7.1: The percentage weight loss, oxygen vacancy content (δ) and the corresponding total oxygen storage capacity of CeO_2–HfO_2/Al_2O_3 (CHA), CeO_2–HfO_2/TiO_2 (CHT), and CeO_2–HfO_2/SiO_2 (CHS) samples calcined at 773 K in the temperature range 573–1073 K in flowing air environment

Catalyst	Weight loss (%)	Oxygen vacancy content (δ)	Total OSC (μ moles O_2/ g Ce-Hf-Ox)
CHA	2.6002	0.832	1273.4
CHT	2.275	0.728	1026.8
CHS	2.115	0.676	881.8

From the Table 7.1, it could be seen that alumina supported CeO_2–HfO_2 (CHA) showed highest total OSC, which is followed by CHT and CHS samples. The total OSC of unsupported CeO_2–HfO_2 and CeO_2–ZrO_2 samples calcined at 773 K were fund to be 185.5 and 156.3 μ moles O_2/ g Ce-Hf-Ox and Ce-Zr-Ox, respectively. These values were obtained due to the 0.59347% weight loss for CH and 0.5% weight loss for CZ, respectively in the second heat cycle of the measurement. Thus, the influence of support is evident from the enhancement in their OSC values. Among the supported systems, the OSC of CHS sample calcined at 773 K was found to be the lowest one, which however is higher than unsupported Ce-Hf composite oxide. The OSC of ceria-based solid solutions depends on several factors, such as surface area, particle size, method of preparation, and nature of dopants. The process of oxygen-vacancy formation is closely related to the quantum effect of localization/delocalization of the 4f electron of cerium, which is the basis for the oxygen storage capacity of the cerium oxide [19]. Under reduction conditions,

oxygen leaves the surface and vacant sites are formed. This process is facilitated by a simultaneous condensation of two electrons into localized f-level traps on two cerium atoms. When an oxygen atom moves diffusively toward the surface or oxygen vacancy moves, these electrons localize on cerium atoms in the immediate surrounding of the vacancy, and correspondingly, they delocalize and transfer to oxygen from Ce sites when the vacancy leaves. Thus, the formation of reduced oxides is a combined process of formation, migration, and ordering of virtual Ce^{3+}-vacancy complexes. When the external conditions change from oxygen poor to oxygen rich, this process behaves reversibly. This makes the oxygen storage-and-release ability of ceria a remarkable property used in many modern environmentally friendly applications [19].

7.3 CO Oxidation Reaction

The oxidation of CO was conducted at atmospheric pressure and at temperatures in the range of 300–773 K using the fixed bed micro-reactor under plug flow conditions at the heating rate of 5 K min^{-1}. About 100 mg of the catalyst of the 250–355 μm sieve fraction was placed in the quartz reactor. These samples were diluted with quartz particles of the same sieve fraction. The temperature was measured directly from the fixed bed using a thermocouple that was placed in the hollow part of the reactor. The gas mixtures used were 10.2% O_2 in argon; and 9.98% CO in argon. The total flow rates were maintained by mass flow controllers.

The catalytic activity for conversion of CO and yield of CO_2 of the unsupported Ce-Hf-oxide and Ce-Zr-oxide samples calcined at 773 K in the temperature range 400 to 773 K are presented in Figures 7.1 and 7.2, respectively. It is evident from Fig. 7.1 that the Ce-Hf-oxide sample exhibits better activity in terms of total conversion as well as light off temperature (50% conversion, $T_{1/2}$). The Ce-Hf-oxide sample shows ~100% conversion at 773 K (highest temperature investigated) with a $T_{1/2}$ of 577 K. On the other hand, Ce-Zr-oxide provides 85% with a $T_{1/2}$ of 695 K, under the same experimental conditions [20,21]. The yield of CO_2 for the CH and CZ samples are presented in Fig. 7.2. The yield of CO_2 suggests that there is no mass loss in the reaction process with the yield almost identical to the CO conversion. This reflects the accuracy in the experimental setup also. Figures 7.3 and 7.4, respectively show the conversion of CO and yield of CO_2 for the CH and CZ

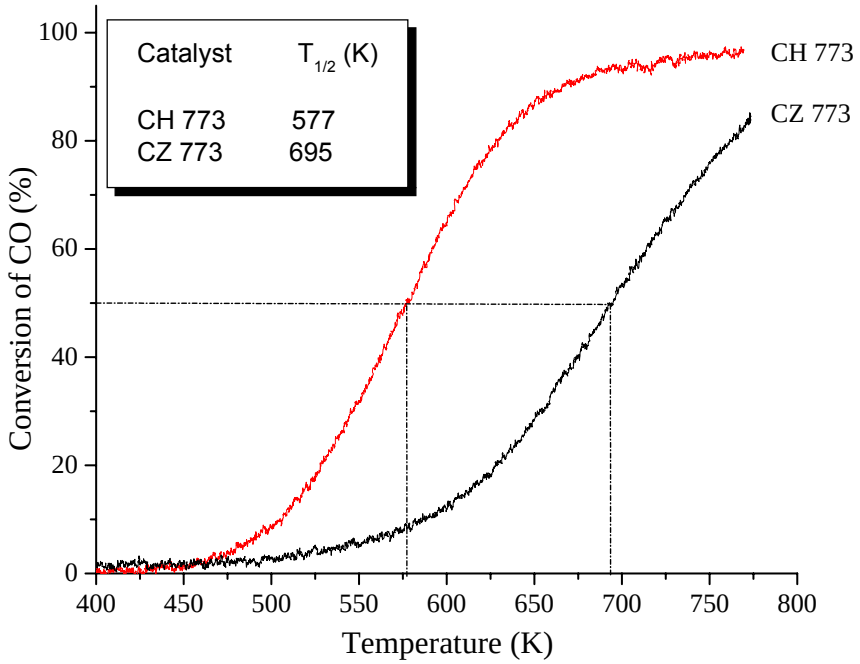

Figure 7.1: Conversion of CO over CeO_2–HfO_2 (CH) and CeO_2–ZrO_2 (CZ) catalysts calcined at 773 K as a function of reaction temperature. Inset shows the corresponding $T_{1/2}$.

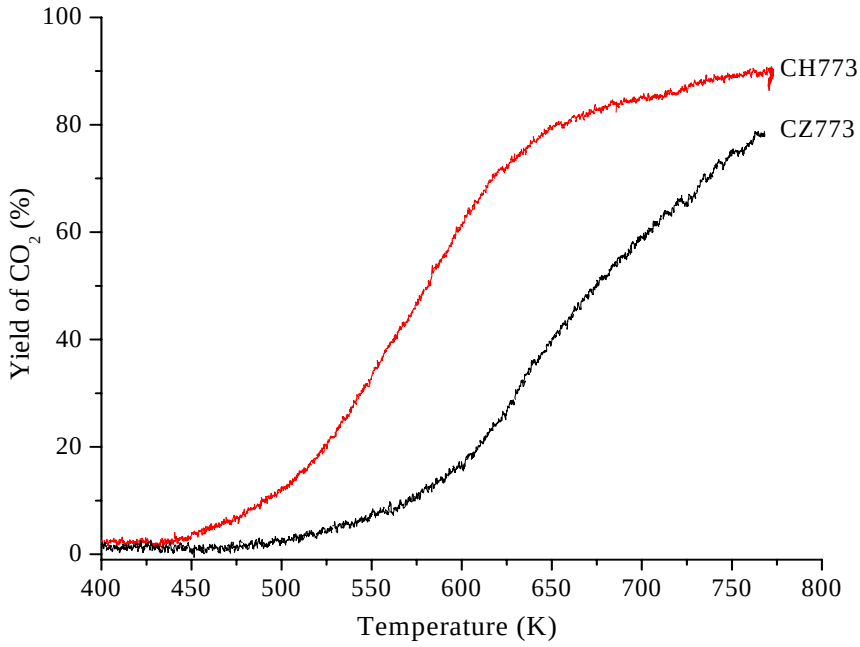

Figure 7.2: Yield of CO_2 over CeO_2–HfO_2 (CH) and CeO_2–ZrO_2 (CZ) catalysts calcined at 773 K as a function of reaction temperature.

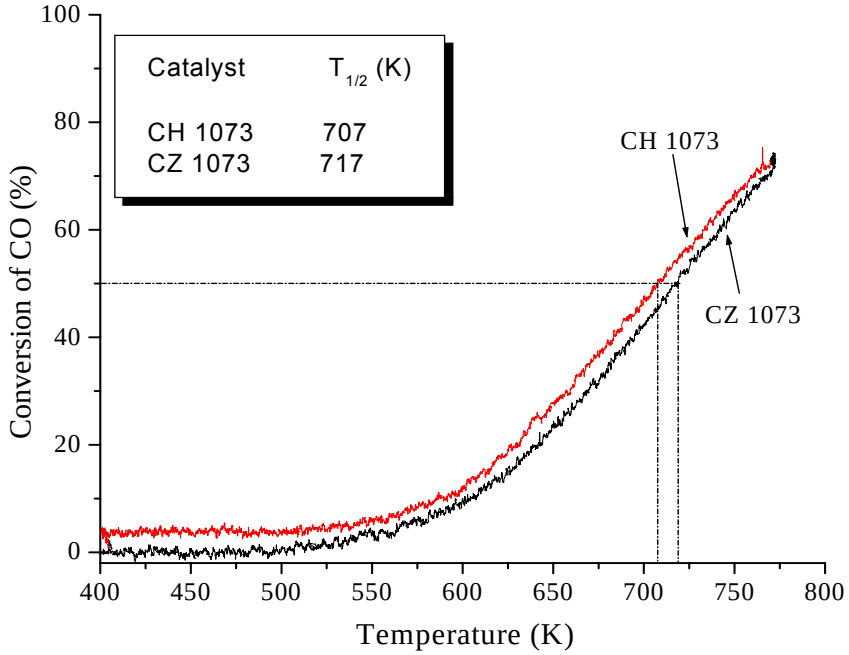

Figure 7.3: Conversion of CO over CeO_2–HfO_2 (CH) and CeO_2–ZrO_2 (CZ) catalysts calcined at 1073 K as a function of reaction temperature. Inset shows the corresponding $T_{1/2}$.

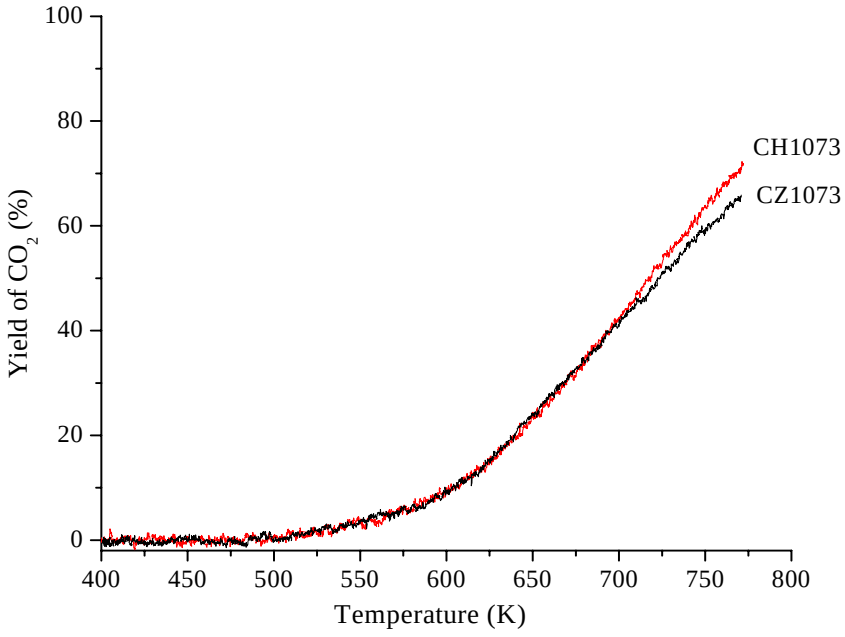

Figure 7.4: Yield of CO_2 over CeO_2–HfO_2 (CH) and CeO_2–ZrO_2 (CZ) catalysts calcined at 1073 K as a function of reaction temperature.

samples calcined at 1073 K. It follows similar order for both CO conversion and CO_2 yield as that of 773 K calcined samples. CH and CZ samples calcined at 1073 K exhibited $T_{1/2}$ of 707 and 717 K, respectively. Thus, the CO activity results suggest that CH is better catalyst compared to CZ samples irrespective of calcination temperature. Their OSC could be correlated with the domain size, that is, the interfacial area between CeO_2 and the constituent oxide enriched regions rather than with the surface area of the samples. Interestingly, a significant lowering of the starting reduction temperature is noticed for the CH compared to the CZ sample as presented in chapter 3. The redox reactivity of ceria, especially toward CO, might strongly depend on the type and amount of surface exposed to the gas phase. The increase in CO oxidation activity for the CH sample compared to that for the CZ sample may be correlated to ISS measurement results. As mentioned, a slight surface enrichment of cerium in CH may be responsible for showing a better reducible property at lower temperatures. As a consequence one can observe light off temperature at much lower value for CH compared to CZ. The OSC values of the studied catalysts could also be directly correlated to the CO oxidation activity. As it is mentioned in the earlier section CH sample bear higher OSC compared to CZ sample. Further, the results from UV- and visible-Raman and UV-vis DRS studies (chapter 3) also support the formation of oxygen vacancy and defect sites in the Ce-Hf and Ce-Zr mixed oxide crystal lattices. Especially, the presence of $Ce^{3+} \leftarrow O^{2-}$ transitions in the UV-vis DRS spectra infers the presence of oxygen vacancy defects, which is more prominent in the case of the CH sample. These factors affect the catalytic activity of the ceria-based solid solutions, which reveals the CH sample is better for CO oxidation compared to that of the CZ sample.

The ease of reducibility of ceria-based composite oxides depends on vacancy formation energy (VFE). Low VFE means high reducibility, which can lead to high OSC and improved catalytic activity. It is already reported that VFE for ceria-based composite oxides decreases compared to ceria when smaller cations replace Ce in the lattice [22]. It is also known that VFE depends almost linearly on the ionic radius of the solute ions [23]. Apparently, in the present case, VFE for CH and CZ decrease maintaining the same trend. Moreover, one explanation is also that the presence of these smaller cations decreases the O-2p-Ce-4f band gap separation. Again, in the case of CH, phase segregagation phenomenon is not observed even after the exposure of the samples to higher temperatures. Therefore, the lowering of the activity for the 1073 K calcined sample can be accounted for by loss of surface area alone. The lower reduction temperature of

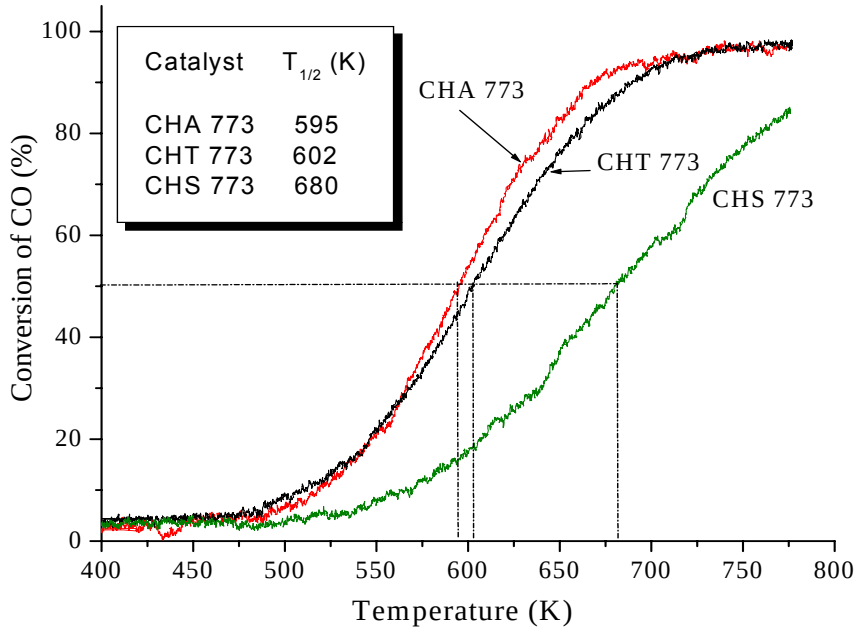

Figure 7.5: Conversion of CO over CeO_2–HfO_2/Al_2O_3 (CHA), CeO_2–HfO_2/TiO_2 (CHT) and CeO_2–HfO_2/SiO_2 (CHS) catalysts calcined at 773 K as a function of reaction temperature. Inset shows the corresponding $T_{1/2}$.

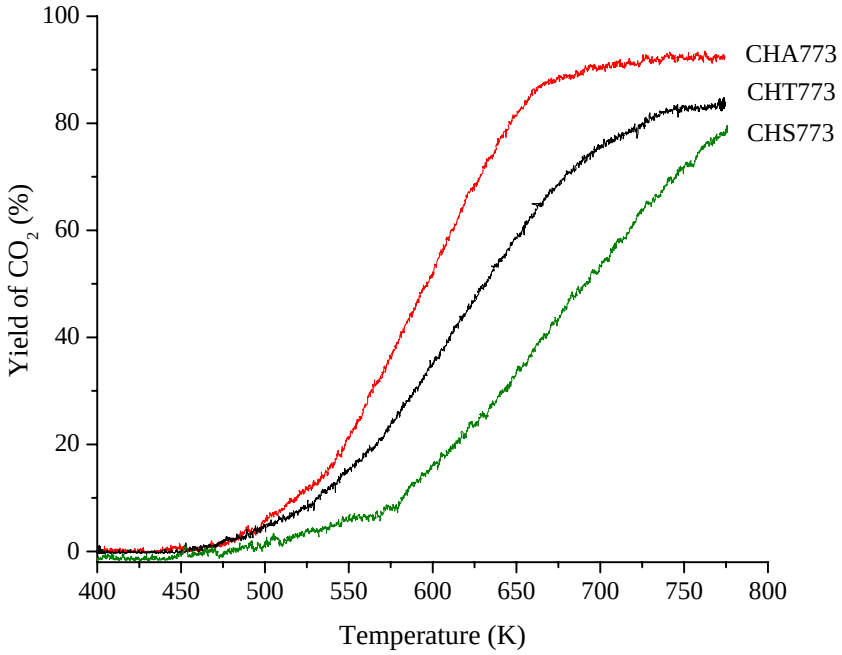

Figure 7.6: Yield of CO_2 over CeO_2–HfO_2/Al_2O_3 (CHA), CeO_2–HfO_2/TiO_2 (CHT) and CeO_2–HfO_2/SiO_2 (CHS) catalysts calcined at 773 K as a function of reaction temperature.

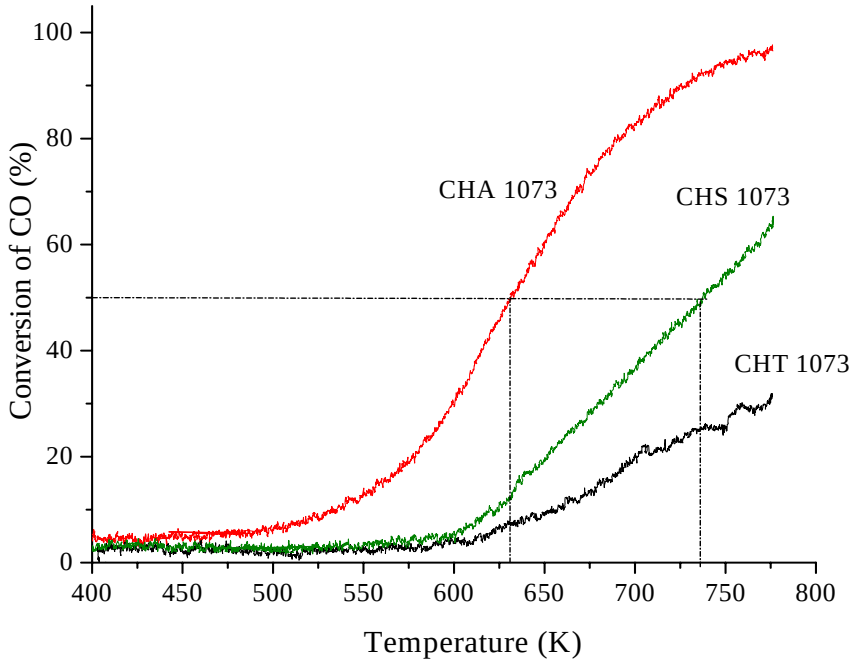

Figure 7.7: Conversion of CO over CeO_2–HfO_2/Al_2O_3 (CHA), CeO_2–HfO_2/TiO_2 (CHT) and CeO_2–HfO_2/SiO_2 (CHS) catalysts calcined at 1073 K as a function of reaction temperature.

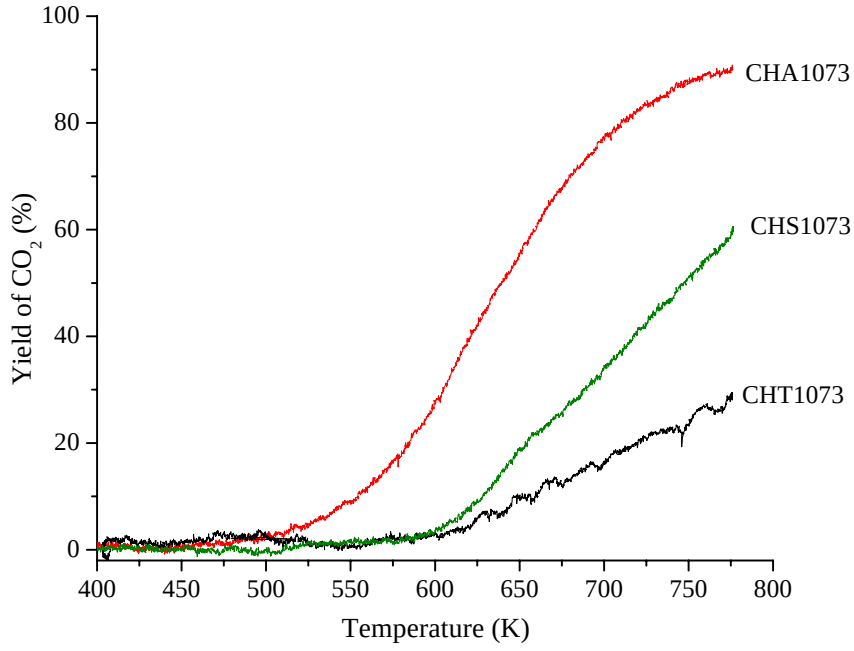

Figure 7.8: Yield of CO_2 over CeO_2–HfO_2/Al_2O_3 (CHA), CeO_2–HfO_2/TiO_2 (CHT) and CeO_2–HfO_2/SiO_2 (CHS) catalysts calcined at 1073 K as a function of reaction temperature.

Ce^{4+} and thus the increased ability of CeO_2-based composite oxide to shift between Ce^{4+} and Ce^{3+} at a much lower temperature is the key for the increased oxidation activity. From our observations, we can come to the consensus that the difference in OSC and CO oxidation activity is not dependent on the ionicity of Hf-O or Zr-O bonds. As the ionicity of Hf-O bond is larger than that of Zr-O bonds, it is possible that the release of oxygen from the CZ sample is easier than that from CH to reduce Ce^{4+} in the corresponding composite oxides. Interestingly, our experimental results did not follow the trend [20,21]. Therefore, it is thought that the ionic radii of the dopant cations have played a significant role in the observed results.

The CO oxidation activity results and their corresponding yield of CO_2 pertaining to the 773 K calcined CHA, CHT, and CHS catalysts are presented in Figures 7.5 and 7.6, respectively. It is evident from the Fig. 7.5 that the samples are exhibiting reasonably good activity in terms of total conversion and light off temperature (50% conversion, $T_{1/2}$). Among the three different samples, CHA showed higher activity towards CO oxidation reaction. The $T_{1/2}$ observed for the CHA, CHT, and CHS catalysts were 595, 602, and 680 K, respectively. As presented in Fig. 7.6, the yield of CO_2, evaluated as per the formula presented in the experimental section for different catalysts suggests that there is no mass loss in the reaction process with the yield almost identical to the CO conversion. This reflects the accuracy in the experimental setup also. Figures 7.7 and 7.8, respectively show the conversion of CO and yield of CO_2 of various supported ceria-hafnia catalysts calcined at 1073 K. As could be seen from Fig. 7.7, 1073 K calcined CHA sample exhibited higher activity compared to the titania and silica supported samples. The corresponding yields of CO_2 also follow similar order. As expected CHT sample exhibited very low activity in comparison to CHA and CHS samples calcined at 1073 K. The CHT sample calcined at 1073 K showed only 30% conversion. On the other hand, the $T_{1/2}$ observed for the CHA and CHS catalysts were 631 and 738 K, respectively. The activity results could be explained in terms of several factors. The OSC of the dispersed Ce–Hf-oxide strongly influences the catalytic activity of the material. As could be observed from Table 7.1, CHA exhibits higher OSC compared to the CHT and CHS samples. UV-Raman studies of CHA samples (chapter 6, Fig. 6.9) showed that there is more amount of defect generation with the formation of higher content of surface oxygen vacancy compared to CHT and CHS samples. The highest intensity of the band around 620 cm^{-1} in the Raman spectra of CHA samples suggests higher vacancy in the crystal lattice of Ce-Hf-oxide, thereby more exposed sites with Ce^{3+}. The XPS and UV-vis DRS studies also support

these observations. The reducibility of the composite oxides as investigated by CO-TPR measurements showed that Al_2O_3 support induces the lowering of reduction temperature to a remarkable extent which helps the lattice oxygen of surface region to take part in the CO oxidation reaction. Moreover, a definite balance between the structural defects and the composition of Ce–Hf-oxide is essential for the CO oxidation activity [24]. During the oxidation of CO, the rapid transformation of adsorbed CO into CO_2 strongly depends on the availability of lattice oxygen or OSC, as the participation of lattice oxygen and the degree of reducibility significantly affect the performance of ceria-based catalysts [24].

The non-uniformity and higher order of defects with different contrasts in the crystal structure of very small ceria-hafnia nanocomposite oxides, as observed from TEM-HREM studies (chapter 4), may be the cause of poor OSC of CHS sample leading to inferior performance in the CO conversion among the 773 K calcined various supported ceria-hafnia samples. It should be noted that there is no difference in the composition of various supported Ce–Hf-oxides except their specific surface areas. However, the reactivity could not be correlated with the specific surface areas of the samples. Hence the catalytic performance of Ce–Hf-oxide is certainly influenced by the nature of the support.

The activity results for the 1073 K calcined CHA, CHT, and CHS samples showed lower conversion as expected. This can be accounted for the significance of following effects when the sample was calcined at high temperature: (1) the loss of surface area, increase in particle size, and formation of more agglomerated microstructures losing dispersion of the active composite metal oxide; (2) phase transformation of the composite oxide, and (3) a change in the redox state in the composite oxide. The very low activity of CHT sample calcined at 1073 K is due to the emergence of unfavorable TiO_2-rutile phase as observed from visible-Raman spectra (chapter 5, Fig. 5.10). Thus, from the above discussion it could be concluded that formation of oxygen vacancy with the generation exposed Ce^{3+} content in the surface of ceria-based catalysts along with easy reducibility and higher OSC, are very important factors to have better activity towards CO oxidation. Recent studies of scanning tunneling microscopy (STM) on a ceria surface combined with state-of-the-art quantum mechanical calculations using density functional theory (DFT) showed that linear clusters of surface oxygen vacancies are formed on CeO_2(111) surface at high temperatures [25]. These vacancy clusters expose exclusively Ce^{3+} ions to gas-phase reactants. It has been proposed that surface oxygen vacancies participate in many chemical reactions catalyzed by metal oxides. When an adsorbate is oxidized at the

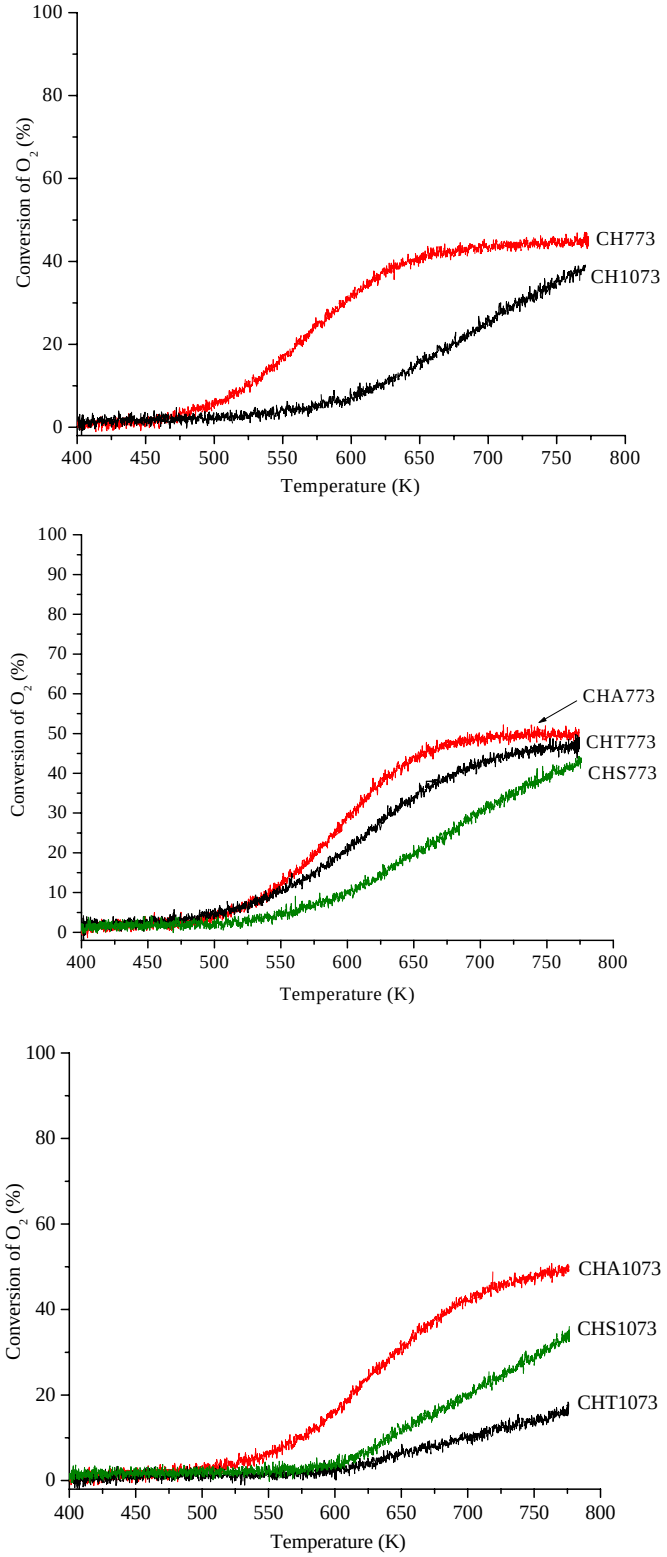

Figure 7.9: Conversion of O_2 over CeO_2–HfO_2 (CH), CeO_2–HfO_2/Al_2O_3 (CHA), CeO_2–HfO_2/TiO_2 (CHT), and CeO_2–HfO_2/SiO_2 (CHS) catalysts calcined at 773 and 1073 K as a function of reaction temperature.

surface, the oxidant is often a surface lattice oxygen atom, thus creating a surface oxygen vacancy (the Mars-van Krevelen mechanism). Vacancies also bind adsorbates more strongly than normal oxide sites and assist in their dissociation. These groups of exposed Ce^{3+} ions on CeO_2 are a potentially effective surface site for catalysis, because adsorbed gases or catalytic reaction intermediates could interact simultaneously with several Ce^{3+} ions. Similar mechanism could be expected in our present investigation also.

Figure 7.9 shows the conversion of O_2 for the unsupported and various supported CeO_2–HfO_2 composite oxide catalysts calcined at 773 and 1073 K. These results were presented to show the evidence of stoichiometry of the reaction, i.e. $CO + ½\ O_2 \rightarrow CO_2$. The results revealed that the O_2 undergoes ca. 50% conversion relative to the CO conversion results during the course of the reaction according to the reaction scheme. As initially we have used 1% CO/Ar and 1% O_2/Ar with the feed ratio 1, only half of the O_2 concentration has been utilized for the reaction showing the conversion of O_2 around 50%.

7.4 Soot Oxidation Reaction

The soot oxidation activity was performed for the synthesized catalysts by using thermogravimetry methods. The measurements were carried out for both loose (mixed with spatula) and tight (mixed in agate mortar) contact condition of catalyst and soot. The activity data for loose contact condition were collected in a TG-QMS instrument, while for tight contact condition was collected in a TG-SDTA instrument, respectively. Figures 7.10–7.14 show the DTG and QMS plots of the bare soot and mixture of catalyst and soot in 4:1 wt.% ratio. As observed from the DTG-QMS plots (Fig. 7.10) of bare soot show the features corresponding to the mass of H_2O (M18), CO (M28), O_2 (M32), and CO_2 (M44), respectively. As observed there is only one feature for CO_2 formation when temperature is increased, while there is loss of mass pertaining to O_2 was observed. As could be seen from the Figs. 7.11 to 7.14, for different catalyst and soot mixture the DTG-QMS plots were somewhat different. In addition to the above observations, the catalyst-soot mixtures for different samples show two distinct features for the formation of CO_2, which reveal the conversion of soot to higher extent when catalysts were used. However, from loose contact conditions we could not determine the exact conversion of soot. Loose contact did not show a significant decrease in the soot oxidation temperature irrespective of the selected catalysts, consistent with reported literature [11-13]. When the soot particle is not

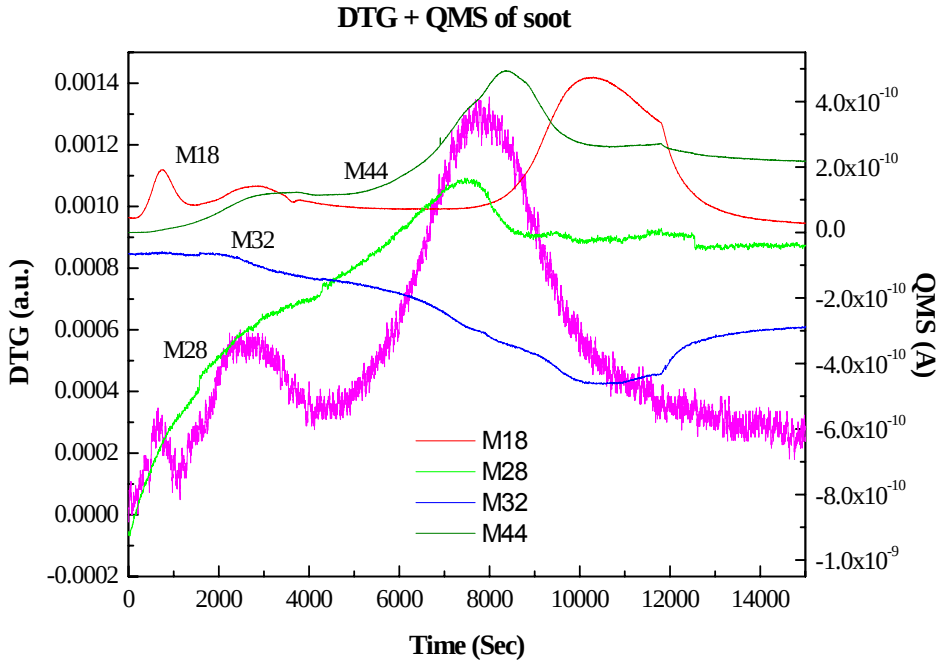

Figure 7.10: DTG and QMS plots of bare soot. The legends M18, M28, M32, and M44 represent the mass of H_2O, CO, O_2, and CO_2, respectively.

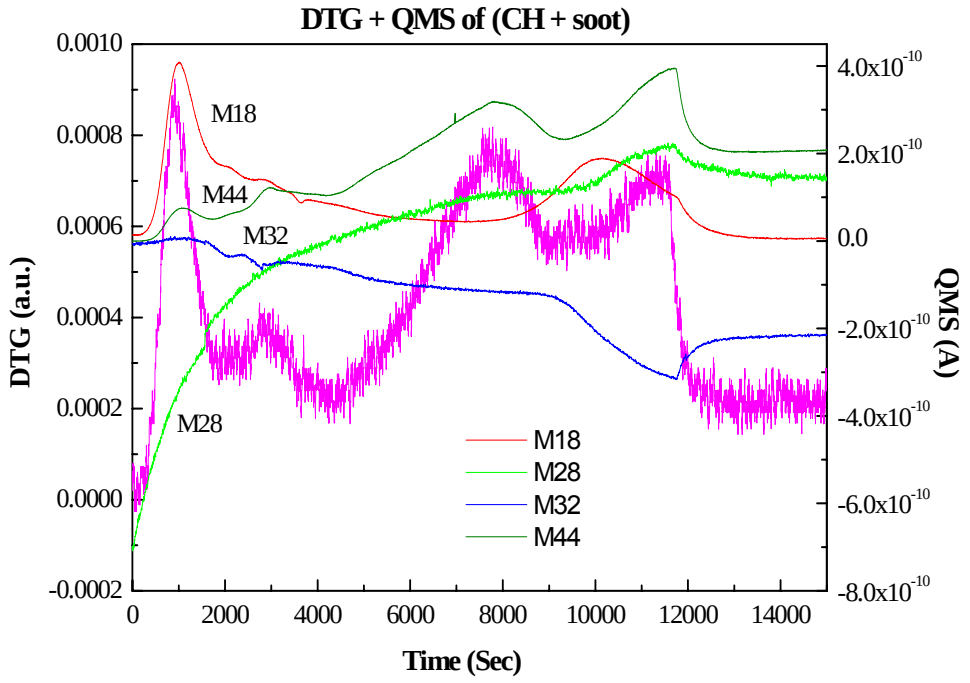

Figure 7.11: DTG and QMS plots of the mixture of CeO_2–HfO_2 (CH) and soot. The legends M18, M28, M32, and M44 represent the mass of H_2O, CO, O_2, and CO_2, respectively.

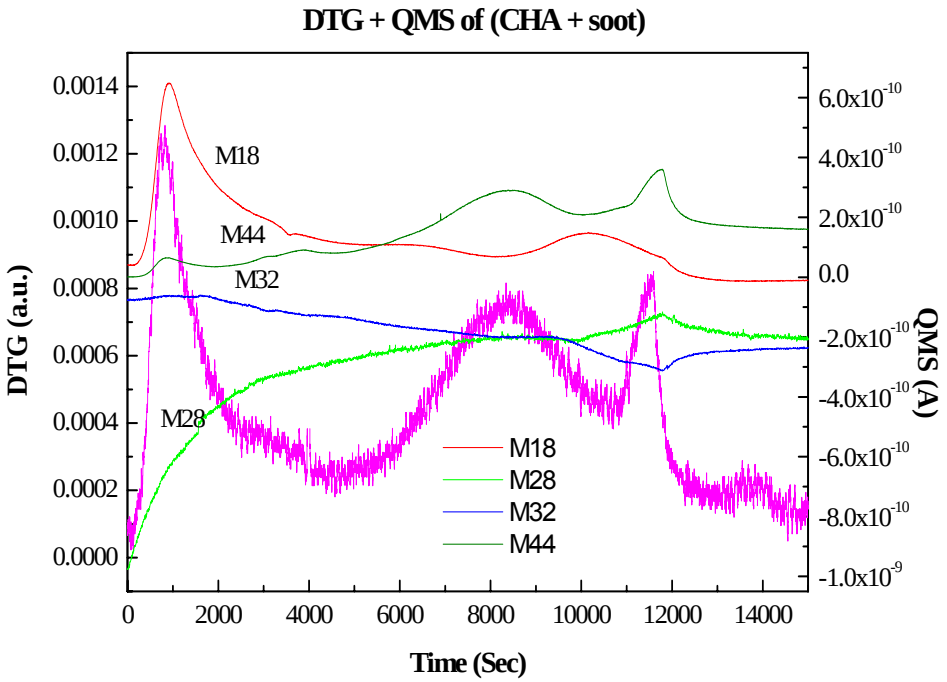

Figure 7.12: DTG and QMS plots of the mixture of CeO_2–HfO_2/Al_2O_3 (CHA) and soot. The legends M18, M28, M32, and M44 represent the mass of H_2O, CO, O_2, and CO_2, respectively.

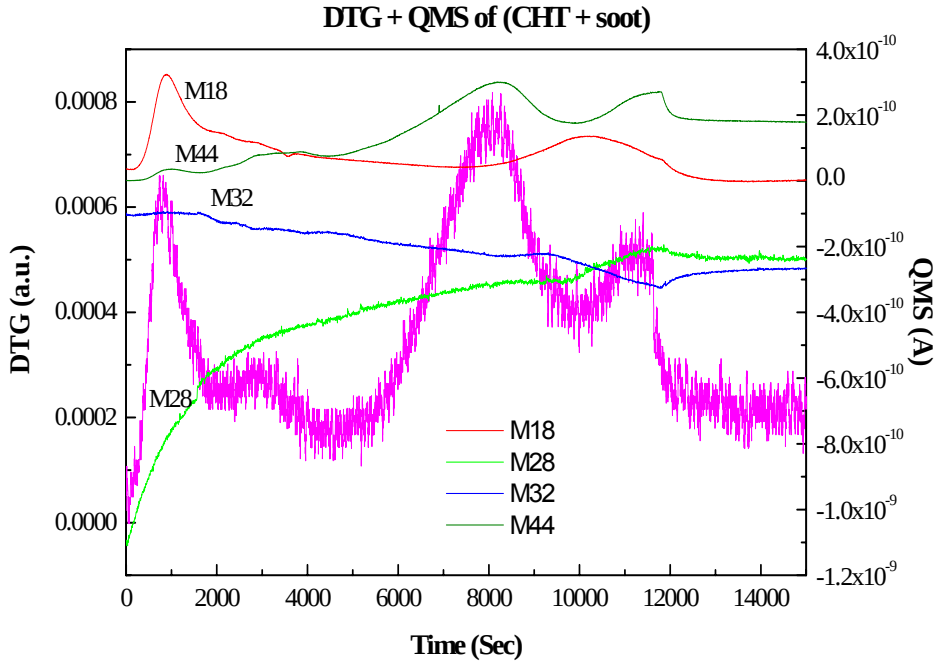

Figure 7.13: DTG and QMS plots of the mixture of CeO_2–HfO_2/TiO_2 (CHT) and soot. The legends M18, M28, M32, and M44 represent the mass of H_2O, CO, O_2, and CO_2, respectively.

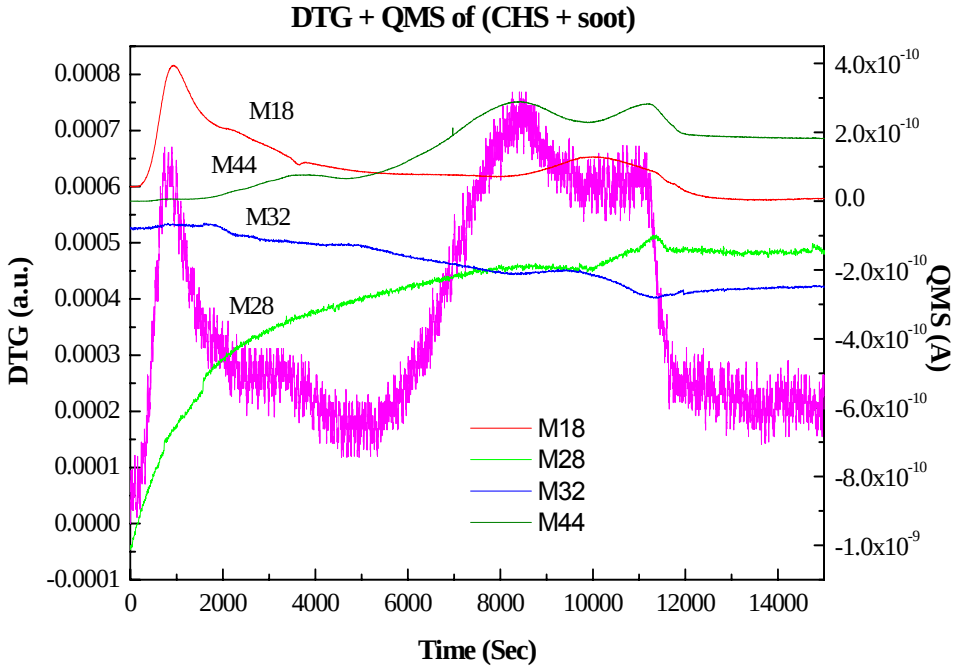

Figure 7.14: DTG and QMS plots of the mixture of CeO_2–HfO_2/SiO_2 (CHS) and soot. The legends M18, M28, M32, and M44 represent the mass of H_2O, CO, O_2, and CO_2, respectively.

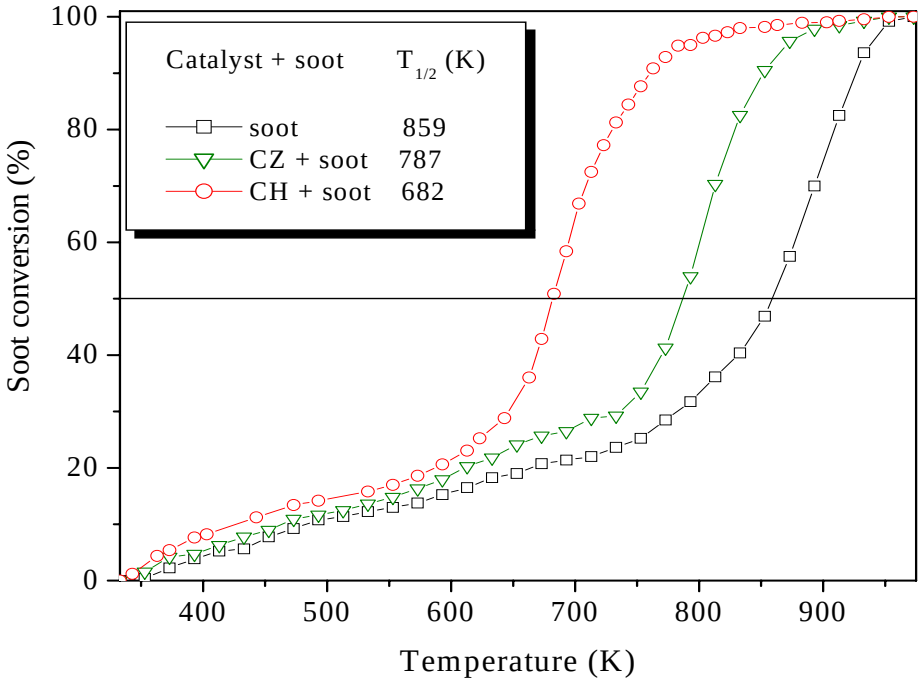

Figure 7.15: Conversion of soot over pure soot, mixture of CeO_2–HfO_2 (CH) and CeO_2–ZrO_2 (CZ) with soot. Inset shows the $T_{1/2}$ for the soot conversion.

in a close contact with the catalyst surface, the catalyst lattice oxygen cannot be transferred to the soot surface [26–28]. Therefore, it is adopted to test the catalysts using a tight contact condition. The oxygen involved for soot combustion comes from two aspects: the gaseous oxygen and the oxygen released from catalysts. The better catalytic activity may be contributed from the dissociation centers for the adsorption oxygen provided by the metal oxides [12,28]. The high catalytic activity of CeO_2 for soot oxidation in air was attributed to the generation of highly active oxygen in the lattice due to the oxygen exchange between gas phase O_2 and oxygen in the oxide framework, as mentioned [12], and the redox cycle Ce^{3+}/Ce^{4+} seems to play an important role in the oxygen exchange process.

Figure 7.15 compiles the conversion of soot as a function of temperature for the mixture of CeO_2–HfO_2 (CH)-soot and CeO_2–ZrO_2 (CZ)-soot along with bare soot. The measurements were carried out using air as O_2 source in tight contact conditions. Both the catalysts showed decreased in soot oxidation temperature, as expected. The soot conversion temperature significantly decreased for catalysts-soot mixture in comparison to bare soot. The light-off temperature (temperature at 50% conversion or $T_{1/2}$) has decreased to lower temperatures after introduction of catalysts to the soot. The $T_{1/2}$ for bare soot was observed at ca. 860 K. But the $T_{1/2}$ for the CH- and CZ-soot mixtures are observed at ca. 682 and 787 K, respectively. This is a significant observation in the present study. As it is always desirable to develop better catalysts which could lower the temperature at 50% soot conversion. The possible reasons for the increase in activity of doped CeO_2 catalysts in the soot oxidation with O_2 are probed by the different catalyst characterization techniques. Among the various parameters that can explain the differences in catalyzed soot oxidation temperature with O_2, are the catalyst surface area, formation of oxygen vacancies in the catalysts structures and low temperature reducibility. Comparison of the BET surface areas of all catalysts (chapter 3, Table 3.1) shows that there is nearly a direct correlation between the BET surface area and soot oxidation results. It is always desirable to have ceria-based composite oxides with the highest possible specific surface area, though it is suggested that the surface area may not be the only parameter that determines the catalytic efficiency of ceria [20,21]. The formation of oxygen vacancies in the CH and CZ samples were identified from Raman and UV-vis DRS studies. These results correlate well with the activity measurements. Among the supported CeO_2–HfO_2 catalysts, alumina supported one showed higher soot conversion at lower temperatures. As could be observed from the Fig. 7.16, the $T_{1/2}$ for CHA, CHT, and

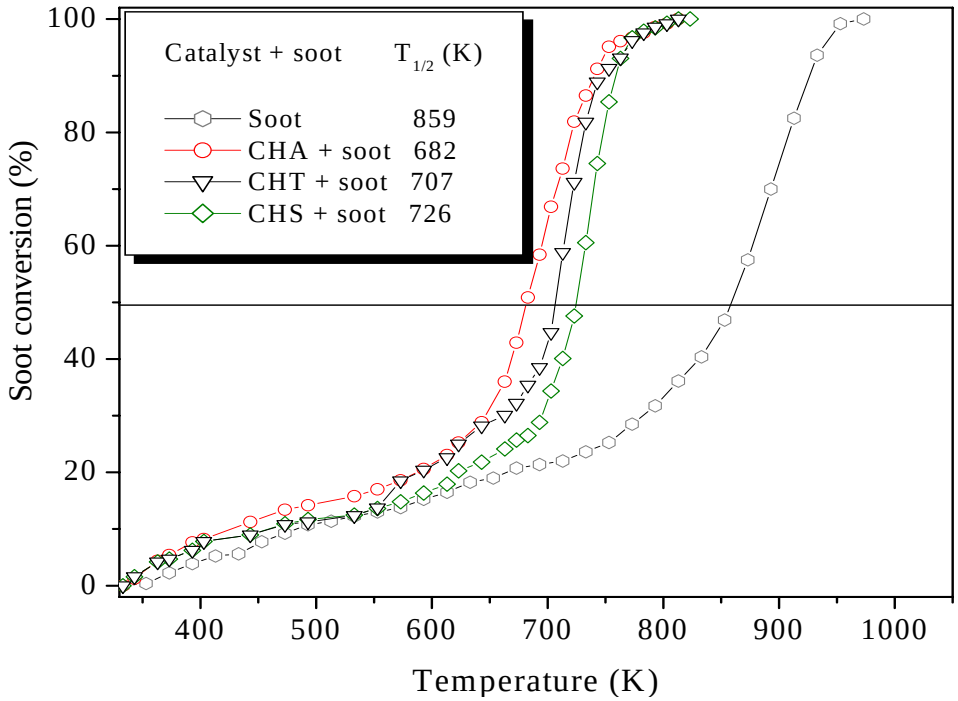

Figure 7.16: Conversion of soot over pure soot, mixture of CeO_2–HfO_2/Al_2O_3 (CHA), CeO_2–HfO_2/TiO_2 (CHT), and CeO_2–HfO_2/SiO_2 (CHS) with soot. Inset shows the $T_{1/2}$ for the soot conversion.

CHS are 682, 707, and 726, respectively. The activity data could be explained in terms of several factors. As could be observed from Table 7.1, CHA exhibits higher OSC compared to the CHT and CHS samples. UV-Raman studies of CHA samples (chapter 6, Fig. 6.9) also showed that there is more amount of defect generation with the formation of higher content of surface oxygen vacancy compared to CHT and CHS samples. The highest intensity of the band around 620 cm^{-1} in the Raman spectra of CHA samples suggests higher vacancy in the crystal lattice of Ce-Hf-oxide, thereby more exposed sites with Ce^{3+}. The XPS and UV-vis DRS studies also support these observations. The reducibility of the composite oxides as investigated by CO-TPR measurements showed that Al_2O_3 support induces the lowering of reduction temperature to a remarkable extent which helps the lattice oxygen of surface region to take part in the soot oxidation reaction.

We have seen the similarity in the behavior of CO and soot oxidation in line with earlier reports, which put forwarded a hypothesis of mechanism of it [1,20,26,28]. This is in analogy to what has been done for CO oxidation, by invoking a redox mechanism with a simple redox route for soot oxidation, which utilizes oxygen activated from the support in a typical reduction/oxidation mechanism (Mars–Van–Krevelen type) in which the catalyst

undergoes a partial reduction. Oxygen storage is therefore important because it provides an alternative route for the oxidation of big soot particles. An alternative redox route involves oxygen from the support and gas-phase which reacts with soot to form adsorbed CO_2 in the form of carbonates. Decomposition of carbonate is then stimulated by gas phase oxygen that provides also reoxidation of the support.

7.5 Dehydration of 4-methylpentan-2-ol

Acid-base properties of metal oxides play a vital role in catalysis and there are several chemical processes that have been industrially exploited for various applications based on surface acid-base sites of the metal oxide catalysts [15,29–32]. To test the acid-base character of the synthesized catalysts, selective dehydration of 4-methylpentan-2-ol was conducted in normal atmospheric pressure for CeO_2–HfO_2 and SiO_2 supported CeO_2–HfO_2 composite oxides. The dehydration of 4-methylpentan-2-ol could represent an alternative route to the preparation of 4-methylpent-1-ene, a starting material for the manufacture of thermoplastic polymers of high technological significance. The conversion of 4-methylpentan-2-ol produces mainly 4-methylpent-1-ene and 4-methylpent-2-ene with trace amounts of C_6 alkenes as dehydration products. Besides dehydration, dehydrogenation of the reactant alcohol gives rise to 4-methylpentan-2-one and higher ketones (in very low amounts). Previous works on zirconia, ceria and lanthana-based oxides revealed the involvement of three different mechanistic pathways (E1cB, E1 and E2) to form the desired and undesired products [33–36]. When the acid and base functions of the catalyst are well balanced in terms of site concentrations, a two-point adsorption of the reactant alcohol occurs, in which the most acidic hydrogen (i.e. H of terminal methyl group) interacts with a base site while the acid centre interacts with the OH group of the alcohol. The fate of this adsorbed species depends on the relative strength of the acid and base sites. If the acid sites are weak and the base sites are strong enough, rupture of the C–H bond with carbanion formation occurs first and an E1cB mechanism sets in leading to the preferential formation of 1-alkene (Hofmann product). If the strengths of the acid and base sites are comparable, no intermediate carbanion is formed. In this situation, the transformation of the adsorbed species into the olefin takes place via concerted mechanism (E2 pathway) and 2-alkene is then the preferred product (Saytzeff product). Such co-operative action of the sites is disfavored when either the acid or the base sites are predominant. In the former case, the reaction is

initiated by the attack of the acid sites to the hydroxy group of the alcohol leading to the formation of a carbocation intermediate, which transforms into alkenes with internal double bonds (E1 mechanism, Saytzeff product). When the base sites on the catalyst surface are predominant and strong, adsorption occurs by means of a hydrogen bond involving the OH group of the alcohol and a base site. Here abstraction of α-H by interaction with a positively polarized H atom on the surface (originating from the previously split OH group of the alcohol) occurs and a ketone is formed instead of an alkene.

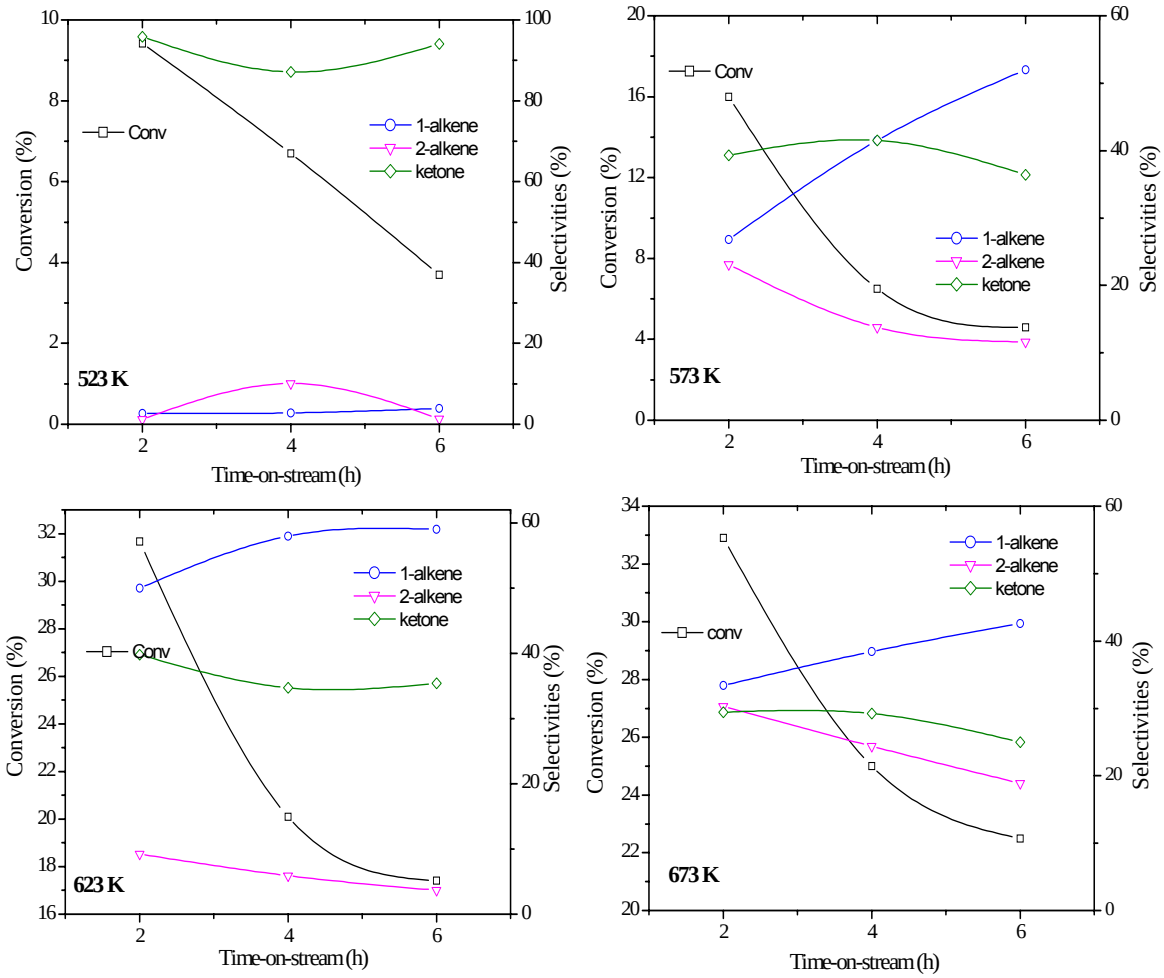

Figure 7.17: Conversion of 4-methylpentan-2-ol and selectivities to 4-methylpent-1-ene (1-alkene), 4-methylpent-2-ene (2-alkene) and 4-methylpentan-2-one (ketone) versus time-on-stream for CeO_2–HfO_2 (CH) catalyst at different reaction temperatures.

Based on aforesaid background, we have examined the dehydration of 4-methylpentan-2-ol over CH and CHS samples calcined at 773 K, in the present investigation. The conversion of 4-methylpentan-2-ol and selectivities to 4-methylpent-1-ene (1-alkene), 4-methylpent-2-ene (2-alkene) and 4-methylpentan-2-one (ketone) versus 6h time-on-stream for CeO_2–HfO_2 (CH) and CeO_2–HfO_2/SiO_2 (CHS) catalysts at different reaction temperatures are presented in Figures 7.17 and 7.18, respectively.

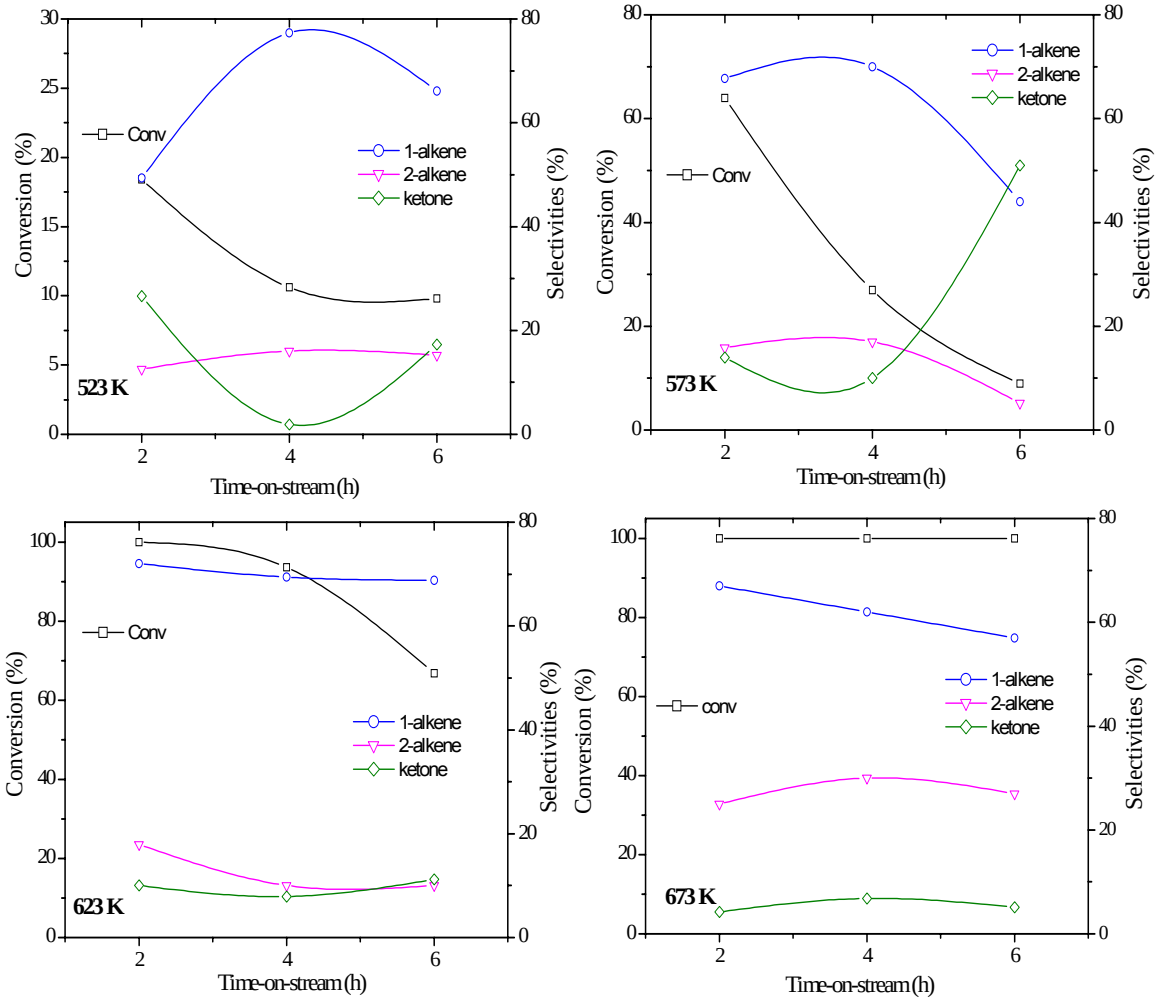

Figure 7.18: Conversion of 4-methylpentan-2-ol and selectivities to 4-methylpent-1-ene (1-alkene), 4-methylpent-2-ene (2-alkene) and 4-methylpentan-2-one (ketone) versus time-on-stream for CeO_2–HfO_2/SiO_2 (CHS) catalyst at different reaction temperatures.

As could be observed from Figs. 7.17 and 7.18, the conversion of alcohol increases with increasing reaction temperature for both the catalysts. Up on dispersing ceria-hafnia over SiO_2, the conversion of the alcohol is drastically increased. At 523 K after 2h of

reaction the alcohol conversion was 9% for CH, which increased to 16% for CHS. At 673 K (highest reaction temperature), the CH sample after 6h of reaction exhibited 23% conversion, whereas CHS showed 100% conversion. This is a remarkable observation in the present investigation. The selectivity towards 4-methylpent-1-ene (1-alkene; desired product) are comparatively higher for CHS than CH, in general. At 523 K after 4h of reaction the selectivity towards 1-alkene was found to be < 5% for CH, whereas CHS exhibited > 75% selectivity for 1-alkene. Moreover, the selectivity of the dehydrogenation product, 4-methylpentan-2-one was higher for CH compared to CHS sample, which was inferior from the practical point of view. However, there is no appreciable change in the selectivity of 4-methylpent-2-ene with increasing reaction temperature for all the catalysts. The present study indicates the involvement of the E1cB mechanistic pathway through the formation of carbanion intermediate to form the highly selective 1-alkene. The following observations could be related to the highly dispersed Ce-Hf-oxide over SiO_2 with balanced acid-base and redox sites. The high dispersion of CeO_2–HfO_2 over SiO_2 to form ceria crystallites of ~3–5 nm size accounts for an increase in the conversion of the alcohol, as high dispersion of active oxide always provides more active sites for the reactant molecules to interact with more balanced acid-base surface sites. Further, Raman results (chapter 4) of silica supported ceria-hafnia composite oxide showed the formation of oxygen vacancies to higher extent compared to ceria-hafnia (chapter 3). The emergence of Raman band at ~620 cm^{-1} in the visible-Raman spectra is related to the oxygen vacancy concentration, which is more prominent in the case of CHS sample (chapter 4, Fig. 4.10). The formation of oxygen vacancy in CHS provides more Ce^{3+} sites, which may lead to an increase in the ability of O^{2-} ions to abstract a proton in comparison to the O^{2-} ions connected to Ce^{4+}. This facilitates the E1cB mechanistic pathway to form the desired 1-alkene selectively. The XPS and ISS results (chapter 4, Figs. 4.12 and 4.16, respectively) also support the observation concluded from Raman studies.

7.6 Conclusions

The catalysts synthesized in the present investigation were evaluated for OSC properties, CO oxidation, and soot oxidation activity to test their effectiveness. Some of the catalysts were also examined for the acid-base nature of the samples. The unsupported ceria-hafnia composite oxide is better in terms of OSC, CO oxidation, and soot oxidation ability compared to well reported unsupported ceria-zirconia composite

oxide. The redox behavior is quite interesting for the ceria-hafnia system. Among the supported ceria-hafnia catalyst systems alumina supported composite oxide showed higher activity for OSC, CO oxidation, and soot oxidation reaction, respectively. All the three catalytic properties are interrelated, as observed from our experimental results and physicochemical characteristics of the composite oxide systems. The fourth reaction studied was selective dehydration of 4-methylpentan-2-ol, which is used as a test reaction to evaluate the acid-base character of oxide catalysts. Silica supported ceria-hafnia system showed highest activity toward the dehydration of the 4-methylpentan-2-ol selectively.

7.7 References

[1] M. Fernández-García, A. Martínez-Arias, J.C. Hanson, J.A. Rodríguez, Chem. Rev. 104 (2004) 4063.

[2] A. Trovarelli, Catal. Rev.-Sci. Eng. 38 (1996) 439.

[3] P. Ratnasamy, D. Srinivas, C.V.V. Satyanarayana, P. Manikandan, R.S. Senthil Kumaran, M. Sachin, V.N Shetti, J. Catal. 221 (2004) 455.

[4] D. Ciuparu, L. Pfefferle, Catal. Today 77 (2002) 167.

[5] E. Aneggi, J. Llorca, M. Boaro, A. Trovarelli, J. Catal. 234 (2005) 88.

[6] M.F. Milkes, P. Hayden, A.K. Bhattacharya, J. Catal. 219 (2003) 295.

[7] W. Liu, M. Flytzani-Stephanopoulos, J. Catal. 153 (1995) 304.

[8] Y. Madier, C. Descorme, A.M. LeGovic, D. Duprez, J. Phys. Chem. B 103 (1999) 10999.

[9] R.H. Nibbelke, A.J.L. Nievergeld, J.H.B.H. Hoebnik, G.B. Marin, Appl. Catal. B: Environ. 19 (1998) 245.

[10] K. Krishna, A. Bueno-Lopez, M. Makkee, J.A. Moulijn, Appl. Catal. B: Environ. 75 (2007) 189.

[11] M.A. Małecka, L. Kepinski, W. Mista, Appl. Catal. B: Environ. 74 (2007) 290.

[12] A. Bueno-Lopez, K. Krishna, M. Makkee, J.A. Moulijn, J. Catal. 230 (2005) 237.

[13] L. Zhua, J. Yu, X. Wang, J. Hazardous Mater. 140 (2007) 205.

[14] J. Liu, Z. Zhao, C. Xu, A. Duan, L. Wang, S. Zhang, Catal. Commun. 8 (2007) 220.

[15] B.M. Reddy, In Metal Oxides: Chemistry and Applications; J.L.G. Fierro, Ed.; Taylor & Francis: New York, 2006, Chapter 8; pp 215.

[16] M. Sugiura, Catalysis Surv. Asia 7 (2003) 77.

[17] M. Ozawa, C.N.K. Loong, Catal. Today 50 (1999) 329.

[18] A.D. Logan, M. Shelef, J. Mater. Res. 9 (1994) 468.

[19] N.V. Skorodumova, S.I. Simak, B.I. Lundqvist, I.A. Abrikosov, B. Johansson, Phys. Rev. Lett. 89 (2002) 166601.

[20] B.M. Reddy, P. Bharali, P. Saikia, A. Khan, S. Loridant, M. Muhler, W. Grunert, J. Phys. Chem. C 111 (2007) 1878.

[21] B.M. Reddy, P. Bharali, P. Saikia, S.-E. Park, M.W.E. van den Berg, M. Muhler, W. Grünert, J. Phys. Chem. C 112 (2008) 11729.

[22] D.A. Andersson, S.I. Simak, N.V. Skorodumova, I.A. Abrikosov, B. Johansson, Appl. Phys. Lett. 90 (2007) 031909.

[23] R.D. Shannon, Acta Crystallogr., Sect. A: Cryst. Phys. Diffr., Theor. Gen. Crystallogr. 32 (1976) 751.

[24] E. Aneggi, M. Boaro, C. de Leitenburg, G. Dolcetti, A. Trovarelli, J. Alloys Compd. 408-412 (2006) 1096.

[25] F. Esch, S. Fabris, L. Zhou, T. Montini, C. Africh, P. Fornasiero, G. Comelli, R. Rosei, Science 309 (2005) 752.

[26] E. Aneggi, C. de Leitenburg, G. Dolcetti, A. Trovarelli, Catal. Today 114 (2006) 40.

[27] A. Bueno-Lopez, K. Krishna, M. Makkee, J.A. Moulijn, Catal. Lett. 99 (2005) 203.

[28] K. Krishna, A. Bueno-Lopez, M. Makkee, J.A. Moulijn, Top. Catal. 44- 45 (2007) 221.

[29] M.C. Kung, H.H. Kung, Catal. Rev. Sci. Eng., 27 (1985) 425.

[30] K. Tanabe, in: Solid Acid and Bases, Kodansha, Tokyo and Academic Press, New York, 1970.

[31] K. Tanabe, M. Misono, Y. Ono, H. Hattori, in: New Solid Acid and Bases, Kodansha, Tokyo and Elsevier, Amsterdam, 1989.

[32] J.M. Winterbottom, in: Catalysis, Specialist Periodical Reports, The Royal Society of Chemistry, London, Vol. 4, 1981.

[33] M.G. Cutrufello, I. Ferino, V. Solinas, A. Primavera, A. Trovarelli, A. Auroux, C. Picciau, Phys. Chem. Chem. Phys. 1 (1999) 3369.

[34] M.G. Cutrufello, I. Ferino, R. Monaci, E. Rombi, V. Solinas, Top. Catal. 19 (2002) 225.

[35] V. Solinas, E. Rombi, I. Ferino, M.G. Cutrufello, G. Colon, J.A. Navio, J. Mol. Catal. A: Chem. 204-205 (2003) 629.

[36] B.M. Reddy, P. Lakshmanan, P. Bharali, P. Saikia, J. Mol. Catal. A: Chem. 258 (2006) 355.

PUBLICATIONS/ PATENTS

Book Chapters

1. A Comprehensive Overview on Synthesis Techniques of Nanostructured Oxides
   B.M. Reddy, **P. Bharali**, and P. Saikia
   In **New Nanotechniques** (Ed., F. Columbus), Nova Science Publishers, Inc., New York, 2009 (In press).

2. Catalytic Regulation and Utilization of Greenhouse Gases
   B.M. Reddy, G. Thrimurthulu, and **P. Bharali**
   In **The Developments in Environmental Pollution and Climate Change** (Ed., Ahmed El Nemr), Springer Publishers, 2009 (In press).

Journals

3. B.M. Reddy, P. Saikia, **P. Bharali**, S.-E. Park, M. Muhler, W. Grünert:
   Physicochemical Characteristics and Catalytic Activity of Alumina Supported Nanosized Ceria-terbia Solid Solutions
   Journal of Physical Chemistry C 113 (2009) 2452 – 2462.

4. B.M. Reddy, P. Saikia, **P. Bharali**, L. Katta, G. Thrimurthulu:
   Highly Dispersed Ceria and Ceria-Zirconia Nanocomposites over Silica Surface for Catalytic Applications
   Catalysis Today, 141 (2009) 109 – 114.

5. B.M. Reddy, **P. Bharali**, P. Saikia, G. Thrimurthulu, Y. Yamada, T. Kobayashi:
   Thermal Stability and Dispersion behavior of Nanostructured $Ce_xZr_{1-x}O_2$ Mixed Oxides on Anatase-TiO_2: A Combined Study of CO Oxidation and Characterization by XRD, XPS, TPR, HREM, and UV-vis DRS
   Industrial & Engineering Chemistry Research 48 (2009) 453 – 462.

6. B.M. Reddy, P. Saikia, **P. Bharali**, Y. Yamada, T. Kobayashi, M. Muhler, W. Grünert:
   Structural Characterization and Catalytic Activity of Nanosized Ceria-Terbia Solid Solutions
   Journal of Physical Chemistry C 112 (2008) 16393 – 16399.

7. B.M. Reddy, P. Saikia, **P. Bharali**:
   Highly Dispersed $Ce_xZr_{1-x}O_2$ Nano-oxides over Alumina, Silica and Titania Supports for Catalytic Application
   Catalysis Surveys from Asia, 12 (2008) 214 – 228.

8. B.M. Reddy, **P. Bharali**, Y.-H. Seo, E.A. Prasetyanto, S.-E. Park:
   Surfactant-Controlled and Microwave-Assisted Synthesis of Highly Active $Ce_xZr_{1-x}O_2$ Nano-oxide for CO Oxidation
   Catalysis Letters 126 (2008) 125 - 133.

9. B.M. Reddy, **P. Bharali**, P. Saikia, S.-E. Park, M.W.E. van den Berg, M. Muhler, W. Grünert:
   Structural Characterization and Catalytic Activity of Nanosized $Ce_xM_{1-x}O_2$ (M = Zr and Hf) Mixed Oxides
   Journal of Physical Chemistry C, 112 (2008) 11729 – 11737.

10. B.M. Reddy, **P. Bharali**, G. Thrimurthulu, P. Saikia, L. Katta, S.-E. Park:
    Catalytic Efficiency of Ceria-Zirconia and Ceria-Hafnia Nanocomposite Oxides for Soot Oxidation
    Catalysis Letters, 123 (2008) 327 – 333.

11. B.M. Reddy, G. Thrimurthulu, P. Saikia, **P. Bharali**:
    Silica Supported Ceria and Ceria-Zirconia Nanocomposite Oxides for Selective Dehydration of 4-methylpentan-2-ol
    Journal of Molecular Catalysis A: Chemical, 275 (2007) 167 – 173.

12. B.M. Reddy, P. Lakshmanan, **P. Bharali**, P. Saikia, G. Thrimurthulu, M. Muhler, W. Grünert:
    Influence of Alumina, Silica, and Titania Supports on the Structure and CO Oxidation Activity of $Ce_xZr_{1-x}O_2$ Nanocomposite oxides
    Journal of Physical Chemistry C, 111 (2007) 10478 – 10483.

13. B.M. Reddy, **P. Bharali**, P. Saikia, A. Khan, S. Loridant, M. Muhler, W. Grünert:
    Hafnium Doped Ceria Nanocomposite Oxide as a Novel Redox Additive for Three-way Catalysts
    Journal of Physical Chemistry C, 111 (2007) 1878 – 1881.

14. B.M. Reddy, P. Lakshmanan, **P. Bharali**, P. Saikia:
    Dehydration of 4-methylpentan-2-ol over $Ce_xZr_{1-x}O_2/SiO_2$ nano-composite catalyst
    Journal of Molecular Catalysis A: Chemical, 258 (2006) 355 – 360.

15. B.M. Reddy, K.N. Rao, G.K. Reddy, **P. Bharali**:
    Characterization and catalytic activity of $V_2O_5/Al_2O_3–TiO_2$ for selective oxidation of 4-methylanisole
    Journal of Molecular Catalysis A: Chemical, 253 (2006) 44 – 51.

16. B.M. Reddy, **P. Bharali**, G. Thrimurthulu, P. Saikia:
    Influence of Dopant Cations on the Structural Properties and Catalytic Activity of $Ce_xZr_{1-x}O_2$ Mixed Oxides
    Chemistry – An Asian Journal (Submitted).

17. B.M. Reddy, **P. Bharali**, G. Thrimurthulu, Y. Yamada, T. Kobayashi:
    Nanostructured $Ce_xHf_{1-x}O_2/SiO_2$ Mixed Oxide: Structural Characterization and Catalytic Activity for Dehydration of 4-methylpentan-2-ol
    Journal of Catalysis (Submitted).

18. B.M. Reddy, **P. Bharali**, G. Thrimurthulu, K.N. Rao:
    Structural Characteristics, Thermal Stability and Catalytic Properties of Al_2O_3 Supported Nanostructured $Ce_{0.8}Hf_{0.2}O_2$ Solid Solutions
    Chemistry of Materials (To be submitted)

Patents Filed

1. Process for preparing nanosized multicomponent metal oxides possessing better thermal stability, high surface area, superior oxygen storage and release capacity and CO oxidation activity
   B.M. Reddy, **P. Bharali**, P. Saikia, G. Thrimurthulu
   Filed in USA and India

2. A process for preparing nanosized multicomponent metal oxides containing cerium and terbium with superior physicochemical properties and catalytic activity
   B.M. Reddy, P. Saikia, **P. Bharali**, G. Thrimurthulu
   Filed in USA and India

SYMPOSIA/ CONFERENCE/ PRESENTATIONS

1. L. Katta, P. Saikia, **P. Bharali**, G. Thrimurthulu, B.M. Reddy:

   A comparative study on catalytic behaviour of Al_2O_3 supported nanostructured ceria-based mixed oxides **(Awarded best poster)**

   *National Conference on Recent Advances in Chemical Research (NCRACR-2009), Hyderabad, 6th – 7th February, **2009** (Council of Scientific and Industrial Research, New Delhi & Osmania University, Hyderabad).*

2. G. Thrimurthulu, **P. Bharali**, P. Saikia, B.M. Reddy:

   Structural characterization and CO oxidation activity over metal-ion-doped $Ce_xZr_{1-x}O_2$ mixed oxides **(Awarded best poster)**

   *National Conference on Recent Advances in Chemical Research (NCRACR-2009), Hyderabad, 6th – 7th February, **2009** (Council of Scientific and Industrial Research, New Delhi & Osmania University, Hyderabad).*

3. L. Katta, P. Saikia, **P. Bharali**, G. Thrimurthulu, B.M. Reddy:

   A comparative study on catalytic behaviour of Al_2O_3 supported nanostructured ceria-based composite oxides

   *CATSYMP-19: Catalysis for Sustainable Energy and Chemicals, Pune, 18th – 21st January, **2009** (Catalysis Society of India).*

4. G. Thrimurthulu, **P. Bharali**, P. Saikia, B.M. Reddy:

   Structural characterization and CO oxidation activity over metal-ion-doped $Ce_xZr_{1-x}O_2$ composite oxides

   *CATSYMP-19: Catalysis for Sustainable Energy and Chemicals, Pune, 18th – 21st January, **2009** (Catalysis Society of India).*

5. P. Saikia, **P. Bharali**, G. Thrimurthulu, L. Katta, B.M. Reddy:

   Doping of different isovalent cations (Hf^{4+}, Zr^{4+} and Tb^{4+}) into ceria and their influence on OSC and CO oxidation activity (**Awarded best poster**)

   *National Workshop on Catalysis: Futuristic Materials as Catalysts and Adsorbents, Bhubaneswar, 18th – 20th February, **2008** (Catalysis Society of India).*

6. L. Katta, G. Thrimurthulu, P. Saikia, **P. Bharali**, B.M. Reddy:

   Influence of isovalent cations on OSC and CO oxidation activity of cerium oxide *National Symposium on Chemistry-Technology Interface: A Synergistic Approach, Hyderabad, 30th September – 2nd October, **2007** (Department of Chemistry, Nizam College, Osmania University).*

7. P. Saikia, **P. Bharali**, G. Thrimurthulu, P. Lakshmanan, B.M. Reddy:

   Stabilization of ceria and ceria-zirconia nano-oxides over silica support for catalytic applications

   *18th National Symposium on Catalysis, Catalysis for future fuels, Dehradun, 16–18 April, **2007** (Catalysis Society of India).*

8. G. Thrimurthulu, **P. Bharali**, P. Saikia, A. Khan, B.M. Reddy:

   Thermal and redox properties of nanosized CeO_2 and CeO_2−ZrO_2: A comparative study

   *18th National Symposium on Catalysis, Catalysis for future fuels, Dehradun, 16–18 April, **2007** (Catalysis Society of India).*

9. B.M. Reddy, **P. Bharali**, P. Saikia, S. Loridant, M.W.E. van den Berg, M. Muhler, W. Grünert:

   Hafnium doped ceria nano-composite oxide – a promising catalyst for low temperature CO oxidation

   *German Catalysis Conference, Weimar, 14–16 March, **2007** (German Catalysis Society, Weimar).*

10. **P. Bharali**, G. Thrimurthulu, P. Saikia, B.M. Reddy:

    Synthesis and characterization of novel nanosized cerium-hafnium composite oxides

    *National Review and Coordination Meeting on Nanoscience and Nanotechnology, Hyderabad, 21–23 February, **2007** (ARCI, Hyderabad).*

11. **P. Bharali**, G. Thrimurthulu, P. Saikia, B.M. Reddy:

    Application of nano-oxides in auto exhaust gas purification

    *Recent trends in nanomaterial science, ASTC, Hyderabad, 28 August, **2006** (Academy for Science, Technology and Communication, Hyderabad).*

12. B.M. Reddy, **P. Bharali**, P. Saikia, P. Lakshmanan:

    Design of supported nanosized $Ce_xZr_{1-x}O_2$ mixed oxide catalysts

    *National workshop on catalysis for energy, Varanasi, 23–25 February, **2006** (Catalysis Society of India).*